Mémoire d'Habilitation à Diriger des Recherches (HDR)
Université Paris Diderot (Paris 7)
Spécialité : Physique

Description de quelques phénomènes physiques dans les plasmas et gaz avec ou sans collisions.

Filippo Pantellini

Présenté le 12 janvier 2009, à 15h
à Meudon (Observatoire de Paris)

Jury

Marcello Fulchignoni	Université Paris Diderot	Président
Gérard Belmont	CETP, Velizy	Rapporteur
Pierluigi Veltri	Università della Calabria	Rapporteur
Jean-Claude Adam	CPHT, École Polytechnique, Palaiseau	Examinateur
Jacques Léorat	LUTH, Observatoire de Paris	Examinateur
Jean-Claude Vial	Institut d'Astrophysique Spatiale, Orsay	Examinateur

Préface

Je résume dans cet ouvrage quelques uns des sujets de recherche sur lesquels j'ai travaillé au cours de la dernière douzaine d'années. La présentation est volontairement peu détaillée et peu technique, dans la mesure où il m'aurait été difficile d'aller au fond des choses pour chacun des sujets traités dans ce mémoire. Les références bibliographiques, les notes de bas de page et les articles en annexe pourront cependant guider le lecteur curieux vers les articles pointus de la littérature spécialisée. Les choix thématiques au sein de chaque chapitre sont plus dictés par leur relation avec mon propre travail que par leur importance absolue dans le domaine de la science traité au sein du chapitre. Certains travaux, notamment d'écriture de codes, qui m'ont souvent pris des mois de travail mais qui n'ont pas donné les résultats escomptés ne sont pas présentés ici.

Même si le centre de gravité de mes activités de recherche se situe dans le domaine de la physique des plasmas spatiaux, il m'est difficile de classer sous une dénomination commune les sujets traités dans ce mémoire. Il est cependant possible de relier les différentes activités de recherche qui m'ont occupé depuis mon doctorat, par un lien logique que l'on devrait pouvoir classer dans la catégorie des liens dits "de fil en aiguille". Au début du fil il y a des travaux sur la simulation de chocs dans les plasmas non collisionnels (chapitre 2). Suivent des travaux sur l'instabilité miroir (chapitre 3) qui est une instabilité des plasmas non collisionnels, souvent observée dans les plasmas spatiaux et quelques fois en association avec des chocs. Après ces débuts dans le domaine des plasmas non collisionnels lesquels, il est vrai, trouvent un champ d'application formidablement riche dans le contexte de l'exploration du vent solaire et des environnements planétaires, je me suis intéressé aux plasmas collisionnels que l'on trouve aussi bien en astrophysique qu'au laboratoire. Au départ de cette nouvelle phase dans ma vie de chercheur, il y a eu un petit code en fortran, à destination des étudiants en maitrise de physique à l'Université Paris Diderot dans laquelle j'ai enseigné la mécanique des fluides par l'intermédiaire de la simulation numérique pendant une dizaine d'années. Le code, léger et facile d'utilisation, permet de simuler en une seule dimension[1] et sans hypothèses arbitraires, l'établissement de l'équilibre hydrostatique d'un gaz dans un champ gravitationnel constant donné

[1] L'unidimensionalité du domaine de simulation est la principale raison de l'efficacité du code en raison du petit nombre de molécules (de l'ordre de 50) nécessaires pour modéliser une atmosphère statique sur une distance de plusieurs fois l'échelle de hauteur.

par la formule barométrique établie pour la première fois, en 1686, par l'astronome anglais E. Halley (cf annexe 5). Le code était initialement conçu pour la simulation d'un gaz dans lequel les molécules subissent des collisions élastiques de type boules de billard. Très rapidement, l'envie d'adapter le code à la simulation de plasmas collisionnels s'est fait sentir. Malgré les difficultés techniques innombrables, inhérentes à toute conception et mise en oeuvre d'un nouveau code numérique, l'adaptation au cas plasma a finalement pu se faire, en grande partie, pendant le doctorat de Simone Landi. Coté applications, dans un premier temps à deux, Simone et moi, nous nous sommes intéressés au problème de la conduction de la chaleur dans des plasmas peu collisionnels, tels la couronne solaire (chapitre 5) et le vent solaire (chapitre 6). Voici que, inspiré et fasciné par l'étrangeté du comportement des systèmes granulaires dans lesquels les collisions entre particules (par exemple des grains de sable) sont inélastiques, j'ai une fois de plus, adapté le code pour étudier l'évolution d'un système de particules interagissant de façon inélastique entre elles (cf chapitre 7), avec l'idée de l'appliquer par la suite à l'étude de situations astrophysiques. A côté de cette recherche sur les systèmes granulaires, a priori fort éloignée de la physique des plasmas spatiaux, mais néanmoins très riche en enseignements, j'ai eu l'idée d'adapter un code de type N-corps (normalement utilisé pour simuler les mouvements d'étoiles dans une galaxie) pour la simulation d'un plasma collisionnel. Avec Arnaud Beck, actuellement doctorant dans notre équipe, je me suis ainsi aventuré dans le domaine, très peu exploré, de la simulation numérique des plasma modérément couplés et peu collisionnels (cf 8). Cette dernière partie est un peu plus détaillée que les autres ; non qu'elle soit plus importante, ou que je lui ai consacré plus de temps, mais parce qu'elle fait appel à des notions de physique des plasmas qui sont peu familières au sein de la communauté des physiciens des plasmas spatiaux.
Aucun des sujet n'est traité dans le détail. Je me suis simplement efforcé, dans chacun des chapitres, de présenter les ingrédients physiques et/ou techniques de base pouvant permettre la compréhension des articles en annexe, même lorsque le lecteur n'est pas un spécialiste de la discipline. L'enchaînement général des sujets peut se résumer de façon expressionniste : plasmas non collisionnels → gaz collisionnels → plasmas collisionnels peu couplés → systèmes granulaires (collisions inélastiques) → plasmas collisionnels modérément couplés.
Je voudrais remercier, tout particulièrement, Pierluigi Veltri de l'Université de Calabre à Arcavacate di Rende et Gérard Belmont du Centre d'Etudes des Environnements Terrestre et Planétaires à Velizy, pour avoir accepter d'écrire un rapport sur mon travail, ainsi que Marcello Fulchignoni, professeur à l'université Paris Diderot qui a bien voulu écrire le troisième rapport et présider le jury d'habilitation. Merci également à Jean-Claude Adam de l'École Polytechnique à Palaiseau, à Jacques Léorat de l'Observatoire de Paris et à Jan-Claude Vial de l'Institut d'Astrophysique Spatiale à Orsay pour avoir bien voulu faire partie du jury.

Table des matières

Chapitre 1

La préhistoire

Le présent ouvrage est un résumé, non exhaustif, de mes travaux de recherche au cours d'un peu plus d'une décennie. Les sujets que j'ai eu le plaisir d'aborder au cours de cette période, avec collègues et étudiants, se distinguent de ceux que j'ai eu à traiter au cours de ma thèse à l'Observatoire de Paris et, encore avant, à l'école polytechnique de Zurich où j'ai été formé à la physique. J'ai en effet commencé ma vie de scientifique et physicien (accessoirement d'astrophysicien) avec un stage de maîtrise dans le groupe d'astronomie du Polytechnique de Zurich en 1986. A l'époque, sous la direction de J. Stenflo et S. Solanki, je me suis intéressé à l'étude des tubes de flux photosphériques du Soleil en utilisant des observations en lumière polarisée obtenues au télescope McMath à Kitt Peak en Arizona. Dans une première publication Solanki *et al.* (1987), nous avions établi une liste de lignes photosphériques particulièrement bien adaptées, en raison de leur grande sensibilité à l'effet Zeeman, pour l'étude des mouvements et des propriétés thermodynamiques à l'intérieur des tubes de flux magnétique qui, en ce temps, échappaient à l'observation directe. Une analyse statistique détaillée du profil de température et des vitesses fluides à l'intérieur de ces tubes a été publiée dans un travail ultérieur Pantellini *et al.* (1988) dans lequel nous avions montré que la température dans les tubes dépend de la densité des tubes par unité de surface (le "filling factor") et que les mouvements à l'intérieur de ceux-ci sont aussi bien verticaux qu'horizontaux. Ce premier contact avec la recherche en astrophysique m'a donné envie de chercher un sujet de thèse dans un laboratoire européen. Les places de doctorant étant très peu nombreuses dans le petit groupe de physique solaire zurichois, je me suis inscrit en DEA à l'Observatoire de Paris, histoire de me perfectionner en astrophysique mais aussi pour améliorer mon français hésitant. Au cours de la foire aux stages du DEA je me suis trouvé face à André Mangeney qui m'a proposé un sujet sur l'instabilité de Kelvin-Helmholtz dans les plasmas non collisionnels, avec l'idée que cette instabilité, responsable de la formation des vagues sur l'eau par jour de vent, puisse être active dans la magnétosphère terrestre, là où des forts gradients de vitesse ont été mesurés par de nombreuses sondes spatiales. Après des mois de travail de dépouillement statistique de raies photosphériques, je me suis dit que je tenais là la possibilité de faire de la

physique, et pourquoi pas de la physique des plasmas. Le stage s'étant bien passé, André Mangeney m'a proposé un sujet de thèse axé principalement sur la simulation numérique des chocs sans collisions[1] avec un code écrit par J.C. Adam et A. Heron de l'école polytechnique de Palaiseau. Bien sûr, j'ai accepté, avec le grand enthousiasme qui envahit, je suppose, l'explorateur qui lève l'ancre pour partir à la recherche du mythique passage du Nord-Ouest. Commençait alors ma deuxième expérience dans le monde de la recherche scientifique, sur une thématique plutôt éloignée de la première. Même si mon travail en physique solaire n'avait pas été de tout repos, étant "condamné" à un travail d'extraction d'informations dans un ensemble de données (des raies spectrales) dont on ne pouvait pas savoir à l'avance si elles contenaient l'information recherchée, j'ai pu constater, au cours de cette deuxième expérience de la difficulté de la mise en oeuvre et de l'exploitation d'un code numérique destiné à la modélisation d'un phénomène physique, en l'occurrence des chocs sans collisions. Les difficultés étaient, bien sûr, d'ordre informatique (algorithmique, vectorisation, etc.) mais également, et surtout, d'ordre conceptuel. Se posait en effet, la question du comment transformer un code périodique[2] pour simuler des chocs dont la structure spatiale de base n'est absolument pas périodique puisque, par définition, un choc sépare spatialement un plasma en mouvement supersonique (le plasma amont) d'un plasma en mouvement subsonique. Il est bien évidemment possible de simuler des structures spatialement non périodiques, en choisissant une périodicité spatiale du domaine de simulation très grande par rapport aux échelles spatiales caractéristiques des chocs. Ainsi, par exemple, dans le vent solaire, l'échelle caractéristique de variation de la structure d'un choc est déterminée principalement par le rayon de giration des ions majoritaires (protons et particules alpha) dans le champ magnétique interplanétaire, c.à.d. de l'ordre de la centaine de kilomètres. On pourrait alors décider de simuler un choc interplanétaire avec un code périodique en choisissant une période spatiale de l'ordre de plusieurs dizaines de fois le rayon de giration des ions, afin de cantonner le choc dans une zone restreinte du domaine de simulation comme illustré dans le panneau du haut de la figure 1.1. Les limites en mémoire et en vitesse de calcul des machines de l'époque m'ont bien sûr conduit à choisir de simuler des chocs en les enfermant dans des domaines de simulation non périodiques, comme illustré dans le panneau du bas de la figure 1.1. Malgré les très gros problèmes de contamination de l'intérieur du domaine de simulation par les bords que pose ce type de simulation[3], nous avons pu montrer dans Pantellini *et al.*

[1] Il faudrait plutôt parler de chocs dans les plasmas sans collisions mais l'usage en a décidé autrement.

[2] Dans un code dit périodique l'univers à simuler est d'extension infinie, mais en ajoutant une condition de périodicité spatiale, cela revient à considérer un système (souvent appelé familièrement "boîte de simulation") de dimension égale à la longueur de la périodicité dans chacune des dimensions spatiales (de 1 à 3) retenues pour le calcul. Le grand avantage des boîtes de simulation périodiques est qu'elles ne comportent aucun bord réel, le système simulé étant de dimension infinie.

[3] Notons que dans les simulations périodiques la contamination existe également, non pas à cause des bords qui sont un lieu particulier dans les simulations non périodique, mais à cause de la

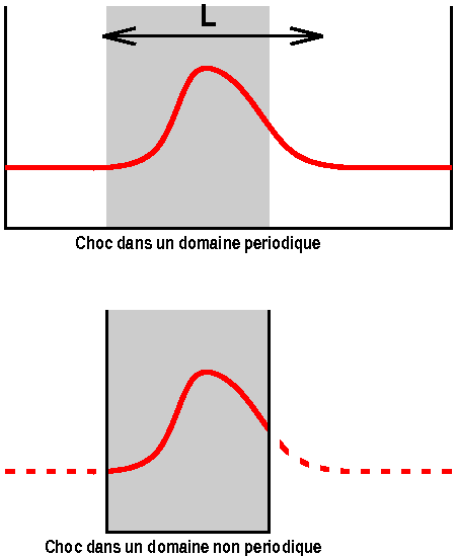

FIG. 1.1 – On peut simuler un choc (ici en rouge, schématiquement, le profil de densité observé par les instruments d'une sonde spatiale) en utilisant un code périodique (figure du haut). Dans ce cas le domaine de simulation doit être plus grand que l'extension spatiale caractéristique L du choc afin que la densité, et tous les autres champs tels la température, la vitesse du fluide, l'intensité du champ magnétique, etc. ne soient pas discontinus entre les bords du domaine, même si la zone qui intéresse le simulateur se limite à la zone grise. Dans un code non périodique (figure du bas) on peut limiter la zone de simulation à la zone intéressante (la zone grise), les bords du domaine de simulation n'étant pas reliés par la condition de périodicité. Le domaine simulé est dans ce cas plus petit que dans le cas de la simulation périodique, mais se pose alors le problème du choix des conditions du plasma au voisinage des limites du domaine de simulation.

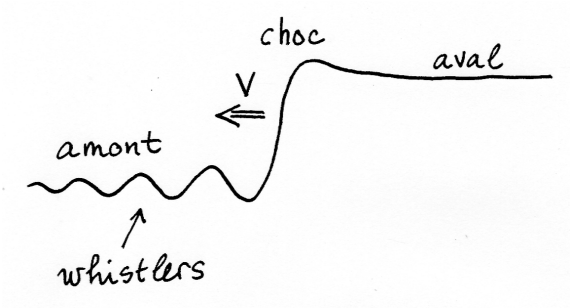

FIG. 1.2 – Si les conditions sont favorables, un train d'ondes stationnaires (dans le repère du choc) peuvent exister en amont d'un choc. Dans un plasma non collisionnel ce train d'ondes "whistler" est parfois associé à un comportement non stationnaire du choc (cf Pantellini *et al.* (1992)).

(1992) que dans certains cas les chocs en propagation quasi-parallèle par rapport au champ magnétique ambiant (cf figure 2.1) sont instables et subissent des destructions cycliques, en raison d'ondes dites "whistler" émises vers l'amont du choc (cf figure 1.2). J'ai continué à travailler dans le domaine de la simulation des chocs non collisionnels après ma thèse, au cours de mon postdoc au Queen Mary College de Londres avec principalement David Burgess et Steve Schwartz. C'est le sujet du prochain chapitre, dans lequel je détaille la question des ondes dites "whistler" (siffleurs en français) dans les chocs.

condition de périodicité elle même qui permet, par exemple, à une fluctuation de densité sortant à droite de revenir par la gauche.

Chapitre 2

Sur les chocs non collisionnels

2.1 Généralités sur les chocs non collisionnels, spatiaux en particulier

Depuis plusieurs décennies, les chocs sans collisions constituent un champ d'exploration particulièrement riche pour tous les simulateurs de plasmas sans collisions. La raison principale, mais non unique, est qu'un choc non collisionnel est un objet d'une complexité stupéfiante. Il suffit, pour s'en convaincre, de parcourir la littérature spécialisée sur les observations de chocs non collisionnels dans l'héliosphère pour constater qu'il n'y en a jamais deux qui se ressemblent (voir les exemples dans l'article de revue sur les observations des sondes ISEE1 et ISEE2 Russell et Greenstadt, 1979). Comment peut-on, dans ces conditions, arriver à résumer succinctement le "fonctionnement" d'un choc sans collisions ? Bien évidemment, la structure du choc dépend des paramètres du plasma dans lequel il se propage. Citons, parmi les paramètres importants, le "beta" du plasma $\beta \equiv p_{\rm g}/p_{\rm m}$, i.e. le rapport entre la pression gazeuse $p_{\rm g}$ (due à l'agitation thermique des ions et des électrons du plasma) et la pression magnétique $p_{\rm m} = B^2/2$, mais également, puisque le plasma est non collisionnel et donc potentiellement hors équilibre thermodynamique, le rapport entre la température des ions $T_{\rm i}$ et la température des électrons $T_{\rm e}$. Mais ce n'est pas tout, car en plus des paramètres du plasma, interviennent les paramètres du choc lui même, lesquels, dans le cas le plus simple d'un choc plan et unidimensionnel, sont au minimum deux : 1) le nombre de Mach M, c.à.d., le rapport entre la vitesse de propagation du choc V le long de la normale au choc $\vec{n}$ et une vitesse caractéristique du milieu (par exemple la vitesse du son) et 2) l'angle $\theta_{\rm Bn}$ entre la normale au front du choc et la direction du champ magnétique $\vec{B}$, comme illustré dans la figure 2.1. En outre, les chocs naturels ne sont jamais plans. Ainsi, les ondes de choc formées par l'interaction des magnétosphères planétaires avec le vent solaire dont le rayon de courbure est typiquement de l'ordre de un ou deux fois le rayon de la planète (c'est le cas de Mercure) voire une dizaine ou plus de fois le rayon de la planète (c'est la cas de la Terre ou des planètes géantes du système solaire). Les rayons de courbure des chocs se propageant dans le milieu interplanétaire où des ondes de

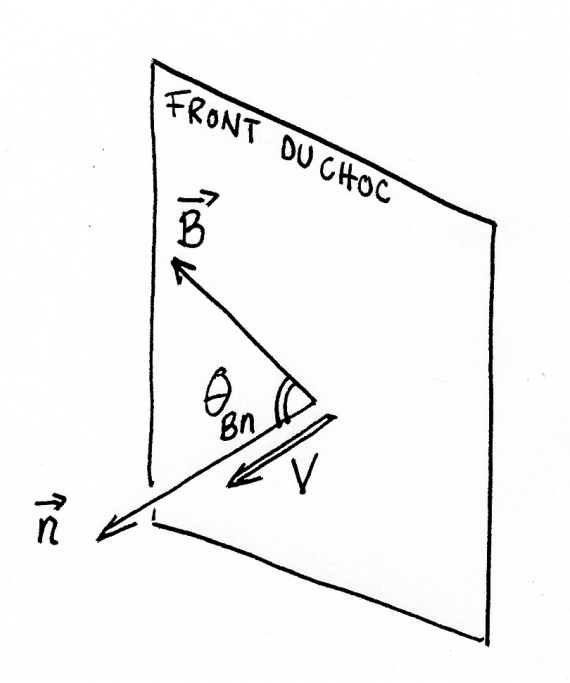

FIG. 2.1 – Sans compter les paramètres qui spécifient le plasma, la structure d'un choc stationnaire, plan et infini, dépend uniquement de l'angle $\theta_{\rm Bn}$ entre le champ magnétique $\vec{B}$ et la normale au choc $\vec{n}$ et de sa vitesse de propagation V le long de $\vec{n}$.

choc engendrées dans le milieu interstellaire par l'explosion d'étoiles (les chocs de supernovae) sont évidemment encore bien plus grands pouvant atteindre, dans ce dernier cas, des courbures de l'ordre de plusieurs parsecs. La complication inhérente aux chocs non collisionnels et non plans est que certaines zones du choc peuvent être "contaminées" par d'autres zones du choc, l'absence de collision permettant, dans certains cas, la remontée de particules de l'aval vers l'amont en suivant les lignes de champ magnétique. C'est un moyen efficace, trouvé par les chocs non collisionnels à grand nombre de Mach[1] pour transformer l'énergie cinétique du plasma incident en énergie thermique, ce qui au fond est le "job" d'un choc. La figure 2.2 montre la magnétosphère terrestre et le choc formé par son interaction avec le vent solaire avec, en couleurs, les zones en amont du choc "contaminées" par les électrons et les protons réfléchis. En jaune la zone dominée par des électrons réfléchis (précurseur électronique), en rouge la zone où on retrouve aussi bien des ions que des électrons réfléchis (précurseur ionique). De toute évidence, les électrons et les protons ne sont pas réfléchis de la même manière. La différence est bien évidemment la conséquence

[1] On nomme ces chocs supercritiques, par opposition aux chocs sous critiques qui ne réfléchissent aucune particule vers l'amont du choc, les instabilités cinétiques à petite échelle localisées dans la rampe du choc étant suffisamment efficaces pour transformer l'énergie cinétique dirigée en énergie thermique. Dans le vent solaire, le nombre de Mach alfvénique d'un choc supercritique doit satisfaire à $M_{\rm A} \gtrsim 2$, mais cette limite dépend de l'angle de propagation $\theta_{\rm Bn}$.

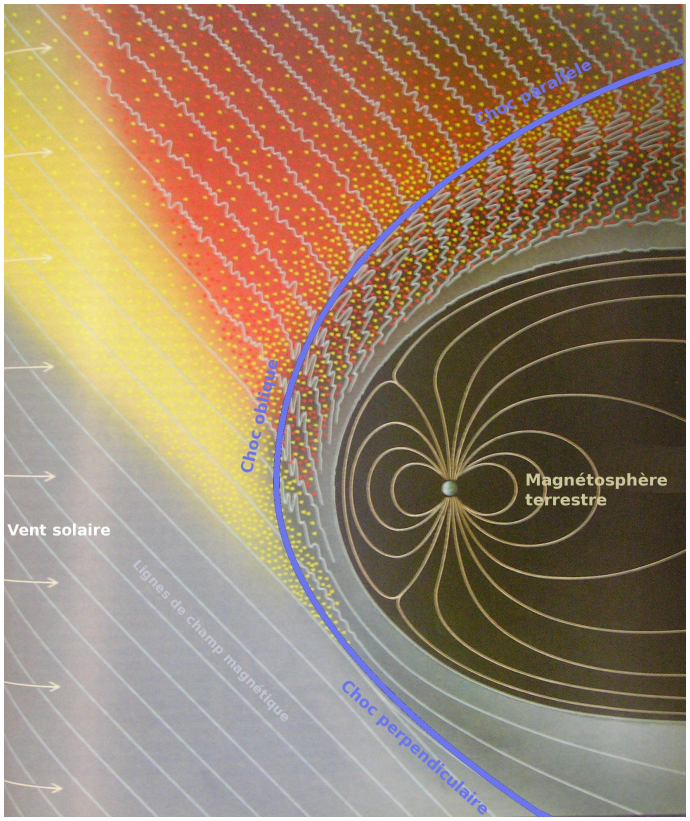

FIG. 2.2 – En jaune la zone en amont du choc de la Terre peuplée par des électrons réfléchis (précurseur électronique), en rouge la zone peuplée par des ions et des électrons réfléchis (précurseur ionique). Les courbes grises représentent les lignes de force du champ magnétique interplanétaire. Les courbes marron représentent les lignes de force du champ magnétique terrestre. Adapté de Sagdeev et Kennel (1991).

de la différence de masse entre les deux espèces de particules. En effet, dans un plasma à température T la vitesse caractéristique des particules de masse m est de l'ordre de $\sqrt{k_\mathrm{B}/m}$. Il s'en suit que, si les températures des espèces sont du même ordre, les électrons sont environ 40 fois plus rapides que les protons, et peuvent donc remonter beaucoup plus facilement le long d'une ligne de champ magnétique advectée par le vent solaire[2]. Même lorsque l'angle θ_Bn est proche de 90° les électrons (largement plus rapides que le choc) sont en mesure de remonter vers l'amont, alors que pour les ions, cela n'est en général possible que pour des angles $\theta_\mathrm{Bn} \lesssim 50°$. C'est la raison de la ségrégation spatiale entre électrons et ions réfléchis en amont du choc de la Terre. Par ailleurs, la figure 2.2 illustre le fait que lorsque l'amont du choc est fortement perturbé par des ions réfléchis, c.à.d. dans la région en amont du choc parallèle ou oblique, la structure magnétique du choc est très irrégulière avec de fortes

[2]La très bonne conductivité électrique du milieu interplanétaire a pour conséquence que le champ magnétique est advecté par la matière. Cette propriété des fluides infiniment conducteurs est un théorème de la MHD idéale connu sous le nom de "théorème du gel".

fluctuations en amplitude, en nette contraste avec la transition monotone et lisse observée coté choc perpendiculaire. La Figure 2.2 illustre et résume donc de façon impressionniste la complexité d'une onde de choc dans un plasma non collisionnel.

2.2 Résultats d'une simulation PIC en deux dimensions spatiales

Dans l'article Krauss-Varban *et al.* (1995) de l'annexe 1, nous utilisons le code PIC [3] en deux dimensions spatiales afin de simuler un choc en propagation quasi-perpendiculaire, i.e. $\theta_{\mathrm{Bn}} = 60°$. Les simulations sont basées sur le code PIC que j'avais précédemment utilisé pendant mon doctorat, mais avec un rapport de masse entre proton et électron $m_{\mathrm{p}}/m_{\mathrm{e}} = 400$, ce qui était une valeur très élevée pour l'époque où l'on se limitait le plus souvent à des valeurs inférieures à 100. Comme le montre la relation de dispersion des ondes whistler de la figure 1 de l'article, calculée pour des conditions typiques du choc de la Terre, un rapport de masse trop faible (par exemple $m_{\mathrm{p}}/m_{\mathrm{e}} = 100$), change le sens de propagation des ondes whistler dans le repère du choc. En d'autres termes, si $m_{\mathrm{p}}/m_{\mathrm{e}} = 100$ la vitesse de phase des whistlers se propageant à 30° par rapport au champ magnétique est dirigée vers l'aval, alors que pour $m_{\mathrm{p}}/m_{\mathrm{e}} \gtrsim 400$, la vitesse de phase de ces mêmes whistlers est dirigée vers l'amont, ce qui évidemment change considérablement la structure du choc. Dans cet article nous montrons que les ondes whistler se propagent vers l'amont du choc dans une direction intermédiaire entre la normale au choc $\vec{n}$ et le champ magnétique $\vec{B}$. Ces ondes sont engendrées par les ions réfléchis, elles sont donc excitées par un mécanisme cinétique ne pouvant pas se produire dans un code fluide (magnétohydrodynamique en l'occurrence). Les caractéristiques des ondes (longueur d'onde, fréquence, compressibilité, etc) sont parfaitement compatibles avec les ondes dites "one-Herz" en raison de leur fréquence caractéristique, observées en amont de chocs non collisionnels. Contrairement aux ions qui subissent un chauffage irréversible et violent lors du passage du choc, les électrons ont un comportement essentiellement adiabatique. Une des nombreuses spécificités qui différencie les chocs non collisionnels des chocs collisionnels est que dans les premiers, le chauffage que le choc produit lors de son passage n'est pas nécessairement le même pour chacune des espèces qui constituent le plasma. En particulier les protons, mais c'est souvent le cas pour les ions en général, sont plus fortement chauffés que les électrons. Mais il y a "pire" : le chauffage est souvent extrêmement anisotrope par rapport à la direction du champ magnétique. Ainsi, par exemple, dans le cas d'un choc quasi-perpendiculaire se propageant dans le vent solaire, le chauffage est quasiment toujours plus efficace dans le

[3] PIC pour "Particles In Cell". Les particules (électrons et protons) se déplaçant sous l'action de champs électriques et magnétiques définis sur les coins d'une grille spatiale en une, deux, ou trois dimensions. Les détails de la méthode dite "méthode directe" sont à chercher dans l'article fondateur de Hewett et Langdon (1987). La version périodique du code avait été écrite par Anne Héron et Jean-Claude Adam de l'École Polytechnique à Palaiseau. La version non-périodique utilisée dans l'article est de moi.

plan perpendiculaire au champ magnétique. Le résultat de ce chauffage anisotrope est la formation d'un gaz de protons dont la température perpendiculaire est plus forte que dans la direction parallèle. C'est une situation potentiellement instable qui peut, sous certaines conditions, provoquer le déclenchement de l'instabilité miroir dont il est question dans le chapitre 3.

Chapitre 3

Sur l'instabilité miroir protonique

3.1 Généralités

Comme nous venons de le souligner à la fin du chapitre 2, dans un plasma non collisionnel, l'agitation thermique des particules (température) n'est pas nécessairement identique parallèlement et perpendiculairement au champ magnétique, le mouvement d'une charge le long du champ étant a priori découplé du mouvement perpendiculaire au champ. Lorsque la température perpendiculaire $T_\perp$ est plus grande que la température parallèle $T_\parallel$ le plasma est potentiellement instable. Une des instabilités possibles est l'instabilité miroir. Si nous considérons le cas d'un plasma homogène et uniforme constitué uniquement de protons et d'électrons, et que nous supposons, dans un premier temps, que les électrons sont complètement froids $T_\mathrm{e} = 0$, nous pouvons imaginer que la distribution en vitesse des protons (de masse m_p) est donnée par la distribution dite bi-maxwellienne

$$f(v_\parallel, v_\perp) = n_0 \frac{\pi^{-3/2}}{v_{\mathrm{T}\perp}^2 v_{\mathrm{T}\parallel}} \exp\left[-\frac{v_\parallel^2}{v_{\mathrm{T}\parallel}^2} - \frac{v_\perp^2}{v_{\mathrm{T}\perp}^2}\right] \tag{3.1}$$

où n_0 est la densité de protons, $v_{\mathrm{T}\parallel}^2 \equiv 2k_\mathrm{B}T_\parallel/m_\mathrm{p}$ la vitesse thermique parallèle, $v_{\mathrm{T}\perp}^2 \equiv 2k_\mathrm{B}T_\perp/m_\mathrm{p}$ la vitesse thermique perpendiculaire, et k_B la constante de Boltzmann. Un iso-contour de la distribution (3.1) dans le plan $(v_\parallel, v_\perp)$ est montré dans la figure 3.1. On devine que cette configuration est potentiellement instable dans la mesure où une partie de l'excès d'énergie cinétique dans la direction perpendiculaire au champ magnétique (voir figure 3.1) peut être utilisée pour alimenter la croissance d'ondes magnétohydrodynamiques. Sans trop rentrer dans le détail, il est intuitivement clair qu'une augmentation du champ magnétique tend à relever le niveau de anisotropie nécessaire pour déclencher l'instabilité. Le calcul rigoureux, à partir de l'équation de Vlasov pour un plasma constitué d'électrons froids et de protons, dont la distribution

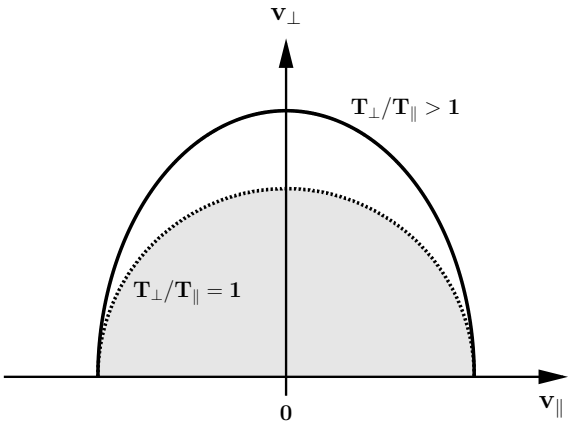

FIG. 3.1 – Isocontour de la fonction de distribution (3.1) dans le cas potentiellement instable $T_\perp/T_\parallel = 2$ (courbe en trait plein). Le cas stable avec $T_\perp/T_\parallel = 1$ est donné comme référence.

à l'équilibre est donnée par (3.1), conduit à la condition d'instabilité [1]

$$\frac{T_\perp}{T_\parallel} > 1 + \frac{1}{\beta_\perp} \tag{3.2}$$

où $\beta_\perp \equiv 8\pi p_\perp / B^2$ est le rapport entre la pression gazeuse des protons $p_\perp$ et la pression magnétique $B^2/8\pi$. Même s'ils n'ont pas été les premiers à s'intéresser à l'instabilité, connue depuis les années 1960, Southwood et Kivelson (1993) ont donné une description détaillée du mécanisme physique de l'instabilité en mettant en avant son caractère fondamentalement cinétique[2]. L'instabilité miroir a été reconnue comme étant à l'oeuvre dans quasiment tous les plasmas spatiaux visités par des sondes, aussi bien dans le vent solaire libre que dans les magnétosphères planétaires. Elle se caractérise principalement, aussi bien dans la phase linéaire que dans la phase saturée, par le fait que les fluctuations du champ magnétique δB et les fluctuations de densité δn sont anticorrélées[3], (cf figure 3.2) mais aussi par le fait que la vitesse de propagation de ces fluctuations est nulle dans le repère du plasma. Si on trace, spatialement et en 2 dimensions, les lignes de champ magnétique après

[1] Lorsque la distribution d'équilibre des protons n'est pas bi-maxwellienne, la condition d'instabilité (3.2) peut différer quelque peu de (3.2) (voir Rose (1965)). D'autre auteurs ont plus récemment généralisé la condition d'instabilité (3.2) au cas d'un plasma comportant plusieurs espèces (Pokhotelov *et al.*, 2002; Hellinger, 2007).

[2] Un comportement cinétique est un comportement qui ne se laisse pas décrire par les équations fluides classiques de la MHD. Cela est souvent lié au fait qu'un petit nombre de particules du plasma se comporte différemment de toutes les autres, par exemple à cause de résonances avec des ondes électromagnétiques.

[3] Notons que les fluctuations de densité et de champ magnétique sont anticorrélées afin d'assurer une pression spatialement constante. De ce fait, les fluctuations de la pression totale (thermique + magnétique) sont nulles. Dans le cas d'instabilités à faible croissance on a $\delta p + B_0 \delta B/4\pi = 0$ (e.g. Pantellini et Schwartz, 1995). Le plasma n'est alors soumis à aucune force, ce qui se manifeste également par une absence de propagation.

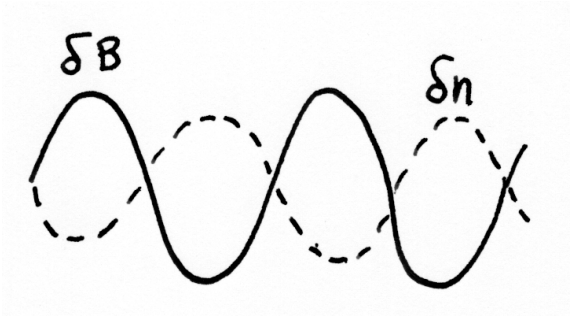

FIG. 3.2 – Variation spatiale des fluctuations de densité et des fluctuations de champ magnétique dans un mode miroir.

croissance de l'instabilité à partir d'une situation initialement uniforme, on obtient des déformations des lignes de champ formant des structures en bouteille comme dans la figure 3.3, avec des zones de concentration et des zones de raréfaction du champ. La fluctuation magnétique dans la figure 3.2 s'obtient, par exemple, en mesurant le champ le long de l'axe de la bouteille (ligne pointillée dans la figure 3.3). Ce type de configuration magnétique permet le piégeage de particules dans la zone de champ magnétique faible, i.e. dans la zone centrale de la bouteille. Le piégeage est une conséquence directe du fait que lorsque le champ magnétique ne varie pas trop lors d'un tour de la particule de masse m autour du champ magnétique local, il y a conservation du moment magnétique $\mu \equiv mv_\perp^2/2B$ (premier invariant adiabatique) et de l'énergie cinétique $mv^2/2$. Ces deux invariants impliquent, dans la limite de fluctuations faibles $\delta B/B \ll 1$, que les particules pour lesquelles les composantes de vitesse $\perp$ et $\parallel$ au voisinage du minimum magnétique (le long de leur trajectoire) satisfaisant à la condition $(v_{0\parallel}/v_{0\perp})^2 \leq 2\delta B/B$ sont piégées dans la bouteille magnétique. La force responsable du piégeage dépend donc de la variation de l'intensité du champ magnétique le long des lignes de champ. La force qu'on appelle pour des raisons évidentes force miroir, dépend donc du moment magnétique de la particule μ et de la variation de l'intensité du champ dans la direction parallèle. Elle s'écrit $f_\mathrm{m} = -\mu \nabla B_\parallel$. Dans l'article de l'annexe 2 (Pantellini *et al.* (1995)) nous montrons, avec des arguments théoriques et avec des simulations à l'appui, que les particules piégées jouent un rôle important dans la phase non linéaire de l'instabilité miroir et que la théorie quasi-linéaire proposée par Shapiro et Shevchenko (1964) ne peut être valable en général puisque le piégeage de particules n'y est pas prévu. Émerge donc l'idée que le piégeage des protons est un ingrédient fondamental de l'évolution non linéaire de l'instabilité miroir.

3.2 Instabilité miroir et trous magnétiques

Dans l'article de l'annexe 4 (Pantellini (1998) je vais plus loin en proposant un modèle purement théorique de la phase non linéaire et de la saturation de l'instabilité miroir toujours avec le piégeage des protons comme ingrédient fondamental. Une des

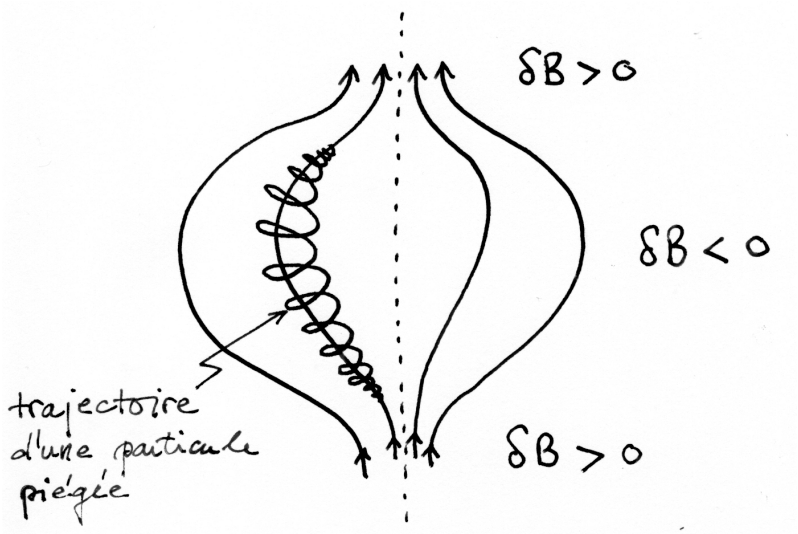

FIG. 3.3 – Lignes de champ magnétique résultant de l'instabilité miroir avec trajectoire caractéristique d'une particule piégée rebondissant entre deux points miroir à l'intérieur de la bouteille magnétique.

raisons qui m'avaient poussé à continuer à travailler sur le sujet était qu'une forte majorité des structures magnétiques statiques, observées dans les plasmas spatiaux et qui pouvaient avoir été engendrées par l'instabilité miroir, était de type "trou magnétique" et non de type bosse magnétique (voir figure 3.4) comme semblaient l'indiquer les simulations numériques parmi lesquelles la simulation de l'annexe 2. Il

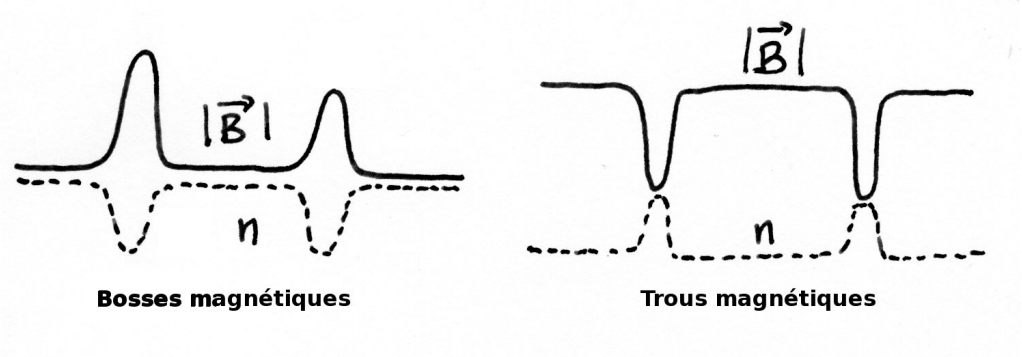

FIG. 3.4 – Les structures magnétiques statiques, observées dans les plasmas spatiaux sont le plus souvent de type "trou" plutôt que de type "bosse" (e.g. Winterhalter *et al.*, 1994).

s'agissait, en fin de compte, d'établir si l'instabilité miroir pouvait être responsable de la formation des trous magnétiques, ce dont peu de connaisseurs du sujet doutaient à l'époque. Le modèle, simple, mais complètement analytique conduit à deux prédictions importantes pour l'instabilité miroir dans des conditions voisines de la stabilité :

1. le mode miroir tend à saturer dans une configuration de type trou magnétique (sauf, peut-être lorsque $\beta_\parallel$ est très grand $\gtrsim 20$),
2. l'intensité maximale du champ saturé est $B_{\max} = B_0\{1 - R + [\beta_\parallel R(1-R)]^{1/3}\}$, où $R \equiv T_\perp/T_\parallel$ et B_0 l'intensité moyenne.

Des simulations PIC avec un très grand nombre de particules ou des simulations Vlasov pourront peut-être confirmer ou infirmer la validité du modèle au cours des années à venir[4].

3.3 Sur le rôle des électrons dans l'instabilité miroir

Dans l'article de l'annexe 3, antérieur à celui sur l'évolution non linéaire, il est question du rôle des électrons dans l'instabilité miroir. Comme souvent, par esprit de simplicité, j'ai adopté l'hypothèse d'une température des électrons nulle $T_\mathrm{e} = 0$. Dans cette limite, les électrons, beaucoup plus légers et mobiles que les protons, se comportent comme un fluide neutralisant sans pression. Lorsque $T_\mathrm{e} \neq 0$, les variations spatiales de la densité électronique n_e (et donc de la pression électronique p_e) engendrent un champ électrique non nul $E_\parallel = -\nabla p_\mathrm{e}/en_\mathrm{e}$, dirigé le long des lignes de champ magnétique. Dans la limite isotherme, $T_\mathrm{e} = const$, les fluctuations linéaires de la densité, du champ magnétique et du champ électrique sont illustrés dans la figure 3.5. La figure illustre le fait que la force électrostatique due aux électrons chauds s'oppose à la force miroir, moteur de l'instabilité. En effet, nous montrons dans l'annexe 3 que les électrons chauds augmentent légèrement l'anisotropie de température $T_\perp/T_\parallel$ nécessaire au déclenchement de l'instabilité (Figure 5 dans Pantellini et Schwartz (1995)) et réduisent sensiblement le taux de croissance du mode le plus instable (Figure 5 dans Pantellini et Schwartz (1995)). Des travaux postérieurs Pokhotelov *et al.* (2000) ont par ailleurs confirmé cette conclusion.

[4]Petr Hellinger (*Institute of Atmospheric Physics* à Prague) me dit qu'il est actuellement en train d'étudier la question de la saturation du mode miroir à l'aide de simulations PIC lourdes, ce qui devrait permettre de trancher la question dans un futur proche.

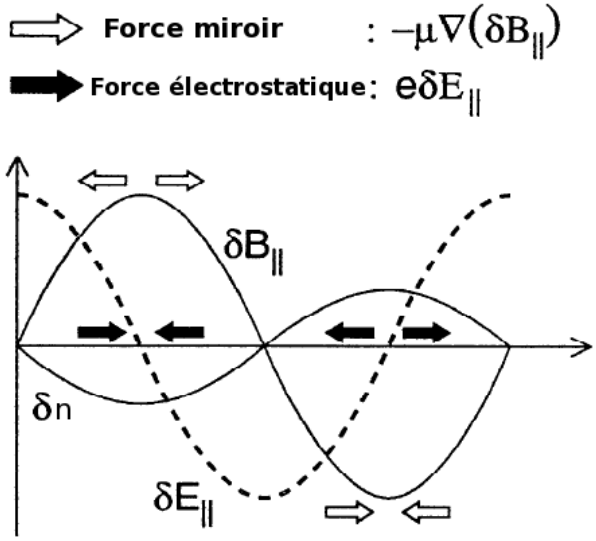

FIG. 3.5 – Profils en fonction de la position le long d'une ligne de champ magnétique de fluctuations de densité, de champ magnétique et de champ électrique associés au mode miroir lorsque la température des électrons est non nulle. On remarque que la force électrostatique s'oppose à la force miroir suggérant qu'une température électronique non nulle s'oppose à l'instabilité miroir (extrait de Pantellini et Schwartz (1995)).

Chapitre 4

Simulations d'un gaz dans un champ gravitationnel

4.1 Introduction

Pour introduire ce chapitre, j'invite le lecteur intéressé à lire l'excellent article de Berberan-Santos *et al.* (1997) qui expose de façon détaillée l'histoire de la découverte de la pression atmosphérique et de sa variation avec l'altitude. Dans le cas le plus simple d'une atmosphère isotherme soumise à un champ gravitationnel constant, la formule barométrique, écrite pour la première fois par E. Halley en 1686, est donnée par

$$p(z) = p_0 \exp(-z/H) \tag{4.1}$$

où p est la pression et z la hauteur au dessus du niveau de référence $z = 0$. Inspiré par l'article de Berberan-Santos *et al.* (1997) je me suis demandé s'il n'était pas possible d'écrire un petit code numérique pour simuler l'établissement du profil de pression prédit par la formule barométrique dans un système de billes (ou boules de billard) semblable au système (a) de la figure 4.1. L'avantage du système (a) par rapport au système (b), plus proche de la réalité, est qu'il est sensiblement plus facile à coder.

4.2 Des simulations basées sur un modèle simple mais efficace

Quelle ne fut pas ma stupeur lorsque en simulant le système (a) j'obtins un profil $p(z)$ proche de celui prévu par (4.1) mais différent tout de même. C'est en constatant la différence, même faible, entre simulation et théorie que je me suis souvenu de mes cours de thermodynamique dans lesquels j'avais appris que le système (a) n'est pas ergodique alors que le système (b), comme l'atmosphère terrestre, sont des systèmes ergodiques [1]. En substance, le système (b) est chaotique alors que le système (a) ne l'est pas, car dans le système (a) à chaque fois que deux sphères se rencontrent, elle ne font qu'échanger leurs vitesses, et puisque les sphères sont identiques c'est comme

[1] cf chapitre II.4 dans l'annexe 5

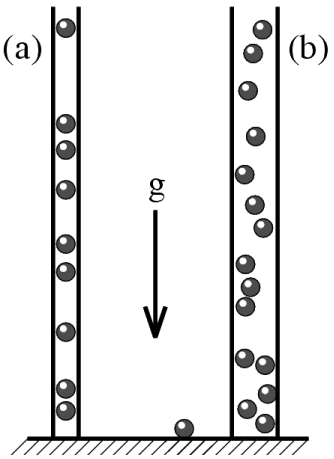

FIG. 4.1 – Collection de billes identiques dans un tube comme modèle pour simuler un gaz dans un champ gravitationnel $\vec{g}$. Dans le système (a) la position de chaque molécule est fonction d'une seule variable d'espace : la hauteur. Dans le système (b) il faut trois coordonnées spatiales pour décrire la position d'une molécule. Malgré l'apparente similarité, seul le système (b) permet de reproduire correctement la formule barométrique (4.1).

si elle se croisaient sans interagir. Dans cette condition, le cas (a) est équivalent à un système de N sphères se mouvant indépendamment les unes des autres, ce qui n'a, bien sûr, rien de chaotique. L'état stationnaire du système est dans ce cas entièrement déterminé par les conditions initiales, alors que dans le cas (b) les conditions initiales sont oubliées après quelques collisions par sphère seulement.
Dans Pantellini (2000), je propose un modèle qui s'apparente au système (b) dans la mesure où les particules se déplacent dans un monde spatialement unidimensionnel (la section du tube étant beaucoup plus petite que sa longueur), mais avec des vitesses tridimensionnelles. La meilleure image d'un tel système est une suite verticale de plans horizontaux, infinis et identiques, pouvant glisser horizontalement les uns par rapport aux autres. Ce système est ergodique, et moyennant les règles de collision établies dans le chapitre III.C de l'annexe 5, la distribution en vitesse des particules tend vers une distribution de Maxwell-Boltzmann isotrope

$$f(v,z) = n(z)\frac{\pi^{-3/2}}{v_{\mathrm{T}}^3}\exp\left[-\frac{v^2}{v_{\mathrm{T}}^2}\right] \tag{4.2}$$

où $n(z)$ est la densité de particules par unité de longueur, $v = |\vec{v}|$, et $v_{\mathrm{T}} \equiv (2k_{\mathrm{B}}T/m)^{1/2}$ la vitesse thermique. La figure 4.2 montre que le système suit rigoureusement, même avec seulement 50 particules, la courbe (en pointillée) prévue par la formule barométrique 4.1 pour une température constante et ceci, indépendamment des conditions initiales.
Le modèle de Pantellini (2000) est très simple à programmer (quelques dizaines de lignes de fortran si on ne cherche pas l'optimisation) et permet d'aborder la question des collisions, de l'ergodicité d'un système thermodynamique et, accessoirement, de

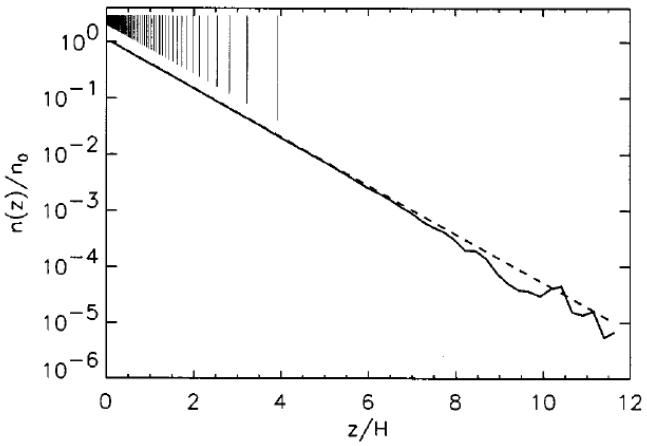

FIG. 4.2 – Profil de densité $n(z)$ (trait plein) obtenu avec 50 particules. Le profil est le résultat d'une moyenne pendant l'intervalle de temps couvrant les premières 10^7 collisions entre l'ensemble des particules du système. Le profil barométrique (en pointillé) est donné comme référence, ainsi que la position moyenne des 50 particules (traits pleins verticaux). Le profil est le résultat d'une moyenne dans le temps (extrait de Pantellini (2000), cf annexe 5)

.

voir s'installer l'équilibre barométrique. Mais, comme nous le verrons dans les chapitres suivants, il permet également de simuler, à bon coût, des plasmas collisionnels. Le principal inconvénient de la version originale de l'algorithme est son inefficacité numérique car le nombre d'opérations mathématiques nécessaires pour atteindre un temps physique donné croît comme N^2. Au cours du doctorat de Simone Landi, nous avons établi un algorithme pour lequel le nombre d'opérations croît comme $N^{3/2}$, sans perte de précision. Typiquement, dans les différentes simulations dont il sera question dans les chapitres 5-7, le nombre de particules N varie entre 10^3 et 10^5. Le gain, en termes de temps de calcul sur un ordinateur donné, est donc d'un facteur tout à fait considérable de 30 à 300 !

Chapitre 5

Simulations d'un plasma dilué soumis à un gradient de température

Vu le succès du modèle numérique du chapitre 4 pour la modélisation d'un gaz dans un champ gravitationnel, j'ai été tenté de l'adapter au cas d'un plasma dans un champ gravitationnel, afin de simuler l'atmosphère solaire dans un premier temps, et le vent solaire dans un second temps. On remplace les boules de billard par des électrons et des protons et le tour est plus ou moins joué. Les choses ne sont évidemment pas si simples que cela. Première difficulté : contrairement aux boules de billard qui n'interagissent qu'avec leurs voisins immédiats, les charges interagissent à longue distance par l'intermédiaire du champ électrique. Deuxième difficulté : la disposition des charges dans le système, même lorsqu'il est en équilibre statique engendre, dans le cas général, un champ électrique à grande échelle qui n'est pas connu a priori. A ce propos, Pannekoek (1922) et Rosseland (1924) ont montré qu'un plasma statique plongé dans un champ gravitationnel est nécessairement associé avec un champ électrique à grande échelle qui assure la quasi-neutralité en tout point du plasma.[1] On calcule facilement le champ de Pannekoek-Rosseland pour un plasma de protons et d'électrons dans la limite statique plongé dans un champ gravitationnel constant g, moyennant une hypothèse de quasi-neutralité $n_{\rm e} = n_{\rm p}$ et une hypothèse d'équipartition de l'énergie $T_{\rm e} = T_{\rm p}$, où n_i et T_i sont respectivement la densité et la température de l'espèce $i = {\rm e}, {\rm p}$. Notons pour commencer que lorsque les forces de friction entre les deux espèces sont nulles ou négligeables (c'est le cas pour une atmosphère isotherme), l'équilibre hydrostatique pour les deux espèces comporte la

[1] On comprend intuitivement que les électrons, étant plus légers que les ions, ont tendance à vouloir se placer au dessus des ions, exactement comme le ferait un fluide peu dense par rapport à un fluide dense. Le champ électrique à grande échelle empêche la décantation des charges et assure la quasi-neutralité.

somme de 3 forces, i.e.

$$n_{\rm p}(m_{\rm p}g + eE_{\rm PR}) - \frac{\partial p_{\rm p}}{\partial z} = 0 \quad (5.1)$$

$$n_{\rm e}(m_{\rm e}g - eE_{\rm PR}) - \frac{\partial p_{\rm e}}{\partial z} = 0. \quad (5.2)$$

où $p_i = n_i k_{\rm B} T_i$ est la pression de la population i, et où nous avons supposé que le champ gravitationnel est dirigé le long de l'axe z, i.e. $\vec{g} = -g\hat{z}$. Les hypothèses de quasi-neutralité et d'équipartition de l'énergie entre protons et électrons impliquent, bien évidemment, l'égalité des pressions $p_{\rm p} = p_{\rm e}$, ce qui permet d'éliminer les termes de pression dans le système ci-dessus pour aboutir à l'équation pour le champ électrique de Pannekoek-Rosseland $E_{\rm PR}$:

$$m_{\rm p}g + eE_{\rm PR} = m_{\rm e}g - eE_{\rm PR}. \quad (5.3)$$

En résolvant l'équation précédente pour le champ électrique, on obtient donc

$$E_{\rm PR} = -\frac{g}{2e}(m_{\rm p} - m_{\rm e}) \approx -\frac{g}{2e}m_{\rm p} \quad (5.4)$$

Dans le cas du proton, la force électrostatique s'oppose au champ gravitationnel alors qu'elle accompagne le champ gravitationnel dans le cas de l'électron. Notons que si une seule des hypothèses utilisées pour obtenir l'équation (5.4) est abandonnée, le champ électrique à grande échelle n'est pas nécessairement égal au champ $E_{\rm PR}$. Ainsi, lorsque le plasma est soumis à un gradient de température, comme par exemple dans le cas de l'atmosphère solaire, où la température passe de 5600K dans la photosphère à 10^6K dans la couronne, un deuxième champ, appelé thermoélectrique $E_{\rm T}$ apparaît dans le système. Contrairement au champ Pannekoek-Rosseland, qui est complètement indépendant de la collisionalité du plasma, le champ thermoélectrique $E_{\rm T}$ n'existe que dans les plasmas collisionnels. Les équations fluides pertinentes, décrivant l'équilibre hydrostatique sont alors :

$$n_{\rm p}eE_{\rm T} - \frac{\partial p_{\rm p}}{\partial z} + \Phi_{\rm p} = 0 \quad (5.5)$$

$$-n_{\rm e}eE_{\rm T} - \frac{\partial p_{\rm e}}{\partial z} + \Phi_{\rm e} = 0. \quad (5.6)$$

où $\Phi_{\rm i}$ représente la force de friction exercée sur les particules de la population i par les collisions avec les particules de toutes les autres espèces dans le système et où nous avons négligé la gravitation. Conservation de la quantité de mouvement implique que $\sum_i \Phi_i = 0$, c.à.d. $\Phi \equiv \Phi_{\rm p} = -\Phi_{\rm e}$ dans (5.5)-(5.6). Comme pour l'obtention du champ de Pannekoek-Rosseland, l'hypothèse de quasi-neutralité associée à l'hypothèse d'équipartition de l'énergie conduit à l'expression

$$E_{\rm T} = -\frac{\Phi}{en} \quad (5.7)$$

La détermination de Φ en fonction des variables thermodynamiques n et T n'est pas simple. Le résultat dépend, en particulier, du choix de l'opérateur de collision. Dans la limite d'un plasma faiblement couplé (cf chapitre 8.2 et la Table 8.1) soumis à un faible gradient de température, Spitzer et Härm (1953) trouvent $\Phi = \alpha n \partial T/\partial z$, et donc

$$E_{\mathrm{T}} = -\frac{\alpha}{e}\,\frac{\partial}{\partial z}(k_{\mathrm{B}}T). \tag{5.8}$$

Le champ thermoélectrique de l'équation (5.8) dépend donc de la variation de la température T en fonction de la position z, de la constante de Boltzmann k_{B} et d'une constante sans dimension α qui vaut $\alpha = 0.71$ dans un plasma protons-électrons faiblement couplé.
Le champ électrique n'est donc pas déterminé, contrairement au champ gravitationnel, par des facteurs externes au plasma. Il faut le calculer de façon autocohérente, ce qui complique notablement les simulations par rapport au cas d'un gaz de molécules discuté au chapitre 4. La deuxième complication inhérente au cas plasma est le traitement des collisions. Dans un gaz, les collisions diffèrent peu du cas de la collision entre sphères dures avec une section efficace pratiquement indépendante de la vitesse relative entre les particules qui font la collision. Dans ce cas, le modèle du chapitre 4 est parfaitement valable. Dans le cas d'un plasma, les collisions sont de type Coulombien, avec une section efficace qui varie comme l'inverse de la vitesse relative entre les particules à la puissance quatre (cf chapitre 2.3 de l'annexe 7).
Lorsqu'on simule numériquement un plasma plongé dans un champ gravitationnel, on est forcé de limiter l'étendu du domaine de simulation. Dans le cas d'une accélération gravitationnelle constante, on doit limiter l'étendue verticale du domaine de simulation afin que l'approximation d'accélération gravitationnelle constante soit acceptable. Par exemple, dans le cas d'une simulation de l'atmosphère du Soleil, la condition de gravitation constante implique que l'étendue verticale de la simulation L (cf figure 5.1) soit petite devant le rayon du Soleil r_0, i.e. $L/r_0 \ll 1$ [2].

5.1 Caractéristiques du modèle utilisé pour les simulations

Un schéma qui résume les caractéristiques générales des simulations d'un plasma soumis à un gradient de température, présentées dans les annexes 6 (sans gravitation) et 7 (avec gravitation), est montré dans la figure 5.1. Le gradient de température est imposé par les conditions sur les vitesses des particules atteignant un des deux bords du domaine de simulation en $z = 0$ et $z = L$. A chaque fois qu'une particule atteint un des deux bords, elle est réinjectée dans le système au même endroit (ce qui assure un flux de masse nul) avec une vitesse qui dépend du choix du programmeur tout

[2] Le Soleil concentre pratiquement toute sa masse en dessous de la photosphère. De ce fait, au dessus de la photosphère, l'accélération gravitationnelle g décroit alors comme l'inverse du carré de la distance au centre du Soleil, i.e. $g(r) \propto 1/r^2$. A une distance L au dessus de la photosphère, le champ gravitationnel est alors approximativement donné par $g(r_0 + L) = g(r_0)(1 - L^2/r_0^2)$ et donc, pour $L/r_0 \ll 1$, $g(r_0 + L) \simeq g(r_0)$.

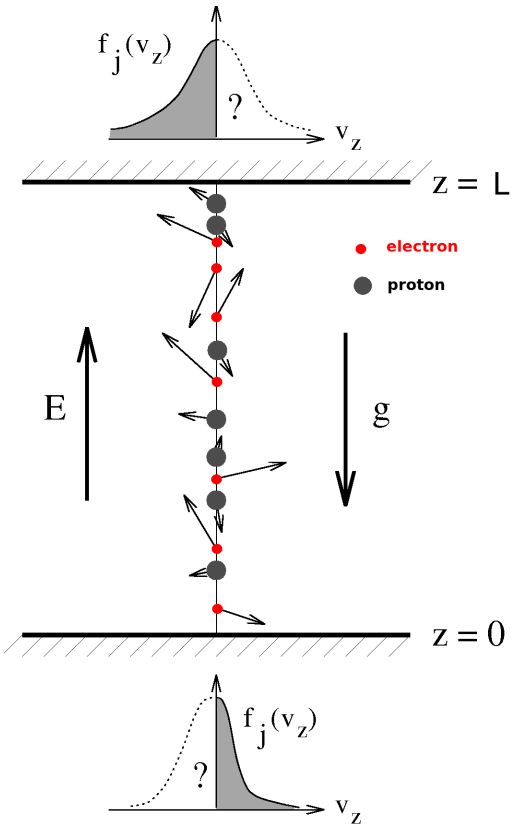

FIG. 5.1 – Schéma général illustrant les ingrédients pour la simulation d'un plasma soumis à un gradient de température et (le cas échéant) un champ gravitationnel constant. Les gradients sont imposés par le choix de la fonction de distribution des vitesses $f_j(\vec{v}, v_z \; entrant)$ (zones grises) pour chaque espèce j (électrons ou protons).

puissant qui décide de la forme de la distribution en vitesse des particules entrantes (zones grises dans la figure 5.1). La trajectoire des particules est calculée en intégrant l'équation du mouvement suivant z :

$$\frac{d^2z}{dt^2} = -g + \mathcal{E}(z) \tag{5.9}$$

où le champ électrique $\mathcal{E}(z)$ est déterminé de manière autocohérente, par ajustements successifs, jusqu'à ce que le plasma soit quasi-neutre partout dans le système.

5.2 Résultats concernant la couronne solaire

Dans l'article Pantellini et Landi (2001) (cf annexe 6) nous simulons un plasma soumis à un gradient de température relativement faible, tel que le libre parcours moyen d'un électron thermique λ_{ee} est petit devant l'échelle de variation caractéristique de la température $L_T \equiv T/\partial T/\partial z$, ce qui implique que le nombre de Knudsen $K_T \equiv \lambda_{ee}/L_T = 0.02 \ll 1$. Le but premier de cet article était de montrer que

le champ thermoélectrique obtenu dans nos simulations était bien celui prévu par l'équation (5.8) avec α de l'ordre de 0.71.

A l'origine de l'article Landi et Pantellini (2001) sur le transport de la chaleur dans la couronne solaire (cf annexe 7), il y a l'article de Dorelli et Scudder (1999) dans lequel les auteurs soutiennent qu'un excès d'électrons suprathermiques[3] dans la couronne (particules que nous pouvons introduire dans nos simulations en agissant sur les parties grises de la fonction de distribution des électrons en $z = 0, L$ dans la figure 5.1), la chaleur est transportée de la zone froide vers la zone chaude. En clair, et contrairement à l'idée généralement admise, le flux de chaleur serait alors dirigé de la photosphère vers la couronne et non l'inverse, à condition qu'un nombre suffisant d'électrons suprathermiques soit présents à la base de la couronne[4]. Ces électrons suprathermiques pourraient être engendrés par des chocs se propageant dans la chromosphère où des mouvements supersoniques sont souvent observés. La conséquence remarquable d'un tel scénario est qu'il explique, sans la nécessité d'invoquer un hypothétique mécanisme de transport de l'énergie entre la chromosphère et la couronne, le pourquoi de l'existence d'une couronne solaire chaude. Et même si l'excès d'électrons suprathermiques est insuffisant pour "chauffer" la couronne, il peut être suffisant pour modifier sensiblement le flux d'énergie de l'ordre de $5\ 10^2 W/m^2$ généralement admis comme nécessaire pour maintenir la couronne à une température de l'ordre du MK.

En réalité, le modèle proposé par Dorelli et Scudder (1999) est une version avec collisions (et dans la couronne il y en a) du modèle non collisionel de "filtrage des vitesses" que Scudder (1992) a proposé comme explication de la couronne chaude. L'essence du modèle de Scudder est illustré dans le figure 5.2. L'idée étant que lorsqu'une population (mettons les électrons) présente un excès de particules suprathermiques à une hauteur de référence $z = 0$ et une température $T_0 = m\langle v_z^2\rangle/k_\mathrm{B}$, cet excès se traduit par une population globalement plus chaude $T(z = h) > T_0$ du fait que les particules avec $v_z^2 < 2gh$ ne peuvent ni monter vers le niveau $z = h$ ni en provenir. Seules les particules avec $v_z^2 > 2gh$ peuvent se retrouver au niveau $z = h$. Ces dernières étant caractérisées par un spectre en énergie globalement plus dur (pente plus faible) que les particules avec $v_z^2 < 2gh$ qui dominent le niveau $z = 0$, la température doit être une fonction croissante de z. Notons que dans le cas d'une distribution de Maxwell-Boltzmann, la température ne varie pas avec la hauteur z et que dans le cas d'une distribution déficiente en particules suprathermiques (ce cas n'est pas illustré dans la figure 5.2), la température décroît avec la hauteur z. Notons également que les distributions de la figure 5.2 sont parfaitement symétriques, ce qui implique un flux de chaleur nul (!) même lorsque la température varie en fonction de z.

[3] L'excès est défini par rapport à la distribution de Maxwell-Boltzmann (4.2). L'adjectif suprathermique dénote les particules dont la vitesse v excède la vitesse thermique $(2k_\mathrm{B}T/m)^{1/2}$.

[4] Le point faible du modèle est qu'il est basé sur la présence d'un excès d'électrons suprathermiques à la base de la couronne. Les observations ne permettent malheureusement pas de confirmer ou invalider la présence d'un excès d'électrons suprathermiques à la base de la couronne.

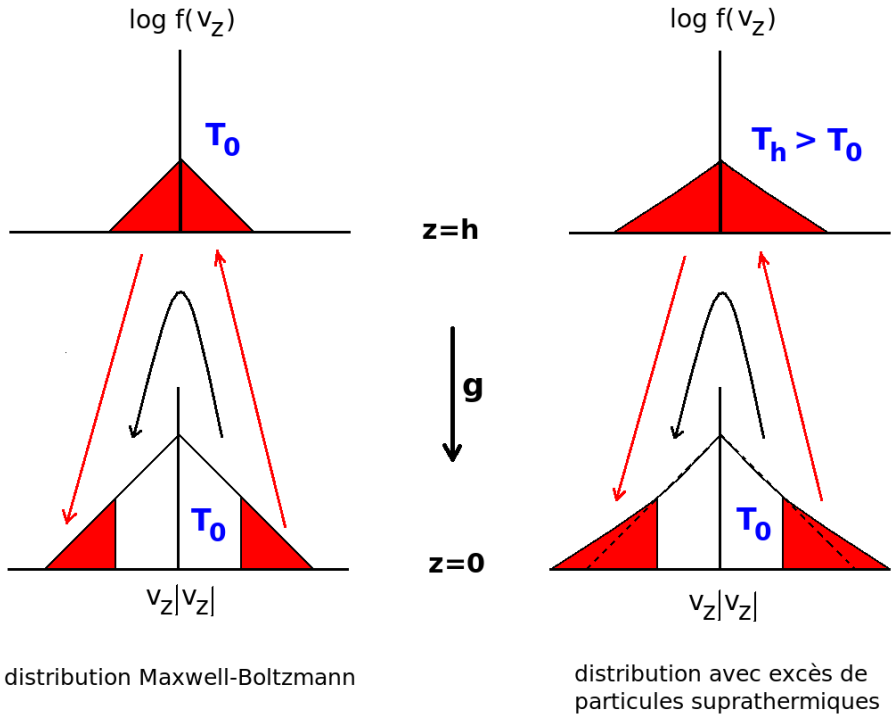

FIG. 5.2 – Variation avec la hauteur z de la fonction de distribution des vitesses $f(v_z)$ dans le cas Maxwellien (gauche) et dans le cas d'une distribution comportant un excès de particules suprathermiques (droite). En raison du champ gravitationnel g, et en l'absence de collisions, seules les particules des zones rouges peuvent transiter entre le niveau $z = 0$ et $z = h$. En conséquence, l'énergie moyenne par particule ne varie pas dans le cas Maxwellien alors qu'elle augmente avec z pour une distribution avec un excès de particules suprathermiques.

Dorelli et Scudder (1999) suggèrent que le mécanisme de filtrage non collisionnel des vitesses de Scudder (1992) reste valable dans la couronne, même en tenant compte des collisions. Les collisions ne sont donc pas, selon eux, suffisamment efficaces pour invalider le modèle non collisionel de Scudder (1992). Les calculs de Dorelli et Scudder (1999) ont l'inconvénient de s'appuyer sur une forme particulière de la fonction de distribution des vitesses des électrons, basée sur un développement en polynômes de Legendre tronqué après le premier ordre seulement. Nos simulations (dans Landi et Pantellini (2001)) ont montré que l'excès d'électrons suprathermiques nécessaires pour inverser le flux de chaleur est beaucoup plus important que prévu par Dorelli et Scudder (1999)[5], mais également que le profil de température dans la couronne ne peut être soutenu sans un apport d'énergie sous la forme d'ondes électromagnétiques et ce, même en supposant un nombre extravagant de particules suprathermiques à la base de la couronne. En résumé, nous trouvons que la couronne ne peut se mainte-

[5]Dans un modèle postérieur, plus élaboré, Dorelli et Scudder (2003) trouvent effectivement des résultats plus proches des nôtres.

nir à 1MK sans apport d'énergie sous forme d'ondes, même en supposant l'existence d'une très forte composante d'électrons suprathermiques à la base de la couronne. Nos résultats contredisent ceux de Dorelli et Scudder (1999, 2003) qui sont une extension, aux plasmas non collisionnels, de la théorie non collisionnel du "filtrage gravitationnel" de Scudder (1992). La raison est à chercher dans le traitement simplifié des collisions par Dorelli et Scudder ce qui se traduit par une sous estimation de leur efficacité à détruire les distributions suprathermiques supposées exister à la base de la couronne.

Chapitre 6

Le rôle des collisions entre charges dans l'accélération du vent solaire

6.1 Considérations géométriques pour la simulation d'un vent stellaire

Dans le chapitre précédent, il a été question de simulations spatialement unidimensionnelles d'un plasma en géométrie cartésienne. La géométrie cartésienne est compatible avec une gravitation constante, ce qui est parfaitement acceptable pour des simulations de tranches fines de l'atmosphère solaire. La géométrie cartésienne ne peut cependant pas permettre la simulation de l'atmosphère étendue du Soleil, laquelle, même lorsqu'on se limite à la couronne, monte à plus d'un rayon solaire de la surface (la photosphère). Même si on suppose que l'accélération gravitationnelle décroît comme $1/z^2$ dans la figure 5.1, cela ne suffit pas pour rendre compte de la symétrie sphérique de l'atmosphère étendue du Soleil. Dans le modèle numérique du chapitre 5, il y a une seule coordonnée spatiale : z (la hauteur) dans le cas cartésien et r (la distance radiale mesurée à partir d'un point) dans le cas sphérique. Nous pouvons facilement nous rendre compte que la coordonnée z du problème cartésien ne peut pas remplacer la coordonnée r du problème sphérique en étudiant le mouvement rectiligne et uniforme, à la vitesse v, d'une particule de masse m.
Supposons que la particule se déplace horizontalement à l'instant $t = 0$, c.à.d. $\vec{v} = v\hat{x}$ dans le cas cartésien et $\vec{v} = v\hat{\theta}$ dans le cas sphérique (cf figure 6.1). Les équations du mouvement sont extrêmement simples dans le cas cartésien :

$$\left.\begin{array}{ll} v_x & = v = const \\ v_y & = 0 = const \end{array}\right\} \Longrightarrow \frac{d^2x}{dt^2} = \frac{d^2y}{dt^2} = 0.$$

Dans le cas sphérique c'est un peu plus compliqué puisque ni v_r ni v_θ ne sont constants. Par contre, en observant que $v_r = v\sin\theta$ et $v_\theta = v\cos\theta$ on obtient que

$$r^2 v_\theta^2 = r^2 v^2 \cos^2\theta = r_0^2 v_\theta^2 = const \tag{6.1}$$

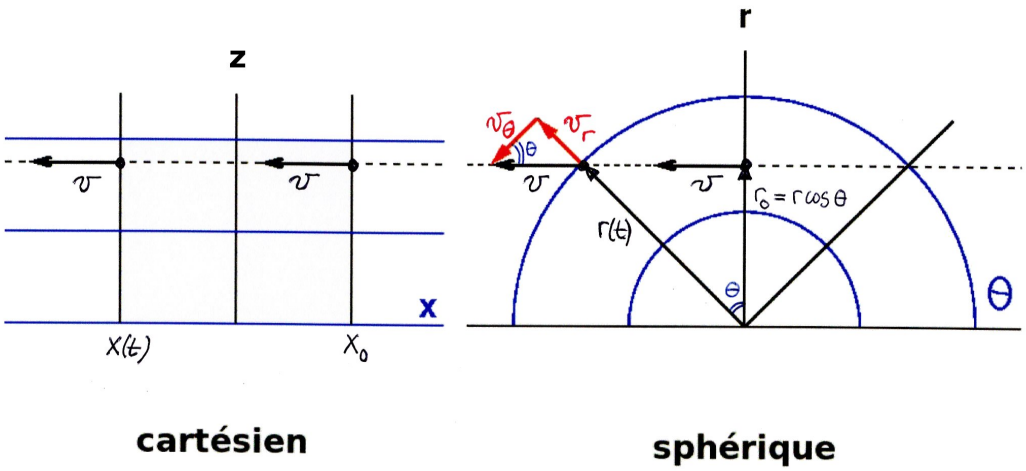

FIG. 6.1 – Particule en mouvement rectiligne et uniforme dans un système de coordonnées cartésiennes et dans un système de coordonnées sphériques.

L'équation (6.1) n'est rien d'autre que l'équation de conservation du moment angulaire $\vec{L} = m\vec{r} \times \vec{v}$ car $L = rv\sin(\pi/2 - \theta) = rv_\theta$. Notant que l'angle θ augmente en fonction du temps suivant $\sin\theta = vt/r$, nous pouvons écrire l'équation du mouvement radial de la particule :

$$\begin{aligned} \frac{dv_r}{dt} = v\frac{d}{dt}\sin\theta &= v\left(\frac{v}{r} - \frac{vt}{r^2}\frac{dr}{dt}\right) \\ &= \frac{v^2}{r}\left(1 - \sin\theta\,\frac{v_r}{v}\right) \\ &= \frac{r^2 v_\theta^2}{r^3} = \frac{L^2}{m^2 r^3} \end{aligned} \tag{6.2}$$

Donc, contrairement au cas cartésien où toutes les composantes de la vitesse sont constantes, dans le cas sphérique, la particule subit une force apparente le long de la direction radiale. Si la particule se trouve dans le champ gravitationnel central du Soleil, qu'on choisira logiquement de placer au centre du système de coordonnées sphériques, on ajoutera l'accélération gravitationnelle GM/r^2 (cf Newton (1687)), où M est la masse du Soleil, à la force apparente de l'équation (6.2) ainsi que la contribution du champ électrique neutralisant $q\mathcal{E}(r)/m$. On obtient ainsi l'équation générale du mouvement radial d'une particule dans un monde à symétrie sphérique (cf équation (1) dans l'annexe 8) :

$$\frac{d^2r}{dt^2} = -\frac{GM}{r^2} + \frac{L^2}{m^2r^3} + \frac{q}{m}\mathcal{E}(r). \tag{6.3}$$

Cette équation est le pendant en sphérique de l'équation (5.9) en cartésien. Alors que l'équation du mouvement est très différente en cartésien et en sphérique, le traitement des collisions est pratiquement identique dans les deux cas. Seule différence :

dans le cas cartésien, la probabilité de collision entre deux particules ne dépend pas de z, alors que dans le cas sphérique celle-ci décroît comme $1/r^2$. [1]

6.2 Résultats des simulations

Dans l'annexe 8 nous appliquons le modèle sphérique à la simulation du vent solaire de la couronne jusqu'à des distances héliosphériques de l'ordre de $50r_0$, où $r_0 = 6.69\ 10^8$m est le rayon moyen du Soleil. Ce qui est absolument remarquable c'est que $N = 6400$ particules suffisent pour simuler un domaine aussi étendu couvrant à la fois la zone d'accélération et la zone de croisière du vent[2]. La courbe du haut

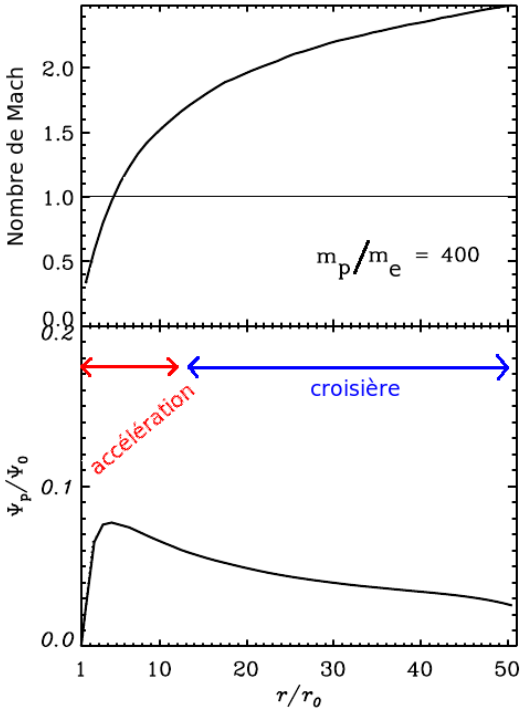

FIG. 6.2 – Profil du nombre de Mach du vent solaire (courbe du haut) et profil de la variation du potentiel total (gravitationnel et électrostatique) en fonction de la distance au soleil. (adapté de Landi et Pantellini (2003), cf annexe 8)

dans la figure 6.2 montre la variation du nombre de Mach avec la distance au Soleil obtenu dans une simulation avec un rapport de masse proton/électron $m_\mathrm{p}/m_\mathrm{e} = 400$. Des simulations plus récentes, non publiées, avec un rapport $m_\mathrm{p}/m_\mathrm{e} = 1836$

[1] Ceci pour tenir compte du fait que la contribution d'une particule à la densité dans une coquille sphérique d'épaisseur dr dépend de la distance, i.e. $n_1(r) = 1/(4\pi r^2 dr)$. En somme, une particule à la distance r couvre un angle solide 4 fois plus grand qu'à la distance $2r$.

[2] La zone de croisière correspond très vaguement à $r \gtrsim 10r_0$, distance au delà de laquelle le vent est largement supersonique et sa vitesse approximativement constante, signe que son énergie cinétique $\varrho v_r^2/2$ est désormais largement supérieure à l'énergie gravitationnelle $\varrho GM/r$.

montrent peu de différences avec les résultats de Landi et Pantellini (2003). Notons que l'augmentation du nombre de Mach $M = v_r/v_{\mathrm{pT}\|}$ avec la distance r est due, un peu, à la croissance de v_r avec r, mais surtout à la décroissance de la température avec r. Le profil du nombre de Mach diffère fort peu des courbes obtenues par "l'inventeur" du vent solaire. Parker (1958) avec un modèle hydrodynamique. La principale différence est que le profil de la figure 6.2 a été obtenu avec un plus petit nombre d'hypothèses. Premièrement, Parker se donne un profil de température, alors que celle-ci est libre dans le cas de notre modèle. Ensuite, Parker suppose que la température est la même dans la direction radiale et dans la direction transverse, ce qui n'est pas justifiable a priori, en raison de la faible collisionnalité du vent solaire[3]. Les principaux apports des simulations de Landi et Pantellini (2003) (annexe 8) sont au nombre de trois. Premièrement, nous montrons que l'accélération du vent à des vitesses supersoniques peut se faire sans la contribution d'ondes électromagnétiques, le flux de chaleur porté par les électrons suffit à cet effet. Deuxièmement, nous montrons que le flux de chaleur électronique q_{e} ne se laisse pas décrire par la formule classique $q_{\mathrm{e}} \propto T^{5/2}\partial T/\partial r$ obtenue par Spitzer et Härm (1953) dans le contexte des plasmas collisionnels. Nous trouvons que le flux de Spitzer et Härm est une piètre estimation du flux même dans la zone d'accélération du vent, là où les taux de collisions sont les plus élevés de tout le domaine simulé (cf 6.2). Le flux que nous observons dans nos simulations est généralement bien plus intense que le flux de Spitzer et Härm. Son intensité se trouve être bien mieux décrite par l'expression non collisionnelle $q_{\mathrm{NC}} \propto nvk_{\mathrm{B}}T$, où v est la vitesse du vent et n la densité électronique, proposée par Hollweg (1974). Troisièmement, nous montrons, pour la première fois dans une simulation autocohérente, que le potentiel protonique possède un maximum au voisinage du point sonique (courbe du bas dans la figure 6.2)[4].

[3]Les observations in situ dans le vent solaire, à des distances supérieures à $50r_0$, montrent cependant que la température du plasma est généralement du même ordre dans la direction radiale et transverse, alors que les simulations cinétiques, comme les nôtres, suggèrent une forte anisotropie en faveur de la direction radiale. On estime que des instabilités plasmas, en particulier l'instabilité "firehose", absentes de nos simulations, empêchent le développement de ces anisotropies (Matteini *et al.*, 2007, e.g.).

[4]Notons que Jockers (1970), en se basant sur une démonstration graphique, a été le premier à préconiser l'existence d'un maximum dans le profil du potentiel protonique. Une discussion approfondie des caractéristiques du maximum en fonction des paramètres du vent, ainsi que sa relation avec le point sonique du modèle fluide de Parker a été publiée dans Scudder (1996).

Chapitre 7

Simulations de systèmes granulaires

7.1 Introduction

Depuis les années 1930, il paraissait clair, en particulier suite aux observations de Bernard Lyot avec le coronographe de son invention, que la température de la couronne solaire est bien plus élevée que la température de la surface sous-jacente. Ce n'est que grâce à l'identification d'ions hautement ionisés par Edlén (1943) que nous savons avec certitude que la température de la couronne est près de 200 fois plus élevée que la température de la photosphère. Depuis lors, de nombreuses théories ont été proposées pour tenter d'expliquer la raison de cette vertigineuse croissance de la température au dessus de la surface du Soleil. La plupart de ces théories sont basées sur un mécanisme de chauffage de la couronne par des ondes plasmas engendrées par les mouvements turbulents dans la photosphère et dissipées, après propagation, dans la couronne. Une théorie alternative (e.g. Scudder, 1992), dont il a été question à la fin du chapitre 5, se base sur le fait qu'un plasma peu collisionnel soumis à un champ de pesanteur constant voit sa température varier avec la hauteur, tant que la distribution des vitesses des particules n'est pas de type Maxwell-Boltzmann[1].
L'extraordinaire augmentation de la température entre la chromosphère et la couronne semble violer le deuxième principe de la thermodynamique. La source de chaleur se situant au coeur du Soleil, on ne voit pas, a priori, comment la température pourrait augmenter en s'en éloignant. On dirait qu'un démon de Maxwell, qu'on pourrait localiser dans la région de transition (cf Figure 7.1), filtre les particules en laissant transiter de la chromosphère vers la couronne seulement les plus énergétiques.
C'est précisément en cherchant sur internet avec les mots clés "démon" et "Maxwell" que je suis tombé sur un article fort intéressant de Eggers (1999) relatant, avec explication physique à l'appui, l'expérience de la figure 7.2. J'admets volontiers que le lien entre l'expérience décrite par Eggers et le problème du chauffage de la

[1]Une croissance de la température électronique entre la chromosphère et la couronne par effet de filtrage gravitationnel ((Scudder, 1992)) nécessite l'existence d'un excès d'électrons suprathermiques par rapport à la distribution de Maxwell-Boltzmann (cf chapitre 5).

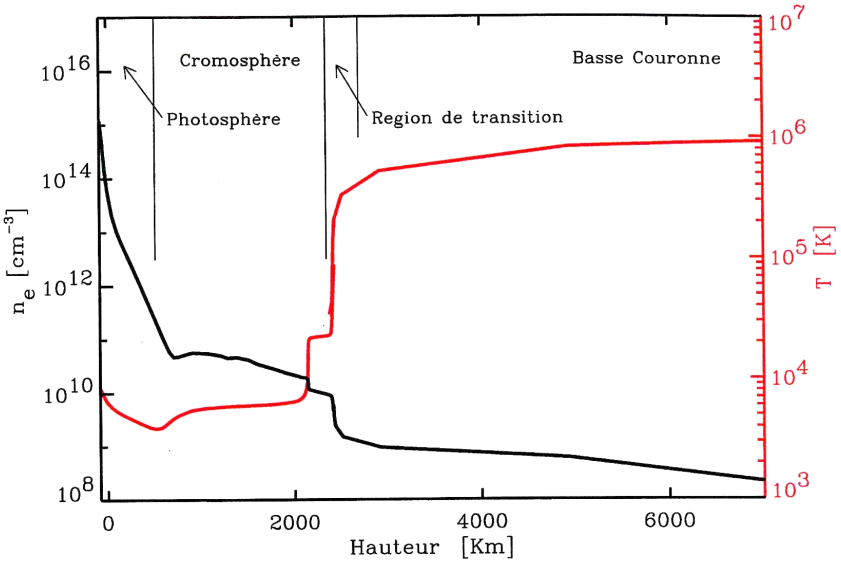

FIG. 7.1 – Modèle empirique de la densité et de la température dans l'atmosphère solaire (extrait de Landi (2001))

couronne n'est pas immédiatement apparent : il sera plus clair par la suite. L'expérience illustrée dans la figure 7.2 est facilement réalisable chez soi si on est un peu bricoleur. Elle consiste en un récipient (par exemple un aquarium en plastique) séparé en deux parties égales par une paroi comportant un petit trou près du fond. Le récipient, rempli avec des petites boules en plastique pouvant passer par le trou, est agité verticalement avec une fréquence ω. Lorsque la fréquence ω est suffisamment élevée, on observe que les boules finissent par se repartir uniformément dans les deux compartiments, indépendemment des conditions initiales (cas A dans la figure 7.2). Si maintenant on baisse la fréquence d'oscillation ω en dessous d'un seuil critique, un phénomène curieux se produit : spontanément un nouvel état stationnaire s'installe avec un plus grand nombre de particules dans un des deux compartiments, mais avec des particules plus énergétiques, en moyenne, dans l'autre compartiment. En somme, on se retrouve avec un compartiment avec du "gaz" froid et dense (compartiment de droite dans le cas B de la figure 7.2) et un compartiment avec du "gaz" chaud et dilué. L'explication détaillée du phénomène est un peu compliquée, mais la raison fondamentale de l'apparition de deux états distincts se trouve dans la non élasticité des collisions entre les petites boules en plastique. Dans le cas élastique (comme dans un gaz où les collisions entre molécules sont parfaitement élastiques), la solution d'équilibre est toujours symétrique, alors que dans le cas inélastique, la solution d'équilibre n'est pas toujours symétrique. Mais ce n'est pas tout, concernant le comportement exotique du système de la figure 7.2. Une analyse détaillée du profil de température vertical dans le récipient, conduite par Ramírez et Soto (2003), montre que contrairement à ce qu'on pourrait soupçonner naïvement, la température

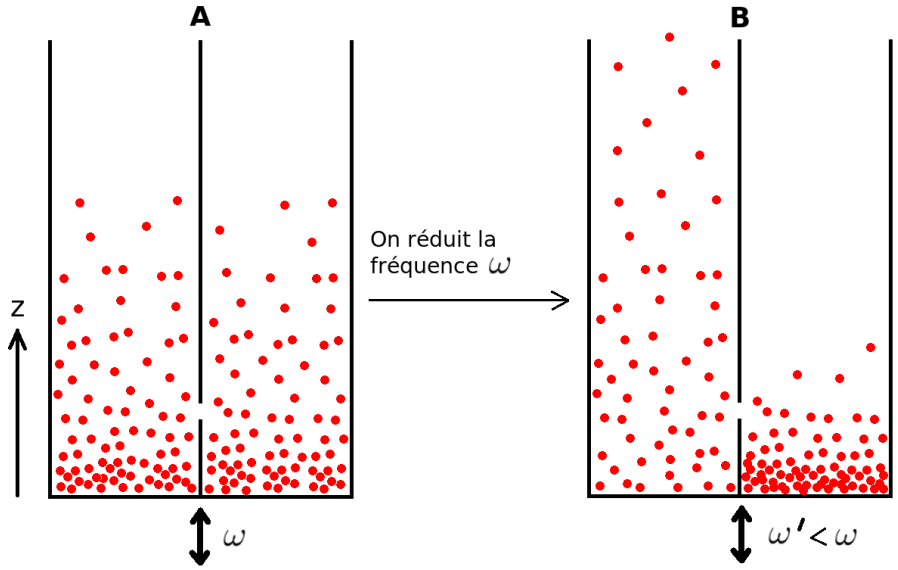

FIG. 7.2 – Expérience du récipient contenant des boules en plastique. Le récipient est agité verticalement avec une fréquence ω. Adapté de Eggers (1999)

n'est pas une fonction monotone et décroissante de la hauteur z. Comme l'illustre la figure 7.3, la température décroît effectivement dans la partie dense du système, mais le gradient finit par s'inverser et la température augmenter en s'éloignant de la source d'énergie, exactement comme dans l'atmosphère du Soleil au dessus de la chromosphère.

L'expérience de la figure 7.2 illustre de manière exemplaire le comportement parfois très exotique des systèmes de particules interagissant de manière inélastique. Les exemples de matière granulaire[2] que l'on rencontre quotidiennement sont très nombreux. Citons : le café, le sable, la neige, les tas de pomme de terre, etc. Les systèmes de matière granulaire ne sont pas moins fréquents en astrophysique. Citons : les anneaux astrophysiques (e.g. les anneaux de Saturne), les nuages protoplanétaires et la matière interstellaire froide en générale. Le lecteur intéressé trouvera dans la revue de Jaeger *et al.* (1996) la description d'expériences de laboratoire mettant en évidence les propriétés spécifiques des systèmes granulaires, et en quoi leur comportement diffère de celui des gaz ou liquides ordinaires.

Mais revenons à notre discussion sur l'atmosphère du Soleil. Évidemment, le plasma de l'atmosphère du Soleil n'est pas un système granulaire. Les particules ne sont pas des boulettes en plastique mais des charges élémentaires (principalement ions et électrons) interagissant de façon élastique. Il n'y a donc aucune raison, a priori, pour

[2]Matière granulaire : conglomérat de particules macroscopiques interagissant par l'intermédiaire de collisions non élastiques, i.e. avec perte d'énergie.

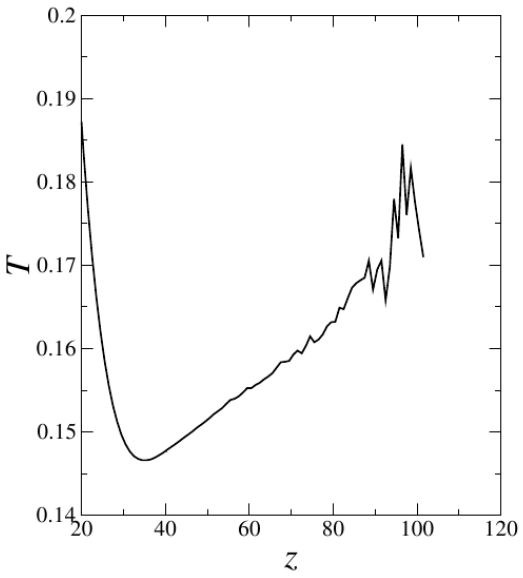

FIG. 7.3 – Profil de température vertical caractéristique dans une expérience similaire à celle de la figure 7.2. Adapté de Ramírez et Soto (2003)

que le profil de température augmente avec la hauteur comme dans la figure 7.3. Cependant, si on tient compte du fait qu'une (petite) partie de l'énergie cinétique des charges interagissant entre elles est perdue sous forme de rayonnement, la différence entre système granulaire et plasma n'est plus aussi grande qu'il n'y paraît. La simulation de l'atmosphère solaire, en incluant les collisions inélastiques, constitue la suite prévisible du travail que je présente dans ce chapitre. Mais avant d'en arriver à traiter l'atmosphère solaire avec les outils de la physique des systèmes granulaires, j'ai dû me familiariser avec un sujet complètement étranger à mes préoccupations antérieures et bien plus complexe et riche que ce que j'imaginais au départ.

7.2 Ségrégation d'espèces dans un système granulaire unidimensionnel

Même le comportement des systèmes granulaires les plus simples, tels le collier de billes de la figure 7.4, n'a pas encore été entièrement élucidé à ce jour. C'est la raison qui m'a poussé à "recycler" le code précédemment utilisé pour simuler un gaz dans un champs gravitationnel (cf chapitre 4), avec l'idée de traiter, dans un premier temps, le système de la figure 7.4, sans bien sûr tenir compte de la courbure du collier, ni même de la taille des billes que nous supposons ponctuelles.
Le système est proche du système non-ergodique (a) de la figure 4.1, mais cette fois les collisions ne sont pas élastiques et l'énergie cinétique totale des billes n'est pas constante, car à chaque collision une petite fraction de l'énergie cinétique des particules interagissantes est perdue. Le système a été étudié mathématiquement

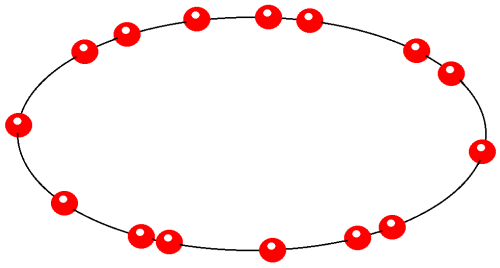

FIG. 7.4 – Le modèle numérique utilisé dans le chapitre 4.1 de l'article Pantellini et Landi (2008) (cf annexe 9) ressemble schématiquement au problème d'une série de billes identiques sur un fil périodique. Ce système n'est pas ergodique dans la limite élastique.

par plusieurs auteurs au cours des deux dernières décennies, mais le lecteur intéressé trouvera l'essentiel, avec références et explications, dans l'excellent article de Baldassarri *et al.* (2002). Une des caractéristiques marquantes du système de la figure 7.4, mais qui est également une caractéristique quasi-universelle de tout système granulaire, est sa tendance à vouloir former des grumeaux, c.à.d. à concentrer les billes dans des groupes, même lorsque la distribution initiale est uniforme.

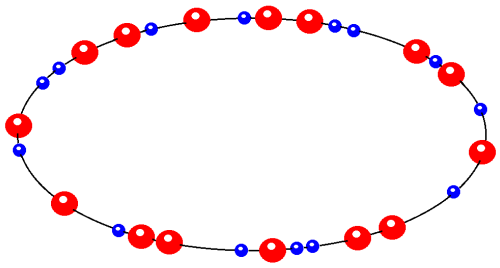

FIG. 7.5 – Le modèle numérique utilisé dans le chapitre 4.2 de l'article Pantellini et Landi (2008) (cf annexe 9) ressemble schématiquement au problème d'une série de billes non identiques sur un fil périodique. Le comportement de ce système est profondément différent de celui d'un ensemble de particules identiques de la figure 7.4. Il est ergodique dans la limite élastique et peut se décrire avec des équations fluides.

Le système 7.4 ayant été décrit de façon détaillée par Baldassarri *et al.* (2002), nous avons décidé (cf annexe 9 ou Pantellini et Landi (2008)) d'étudier numériquement le cas plus compliqué d'un système à deux espèces de billes de masses différentes comme illustré sur la figure 7.5. Malgré les apparences, les deux systèmes des figures 7.4 et 7.5 évoluent de façon très différente, même avant la formation de grumeaux. La figure 7.6 montre l'état de la fonction de distribution d'un système de $N = 19600$ particules identiques (figure 7.4) et d'un système de $N/2$ particules de masse $m = 1$

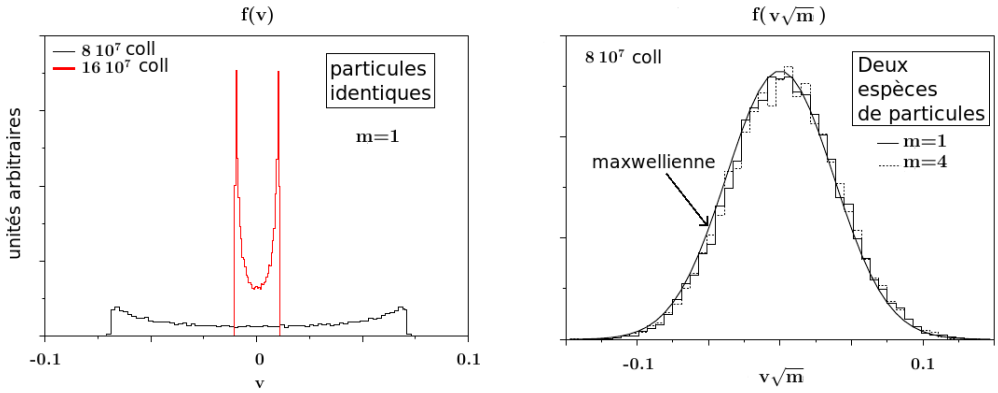

FIG. 7.6 – Évolution de la fonction de distribution des vitesses pendant la phase homogène, pour un système de N particules identiques (gauche) et un système de $N/2$ particules de masse $m = 1$ et $N/2$ particules de masse $m = 4$ (droite).

et $N/2$ particules de masse $m = 4$ (figure 7.5) au cours de la phase dite homogène, c.à.d. avant la formation d'inhomogénéités dans la distribution spatiale des billes. Dans les deux cas, le coefficient de dissipation ε qui représente, en gros, la fraction d'énergie perdue à chaque collision entre deux particules, est $\varepsilon = 5\,10^{-4} \ll 1$ (cas faiblement inélastique). En outre, dans les deux cas, la vitesse initiale des particules est distribuée uniformément dans l'intervalle $[-0.5, 0.5]/\sqrt{m}$, afin que l'énergie moyenne par particule soit la même pour toutes les espèces. La différence entre les deux distributions de la figure 7.6 est frappante. Dans le cas de particules identiques on observe une tendance à la formation d'une distribution à deux pics (surtout visible après $16\,10^7$ collisions) alors que dans le cas à deux espèces, les distributions sont parfaitement bien décrites par une distribution maxwellienne.[3] La différence est bien sûr due au fait que, comme nous l'avions déjà souligné dans le chapitre 4, un système unidimensionnel de particules identiques, comme celui de la figure 7.4, n'est pas ergodique. Remarquons cependant que la distribution des vitesses n'évolue nullement dans le cas élastique, alors qu'elle évolue considérablement dans le cas inélastique comme illustré dans le panneau de gauche de la figure 7.6.
Le fait que les distributions en vitesse sont bien décrites par des distributions maxwelliennes, nous a incité à établir des équations fluides qualitatives[4] pour un système unidimensionnel à deux espèces et un petit coefficient de dissipation ε (cf chapitre

[3] Benedetto *et al.* (1997) ont montré que dans la limite quasi-élastique $\varepsilon \to 0^+$ la distribution en vitesse du système de particules identiques évolue vers une somme de deux distributions de Dirac, que l'on devine clairement dans la figure 7.6.

[4] Nous ne donnons pas dans l'article de l'annexe 9 les expressions exactes des coefficients de transport pour le cas 1d qui nous occupe. Les calculs sont excessivement compliqués et de peu d'intérêt en 1d, entre autre en raison de la non ergodicité des systèmes à une seule espèce. En outre, une connaissance détaillée des coefficients de transport n'est pas nécessaire pour la compréhension de la physique du système. Un calcul détaillé des coefficients de transport dans un mélange de 2

2 dans l'annexe 9). Les équations fluides nous ont permis d'appréhender beaucoup plus facilement le comportement du système à deux espèces. Dans l'annexe A de Pantellini et Landi (2008) nous linéarisons les équations fluides correspondant au système unidimensionnel à deux espèces de la figure 7.5 et montrons que le mode le plus instable, celui donc qui est responsable de la formation des grumeaux, n'est pas le mode sonore mais le mode à équilibre de pression, appelé parfois mode entropique. Nous établissons également que la longueur d'onde du mode le plus instable $\lambda_{\max}$ est de l'ordre de $\lambda_{\max} \sim 10\pi L/N\varepsilon$ (L étant la dimension physique du système, c.à.d. la longueur du fil dans le système de la figure 7.5).
L'instabilité de "clustering", c'est son nom, génère donc des fluctuations de la densité de particules à l'échelle $\lambda_{\max}$. Les fluctuations de densité ainsi engendrées par l'instabilité conduisent généralement le système vers une catastrophe que l'on appelle effondrement inélastique ("inelastic collapse" en anglais). L'effondrement inélastique se produit à l'endroit où apparaissent des surdensités de particules. Il est dû au fait que dans les lieux de surdensité, la dissipation est plus forte qu'ailleurs, ce qui engendre un ralentissement de l'agitation des particules et donc une baisse de la température, laquelle baisse engendre à son tour une augmentation de la densité afin d'assurer l'équilibre spatial de la pression : c'est l'effondrement. Très rapidement le système se remplit de grumeaux formés de particules collées les unes aux autres pratiquement sans plus aucun mouvement relatif (voir les grumeaux A et B dans la figure 7.7)

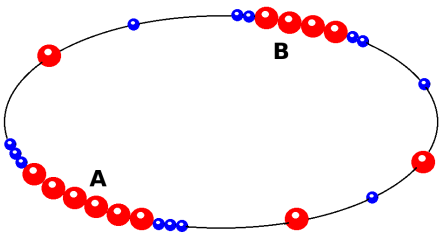

FIG. 7.7 – Les systèmes 7.4 et 7.5 ont une tendance à former des grumeaux. Lorsqu'on permet aux particules d'échanger leur position relative au cours des collisions, les grumeaux (A et B sur la figure) expulsent les particules légères vers leur périphérie.

La tendance vers la formation de grumeaux de particules est une caractéristique universelle des systèmes granulaires. Elle se produit aussi bien dans les systèmes de particules identiques que dans les systèmes multi-espèces. Avec l'estimation de la $\lambda_{\max}$ ci-dessus, on peut évaluer le nombre de particules N_c dans un grumeaux à $N_c \sim 5\pi/\varepsilon^5$.

espèces en 3 dimensions spatiales et en fonction du coefficient d'inélasticité ε, de la taille et de la masse des des grains a été publié récemment par Garzó *et al.* (2006).

[5] On obtient N_c en prenant le nombre de particules moyennes dans la demie longueur d'onde $\lambda_{\max}/2$, correspondant à la portion de surdensité de l'onde.

Ce que nous avons voulu explorer dans Pantellini et Landi (2008), c'était comment les particules de masse différente se distribuent dans un grumeau lors de son effondrement. Évidemment, dans un système 1d comme celui des figures 7.5 et 7.7, la distribution relative des particules est entièrement déterminée par la distribution initiale, alors que dans un système à 2 ou 3 dimensions, les particules peuvent échanger leur position par rapport au centre du grumeau. Pour éviter que la distribution spatiale des espèces dans notre système unidimensionnel soit figée par le choix initial, nous permettons à deux particules qui entrent en collision d'échanger leur position relative avec une probabilité de 50%. Lorsque la distribution spatiale initiale est uniforme pour les deux espèces séparément, l'introduction de la possibilité d'échanger les positions n'affecte guerre l'évolution du système. Par contre, au moment de l'effondrement, on observe que les particules légères sont expulsées vers les bords du grumeau comme illustré dans la figure 7.7. Nous montrons que la force de friction est responsable de la ségrégation des espèces dans les grumeaux en effondrement. La force de friction est non nulle en raison du gradient de température, les particules lourdes subissant une force dirigée vers les zones froides, i.e. le centre des grumeaux, alors que les particules légères subissent une force qui les écarte du centre des grumeaux.
Dans Pantellini et Landi (2008) nous montrons également que les mouvements d'ensemble des grumeaux au moment de l'effondrement sont supersoniques si le nombre de particules N dans le système 1d est supérieur à un seuil de l'ordre de $4\pi/\varepsilon$.
Ces résultats ont été établis en analysant numériquement et théoriquement des systèmes unidimensionnels. L'extrapolation à des systèmes à 2 ou 3 dimensions n'est pas évidente. Nous prétendons que la ségrégation entre les espèces de masse différente à l'intérieur des grumeaux est un phénomène universel dans la mesure où il est dû à l'action d'une force qui n'est pas l'apanage des systèmes 1d.

Chapitre 8

Simulations d'un plasma avec un code N-corps

Ce chapitre est volontairement un peu plus détaillé que les autres. Non que je considère les sujets traités ici plus importants que ceux des chapitres précédents mais simplement parce que, d'une part, la technique de simulation numérique dont il sera question ci-dessous est extrêmement peu répandue, voire inexistante en physique des plasmas et que, d'autre part, des paramètres fondamentaux, tels le paramètre de couplage Γ ou le logarithme de Coulomb λ ainsi que le rayon d'interaction forte $r_{\rm s}$, sont incontournables pour la caractérisation des plasmas, qu'ils soient naturels ou de laboratoire. Ces paramètres sont finalement peu ou mal connus dans la communauté des plasmas naturels (spatiaux ou astrophysiques). Cela s'explique vraisemblablement par le fait que dans bien des cas il est plus simple, et souvent parfaitement justifié, de se contenter soit d'une description fluide, soit d'une description complètement non collisionnelle du plasma. Il est effectivement parfaitement raisonnable d'appliquer les équations fluides de la magnétohydrodynamique (MHD) au plasma très collisionnel de l'intérieur des étoiles convectives. Il est également parfaitement raisonnable d'appliquer l'équation de Vlasov, décrivant les plasmas non collisionnels, aux magnétosphères planétaires dans la mesure où le libre parcours moyen des ions et électrons qui s'y trouvent sont des centaines de fois plus grands que les dimensions caractéristiques de ces mêmes magnétosphères. De nombreux plasmas peuvent cependant se trouver entre ces deux extrêmes. Ce sont les plasmas dans lesquels les échelles spatiales de variation des quantités macroscopiques, tels la densité ou la température, ne sont pas énormément plus grandes que les libres parcours des particules, c.à.d. les plasmas caractérisés par un nombre de Knudsen thermique (voir chapitre 5) $K_{\rm T} \equiv \lambda_{\rm ee}/L_{\rm T}$ entre 10^{-4} et 10^{-11}. De nombreux plasmas astrophysiques et de laboratoire peuvent se trouver dans ce régime, en particulier lorsqu'ils sont stratifiés par la gravitation (atmosphères planétaires ou stellaires, e.g. chapitre 5)

[1]Dans cette expression $\lambda_{\rm ee}$ est le libre parcours moyen caractéristique d'un électron dû à son interaction avec les autres électrons du plasma et $L_{\rm T} \equiv T/\partial T/\partial z$ l'échelle de variation caractéristique de la température T.

mais également à l'interface plasma-vide, situation fréquente dans les expériences laser-plasma. Dans ces cas, ni l'approche fluide, ni l'approche non collisionnelle se justifient réellement, mais c'est précisément dans ce type de plasmas que les simulations de type N-corps trouvent leur principal champ d'application. Notons que même le vent solaire, dans lequel le libre parcours moyen est de l'ordre de l'unité astronomique ne peut être considéré comme non collisionel à grande échelle, car les variations de la température avec la distance héliocentrique ne sont significatives qu'à des échelles à peine plus petites que l'unité astronomique.
En 2003, en feuilletant sans rien chercher de précis, un volume du Journal of Computational Physics je suis tombé, un peu par hasard, sur l'article de W. Dehnen (Dehnen, 2002), traitant du problème du calcul de l'interaction gravitationnelle entre un grand nombre de particules ponctuelles. Ce qui avait surtout retenu mon attention, c'était le titre de l'article qui annonçait un algorithme de type N-corps (appelé FalcON par l'auteur) d'une complexité algorithmique d'ordre N. Dit autrement, le temps d'ordinateur nécessaire pour calculer l'interaction gravitationnelle entre N particules avec FalcON augmente linéairement avec N. Lorsque le nombre de particules N est de l'ordre du million, voire du milliard, le gain en temps de calcul par rapport à l'algorithme en $L\log(N)$ de Barnes et Hut (Barnes et Hut, 1986), largement répandu dans la communauté astrophysique, devient considérable. D'autres algorithmes affichaient à l'époque une complexité d'ordre N, mais aucun d'entre eux n'avait vraiment fait la preuve de son efficacité (voir les explications dans l'introduction de l'articles de W. Dehnen sur ce point). Je demandais à l'auteur s'il voulait bien m'envoyer une version de son algorithme. Je reçus donc, immédiatement, une version en C++, parfaitement bien documentée de FalcON. J'ai un peu joué avec le code, histoire d'en comprendre le fonctionnement avant de me poser la question de sa transposition au cas de l'interaction coulombienne entre charges électriques, l'interaction gravitationnelle entre deux masses ponctuelles et l'interaction électrostatique entre deux charges ponctuelles obéissant à la même équation. Le fait que l'interaction gravitationnelle entre masses est toujours attractive, alors que l'interaction électrostatique peut être attractive ou répulsive, implique une adaptation de FalcON pour le rendre efficace dans les applications électrostatiques. C'est le sujet du chapitre 8.1.

8.1 Quelques aspects techniques

Des essais avec un petit nombre de charges semblaient montrer que la transposition du cas gravitationnel vers le cas électrostatique ne comportait aucun problème. Cependant, les mesures de temps de calcul par A. Beck au cours de son stage de master ont montré que le temps de calcul était, dans le cas électrostatique, proportionnel à N^2 alors qu'il était proportionnel à N dans le cas gravitationnel. Nous nous sommes rapidement rendus compte que le problème provenait du fait qu'en première approximation, lorsqu'on veut calculer la force exercée par un groupe de particules dont les positions y_i tombent dans la cellule B sur une particule distante

en position x (cf Figure 8.1), celle-ci est simplement donnée par $\sum_{y_i \in B} m_i/r^2$ où $r = |x - z|$ est la distance de la particule au barycentre z définie par l'ensemble des particules dans la cellule B, i.e.

$$z \equiv \frac{\sum\limits_{y_i \in B} m_i x_i}{\sum\limits_{y_i \in B} m_i} \tag{8.1}$$

Donc, si $M_B \equiv \sum_{y_i \in B} m_i$ dénote la masse totale dans la cellule B, la force exercée

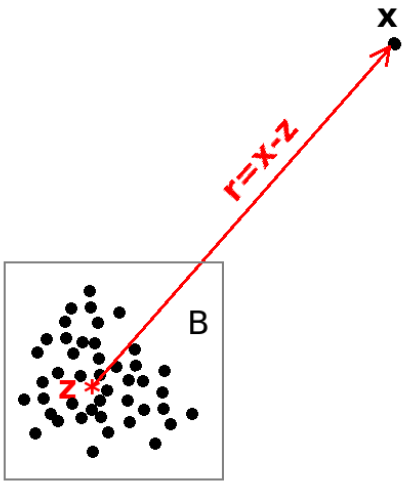

FIG. 8.1 –

par les particules de la cellule B sur la particule en x est simplement M/r^2, comme si toutes les particules étaient concentrées en un seul point z. Il est donc raisonnable, dans le cas gravitationnel d'utiliser l'équation (8.1) comme définition du centre du développement pour l'expansion multipolaire de la contribution de la cellule B au champ gravitationnel ressenti par la particule en x. Dans le cas Coulombien, le choix de (8.1) comme centre d'expansion est calamiteux. Ainsi, comme le montre schématiquement l'exemple à deux charges de la figure 8.2, le barycentre z_{elec} calculé sur la base de la définition (8.1), en remplaçant les masses par des charges, n'est même pas localisé entre les deux charges, car avec une charge $2q$ en $z = 0$ et une charge $-q$ en $z = d$, le barycentre se trouve en $z = -d$. Plus extrême encore, pour deux charges q_1 et q_2 de signes opposés mais de force presque égale $|q_2/q_1| = 1 + \varepsilon$, le barycentre calculé sur la base de (8.1) se trouverait à une distance de l'ordre de $d/\varepsilon \gg 1$, voire à une distance infinie dans le cas $q_2 = -q_1$. Afin de ramener le centre du développement dans la zone où sont concentrées les charges, nous utilisons la définition plus pertinente :

$$z^* \equiv \frac{\sum\limits_{y_i \in B} |q_i| x_i}{\sum\limits_{y_i \in B} |q_i|} \tag{8.2}$$

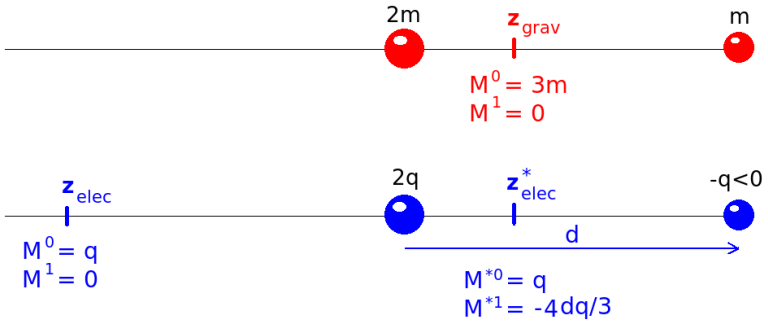

FIG. 8.2 –

Cette nouvelle définition ramène le centre de développement au milieu des charges (cf z^* dans la figure 8.2) avec la conséquence importante que le moment multipolaire d'ordre 1 $M^{*1} = \sum_i q_i(y_i - z^*)$ (le moment dipolaire) est non nul. Le moment M^{*1} étant nul dans le cas gravitationnel, il n'est pas possible d'utiliser, sans modifications, les expansions multipolaires du potentiel données par Dehnen. Le développement multipolaire du potentiel produit par les particules dans la cellule B sur la particule en x, en incluant les contributions du moment M^{*1} est présenté dans l'annexe 12.

Solution sale mais bon marché

Il existe une solution "bon marché" pour utiliser de façon efficace le code FalcON dans le cas d'un plasma sans nul besoin de modifier l'algorithme de base.
La solution "bon marché" consiste à calculer dans un premier temps le champ de force produit par l'ensemble des particules de charge positive et d'y soustraire ensuite le champ de force produit par l'ensemble des particules de charge négative. Techniquement cela consiste à attribuer, dans un premier temps, une charge positive mais quasi-nulle ϵ à toutes les particules de charge négative. On demande alors à FalcOn de calculer l'accélération $a_p(x_i)$, pour chaque particule i à l'emplacement x_i. FalcON n'a aucun problème pour le faire dans la mesure où toutes les charges sont maintenant positives, comme dans le cas gravitationnel. Dans un deuxième passage, on attribue une charge ϵ à toutes les charges positives et la valeur absolue de leur charge aux charges négatives, et on demande une deuxième fois à FalcOn de calculer l'accélération $a_e(x_i)$. La force totale $f(x_i)$ exercée par l'ensemble des charges sur la charge i est alors donnée par $f(x_i) = q_i[a_p(x_i) - a_e(x_i)]$ où q_i est la charge réelle (négative ou positive) de la particule i.
Cette solution "bon marché" présente l'avantage considérable de ne pas nécessiter de transformation de l'algorithme original de W. Dehnen. Elle a l'inconvénient de nécessiter deux appels à la routine de calcul des forces. Une solution plus précise nécessitant un seul appel à la routine de calcul des forces est présenté dans l'annexe 12.

8.2 Les collisions dans un plasma

Les applications d'un code de type N-corps en physique des plasmas sont nombreuses, mais tous les plasmas ne sont pas forcément de bons candidats pour des simulations N-corps. Par exemple, dans les plasmas dits non collisionnels, dont il a été question dans les chapitres 2 et 3, le mouvement d'une particule n'est que très rarement dominé par l'effet du champ électrique d'une seule particule voisine. Le plus souvent, le mouvement d'une particule donnée est piloté par le champ cumulé d'un très grand nombre de particules localisées dans son entourage plus au moins proche. Dans un tel cas, le plasma est dit "collectif" et se laisse décrire avantageusement par l'intermédiaire d'une fonction de probabilité $f_i(t, x, v)$ (une pour chaque espèce i de particules dans le système) plutôt que par un ensemble N de particules. L'évolution spatiale et temporelle d'un tel plasma est dans ce cas convenablement décrit par des équations cinétiques faisant intervenir $f_i(t, x, v)$, ses dérivés spatiales et temporelles, ainsi que ses dérivées, d'ordre plus au moins élevé par rapport à la vitesse[2].

Deux longueurs caractéristiques fondamentales

Lorsque dans un plasma les effets quantiques ne jouent aucun rôle, c.à.d. lorsque les distances caractéristiques entre les charges sont sensiblement plus grandes que les longueurs de De Broglie qui leur sont associées[3], son comportement est conditionné par deux longueurs caractéristiques : la longueur de Debye et le rayon d'interaction forte.

Prenons, par simplicité, le cas d'un plasma uniforme, globalement neutre, composé uniquement de protons et d'électrons (ionisation totale). Lorsque l'interaction entre particules voisines est faible, et que le plasma est proche de l'équilibre thermodynamique, il n'est pas surprenant que le plasma soit entièrement caractérisé par des quantités macroscopiques telles la densité numérique n, la température T, et la charge élémentaire e. En combinant ces quantités avec les constantes fondamentales ϵ_0 (la permittivité du vide) et k_B (la constante de Boltzmann) on construit une longueur caractéristique, la longueur de Debye :

$$\lambda_\mathrm{D} \equiv \left(\frac{\epsilon_0 k_\mathrm{B} T}{n\, e^2} \right)^{1/2} \tag{8.3}$$

[2]Dans l'équation de Vlasov (e.g. Delcroix et Bers, 1994; Golant *et al.*, 1980) $\partial f_i/\partial t + v\partial f_i/\partial x + a_i \partial f_i/\partial v = 0$, qui décrit l'évolution de la fonction de distribution f_i sous l'effet d'une accélération $a_i(t, x)$, apparaissent uniquement les dérivées premières par rapport à la vitesse. Dans l'équation de Fokker-Planck (e.g. Delcroix et Bers, 1994; Golant *et al.*, 1980) apparaissent également les dérivées d'ordre deux, ce qui permet de prendre en compte l'effet des collisions produisant des faibles déviations de la trajectoire des particules par rapport au cas non collisionnel. Une description complète de l'évolution de la fonction de distribution implique, en principe, l'intégration d'une équation cinétique comportant un nombre infini de termes comportant les dérivées de f_i par rapport à la vitesse à tous les ordres.

[3]Pour une particule de masse m se déplaçant à la vitesse v la longueur de De Broglie est définie par $\hbar/(mv)$ où $\hbar$ est la constante de Planck divisée par 2π.

On interprète généralement la longueur de Debye comme étant la longueur au delà de laquelle le champ électrique d'une charge test positive placée dans le plasma est complètement écrantée par le nuage d'électrons qu'elle concentre autour d'elle. Par extrapolation, on admet en général que les particules du plasma séparées d'une distance supérieure à λ_{D} ne peuvent interagir directement. La longueur de Debye est donc souvent considérée comme étant la limite supérieure du paramètre d'impact pour les collisions dans un plasma. Évidemment, la définition de la longueur de Debye, faisant intervenir les quantités macroscopiques n et T, n'a de sens que lorsque le nombre de particules dans un volume λ_{D}^3 est grand devant l'unité.
Dans un plasma classique, c.à.d. dans un plasma où les distances entre particules sont plus grandes que les longueurs de De Broglie de ces mêmes particules, il est possible de définir une autre longueur caractéristique, indépendante de la densité :

$$r_{\mathrm{s}} \equiv \frac{e^2}{12\pi\epsilon_0 k_{\mathrm{B}} T} \tag{8.4}$$

appelée rayon d'interaction forte ou rayon de Landau. Dans (8.4) r_{s} représente la distance entre deux électrons pour laquelle l'énergie électrostatique $e^2/4\pi\epsilon_0 r_{\mathrm{s}}$ est égale à deux fois l'énergie cinétique caractéristique $\frac{3}{2}k_{\mathrm{B}}T$ qui les anime. On en conclut que la trajectoire d'un électron sera fortement infléchie lorsque ce dernier croise un autre électron à une distance de l'ordre de r_{s}. En résumé, r_{s} représente la distance caractéristique pour les collisions proches, avec forte perturbation de la trajectoire, et λ_{D} la distance caractéristique pour les collisions distantes avec faible perturbation de la trajectoire.

Le logarithme de Coulomb

En l'absence de champ magnétique, et de forces extérieures, il est possible de décrire l'état d'un plasma uniforme, complètement ionisé et proche de l'équilibre thermodynamique avec deux variables thermodynamiques indépendantes seulement. Ces deux variables sont, par exemple, la température T et la densité électronique $n = n_{\mathrm{e}}$. La température, à elle seule, permet de définir une échelle de longueur $r_{\mathrm{s}} \propto T^{-1}$, une échelle de vitesse (nous choisissons la vitesse du son adiabatique des électrons $c_{\mathrm{e}} = \sqrt{3k_{\mathrm{B}}T/2m_{\mathrm{e}}}$) et donc une échelle de temps $\tau \equiv r_{\mathrm{s}}/c_{\mathrm{e}}$. Nous pouvons, avec ces échelles de longueur et de temps, dédimensionner les équations du mouvement des particules[4] et faire disparaître la température du système. Ainsi, par exemple, l'accélération d'un électron de masse m et charge e due à l'interaction électrostatique avec un autre électron à une distance r donnée par l'expression bien connue $\ddot{r} = e^2/(m4\pi\epsilon_0 r^2)$ devient $\ddot{\tilde{r}} = 2/\tilde{r}^2$ dans la version adimensionnée (avec $\tilde{r} \equiv r/r_{\mathrm{s}}$ et $\tilde{t} = tc_{\mathrm{e}}/r_{\mathrm{s}}$. Dans le système dédimensionné, la température n'apparaît donc plus de façon explicite, elle n'est donc pas, à elle toute seule, un paramètre fondamental du système. Reste la deuxième variable thermodynamique : la densité électronique.

[4] Les équations du mouvement d'un particule sont $dx/dt = v$ et $dv/dt = a$ où a est l'accélération due à toutes les autres particules dans le système.

En variables adimensionnées cette dernière s'écrit $\tilde{n}_\mathrm{e} = n r_\mathrm{s}^3$ et relie les deux échelles caractéristiques r_s et λ_D :

$$\frac{\lambda_\mathrm{D}}{r_\mathrm{s}} = \frac{1}{12\pi\tilde{n}}. \tag{8.5}$$

Dans la grande majorité des plasmas astrophysiques, la longueur de Debye λ_D est bien plus grande que r_s ce qui, suivant (8.5), signifie $\tilde{n} \ll 0.027$. Cependant, l'usage veut que pour caractériser un plasma, on n'utilise ni $\tilde{n}$ ni le rapport $\lambda_\mathrm{D}/r_\mathrm{s}$, mais bien plus souvent, le logarithme de Coulomb

$$\lambda \equiv \ln\left(\frac{\lambda_\mathrm{D}}{r_\mathrm{s}}\right). \tag{8.6}$$

Le logarithme de Coulomb intervient ainsi dans les coefficients de transport des expressions pour le flux de chaleur, le courant courant électrique, etc. que l'on trouve dans les livres (Braginskii, 1965; Hinton, 1983; Golant *et al.*, 1980, e.g.). Calculons, par exemple, la force de friction exercée par les protons sur un électron se déplaçant à la vitesse caractéristique $c_\mathrm{e} = (3k_\mathrm{B}T/2m)^{1/2}$ le long de la direction z, comme représenté sur la figure 8.3.

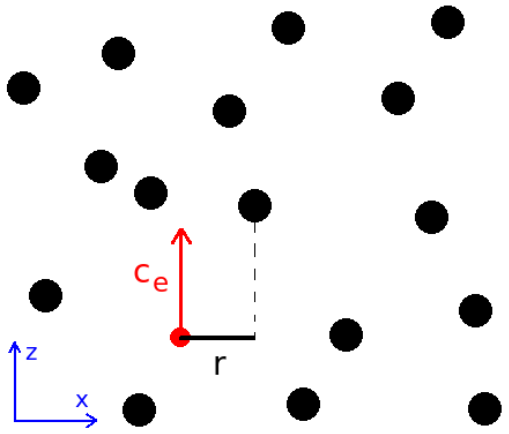

FIG. 8.3 – Electron se mouvant dans un champ de protons à la vitesse c_e le long de l'axe z. Est montré le paramètre d'impact r par rapport à un proton du système. La force de friction F exercée par les protons sur l'électron est donnée par l'équation (8.9). La force F est proportionelle au logarithme de Coulomb λ défini par (8.6)

.

La variation de la quantité de mouvement dans la direction z due à la présence d'un proton avec un paramètre d'impact r se calcule facilement Trubnikov (1965); Landau et Lifshitz (1960) :

$$\Delta p_z = -\sqrt{8}\, c_\mathrm{e} m \frac{r_\mathrm{s}^2}{r^2 + r_\mathrm{s}^2} \tag{8.7}$$

où l'on voit immédiatement que la variation est forte lorsque le paramètre d'impact r est de l'ordre de r_s alors qu'elle est faible pour $r \gg r_\mathrm{s}$. La force de friction F exercée par tous les protons du système s'obtient en intégrant (8.7) pour tous les paramètres d'impact r possibles, et en multipliant le résultat par le flux de protons nc_e vus par l'électron en mouvement, i.e. :

$$F = nc_\mathrm{e} \int_0^\infty 2\pi r dr\, \Delta p_z = 2\sqrt{8}\pi mnc_\mathrm{e}^2 r_\mathrm{s}^2 \int_0^\infty \frac{rdr}{r^2 + r_\mathrm{s}^2} \tag{8.8}$$

Cette intégrale diverge logarithmiquement pour les grandes valeurs du paramètre d'impact r. Pour obtenir une valeur finie, il faut la tronquer. Ayant déjà observé que le potentiel Coulombien d'une charge test dans le plasma est écranté pour des distances supérieures à la longueur de Debye λ_D, s'impose le choix de tronquer l'intégrale dans (8.8) à $r = \lambda_\mathrm{D}$. Si $\lambda_\mathrm{D} \gg r_\mathrm{s}$, comme dans grand nombre de plasmas astrophysiques, on obtient que la force de friction dépend linéairement du logarithme de Coulomb

$$F = 2\sqrt{8}\pi mnc_\mathrm{e}^2 r_\mathrm{s}^2 \int_0^{\lambda_\mathrm{D}} \frac{rdr}{r^2 + r_\mathrm{s}^2} \simeq 2\sqrt{8}\pi mnc_\mathrm{e}^2 r_\mathrm{s}^2 \ln\left(\frac{\lambda_\mathrm{D}}{r_\mathrm{s}}\right). \tag{8.9}$$

D'où l'intérêt de classer les plasmas suivant $\lambda \equiv \ln(\lambda_\mathrm{D}/r_\mathrm{s})$ plutôt que par $\lambda_\mathrm{D}/r_\mathrm{s}$.

Classification des plasmas

On dit d'un plasma qu'il est fortement couplé lorsque $\lambda \lesssim 1$ et qu'il est faiblement couplé lorsque $\lambda \gtrsim 10$. L'intensité du couplage des particules du plasma se mesure en comparant l'énergie électrostatique entre deux électrons voisins[5] et l'énergie cinétique caractéristique d'une particule $3k_\mathrm{B}T/2$. Ce rapport est un nombre sans dimensions appelé paramètre de couplage du plasma, généralement désigné par la lettre Γ dont on montre facilement (en utilisant la définition de Γ de l'annexe 10) qu'il est lié à λ par la relation $\lambda = \ln(\sqrt{3}/\Gamma^{3/2})$. Donc, plus le couplage entre particules voisines est fort moins le logarithme de Coulomb est grand. La table 8.1 montre une classification possible, plus au moins consensuelle, des plasmas en trois catégories distinctes suivant les valeurs de λ ou Γ. Les plasmas fortement couplés sont froids et denses. Leur comportement s'apparentent davantage à celui d'un liquide ou d'un cristal qu'à celui d'un gaz lorsque $\Gamma \gtrsim 10$. Ils peuvent être produits en laboratoire par irradiation de solides avec un faisceau laser mais ils existent également dans les atmosphères d'étoiles dégénérées (par exemple dans les atmosphères de naines blanches (Koester et Chanmugam, 1990)). Dans les plasmas fortement couplés, la dynamique des particules est dominée par le champ des particules proches. A l'autre extrême, les plasmas faiblement couplés sont des plasmas chauds et peu denses au comportement de type gazeux. Pratiquement tous les plasmas spatiaux (vent solaire,

[5]Dans un plasma de densité électronique n la distance moyenne d entre électrons voisins est évidemment de l'ordre de $n^{-1/3}$

TAB. 8.1 – Proposition de classification des plasmas en fonction du logarithme de Coulomb λ et/ou du paramètre de couplage Γ

Log de Coulomb	**Paramètre de couplage**	**Dénomination**
$\lambda \lesssim 1$	$\Gamma \gtrsim 0.5$	fortement couplé
$1 \lesssim \lambda \lesssim 10$	$0.5 \gtrsim \Gamma \gtrsim 2\,10^{-3}$	modérément couplé
$10 \lesssim \lambda$	$2\,10^{-3} \gtrsim \Gamma$	faiblement couplé

magnétosphères planétaires) et même le milieu interstellaire ainsi que les plasmas des tokamak sont faiblement couplés. Dans les plasmas faiblement couplés la dynamique des particules est dominée par le champ collectif des particules distantes. Les collisions binaires peuvent dans ce cas être négligées car relativement peu fréquentes. On devine aisément que dans les plasmas faiblement couplés, deux particules test[6] initialement voisines dans l'espace des phases $(\vec{x}, \vec{v})$ vont le rester pendant longtemps dans la mesure où le champ électrique ressenti par les deux particules ne diffère guère. Dans ce cas, des modèles numériques basés sur l'équation de Vlasov ou de Fokker-Planck sont parfaitement adaptés. Dans les plasmas modérément ou fortement couplés, il arrive plus fréquemment que dans les plasmas faiblement couplés, que des particules se rapprochent à des distances de l'ordre r_s. Dans ces conditions, deux particules test initialement proches dans l'espace des phases $(\vec{x}, \vec{v})$ voient leurs trajectoires diverger en un temps très court[7]. Ces divergences de trajectoires dans l'espace des phases sont incompatibles avec une description de type Vlasov ou Fokker-Planck dans lesquels la divergence entre trajectoires voisines est par définition faible. Dans ces conditions les simulations de type N-corps sont plus pertinentes car elles ne sont pas basées sur une hypothèse de non divergence de trajectoires voisines dans l'espace des phases.

8.3 Exemple 1 : la conduction de la chaleur dans un plasma modérément couplé

Avec Arnaud Beck, nous avons envisagé de simuler le transport de la chaleur dans un plasma modérément couplé d'électrons et protons avec $\lambda = 3.8$ (cf Annexe 10). C'est une valeur compatible avec les paramètres du plasma dans la partie supérieure de la zone convective du Soleil, zone dans laquelle les effets quantiques sont négligeables. Pour un tel plasma nous trouvons que le flux de chaleur transporté par les électrons est approximativement 26% en dessous de la valeur prévue par l'expression classique

[6] Particule test : particule qui se déplace dans le champ global dû aux autres particules du plasma sans influencer ces dernières par sa propre présence.

[7] Pour un électron rencontrant un autre électron le temps d'interaction est bien évidemment de l'ordre de $r_\mathrm{s}/c_\mathrm{e}$.

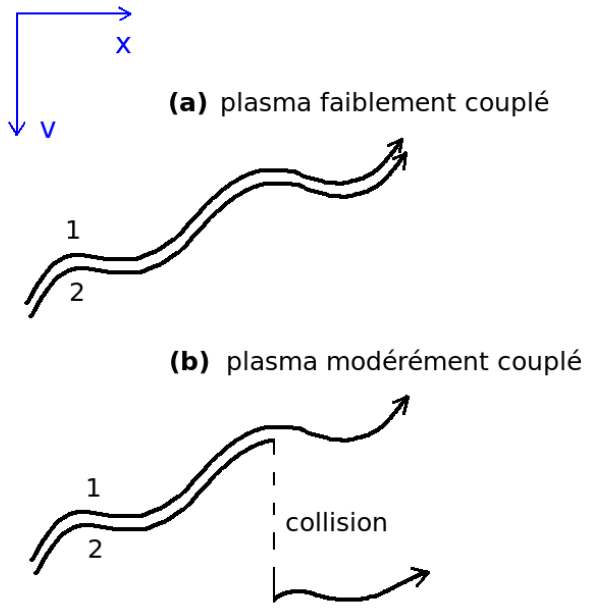

FIG. 8.4 – Dans un plasma faiblement couplé les trajectoires de deux particules test voisines dans l'espace de phase évoluent de façon quasi-identiques (cas (a)). Dans un plasma modérément couplé (et davantage dans un plasma fortement couplé) il n'est pas rare qu'une des particules test se retrouve à une distance de l'ordre de $r_{\rm s}$ d'une autre particule. Dans ce cas, sa vitesse change brutalement en un temps très court (collision sur la trajectoire 2) se séparant considérablement de la trajectoire 1. Les divergences de trajectoires sont d'autant plus fréquentes que le plasma est couplé.

.

de Spitzer et Härm (1953) :

$$q_{\rm e} = 3.2\frac{k_{\rm B}T}{m_{\rm e}} n\tau_{\rm e}\nabla(k_{\rm B}T) \tag{8.10}$$

où $\tau_{\rm e}$ est la fréquence de collision pour les électrons dans la limite de couplage faible (équation (6) Beck et Pantellini, 2007). Dans le traitement de Spitzer et Härm, seules les collisions lointaines, c.à.d. les collisions avec des paramètres d'impact r de l'ordre de $\lambda_{\rm D}$ sont considérées. Dans ces conditions les coefficients de transport ne sont convenablement approximés que pour $\lambda \gtrsim 10$. Pour des valeurs inférieures, on estime que l'erreur sur les coefficients est de l'ordre λ^{-1}. Dans un modèle un peu plus élaboré que celui de Spitzer et Härm, Li et Petrasso (1993) proposent une correction de l'ordre $1/6\lambda^{-1}$ ce qui ne modifie que de 4% environ la valeur classique de Spitzer, loin des 26% que nous trouvons avec nos simulations N-corps.

8.4 Exemple 2 : expansion d'un plasma non collisionnel dans le vide

Dans un travail plus récent Beck et Pantellini (2008) (cf Annexe 11), toujours avec A. Beck, je me suis intéressé au problème de l'expansion dans le vide d'un plasma à géométrie sphérique. Un plasma d'ions froids et d'électrons chauds, initialement confiné dans une sphère de rayon R_0, est laissé libre de se détendre dans le vide. C'est une situation que l'on rencontre dans le contexte de la fusion contrôlée (e.g. Ditmire *et al.*, 1999) où des poussières de matière contenant typiquement entre 10^3 et 10^7 atomes sont irradiées par des impulsions lasers intenses d'une durée de l'ordre de la femtoseconde. L'énergie déposée par le laser dans les grains de poussière chauffe principalement les électrons, lesquels en se séparant des noyaux atomiques laissent derrière eux des grumeaux d'ions qui explosent sous l'effet de la force électrique entre ions chargés positivement. Selon les mesures expérimentales de Ditmire *et al.* (1999) les ions sont accélérés à des énergies de plusieurs keV ce qui, dans le cas d'ions de deutérium, permet le déclenchement d'une réaction de fusion $D + D \rightarrow He^3 + n$ avec une probabilité élevée.
Dans Beck et Pantellini (2008) nous présentons un nouveau modèle semi-analytique et non collisionnel de l'expansion que nous comparons avec des résultats de simulations N-corps. Le modèle que nous proposons reproduit beaucoup mieux les résultats de simulation que le modèle actuellement en vogue de Murakami et Basko (2006), principalement en raison du fait que Murakami et Basko supposent que la température des électrons est spatialement constante, ce qui n'est généralement pas observé dans les simulations numériques. La figure 8.5 montre les profils de densité des ions et des électrons observés dans une simulation N-corps comparés avec les profils théoriques issus de notre modèle. L'accord est bon, voire très bon, si on considère que les conditions initiales[8] de la simulation étaient très éloignées des conditions asymptotiques (pour des temps longs) prévues par le modèle. Dans le cas particulier de la figure 8.5, la principale différence entre modèle et simulation est à chercher dans la densité des électrons pour $r/R \gtrsim 1.3$[9], bien plus forte dans la simulation que dans le modèle. La différence s'explique par le fait que, dans la simulation, une fraction non négligeable d'électrons possède une énergie suffisamment grande pour quitter définitivement le système. Ainsi la densité électronique mesurée dans la simulation pour $r/R \gtrsim 1.3$ est destinée à décroître au fur et à mesure que les électrons libres se séparent de la sphère d'ions $r/R \leq 1$. Malheureusement, des simulations beaucoup plus longues et coûteuses sont nécessaires pour confirmer cette hypothèse, somme toute très raisonnable. Des simulations plus longues devraient également pouvoir confirmer l'existence d'un front électronique, absent du modèle de Murakami et Basko (2006) dans lequel les électrons sont supposés s'étendre jusqu'à l'infini.

[8] La densité des électrons, la densité des ions, ainsi que la température des électrons sont initialement uniformes.

[9] r est la distance au centre de l'expansion et $R(t)$ est la position du front ionique.

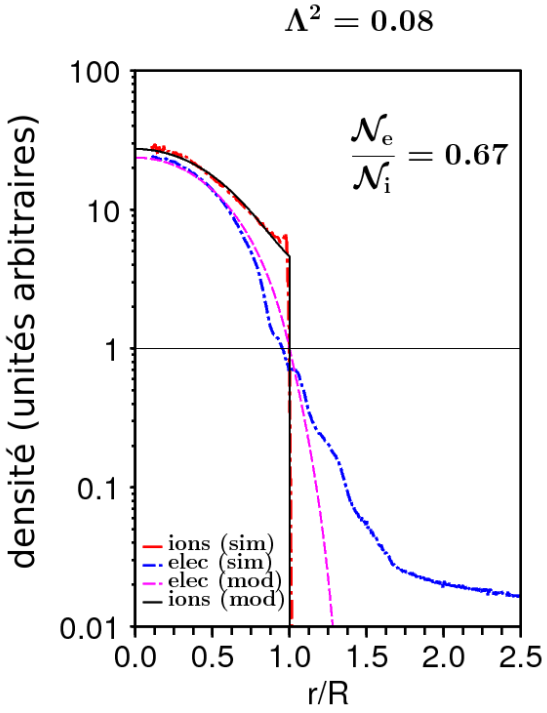

FIG. 8.5 – Profils radiaux des densités électroniques et ioniques observés dans une simulation N-corps de l'expansion d'un plasma à symétrie sphérique, comparés avec les profils issus du modèle de Beck et Pantellini (2008). Les deux paramètres fixant les profils du modèle sont le rapport $\Lambda = \lambda_D(R)/R$ entre la longueur de Debye en $r = R$ et le rayon de la sphère d'ions R ainsi que le rapport entre le nombre total d'électrons non libres $\mathcal{N}_e$ et le nombre total d'ions $\mathcal{N}_i$.

Chapitre 9

Conclusions et perspectives

J'ai essayé, au fil des chapitres de ce mémoire, de donner un aperçu des sujets auxquels je me suis intéressé au cour de ces dernières années de ma vie de chercheur. Les suites possibles sont nombreuses et, comme le montre l'expérience, souvent imprévisibles. Certaines sont déjà une demi-réalité, certaines sont juste des pistes ou des souhaits, et d'autres ne sont pas encore écrites. Je me limiterai ici aux demi-réalités. Ainsi, dans le cadre des simulations de systèmes avec des collisions non élastiques (cf tout particulièrement les chapitres 5 et 7), j'ai commencé avec S. Landi, à étudier le cas d'un gaz ou un plasma stratifié par la gravitation, avec l'idée de tenter de comprendre le rôle des pertes radiatives dans l'atmosphère solaire. Les récentes simulations N-corps d'un plasma, que A. Beck a réalisées au cours de sa thèse, sont très prometteuses. Elles le sont tout spécialement en raison de leur complémentarité par rapport aux simulations largement répandues, réalisées avec les outils classiques (codes Vlasov, Fokker-Planck, MHD, etc.). Dans ce contexte, les simulations d'expansion d'un plasma dans le vide, dont il n'a pas été question dans ce mémoire, sont particulièrement intéressantes en raison du grand nombre d'applications potentielles en astrophysique (e.g. sillage de la lune) et au laboratoire (expériences d'interaction laser-matière). L'autre objectif fort, nécessitant un investissement assez considérable, est l'optimisation du code N-corps suivant les idées présentées dans l'annexe 12 et, objectif encore plus ambitieux, l'inclusion de la force de Lorentz dans le calcul de l'interaction entre les charges en mouvement.
J'ai dans le passé utilisé des codes numériques "classiques" pour simuler des plasmas sans collisions (cf les chapitres 2 et 3). Je continue d'utiliser ces codes dans le cadre de mes tâches d'enseignement, où il m'arrive également d'utiliser des codes fluides hydrodynamiques ou magnétohydrodynamiques. Ces codes seront extrêmement utiles dans le cadre de la mission spatiale Bepi Colombo, qui atteindra la magnétosphère de Mercure au milieu de la décennie 2010-2020, mission pour laquelle je me suis engagé à mettre au point des outils de simulation permettant de modéliser l'environnement complexe de Mercure afin d'aider à l'interprétation des données de la sonde.

Bibliographie

A. Baldassarri, U. Marini Bettolo Marconi et A. Puglisi : Influence of correlations on the velocity statistics of scalar granular gases. *Europhysics Letters*, 58:14–20, avril 2002.

J. Barnes et P. Hut : A Hierarchical O(NlogN) Force-Calculation Algorithm. *Nat*, 324:446–449, décembre 1986.

A. Beck et F. Pantellini : Ab initio simulations of the heat flux in a moderately coupled plasma and steep temperature gradients. *submitted to The European Physical Journal D*, 2007.

A. Beck et F. Pantellini : Spherical expansion of a collisionless plasma into vacuum : self-similar solution and ab initio simulations. *submitted to Plasma Physics and Controlled Fusion*, 2008.

D. Benedetto, E. Caglioti et M. Pulvirenti : A Kinetic equation for granular media. *Math. Mod. Num. Anal.*, 31(5):615–641, 1997.

M. N. Berberan-Santos, E. N. Bodunov et L. Pogliani : On the barometric formula. *American Journal of Physics*, 65:404–412, mai 1997.

S.I. Braginskii : Transport processes in plasmas. *In* M.A. Leontovich, éditeur : *Reviews of Plasma Physics*, volume 1, pages 205–311. Consultants Bureau, New York, 1965.

W. Dehnen : A Hierarchical $\mathcal{O}(N)$ Force Calculation Algorithm. *Journal of Computational Physics*, 179:27–42, juin 2002.

J.L Delcroix et A. Bers : *Physique des Plasmas*. Inter Editions / CNRS Editions, 1994.

T. Ditmire, J. Zweiback, V. P. Yanovsky, T. E. Cowan, G. Hays et K. B. Wharton : Nuclear fusion from explosions of femtosecond laser-heated deuterium clusters. *Nature*, 398:489–492, avril 1999.

J. C. Dorelli et J. D. Scudder : Electron heat flow carried by kappa distributions in the solar corona. *Geophys. Res. Lett.*, 26:3537–3540, décembre 1999.

J. C. Dorelli et J. D. Scudder : Electron heat flow in the solar corona : Implications of non-Maxwellian velocity distributions, the solar gravitational field, and Coulomb collisions. *Journal of Geophysical Research (Space Physics)*, 108:1294–+, juillet 2003.

B. Edlén : Die Deutung der Emissionslinien im Spektrum der Sonnenkorona. Mit 6 Abbildungen. *Zeitschrift fur Astrophysik*, 22:30–+, 1943.

J. Eggers : Sand as Maxwell's Demon. *Physical Review Letters*, 83:5322–5325, décembre 1999.

V. Garzó, J. M. Montanero et J. W. Dufty : Mass and heat fluxes for a binary granular mixture at low density. *Physics of Fluids*, 18:3305–+, août 2006.

V.E. Golant, A.P. Zhilinsky et I.E. Sakharov : *Fundamantals of plasma physics*. John Wiley & Sons, New York, 1980.

P. Hellinger : Comment on the linear mirror instability near the threshold. *Physics of Plasmas*, 14:2105–+, août 2007.

D. W. Hewett et A. B. Langdon : Electromagnetic direct implicit plasma simulation. *Journal of Computational Physics*, 72:121–155, septembre 1987.

F.L. Hinton : Collisional transport in plasma. *In* A.A. Galeev et R.N. Sudan, éditeurs : *Basic Plasma Physics*, volume 1, pages 147–197. North-Holland, Amsterdam, 1983.

J. V. Hollweg : On electron heat conduction in the solar wind. *J. Geophys. Res.*, 79:3845–3850, 1974.

H. M. Jaeger, S. R. Nagel et R. P. Behringer : Granular solids, liquids, and gases. *Reviews of Modern Physics*, 68:1259–1273, octobre 1996.

K. Jockers : Solar wind models based on exospheric theory. *A&A*, 6:219–239, juin 1970.

D. Koester et G. Chanmugam : Physics of white dwarf stars. *Reports of Progress in Physics*, 53:837–915, 1990.

D. Krauss-Varban, F. G. E. Pantellini et D. Burgess : Electron dynamics and whistler waves at quasiperpendicular shocks. *Geophys. Res. Lett.*, 22:2091–2094, 1995.

L.D. Landau et E.M. Lifshitz : *Course of Theoretical Physics*, volume 1. Pergamon Press, Oxford, England, 1 édition, 1960.

S. Landi : *Modèles cinétiques du vent solaire*. Thèse de doctorat, Université Paris 7, décembre 2001.

S. Landi et F. Pantellini : Kinetic simulations of the solar wind from the subsonic to the supersonic regime. *A&A*, 400:769–778, mars 2003.

S. Landi et F.G.E. Pantellini : On the temperature profile and heat flux in the solar corona : Kinetic simulations. *A&A*, 372:686–701, juin 2001.

C.-K. Li et R. D. Petrasso : Fokker-Planck equation for moderately coupled plasmas. *Physical Review Letters*, 70:3063–3066, mai 1993.

L. Matteini, S. Landi, P. Hellinger, F. Pantellini, M. Maksimovic, M. Velli, B. E. Goldstein et E. Marsch : Evolution of the solar wind proton temperature anisotropy from 0.3 to 2.5 AU. *Geophys. Res. Lett.*, 34:20105–+, octobre 2007.

M. Murakami et M. M. Basko : Self-similar expansion of finite-size non-quasi-neutral plasmas into vacuum : Relation to the problem of ion acceleration. *Physics of Plasmas*, 13:2105–+, janvier 2006.

I. Newton : *Philosophiæ Naturalis Principia Mathematica*. S. Pepys, Reg. Soc. Præses, Londini, 1687.

A. Pannekoek : Ionization in stellar atmospheres (Errata : 2 24). *Bulletin of the Astronomical Institutes of the Netherlands*, 1:107–+, juillet 1922.

F. Pantellini et S. Landi : Species segregation in one-dimensional granular-system simulations. *European Physical Journal E*, 25(2):201–212, 2008. ISSN 1292-8941.

F. G. E. Pantellini : A model of the formation of stable nonpropagating magnetic structures in the solar wind based on the nonlinear mirror instability. *J. Geophys. Res.*, 103:4789–+, mars 1998.

F. G. E. Pantellini : A simple numerical model to simulate a gas in a constant gravitational field. *Am. J. Phys.*, 67:61–68, janvier 2000.

F. G. E. Pantellini, D. Burgess et S. J. Schwartz : On the non-linear mirror instability. *Advances in Space Research*, 15:341–344, 1995.

F. G. E. Pantellini, A. Heron, J. C. Adam et A. Mangeney : The role of the whistler precursor during the cyclic reformation of a quasi-parallel shock. *J. Geophys. Res.*, 97:1303–1311, février 1992.

F. G. E. Pantellini et S. J. Schwartz : Electron temperature effects in the linear proton mirror instability. *J. Geophys. Res.*, 100:3539–3549, mars 1995.

F. G. E. Pantellini, S. K. Solanki et J. O. Stenflo : Velocity and temperature in solar magnetic fluxtubes from a statistical centre-to-limb analysis. *A&A*, 189: 263–276, janvier 1988.

F.G.E. Pantellini et S. Landi : A simulation method for semicollisional plasmas. *Ap&SS*, 277:149–152, janvier 2001.

E. N. Parker : Dynamics of the interplanetary gas and magnetic fields. *ApJ*, 128:664+, novembre 1958.

O. A. Pokhotelov, M. A. Balikhin, H. S.-C. K. Alleyne et O. G. Onishchenko : Mirror instability with finite electron temperature effects. *J. Geophys. Res.*, 105:2393–2402, février 2000.

O. A. Pokhotelov, R. A. Treumann, R. Z. Sagdeev, M. A. Balikhin, O. G. Onishchenko, V. P. Pavlenko et I. Sandberg : Linear theory of the mirror instability in non-Maxwellian space plasmas. *Journal of Geophysical Research (Space Physics)*, 107:1312–+, octobre 2002.

R. Ramírez et R. Soto : Temperature inversion in granular fluids under gravity. *Physica A Statistical Mechanics and its Applications*, 322:73–80, mai 2003.

D. J. Rose : General Criterion for Mirror Instability of a Plasma. *Physics of Fluids*, 8:951–955, mai 1965.

S. Rosseland : Electrical state of a star. *MNRAS*, 84:720, juin 1924.

C. T. Russell et E. W. Greenstadt : Initial ISEE magnetometer results - Shock observation. *Space Science Reviews*, 23:3–37, mars 1979.

R. Z. Sagdeev et C. F. Kennel : Collisionless shock waves. *Scientific American*, 264:106–113, avril 1991.

J. D. Scudder : On the causes of temperature change in inhomogeneous low-density astrophysical plasmas. *ApJ*, 398:299–318, octobre 1992.

J. D. Scudder : Electron and ion temperature gradients and suprathermal tail strengths at parker's solar wind sonic critical point. *J. Geophys. Res.*, 101:11039–11054, mai 1996.

V. D. Shapiro et V. I. Shevchenko : Quasilinear theory of instability of a plasma with an anisotropic ion velocity distribution. *Soviet Physics - JETP*, 18:1109, 1964.

S. K. Solanki, F. G. E. Pantellini et J. O. Stenflo : Lines in the wavelength range 4300-6700 A with large Stokes V amplitudes outside sunspots. *Sol. Phys.*, 107:57–61, janvier 1987.

D. J. Southwood et M. G. Kivelson : Mirror instability. I - Physical mechanism of linear instability. *J. Geophys. Res.*, 98:9181–9187, juin 1993.

L. Spitzer et R. Härm : Transport phenomena in a completely ionized gas. *Phys. Rep.*, 89:977–981, mars 1953.

B. A. Trubnikov : Particle Interactions in a Fully Ionized Plasma. *Reviews of Plasma Physics*, 1:105–+, 1965.

D. Winterhalter, M. Neugebauer, B. E. Goldstein, E. J. Smith, S. J. Bame et A. Balogh : ULYSSES field and plasma observations of magnetic holes in the solar wind and their relation to mirror-mode structures. *J. Geophys. Res.*, 99:23371–+, décembre 1994.

Annexes

1 Une simulation de choc sans collisions

GRL, 22, 2091-2094 (1995)

GEOPHYSICAL RESEARCH LETTERS, VOL. 22, NO. 16, PAGES 2091-2094, AUGUST 15, 1995

Electron dynamics and whistler waves at quasi-perpendicular shocks

D. Krauss-Varban

Department of Electrical and Computer Engineering, University of California, San Diego, La Jolla

F. G. E. Pantellini[1] and D. Burgess

Astronomy Unit, Queen Mary and Westfield College, London

Abstract. The collisionless, supercritical, quasi-perpendicular fast shock is investigated on sub-ion scales using an implicit, two-dimensional (2-D) full particle code. For the first time, simulations are carried out with realistic characteristic frequencies and sufficiently high mass ratio between the protons and electrons. As a result, there is relatively little scattering of the electrons, i.e., they behave largely adiabatically as previously suggested based on spacecraft observations at the Earth's bow shock. The large mass ratio also allows for a realistic description of the whistler mode dispersion. Phase-standing whistlers with propagation along the shock normal appear as transients. The dominant whistlers found at late times in the simulations have upstream directed group velocity but propagate at oblique direction between the shock normal and the ambient magnetic field. Their properties match those of the ubiquitous observed upstream whistlers ("one-Hertz waves").

1. Introduction

Through a combination of spacecraft observations, theory, and simulations, much progress has been made in our understanding of collisionless shocks, such as the Earth's and other planetary bow shocks. At supercritical quasi-perpendicular shocks (angle between the upstream magnetic field $\mathbf{B_0}$ and shock normal $\mathbf{n}$ is $\theta_{Bn} \gtrsim 45°$), ion thermalization and the global shock structure are dominated by reflected ions, which are convected back into the shock [*Leroy et al.,* 1982; *Sckopke et al.,* 1983; *McKean et al.,* 1995, and references therein]. Compared to the ions, electron thermalization and associated wave processes are only understood to a much lesser extent. The microphysical description of the electrons constitutes one of the outstanding problems of shock physics. It is not known to what extent the ion and electron dynamics at the shock are coupled. This paper presents initial results of two-dimensional (2-D) implicit full particle simulations that are carried out to address this topic.

Observationally, a number of points relevant to the present study have been established: (1) The Earth's bow shock shows various features in the electron velocity distribution such as a loss-cone, temperature anisotropies, and beams before a thermalized, flat-topped distribution is reached downstream [*Feldman et al.,* 1983]. (2) Still, the observed distributions are consistent with the idea that electrons behave mostly adiabatically (i.e., conserving the magnetic moment), with only moderate scattering that may fill in otherwise inaccessible parts of the phase space [*Feldman et al.,* 1983; *Scudder et al.,* 1986]. (3) While the overall shock ramp appears to be of the order of the proton inertial length c/ω_p, the steepest part may have an exponential scale that is only a fraction of that ($\sim 0.2\ c/\omega_p$, *Scudder et al.* [1986]). (4) In addition to electrostatic turbulence, electromagnetic whistler waves are observed both upstream and in the shock transition [*Gurnett,* 1985]. In the upstream, these waves were sometimes called "one-Hertz waves" [*Hoppe and Russell,* 1983] but are now simply referred to as "upstream whistlers" [*Orlowski et al.,* 1993, 1995].

It is generally believed that in addition to the macroscopic fields, which determine the overall mapping of the distribution function, the above mentioned waves are responsible for the pitch-angle scattering (and any additional thermalization) of the electrons [*Feldman et al.,* 1983; *Krauss-Varban,* 1992; *Veltri and Zimbardo,* 1993]. However, a genuine physical explanation of the wave generation, electron dynamics, and any sub-ion scale shock structure requires analysis of the evolution of the electron distribution in the self-consistent fields. The ideal tool for such a study are particle simulations which include processes in which both electrons and ions are involved. Due to the different temporal and spatial scales of these particles, such simulations are extremely difficult to perform. Below we show that for a realistic ordering of the frequencies and to capture the correct propagation characteristics of the waves, a large mass ratio between the protons and electrons is necessary. Simply speaking, a low mass ratio implies artificially strong coupling between the protons and electrons. This affects not only the wave properties but also leads to unphysical heating of the electrons and protons. Since most previous simulations employed the conventional explicit particle codes [*Forslund et al.,* 1984; *Lembège and Dawson,* 1987; *Savoini and Lembège,* 1994], which require time steps smaller than the inverse electron plasma frequency, the goal of a realistic mass ratio could not be achieved except in short duration 1-D simulations [*Liewer et al.,* 1991]. Making use of an implicit full particle code, which does not have the above time step restriction, we present here for the first time results of realistic, large mass-ratio 2-D shock simulations.

[1]Now at DESPA, Observatoire de Paris, Meudon, France.

Paper number 95GL01782
0094-8534/95/95GL-01782$03.00

2. Simulation

The implicit, full particle simulation code is based on the so-called direct (predictor-corrector) method as described by *Hewett and Langdon* [1987], with several improvements due to *Heron and Adam* [1989]. A variant of this code has previously been used for simulations of the quasi-parallel bow shock [*Pantellini et al.*, 1992]. The particles and fields are initialized according to Rankine-Hugoniot, with an initial linear shock ramp 4 c/ω_e wide in the center of the box. Particles are continuously injected and allowed to escape at both sides (along the x-axis) to maintain upstream and downstream Maxwellian distributions. The total flux through the system is constant such that the shock remains in the center of the box, and the number of simulation particles is kept constant. The -**x** direction is aligned with the shock normal **n**. The second simulation direction is along **y** with periodic boundary conditions. The upstream magnetic field $\mathbf{B_o}$ is kept in the simulation plane, making an angle of $\theta_{Bn} = 60°$ with the shock normal. The other plasma parameters are set to reflect generic bow shock conditions: the Alfvén Mach number is $M_A = 5$, and the electron and ion upstream beta are $\beta_e = \beta_i = 0.5$.

The electron plasma to cyclotron frequency ratio is $\omega_e/\Omega_e = 100$ and the proton to electron mass ratio is set to $m_p/m_e = 400$. This separates the characteristic frequencies (ω_e, Ω_e, Ω_{LH}, Ω_p) by more than an order of magnitude each. Here, Ω_{LH} is the lower hybrid frequency and Ω_p is the proton cyclotron frequency. Also, this gives a ratio of $(c/\omega_p)/(c/\omega_e) = 20$ between the proton and electron inertial lengths. The cell sizes are $\Delta x = 0.25\ c/\omega_e$ and $\Delta y = 1.0\ c/\omega_e$, with a box size $X \times Y$ of 1600×64 cells or $20 \times 3.2\ c/\omega_p$, and an average of 20 particles per cell for each species. The simulation is run in two parts with 10,000 time steps each. The initial part has a time step $\Delta t = 0.16\ \Omega_e^{-1}$, the second part has 1/2 of this to properly resolve the electron gyromotion. The total run time is $6\ \Omega_p^{-1}$. The above parameters are carefully balanced to satisfy numerical conditions, allow a sufficiently large space-time domain, and avoid excessive numerical cooling or scattering within a feasible total CPU.

For the fast mode shock transition, and to differentiate between shock-generated phase-standing and instability-generated propagating waves, it is crucial to describe the whistler dispersion properly. Figure 1 shows the dispersion relation $\omega(k)$ normalized to ion scales and in the shock frame for several mass ratios m_p/m_e, as indicated. The propagation angle is (a) $\theta_{kB} = 30°$, i.e.,

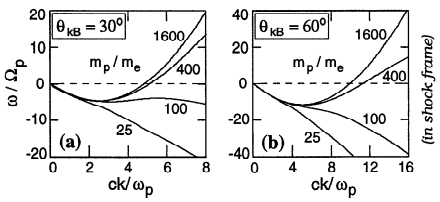

Figure 1. Dispersion relation $\omega(k)$ for whistler waves (a) propagating at an angle $\theta_{kB} = 30°$ and (b) at $\theta_{kB} = 60°$ with respect to $\mathbf{B_o}$, for mass ratios as indicated.

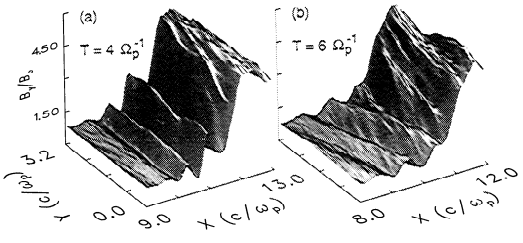

Figure 2. Compressional magnetic field component at (a) early and (b) late time in the simulation. Note the transition from phase-standing waves to oblique, upstream propagating whistlers.

wavevector **k** between $-\mathbf{B_o}$ and **n**, and (b) $\theta_{kB} = 60°$, i.e., **k** || **n**. Except for the scale there are few differences. One can conclude that a value of $m_p/m_e \sim 400$, as employed here, is necessary to capture waves that are approximately phase standing or that have an upstream directed group velocity $\partial\omega/\partial k > 0$.

3. Results and Discussion

In this letter we concentrate on the overall shock solution, whistler waves, and the general electron phase space evolution. A more detailed description of the simulation results will be given in a forthcoming publication.

For the Mach numbers common to the front of the bow shock, no phase-standing whistler wave train is found in satellite observations. Such whistlers would be expected to form in a sufficiently thin and steady shock ramp as part of the steepening/evolution of the shock, and should propagate along the shock normal [*cf. Tidman and Northrop*, 1968]. Instead, the whistlers observed in the ramp and upstream propagate at an angle to **n** and have varying phase velocities, although they are still mainly confined to the plane of $\mathbf{B_o}$ and **n** [*Orlowski and Russell*, 1991]. Typical propagation angles between **k** and $\mathbf{B_o}$ at both Earth and Venus are $20° \leq \theta_{kB} \leq 40°$ [*Fairfield*, 1974; *Orlowski and Russell*, 1991], with a strong preference for $\sim 40°$ [*Fairfield*, 1974; *Hoppe et al.*, 1982]. The decreasing amplitude away from the shock led Fairfield to suggest that the waves are generated in the ramp; a more thorough analysis by *Orlowski et al.* [1995] has recently confirmed this and has shown independent evidence that the waves are not generated in situ in the upstream. A lower frequency cut-off has been found to correspond to a wavelength of $\sim 1\ c/\omega_p$, with the conjecture that it coincides with the shock width [*Orlowski et al.*, 1995].

Turning to the simulations: When the shock is first forming, we find some transient, approximately group-standing whistlers that are generated by reflected or leaking ions. Soon after that, a phase-standing wave trains develops. Up to this point the results are similar to 1-D hybrid simulations (kinetic ions, fluid electrons) that we conducted for comparison, with the exception of strong electron Landau damping present here. However, at later times we find that eventually most of the phase-standing wavetrain is suppressed in favor of whistler waves that appear to propagate at some angle between **n** and $\mathbf{B_o}$. Figure 2 shows the compressional

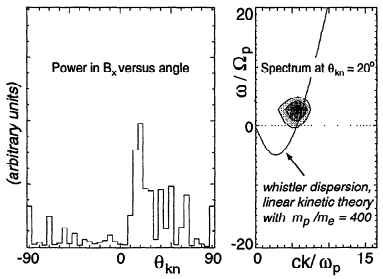

Figure 3. Spectral analysis of waves in Fig. 2*b*. Power peaks at $\theta_{kn} \sim 20°$; waves are on the whistler branch with upstream directed group and phase velocity.

field component B_y at (a) early times ($4\ {\Omega_p}^{-1}$) and (b) late times ($6\ {\Omega_p}^{-1}$) in the simulation, in the shock vicinity. The difference between the early, phase-standing waves and the later, oblique waves is quite evident. At both times the total shock width is approximately one ion inertial length, and it is a fraction of that (~ 0.25 to 0.5 c/ω_p or 5 to 10 c/ω_e) for the e-folding scale of the magnetic field. The latter is in fair agreement with the observations by *Scudder et al.* [1986].

Figure 3 shows a spectral diagnostic of the waves. There is finite power at all angles between $\mathbf{n}$ (0°) and $-\mathbf{B_o}$ (60°), with a peak propagation angle of $\theta_{kn} \sim 20°$ or $\theta_{kB} \sim 40°$, and upstream directed group and phase velocities. The frequency in the plasma rest frame is $\sim 30 \pm 5\ \Omega_p$, the wavelength 1 c/ω_p. Thus, we find that these waves have all the major properties of observed "one-Hertz waves" [*Orlowski et al.*, 1993, 1995]: they are finite bandwidth in the shock frame, generated in the ramp but propagate upstream, they are significantly Landau damped, and have $\mathbf{k}$ in the coplanarity plane at some small angle away from $\mathbf{n}$ but between $\mathbf{n}$ and $\mathbf{B_o}$, with $\theta_{kB} \sim 40°$.

An analysis of the proton phase space shows that the most likely free energy source for these waves is in the reflected, gyrating ions. While a detailed instability calculation remains to be carried out, it is known that the effective anisotropy contained in these ions can drive a variant of the cross-field streaming instability [*Wu et al.*, 1983]. This instability is not driven by the cross-field current. Rather, is related to the anisotropic proton beam instability advanced by *Wong and Goldstein* [1988] to explain upstream whistlers. The main difference here is that the waves are generated in the ramp by the gyrating ions that convect back into the shock, and not in situ upstream by a propagating ion beam as suggested by *Wong and Goldstein*. Indeed, these authors have shown that the growth rate maximizes at oblique propagation if the perpendicular energy of the ions is large, as in the present case.

Figure 4 shows y-averaged profiles of the total magnetic field and the parallel and perpendicular electron temperature (all normalized to upstream values). Also shown is the electron phase space $v_\perp \cdot f(v_\parallel, v_\perp)$, normalized with the upstream thermal velocity, at three selected regions: in the ramp, at the overshoot, and just downstream from the overshoot. There is a factor of two per contour line with an overlayed grey scale. Note that the averaging over y broadens the apparent shock profile. There is very little pre-shock heating of the electrons, although there is a finite upstream directed heat flux as evidenced by the ramp phase space. Although the averaging has diluted some of the finer details of the phase space, the tilt of the ramp distribution shows that it is the electrons with large magnetic moment μ that are preferentially reflected. There is a small temperature anisotropy $T_{e\perp}/T_{e\parallel} > 1$ in the vicinity of the overshoot. Note, however, that the maximum $T_{e\perp}$ is achieved just in front of the overshoot, and its value farther downstream is slightly below what is expected from μ-conservation. We interpret these findings as due to selective reflection of electrons with large μ. There may also be some cooling associated with the filling of the parallel phase space. Values of $T_{e\perp}$ slightly below expectations from μ-conservation have also been found in observations [*Scudder et al.*, 1986]. $T_{e\parallel}$ remains nearly constant downstream. The total energy gain ($E_{th_1} - E_{th_o} = 60$ eV -20 eV) is commensurate with the deHoffmann-Teller frame cross-shock potential determined from the simulation ($e\phi \sim 40$ eV). The distribution downstream from the overshoot has the characteristic shape that results in a flat-top when integrated over $v_\perp$.

Further analysis of the phase space will be presented in a separate publication. Here the central point is that the phase space evolution appears to be largely determined by the macroscopic fields, as originally conjectured by *Feldman et al.* [1983] and *Scudder* [1986] based on detailed spacecraft observations. It should be pointed out that the amount of scattering necessary is small here; it would be larger for a shock with a higher ratio of the cross-shock potential energy to the adiabatic perpendicular energy of the electrons. We find no evidence of additional heating, due to either electrostatic waves or due to strong non-adiabatic motion in a sharp gradient of $\phi(x)$, as was suggested by *Balikhin and Gedalin* [1994]. Note that while simulations with smaller mass ratio or fewer particles per cell may also result in flat-tops, such distributions can be due to a number of reasons, such as scattering in numerical (i.e., non-physical) waves, or unrealistic coupling of the proton and electron scales. The nearly adiabatic behavior of the electrons and lack of additional heating in the present simulations are from a physical viewpoint more significant features than the simple presence of a flat-top. The lack of signatures indicating strong free energy is also compatible with the idea that the upstream whistlers are generated by the reflected ions, with little kinetic contribution by the electrons. However, since these waves are strongly Landau damped, they may be

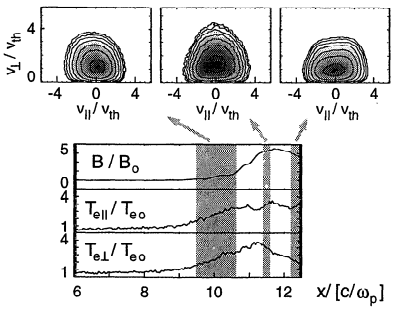

Figure 4. Electron phase-space, and cross-shock profiles of the magnetic field and parallel and perpendicular electron temperature, at the end of the simulation.

responsible for a slight pre-heating of the electrons in the vicinity of the ramp [c.f. *Liewer et al.*, 1991].

4. Summary

We presented the first 2-D full-particle simulations of a quasi-perpendicular shock with a large mass ratio $m_p/m_e = 400$. A large mass ratio is important to achieve the correct wave properties and particle thermalization at the shock. We find that a phase standing whistler wavetrain, which is not seen in satellite observations, is a transient feature. It is eventually replaced by upstream propagating oblique whistlers, most likely generated by the cross-field streaming instability of the reflected ions. The oblique waves satisfy all of the observed properties of upstream whistlers ("one-Hertz waves"). Given that phase-standing waves can only exist if the phase coherence of the ramp is not disturbed, the simulations can explain both the presence of the observed upstream whistlers and the absence of a phase-standing wavetrain. The electron phase-space evolution is largely adiabatic, in agreement with the observations by *Feldman et al.* [1983] and *Scudder* [1986]. The large mass ratio effectively decouples the kinetic evolution of the ions and the electrons.

Acknowledgments. The authors would like to thank K. B. Quest and D. S. Orlowski for many useful discussions. This work was supported by NASA's Space Physics Theory Program, research grant NAG5-1492, and NASA grant NAGW-2618. Work at Queen Mary and Westfield College was supported by PPARC grant GR/J36440. Computations were executed on Cray C-90s of the NSF San Diego Supercomputer Center and at the Atlas Centre, Rutherford Appleton Laboratory, UK.

References

Balikhin, M., and M. Gedalin, Kinematic mechanism of electron heating in shocks: Theory vs. observations, *Geophys. Res. Lett., 21,* 841–844, 1994.

Fairfield, D. H., Whistler waves observed upstream from collisionless shocks, *J. Geophys. Res., 79,* 1368–1378, 1974.

Feldman, W. C., R. C. Anderson, S. J. Bame, S. P. Gary, J. T. Gosling, D. J. McComas, M. F. Thomsen, G. Paschmann, and M. M. Hoppe, Electron velocity distributions near the Earth's bow shock, *J. Geophys. Res., 88,* 96–110, 1983.

Forslund, D. W., K. B. Quest, J. U. Brackbill, and K. Lee, Collisionless dissipation in quasi-perpendicular shocks, *J. Geophys. Res., 89,* 2142–2150, 1984.

Gurnett, D. A., Plasma waves and instabilities, in *Collisionless Shocks in the Heliosphere: Reviews of Current Research,* edited by B. T. Tsurutani and R. G. Stone, pp. 207–224, AGU, Washington, D. C., 1985.

Héron, A., and J. C. Adam, Particle code optimization on vector computers, *J. Comp. Phys., 85,* 284–301, 1989.

Hewett, D. W., and A. B. Langdon, Electromagnetic direct implicit plasma simulation, *J. Comp. Phys., 72,* 121–155, 1987.

Hoppe, M. M., and C. T. Russell, Plasma rest frame frequencies and polarizations of the low frequency upstream waves: ISEE1 and 2 observations, *J. Geophys. Res., 88,* 2021–2028, 1983.

Hoppe, M. M., C. T. Russell, L. A. Frank, T. E. Eastman, and E. W. Greenstadt, Characteristics of the ULF waves asociated with upstream ion beams, *J. Geophys. Res., 87,* 643–650, 1982.

Krauss-Varban, D., Simulation of electron acceleration at collisionless shocks, in *Particle Acceleration in Cosmic Plasmas,* edited by G. P. Zank and T. K. Gaisser, pp. 445–450, 1992.

Lembège, B., and J. M. Dawson, Plasma heating through a supercritical oblique collisionless shock, *Phys. Fluids, 30,* 1110–1114, 1987.

Leroy, M. M., D. Winske, C. C. Goodrich, C. S. Wu, and K. Papadopoulos, The structure of perpendicular bow shocks, *J. Geophys. Res., 87,* 5081–5094, 1982.

Liewer, P., V. K. Decyk, J. M. Dawson, and B. Lembège, Numerical studies of electron dynamics in oblique quasi-perpendicular collisionless shock waves, *J. Geophys. Res., 96,* 9455–9465, 1991.

McKean, M. E., N. Omidi, and D. Krauss-Varban, Wave and ion evolution downstream of quasi-perpendicular bow shocks, *J. Geophys. Res., 100,* 3427–3437, 1995.

Orlowski, D. S., and C. T. Russell, ULF waves upstream of the Venus bow shock: Properties of one-Hertz waves, *J. Geophys. Res., 96,* 11271–11282, 1991.

Orlowski, D. S., C. T. Russell, D. Krauss-Varban, and N. Omidi, On the source of upstream whistlers in the Venus foreshock, in *Plasma environments of non-magnetic planets,* edited by T. I. Gombosi, pp. 217–227, Pergamon Press, Oxford, 1993.

Orlowski, D. S., C. T. Russell, D. Krauss-Varban, N. Omidi, and M. F. Thomsen, Damping and spectral formation of broadband upstream whistlers, *J. Geophys. Res., 100,* in press, 1995.

Pantellini, F. G., A. Heron, J. C. Adam, and A. Mangeney, The role of the whistler precursor during the cyclic reformation of a quasi-parallel shock, *J. Geophys. Res., 97,* 1303–1311, 1992.

Savoini, P., and B. Lembège, Electron dynamics in two- and one-dimensional oblique supercritical collisionless magnetosonic shocks, *J. Geophys. Res., 99,* 6609–6635, 1994.

Sckopke, N., G. Paschmann, S. J. Bame, J. T. Gosling, and C. T. Russell, Evolution of ion distributions across the nearly perpendicular bow shock: Specularly and nonspecularly reflected gyrating ions, *J. Geophys. Res., 88,* 6121–6136, 1983.

Scudder, J. D., A. Mangeney, C. Lacombe, C. C. Harvey, and T. L. Aggson, The resolved layer of a collisionless high beta, supercritical quasi-perpendicular shock wave, 2, Dissipative fluid dynamics, *J. Geophys. Res., 91,* 11,053–11,073, 1986.

Tidman, D. A., and T. G. Northrop, Emission of plasma waves by the Earth's bow shock, *J. Geophys. Res., 73,* 1543–1553, 1968.

Veltri, P., and G. Zimbardo, Electron–whistler interaction at the Earth's bow shock, 2., Electron pitch angle diffusion, *J. Geophys. Res., 98,* 13,335–13,346, 1993.

Wong, H. K., and M. L. Goldstein, Proton beam generation of oblique whistler waves, *J. Geophys. Res., 93,* 4110–4114, 1988.

Wu, C. S., Y. M. Zhou, S. T. Tsai, S. C. Guo, D. Winske, and K. Papadopoulos, A kinetic cross-field streaming instability, *Phys. Fluids, 26,* 1259–1267, 1983.

D. Krauss-Varban, Department of Electrical and Computer Engineering, University of California, San Diego, 9500 Gilman Drive, La Jolla, California 92093-0407 (e-mail: varban@ccc.ucsd.edu).

F. G. E. Pantellini, DESPA, Observatoire de Paris, Meudon, France.

D. Burgess, Astronomy Unit, Queen Mary and Westfield College, London, United Kingdom.

(received April 17, 1995; accepted May 29, 1995.)

2 Sur l'évolution non linéaire de l'instabilité miroir

ASR, vol. 15, No 8/9, 341-344 (1995)

Pergamon

Adv. Space Res. Vol. 15, No. 8/9, pp. (8/9)341–(8/9)344, 1995

0273-1177/95 $9.50 + 0.00

0273-1177(94)00114-6

ON THE NON–LINEAR MIRROR INSTABILITY

F. G. E. Pantellini, D. Burgess and S. J. Schwartz

Astronomy Unit, Queen Mary and Westfield College, Mile End Road, London E1 4NS, U.K.

ABSTRACT

It is argued that quasi-linear theory alone does not provide an adequate description of the non linear evolution of the mirror instability. Based on a simplified model for the motion of particles in a mirror wave, it is found that the main mechanism which ends the linear phase of the instability has to be particle trapping. Quasi-linear effects may still play a role for particles with small velocities perpendicular to the background magnetic field and do probably dominate the late stage of the instability when the wave-particle energy exchange associated with particle trapping becomes inefficient.

INTRODUCTION

It has been noted a long time ago (e.g. refs /1/, /2/) that the instability threshold for the linear proton mirror instability depends on the exact shape of the proton distribution function at small velocities $v_{||}$ (subscript refers to the background magnetic field), i.e. in the region of Landau resonance for this non-propagating mode. The behavior of resonant and non resonant protons in the linear mirror instability has been discussed theoretically (e.g. /3/, /4/) but, as far as we kow, a satisfactory theory of the non linear mirror instability has not yet been proposed. As a first step Shapiro and Shevchenko /1/ have shown that it is possible to apply the methods of standard quasi-linear to the mirror instability, despite that fact that it is non propagating, provided $\gamma \ll k_{||} v_{T||}$ (where γ is the linear growth rate, $k_{||}$ the longitudinal component of the wave vector and $v_{T||}$ the longitudinal thermal velocity of the protons).

Unfortunately a quasi-linear description of the mirror instability can not be entirely correct as it can not cope with particle trapping. The relevant question we address in the present paper is whether or not trapping becomes important before the quasi-linear saturation level is reached.

In the following discussion we make the assumption that the particle motion can be described by adiabatic theory (e.g. /5/). We therefore assume that the growth rate of the instability is small compared to the proton cyclotron frequency Ω_p.

TRAPPING VS QUASI-LINEAR EFFECTS

Trapped particles can efficiently exchange energy with a growing wave as a result of the bouncing between converging or diverging mirror points. As a consequence of magnetic moment conservation trapped particles also lose (gain) energy if they spend most of the time in regions of decreasing (increasing) magnetic field flux very much like the resonant particles described in /3/. Assuming there is no longitudinal electric field , i.e. $T_e = 0$ (Cf. /4/), and applying the adiabatic mirror criterion we find that all particles whose velocity at a field minimum satisfy

$$\left(\frac{v_{||0}}{v_{\perp 0}}\right)^2 \leq 2\left(\frac{\delta B}{B_0}\right)_{tr} \tag{1}$$

are trapped in a mirror wave (note that in (1) $2\delta B$ is the difference in the magnetic field strength

between troughs and peaks assuming $\delta B \ll B_0$). However, a trapped particle only exchanges energy with the wave efficiently when its trapping frequency ω_{tr} exceeds the growth rate of the wave. Taking the trapping frequency ω_{tr} to be given by the approximate expression for particles trapped near the bottom of a static mirror potential

$$\omega_{tr}^2 = \frac{v_{\perp 0}^2 k_{\|}^2}{2} \left(\frac{\delta B}{B_0}\right)_{tr} \tag{2}$$

and comparing ω_{tr}^2 with γ^2 from linear theory (see equation (4) below) it follows that a proton with velocity $v_{\perp 0}$, and satisfying (1), is efficiently trapped (i.e. it bounces more than once during the time γ^{-1}) when the amplitude of the wave satisfies

$$\left(\frac{\delta B}{B_0}\right)_{tr} \gtrsim 2 \left(\frac{v_{T\perp}}{v_{\perp 0}}\right)^2 \Gamma^2 \tag{3}$$

where, assuming a bi-Maxwellian proton distribution with perpendicular and parallel temperatures $T_\perp$ and $T_{\|}$, the normalized linear growth rate Γ, for a weak instability and cold electrons, is given by (e.g. /1/, /3/ and /4/)

$$\Gamma \equiv \frac{\gamma}{v_{T\perp} k_{\|}} = -\frac{1}{\sqrt{\pi}} \left(1 - \frac{T_\perp}{T_{\|}} + \frac{1}{\beta_\perp}\right) \left(\frac{T_{\|}}{T_\perp}\right)^{3/2} \tag{4}$$

From equation (3) it is clear that the first particles to be trapped are those at high $v_{\perp 0}$. As long as the trapping velocity limit is much higher than $v_{T\perp}$ trapping is unlikely to be efficient in ending the linear phase of growth. However, as soon as particles with $v_{\perp 0}/v_{T\perp} \approx 1$ start being trapped linear theory must break down as most of the resonant particles, which drive the linear instability, start bouncing near the magnetic field minima. Of course not all trapped particles are resonant but nearly all of them, except those which have their mirror points close to a field maximum, do contribute to the reduction of the free energy. It is obvious that the above conclusions require that a clear peak-trough structure is formed during the linear phase. In fact such structures always appear to form in simulations as well as in real plasmas.

On the other hand equation (34) in /1/ provides an expression for the saturation level of the magnetic fluctuations in quasi-linear theory, which can be written as

$$\left(\frac{\delta B}{B_0}\right)_{QL} = 8\sqrt{2}\,\Gamma^2 \tag{5}$$

Note that, unlike equation (2), (5) is independent of $v_{\perp 0}$. From (2) and (5) it follows that at a wave amplitude corresponding to the saturation level of quasi-linear theory particles satisfying $(v_{\perp 0}/v_{T\perp})^2 \gtrsim 0.18$, and satisfying (1), are "efficiently" trapped. This includes most of the particles in the trapping sector defined by (1) and suggests that trapping is always an important non linear mechanism. The value 0.18, however, suggests that quasi-linear effects are nevertheless important at low values of $v_{\perp 0}$ where trapping is inefficient. Moreover quasi-linear effects are likely to become important at late stages of the non linear instability as the efficiency of wave-particle energy exchanges associated with trapped particles decreases as growth slows down.

SIMULATION OF A SLOWLY GROWING INSTABILITY

Figure 1 shows the proton distribution function $\delta F(t, v_\perp, v_{\|}) \equiv v_\perp [f(t, v_\perp, v_{\|}) - f(0, v_\perp, v_{\|})]$ in peaks, in troughs, and integrated over the whole simulation domain from a 1D hybrid simulation

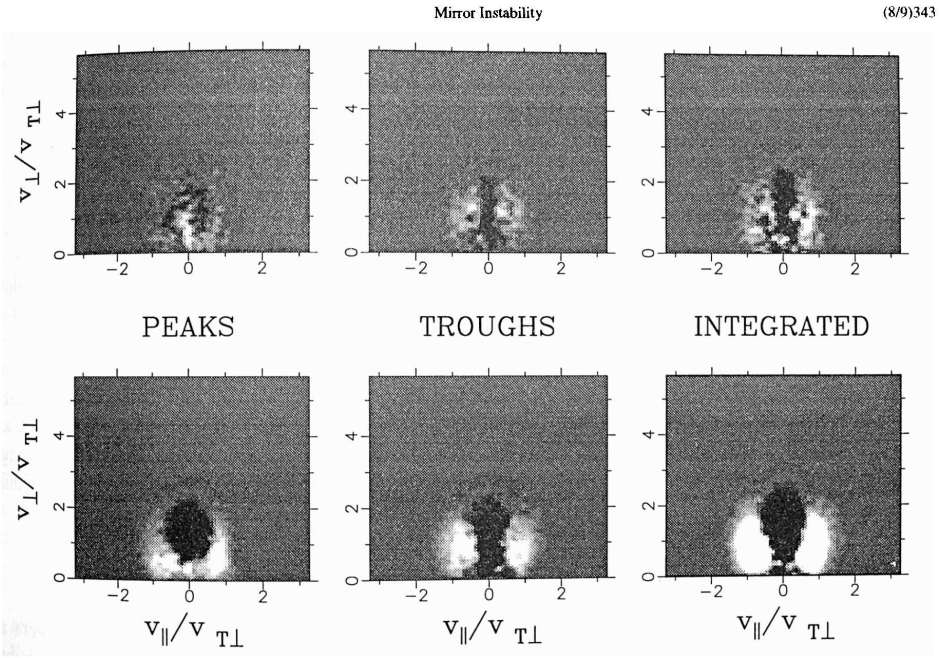

Fig. 1. Plots of $\delta F(t) \equiv v_\perp[f(t) - f(0)]$ during the linear phase of growth of the mirror instability (top panels) and at time of maximum wave field amplitude (bottom panels). The peaks and trough distributions have been collected over a spatial distance of $3c/\omega_p$ around the five peaks and troughs which are present in the simulation. The integrated distribution results from the integration over the whole simulation domain. White (black) corresponds to positive (negative) values of δF. Color saturation occurs at ± 20 counts, with respect to the initial distribution, with a maximum of about 400 counts in peaks and troughs distributions and 1400 in the integrated distribution.

(particle protons, fluid electrons) of a fairly weak instability. The initial proton distribution is a spatially uniform bi-Maxwellian distribution with $T_\perp/T_{||} = 3$ and $\beta_{||} = 1$. The ratio of the proton plasma to the proton cyclotron frequency is $\omega_p/\Omega_p = 3.3 \times 10^3$ and the electrons are cold ($\beta_e = 10^{-4}$). The total size of the system is 54.165 c/ω_p (c is the velocity of light) which corresponds to five times the wavelength λ of the linearly most unstable mode ($\lambda = 10.8c/\omega_p$, $\gamma = 8.3 \times 10^{-2}\Omega_p$). The simulation domains consists of 128 cells and is filled with a total of 3×10^5 particles. The axis of the simulation is oriented at an angle of 56° with respect to the magnetic field which again corresponds to the orientation of wave vector of the fastest growing mode. The upper three panels in the figure show δF during the linear phase of growth, at a time when the amplitude of the magnetic field fluctuations is $\delta B/B_0 \approx 0.05$. The resonant particles near $v_{||} = 0$ are clearly visible in both peaks (white stripe) and troughs (black stripe). At this early time the trapping angle $2tan^{-1}[2(\delta B/B_0)_{tr}]$ is about 35° and according to (3) trapping is already efficient down to $v_{\perp 0} \approx 1$. Thus part of the dark central region in the trough distribution has already widened due to particle trapping. This is the reason why the bright region corresponding to the resonant particles in the peak distribution is not as wide. Even though the noise level is still relatively high, it is possible to identify the signature of the circulating particles (particles with $v_{||} > \gamma/k_{||}$). These particles do not exchange energy with the wave and are responsible for the bright (dark) regions in the trough (peak) phase space and ensure that the density and magnetic field fluctuations are anticorrelated. Even though the magnetic field fluctuations still grow at the linear rate, the non linear effects are already visible in in the panel with the integrated distribution (linear effects cancel in the integration). The signature of the trapped particles at $v_\perp \gtrsim 1$ and $v_{||} \approx 0$ is evident while at low $v_\perp$ poor statistics prevent us from clearly identifying quasi-linear effects which may occur there.

The bottom panels in figure 1 show δF at a time corresponding to the maximum amplitude of the field fluctuations ($\delta B/B_0 \approx 0.15$), i.e. shortly after the end of the linear phase of growth. The trapped particle sector is clearly visible in both the trough and the integrated distribution. Since the wave is not growing any more the resonant particles are no longer visible in the plots. On the other hand circulating particles, which ensure the characteristic magnetic field versus density anticorrelation, remain clearly visible at troughs (bright regions). At peaks, as the instability is not growing any longer, all particles are by definition circulating. Thus, according to linear theory, we expect the distribution function δF to be negative everywhere in velocity space. The appearance of the bright region at low $v_\perp$ particularly in the peak distribution is therefore a clear sign of the non linear instability. Since at this wave amplitude trapping is only efficient down to $v_{\perp 0} \approx 0.7$ (and only in troughs), and since the efficiency of the energy exchange is strongly reduced as growth slows down, this must be due to quasi-linear effects. Quasi-linear effects act everywhere but are stronger at peaks since trapped particles can't reduce the free energy there. Thus, after a spatially structured plasma has been created during the linear phase of growth (the spectrum tends to be initially fairly monochromatic), and after the trapped particles have explosively reduced the available free energy in the troughs (determining, thereby, the end of the linear phase), quasi-linear effects take over and slowly uniformize the plasma (peak and trough distributions will become nearly identical) driving it to saturation. In fact the late time distribution functions (not shown) become increasingly similar in peaks and troughs.

CONCLUSION

We have given arguments which suggest that both particle trapping and quasi-linear effects are important in the non linear mirror instability. This view is enforced by results from 1D hybrid simulations which indicate that efficient proton trapping at high values of $v_\perp$ briskly ends the linear phase while at low $v_\perp$, where trapping is never efficient, quasi-linear effects dominate the instability. Quasi-linear effects eventually drive the instability towards saturation as trapping becomes ineffective as an energy exchange mechanism in a quasi static field. The late dominance of quasi-linear effects would also explain the spatial uniformization of the distribution function which indeed is highly spatially structured after the linear and trapping phase. The above conclusions are not based on any knowledge of the exact particles' motion and should therefore remain valid even in the frame of a more complete theory of the trapping process.

ACKNOWLEDGMENTS

This work has been supported by SERC (UK) grant GR/H09454 and the Commission of the European Community under contract SCI0468-M.

REFERENCES

1. V.D. Shapiro, and V.I. Shevchenko, Quasilinear theory of instability of a plasma with an anisotropic ion velocity distribution, *Soviet Physics - JETP* 18, 1109, 1964.

2. D.J. Rose, General criterion for mirror instability of a plasma, *Phys. Fluids* 8, 951, (1965).

3. D.J. Southwood, and M.G. Kivelson, Mirror instability: 1. The physical mechanism of linear instability, *J. Geophys. Res* 98, 9181, (1993).

4. F.G.E. Pantellini, and S.J. Schwartz, Finite electron temperature effects in the linear proton mirror instability, submitted to *J. Geophys. Res*, (1994).

5. T.G. Northrop, *The adiabatic motion of charged particles*, p. 12, Wiley Interscience, New York, (1963).

3 Le rôle des électrons dans l'instabilité miroir

JGR 100, 3539-3550 (1995)

JOURNAL OF GEOPHYSICAL RESEARCH, VOL. 100, NO. A3, PAGES 3539–3549, MARCH 1, 1995

Electron temperature effects in the linear proton mirror instability

F.G.E. Pantellini[1] and S.J. Schwartz

Astronomy Unit, Queen Mary and Westfield College, London, England, United Kingdom

Abstract. It is shown that when the electron temperature T_e is of the same order of the proton temperature parallel to the background magnetic field, the growth rate of the proton mirror mode in the long-wavelength limit is reduced by the presence of a longitudinal electric field. The field is due to the electron pressure gradient which builds up when $T_e \neq 0$, because the electrons are dragged by nonresonant protons which are mirror accelerated from regions of high into regions of low parallel magnetic field flux. In return, the longitudinal electric field causes the density of nonresonant protons with a perpendicular velocity smaller than a strongly T_e-dependent critical velocity $v_{\perp,\mathrm{crit}}$ to increase (decrease) at maxima (minima) of the parallel magnetic field flux. These nonresonant protons thus behave differently from the "circulating" protons described by Southwood and Kivelson (1993) in the cold electron limit. Although the instability threshold is only weakly affected by changes in T_e, quantities like the growth rate, the compressibility, the polarization, and the angle between wave vector and magnetic field for the most unstable mode, as well as the structure of the perturbed proton distribution itself, are strongly modified by variations in the electron temperature. The predictions of the model are shown to agree well with numerical solutions of the full Vlasov dispersion relation, indicating that most long-wavelength aspects of the proton mirror instability are included in the model.

1. Introduction

The proton mirror instability is a nonpropagating, slowly growing (less than proton cyclotron frequency) long-wavelength (greater than proton Larmor radius) instability driven by a pressure anisotropy $p_\perp/p_\parallel > 1$ where the perpendicular and parallel subscripts refer to the direction of the zeroth order magnetic field. The minimum anisotropy required to destabilize the mode generally depends on other plasma parameters. For example, in a homogeneous and spatially uniform magnetized bi-Maxwellian proton plasma with cold electrons (number density N_0) the instability threshold depends on the ratio $\beta_\perp$ between the perpendicular proton pressure $p_\perp = N_0 T_\perp$ (temperatures are assumed to be multiplied by the Boltzmann constant throughout the paper) and the magnetic field pressure $B_0^2/8\pi$ and is given by $T_\perp/T_\parallel = 1 + 1/\beta_\perp$ [e.g., *Hasegawa*, 1969].

Although the mirror instability has been known for some time [e.g., *Chandrasekhar*, 1958], it has been revisited by a number of authors. As a first step, *Rose* [1965] pointed out how critically the instability threshold depends on the details of the proton distribution at small parallel velocities. Later, *Barnes* [1966] and *Tajiri* [1967], for the case of hot electrons, and *Hasegawa* [1969], for the case of a nonuniform medium, numerically solved the kinetic dispersion relation in the low-frequency and long-wavelength limit. The kinetic treatments revealed that the dispersion relations obtained from fluid treatments are wrong in the prediction that the mirror mode is oscillating when the instability threshold is not exceeded. Furthermore, the growth rates deduced from fluid and kinetic theories differ by a nonnegligible numerical factor.

Until the first observations in the Earth's magnetosheath by *Kaufmann et al.* [1970] the major interest in the mirror instability was related to the problem of plasma confinement by a theta pinch in fusion experiments (see, for example, the collection of reprints published by *Jeffrey and Taniuti* [1966]). Since then, an increasingly large number of observations have confirmed the existence of the mirror instability in virtually all of the explored space plasmas where a proton temperature anisotropy can be generated by some mechanism. Besides the identification in the Earth's magnetosheath, e.g., well downstream from the quasi-perpendicular portion of the Earth bow shock [*Hubert et al.*, 1989], mirror waves have been observed at comets

[1]Now at Observatoire de Paris-Meudon, Département de Recherche Spatiale, Meudon, France.

Paper number 94JA02572.
0148-0227/95/94JA-02572$05.00

[*Russell et al.*, 1987] and in interplanetary space [*Tsurutani et al.*, 1992]. More recently, *Lacombe et al.* [1992] have reported the existence of mirror waves even in the overshoot of the quasi-perpendicular Earth bow shock, suggesting that mirror waves take part, at least in some cases, in the energy dissipation within the shock itself. Moreover, *Anderson and Fuselier* [1993] have shown that in the Earth's magnetosheath, mirror waves tend to occur when the proton temperature anisotropy is small (i.e., $T_\perp/T_\parallel \approx 1.5$) and the proton pressure is high (i.e. $\beta \gtrsim 5$).

Stimulated by the observations and favored by the rapidly increasing capabilities of modern computers, numerical simulations of the instability started to become fashionable during the last decade or so. Thus the one-dimensional simulations of *Price et al.* [1986] showed that the instability can be excited far downstream of supercritical, quasi-perpendicular shocks as a result of the proton temperature anisotropy generated in the shock ramp. *McKean et al.* [1993] investigated the distribution functions from hybrid simulations and found that in the case of slowly growing instability, the results do qualitatively agree with linear theory [*Southwood and Kivelson*, 1993]. Discrepancies are likely to be due to nonlinear effects [cf. *Pantellini et al.*, 1995]. *McKean et al.* [1993] also suggested that wave-particle energy exchanges in the linear instability tend to be most effective along magnetic slopes rather than at magnetic peaks or troughs.

By the end of the 1980s it became clear that another instability which develops under similar conditions, namely the Alfvén Ion Cyclotron (AIC) instability [e.g., *Davidson and Ogden*, 1975], usually has a faster linear growth rate than the mirror instability in a pure proton-electron plasma [*Lacombe et al.*, 1992; *Gary*, 1992], making it difficult to understand why the latter is observed at all. The predominance of the AIC instability over the mirror instability has been confirmed in one- and two-dimensional hybrid simulations [e.g., *McKean et al.*, 1992; *Winske and Quest*, 1988]. At least three possible explanations have been suggested for the fact that mirror waves are nevertheless observed in space plasmas. The first is that the alpha particles in the solar wind, which are usually neglected in numerical simulations, significantly reduce the growth of the AIC but not of the mirror instability [*Price et al.*, 1986; *Gary*, 1992]. The second is that at sufficiently high $\beta_\parallel$ and small temperature anisotropies and given the presence of the alpha particles, the mirror instability grows more rapidly than the AIC instability. Mirror waves have been observed under these conditions by *Anderson and Fuselier* [1993] and *Anderson et al.* [1994]. The third [*Southwood and Kivelson*, 1993] is that from the nonpropagating nature of the unstable mirror mode it follows that its linear development crucially depends on the spatial structure of the field. Such a spatial structure may exist in the plasma prior to the the development of the instability, namely at shocks. As a result, the AIC wave may not be able to grow in the structured field due to the fact that the proton cyclotron resonance condition (the base of the AIC instability) continually changes as the wave moves through the plasma, causing the efficiency of the resonance to be reduced. However, this mechanism has not yet been demonstrated to be efficient in numerical simulations.

The physical mechanism of the proton mirror instability has been investigated only very recently in the limit of cold electrons and small growth rates by *Southwood and Kivelson* [1993]. They pointed out that the growth of the instability crucially depends on the distribution of the Landau resonant protons ($v_\parallel \approx 0$) (see also *Rose* [1965]). This is the fundamental reason for the fluid models to fail in describing some of the main features of the mode such as the fact that it is damped, and not oscillating, below the stability threshold. Although cold electrons do allow for any longitudinal electric field to be short-circuited which, in turn, results in the plasma dispersion relation being much simpler [e.g., *Hasegawa*, 1969], it is clear that in the free solar wind (where the electrons are typically hotter than the protons) and even in the Earth's magnetosheath, the cold electron approximation won't apply in general. We show that besides a slight change to the instability threshold, taking into account the presence of hot electrons strongly modifies some of the characteristics of the proton mirror mode such as the growth rate, the wave's polarization, the compressibility, and even the perturbed proton distribution function. These effects are shown to be ultimately related to the longitudinal electric field which is generated by an electron pressure gradient through the wave. The latter arises because the electrons are dragged away from the regions of high into regions of low parallel magnetic field flux by the protons for which the mirror force dominates.

2. The Physical Model

We start from a spatially homogeneous electron-proton plasma permeated by a magnetic field $\mathbf{B}_0$ pointing in the z direction of a right-handed Cartesian system (x, y, z). The equilibrium electron distribution f_e is Maxwellian with an isotropic and nonzero temperature T_e, while the equilibrium proton distribution f_p is taken to be bi-Maxwellian with perpendicular and parallel temperatures $T_\perp$ and $T_\parallel$ (we use a subscript e for electron quantities for clarity but usually omit a subscript p for the proton quantities).

2.1. The Perturbed Proton and Electron Distribution Functions

Following *Southwood and Kivelson* [1993], we derive an expression for the linear response of the proton and electron distributions in a slowly growing wave (the long-wavelength limit). Accordingly, a change δB in the magnetic field strength produces a change in the

energy δW of a particle following the adiabatic expression [*Northrop*, 1963]

$$\frac{d}{dt}\delta W = \mu\frac{\partial}{\partial t}\delta B_\parallel$$

where $\mu = mv_\perp^2/(2B)$ is the magnetic moment of the particle. If in addition, a longitudinal electric field $\delta E_\parallel$ is present, then the total rate of change in the particle's energy δW contains the work done by this field, namely,

$$\frac{d}{dt}\delta W = \mu\frac{\partial}{\partial t}\delta B_\parallel + qv_\parallel\delta E_\parallel. \tag{1}$$

Noting that $\delta W_\perp = \mu\delta B_\parallel$ and $\delta W_\parallel = \delta W - \mu\delta B_\parallel$, one finds that the rate of change in the particle's perpendicular and parallel energy is given by

$$\frac{d}{dt}\delta W_\perp = \mu\frac{d}{dt}\delta B_\parallel \tag{2a}$$

$$\frac{d}{dt}\delta W_\parallel = \frac{d}{dt}\delta W - \mu\frac{d}{dt}\delta B_\parallel. \tag{2b}$$

Liouville's theorem states that phase space density is constant along particle trajectories. Writing the distribution function $f = f(t, \mathbf{x}, W_\perp, W_\parallel)$ as the sum of a spatially uniform equilibrium distribution $f_0 = f(W_\perp, W_\parallel)$ and a small perturbation $\delta f = \delta f(t, \mathbf{x}, W_\perp, W_\parallel)$, one obtains the linearized version of Liouville's theorem in the form

$$\frac{\partial}{\partial t}\delta f + \mathbf{v}\cdot\frac{\partial}{\partial \mathbf{x}}\delta f + \frac{d}{dt}\delta W_\perp\frac{\partial}{\partial W_\perp}\delta f + \frac{d}{dt}\delta W_\parallel\frac{\partial}{\partial W_\parallel}\delta f = 0.$$

Using $\partial/\partial t + \mathbf{v}\cdot\partial/\partial\mathbf{x} = d/dt$, we can rewrite this in the more compact form

$$\frac{d}{dt}\delta f = -\frac{d}{dt}\delta W_\perp\frac{\partial}{\partial W_\perp}\delta f - \frac{d}{dt}\delta W_\parallel\frac{\partial}{\partial W_\parallel}\delta f \tag{3}$$

Assuming perturbations $\propto \exp[i(k_\perp x + k_\parallel z) + \gamma t]$, one finds that the change of an initially bi-Maxwellian proton distribution is given by

$$\delta f_p = \left[\frac{\mu_p\delta B_\parallel}{T_\perp}\left(1 - \frac{T_\perp}{T_\parallel}\right)\right] f_p + \left[\frac{\gamma}{\gamma + ik_\parallel v_\parallel}\left(\mu_p\delta B_\parallel - \frac{c\delta E_\parallel}{ik_\parallel}\right) + \frac{e\delta E_\parallel}{ik_\parallel}\right]\frac{f_p}{T_\parallel} \tag{4}$$

while that of an initially Maxwellian electron distribution reads

$$\delta f_e = \left[\frac{\gamma}{\gamma + ik_\parallel v_\parallel}\left(\mu_e\delta B_\parallel + \frac{e\delta E_\parallel}{ik_\parallel}\right) - \frac{e\delta E_\parallel}{ik_\parallel}\right]\frac{f_e}{T_e}. \tag{5}$$

In order to compare the different terms in the expressions for the perturbed distribution functions, $\delta E_\parallel$ has to be determined as a function of $\delta B_\parallel$. This can be done by solving the Poisson equation which, in the case of a slowly growing wave (i.e., $\gamma \to 0$), simply reduces to a quasi-neutrality condition

$$\frac{\delta N_p}{N_0} - \frac{\delta N_e}{N_0} = 0 \tag{6}$$

where δN_p and δN_e can be obtained by taking the first moments of δf_p and δf_e respectively. Neglecting terms proportional to $\gamma/(\gamma + ik_\parallel v_\parallel)$, which is justified by the fact that their contribution to the density perturbations is small as $\gamma \to 0$ or more precisely as long as $|\delta N_P/N_0| \gg \sqrt{\pi}\gamma/(k_\parallel v_{T\parallel})$ (see (25)), one obtains the linear response for the density perturbation of the protons

$$\frac{\delta N_p}{N_0} = \frac{\delta B_\parallel}{B_0}\left(1 - \frac{T_\perp}{T_\parallel}\right) + \frac{e\delta E_\parallel}{ik_\parallel T_\parallel} \tag{7}$$

and similarly for the electrons

$$\frac{\delta N_e}{N_0} = -\frac{e\delta E_\parallel}{ik_\parallel T_e}. \tag{8}$$

Equation (8) is nothing else but the usual fluid equation $\nabla_\parallel\delta p_e = -eN_0\delta E_\parallel$ for isothermal electrons. The desired expression for $\delta E_\parallel$ is finally found by using the quasi-neutrality condition (6) which yields

$$\delta E_\parallel = \frac{\delta B_\parallel}{B_0}\left(\frac{T_\perp - T_\parallel}{T_e + T_\parallel}\right)\frac{ik_\parallel}{e}T_e. \tag{9}$$

The parallel electric field $\delta E_\parallel$ can now be eliminated from (4) and (5), and the following expressions for the perturbations of the distributions are obtained

$$\frac{\delta f_p}{f_p} = \left\{\frac{v_\perp^2}{v_{T\parallel}^2}\left(\frac{T_\parallel}{T_\perp} - 1\right) + \frac{\gamma}{(\gamma + ik_\parallel v_\parallel)}\left[\frac{v_\perp^2}{v_{T\parallel}^2} - \left(\frac{T_\perp}{T_\parallel} - 1\right)\frac{T_e}{T_e + T_\parallel}\right] + \left(\frac{T_\perp}{T_\parallel} - 1\right)\frac{T_e}{T_e + T_\parallel}\right\}\frac{\delta B_\parallel}{B_0} \tag{10}$$

$$\frac{\delta f_e}{f_e} = \left\{\frac{\gamma}{(\gamma + ik_\parallel v_\parallel)}\left[\frac{v_\perp^2}{v_e^2} + \frac{T_\perp - T_\parallel}{T_e + T_\parallel}\right] - \left(\frac{T_\perp - T_\parallel}{T_e + T_\parallel}\right)\right\}\frac{\delta B_\parallel}{B_0} \tag{11}$$

where the notations $v_{T\parallel} \equiv (2T_\parallel/m_p)^{1/2}$ and $v_e \equiv (2T_e/m_e)^{1/2}$ have been introduced.

For nonzero values of T_e the last term on the right-hand side of (10) is nonzero and of opposite sign compared to the first term in the same expression. If one ignores, for the moment, the presence of the resonant

protons associated with the second term, which are limited to the small region in velocity space $|v_\parallel| < \gamma/k_\parallel$, it appears that δf_p changes sign as $v_\perp$ exceeds some critical velocity $v_{\perp,\mathrm{crit}}$. This critical velocity can thus be determined by equating the magnitudes of the first and the last term on the right-hand side of (10) to give

$$v_{\perp,\mathrm{crit}} = v_{T\perp}\left(\frac{T_e}{T_e + T_\parallel}\right)^{1/2} \tag{12}$$

with $v_{T\perp} \equiv (2T_\perp/m_p)^{1/2}$ being the perpendicular thermal velocity of the protons. Protons with $v_\perp > v_{\perp,\mathrm{crit}}$ are the circulating protons which, owing to the action of the mirror force, are responsible for the characteristic anticorrelation between $\delta B_\parallel$ and δN_p [*Southwood and Kivelson*, 1993]. Protons with $v_\perp < v_{\perp,\mathrm{crit}}$, on the other hand, act in the opposite way in that they tend to accumulate in regions of high parallel magnetic field flux. A schematic picture of the forces acting on a nonresonant proton in a mirror wave is shown in Figure 1, which illustrates the spatial variation of the longitudinal electric and magnetic field fluctuations, as well as the density fluctuations of the nonresonant particles through one wavelength, and shows that the electrostatic force and the mirror force on a proton always act against each other. However, as it will be shown later (section 2.4), the combined effect of both forces on the nonresonant protons (i.e., protons with $|v_\parallel| > \gamma/k_\parallel$) is such that the anticorrelation between δN and $\delta B_\parallel$ is always preserved even for large electron temperatures.

To understand the reason for the response δf_p of the proton distribution to the longitudinal electric field being of opposite sign with respect to the response to the mirror field, we consider the motion of protons, which are initially (i.e. at $t = -\infty$) on a contour of constant phase space density (Figure 2, stippled thick contour). We then use Liouville's theorem, which states that the phase space density is constant along a particle's trajectory, to determine the deformation of the contour in the field of the growing wave. In Figure 2 we have chosen the end position of the protons (at an arbitrary time) to coincide with the position of a magnetic field maximum. It is obvious that the trajectories of particles reaching a magnetic field minimum are just the same but with a reversed sign.

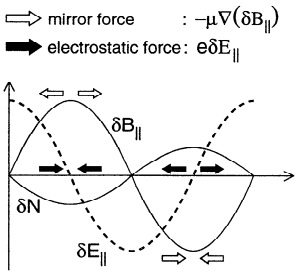

Figure 1. Spatial dependence of δN, $\delta B_\parallel$ (solid curves) and $\delta E_\parallel$ (dashed curve) through one wavelength. All curves are in arbitrary units. The arrows denote the mirror and the electrostatic force acting on a proton, at a minimum, as well as a maximum, of the parallel magnetic field strength. As shown the two forces act against each other, and since the mirror force is proportional to $v_\perp^2$, the electrostatic force can dominate the motion of protons with a small $v_\perp$.

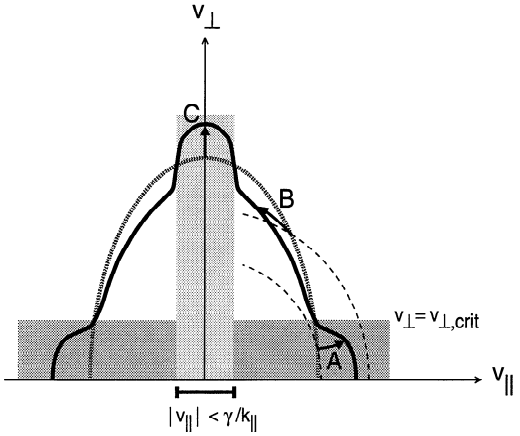

Figure 2. Sketch of the distortion of a proton phase space contour (thick solid line) in the linear mirror instability at a maximum of the magnetic field flux. The labeled arrows indicate the path, starting from the initial equilibrium distribution (thick stippled line), of three distinct types of protons (labeled A, B and C) which exist in the case of a nonzero T_e.

Let's first consider a nonresonant proton with $v_\perp = 0$, i.e., a proton which is not sensitive to the mirror force. On its way to a region of high magnetic field flux such a proton sees its parallel velocity being increased, owing to the fact that the electrostatic potential has a minimum there. Since the particle's perpendicular velocity is not changing, its trajectory in velocity space must go along a path of increasing $|v_\parallel|$. For protons with a nonzero initial perpendicular velocity, $v_\perp$ increases on its way toward a maximum of the magnetic field flux owing to the conservation of the magnetic moment. However, for protons with a small $v_\perp \ll v_{\perp,\mathrm{crit}}$ the mirror force is still insignificant and the behavior is similar to that of particles with $v_\perp = 0$ (Figure 2, type A trajectories). On the other hand, protons with $v_\perp \gg v_{\perp,\mathrm{crit}}$ (Figure 2, type B trajectories) are dominated by the mirror force, which doesn't modify the particle's energy, and do therefore roughly move along circles (Figure 2, dashed curves) although they still gain some energy in the electrostatic field. For a proton with a final velocity of $v_\perp = v_{\perp,\mathrm{crit}}$ the combined action of both the electrostatic and the mirror force causes the particle to move along a path of constant phase space density so that, as shown in Figure 2, the initial distribution function remains unchanged at that particular value of $v_\perp$.

Protons of type C are resonant (i.e., they do not circulate) and can be thought to be immobile as the wave grows. They mainly increase their $v_\perp$, owing to betatron acceleration in the steadily increasing magnetic field intensity. Although the strength of the electrostatic force on a particle is independent of its velocity (see (9)), the kinetic energy change of the particle, due to the electrostatic potential, isn't. In fact, from (2) it appears that for a resonant particle the energy change, due to the electric field, is significantly smaller than for a nonresonant particle. In particular, at $v_\parallel = 0$ the energy change, due to the electrostatic field, vanishes and the particle behaves exactly as described by *Southwood and Kivelson* [1993]; that is, only $v_\perp$ changes (Figure 2, path C). Equation (10) confirms that δf_p is unaffected at $v_\parallel = 0$, anticipating that although many aspects of the mirror instability which are connected with the circulating protons are modified by a nonzero T_e, the basic physics of the instability, which crucially depends on the resonant protons, is preserved even for large values of the electron temperature.

The dependence of $(v_{\perp,\mathrm{crit}}/v_{T\perp})^2$ on the electron temperature is illustrated by the dashed curve in Figure 3. It is interesting to note that in the case of a bi-Maxwellian proton distribution the same curve represents the ratio $-\delta N_{E\parallel}/\delta N_{\mathrm{mir}}$ of the density of protons being dominated by the $\delta E_\parallel$ field to the density of protons being dominated by the mirror force (obtained by integrating over velocity space the last and the first term, respectively, on the left-hand side of (10)). This ratio is always less than unity, so that the anticorrelation between δN_p and $\delta B_\parallel$ is preserved for all values of T_e at least as long as neglecting the contribution from the resonant protons to δN_p is justified (see section 2.4). This also follows from the perspective of the electrons

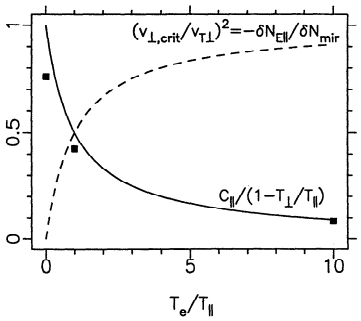

Figure 3. Normalized square critical velocity $v^2_{\perp,\mathrm{crit}}/v^2_{T\perp}$ (dashed curve) and parallel compressibility $C_\parallel$ (solid curve) as a function of $T_e/T_\parallel$ for the case $\beta_\parallel = 1$ and $T_\perp/T_\parallel = 1.8$ (equations (12) and (24)). The squares denote the normalized parallel compressibility for the fastest growing mode calculated by numerically solving the full Vlasov dispersion relation for three different values of $T_e/T_\parallel$ for the case $T_\perp/T_\parallel = 1.8$ and $\beta_\parallel = 1$ (see section 3 in text and Table 1).

being dragged by the protons, so that the sense of proton behavior can not be reversed by the longitudinal electric field.

Since the electron temperature is isotropic, the expression for δf_e in (11) contains only two terms which are the counterparts of the last two in the expression for δf_p. For all practical applications the contribution from the resonant electrons can be neglected, as can be understood from the following arguments. In the case of $T_e \neq 0$ the number of resonant electrons is less than that of the protons by a factor $\sim (T_\parallel m_e/T_e m_p)^{1/2}$ which is less than unity unless the electron temperature is $O(10^{-3}T_\parallel)$. Similarly, the relative energy densities of resonant warm electrons to protons is less than unity unless the electron temperature exceeds that of the protons by a factor $O(m_p/m_e) \sim 10^3$. We shall not consider the case of very cold electrons such that they all lie within the resonance. We note, however, that we are considering the $\gamma \to 0$ limit here, for which the resonance formally shrinks to zero. Thus we can recover previous results which ignored the electron pressure by taking the $T_e \to 0$ limit of our results without contradicting the fluidlike electron behavior which corresponds, in fact, to consideration of only the nonresonant electron population. Thus the perturbed electron distribution is essentially described by the last term on the right-hand side of (11) which simply compensates for the circulating protons which correspond to the first term on the right-hand side of (10). In this limit the light electrons are passively carried around by the massive protons and thus can be interpreted as a massless neutralizing fluid.

2.2. The Dispersion Relation

We now calculate the dispersion relation following *Southwood and Kivelson* [1993] by imposing a pressure balance condition which in the double-adiabatic (or CGL) theory [e.g., *Krall and Trivelpiece*, 1973, chapter 3.10] reads

$$\nabla_\perp \left(p_\perp + \frac{B^2}{8\pi}\right) - \frac{(\mathbf{B}\cdot\nabla)\mathbf{B}}{4\pi}\left(\frac{p_\perp - p_\parallel}{B^2/8\pi} + 1\right) = 0 \tag{13}$$

from which the x component yields (remembering that $k_\perp \delta B_x + k_\parallel \delta B_\parallel = 0$)

$$\delta p_{e\perp} + \delta p_\perp + \frac{B_0 \delta B_\parallel}{4\pi}\left[1 + \left(\frac{k_\parallel}{k_\perp}\right)^2 (\beta_\perp - \beta_\parallel + 1)\right] = 0 \tag{14}$$

with $\beta_\parallel = \beta_\perp T_\parallel/T_\perp$. By consistently omitting the contribution from the resonant electrons (electrons are therefore treated in the fluid approximation) and by finding the pressure perturbations in (14) by taking the second moments of (10) and (11), one obtains the fol-

lowing expression for the growth rate of the proton mirror instability

$$-\frac{\gamma}{k_\parallel v_{T\parallel}} = \frac{1+\left(\frac{k_\parallel}{k_\perp}\right)^2(\beta_\perp-\beta_\parallel+1)}{\beta_\perp\sqrt{\pi}\frac{T_\perp}{T_\parallel}\left[1-\frac{1}{2}\left(1-\frac{T_\parallel}{T_\perp}\right)\frac{T_e}{T_e+T_\parallel}\right]} - \frac{1}{\sqrt{\pi}}\left(1-\frac{T_\parallel}{T_\perp}\right) \quad (15)$$

where we have supposed that $|\gamma/k_\parallel v_{T\parallel}| \ll 1$, which is to say that the ratio of resonant to nonresonant protons is small, and where in the limit $T_e \to 0$ and $k_\parallel/k_\perp \ll 1$ the result of *Southwood and Kivelson* [1993] is recovered. The first term on the right-hand side of (15), which depends on T_e, is always positive and represents the damping element of the mode, while the second term provides the wave growth. It is obvious from (15) that the $k_\perp \gg k_\parallel$ limit yields a growing mode for the smallest temperature anisotropy. However, since $\gamma \propto k_\parallel$, this limit can only be obtained by letting $k_\perp$ tend to infinity. In practice, finite Larmor radius effects determine the $k_\perp$ at maximum growth rate. The nonzero electron temperature increases the damping term essentially because as T_e increases the contribution from nonresonant particles (electrons and protons) to the pressure perturbation in (14) decreases (since it is proportional to $(T_e+T_\perp)/(T_e+T_\parallel)$), so that the contribution from resonant protons, which, as discussed by Southwood and Kivelson, is essentially proportional to γ and of opposite sign, must be smaller to ensure pressure balance.

According to (15) and for a fixed k, maximum growth occurs at $(k_\parallel/k_\perp)^2_{\max}$ given by

$$\left(\frac{k_\parallel}{k_\perp}\right)^2_{\max} = A\left[1+\frac{2}{3}\left(\frac{k_\parallel}{k_\perp}\right)^2_{\max}\right]^{-1} \quad (16)$$

with

$$A \equiv \frac{\left(\frac{T_\perp}{T_\parallel}-1\right)\left[1-\frac{1}{2}\left(1-\frac{T_\parallel}{T_\perp}\right)\frac{T_e}{T_e+T_\parallel}\right]-\beta_\perp^{-1}}{3\beta_\perp^{-1}(\beta_\perp-\beta_\parallel+1)}.$$

Near to the instability threshold, only modes satisfying $(k_\parallel/k_\perp)^2_{\max} \ll 1$ are unstable. Thus

$$\left(\frac{k_\parallel}{k_\perp}\right)^2_{\max} \simeq A \quad (17)$$

provides a good estimate of the **k** vector orientation at maximum growth under weakly unstable conditions. Equation (16) (or (17)) shows that a nonzero electron temperature has the effect of making the wave vector of the fastest growing mode more perpendicular. From (15) it is also possible to obtain an estimate of the upper limit for the range of $(k_\parallel/k_\perp)$ above which unstable modes can't exist (the lower limit being, of course, $k_\parallel/k_\perp = 0$). This limiting value $(k_\parallel/k_\perp)_0$ is determined by the vanishing of the right-hand side of (15) which occurs at

$$\left(\frac{k_\parallel}{k_\perp}\right)^2_0 = 3A \quad (18)$$

which is close to the value found by *Barnes* [1966]. In Figure 4 the functional dependence of θ_{kB} (which denotes the angle between the direction of the magnetic field $\mathbf{B}_0$ and the wave vector of the fastest growing mode) on the electron temperature is shown for the case $\beta_\parallel = 1$ and different values of $T_\perp/T_\parallel$. As could be deduced immediately by inspection of (16) (or (17)), the dependence is rather strong for $T_e \lesssim T_\parallel$ especially as $T_\perp/T_\parallel$ approaches the stability threshold. From (16) (or (17)) it also appears that for $T_e/T_\parallel \gg 1$ the ratio $(k_\parallel/k_\perp)_{\max}$ approaches a finite value for which, given a sufficiently high anisotropy $T_\perp/T_\parallel$, the mode may remain unstable. However, as stated earlier, for $T_e/T_\parallel \gtrsim O(m_p/m_e)$ the energy carried by the resonant electrons exceeds that of the resonant protons, and the approximations made in the present model are no longer valid.

A further remark is in order here about the fact that even though θ_{kB} is assumed to be close to 90° (which is the case just above the instability threshold), the theory turns out to work well even for fairly oblique wave vectors in which case, however, the term with $(k_\parallel/k_\perp)^2$ in (15) is no longer negligible and the growth rate may substantially depend on it. Also from (15) it follows that maximum growth occurs for $k_\perp, k_\parallel \to \infty$. This is obviously wrong, and the reason is that the CGL pres-

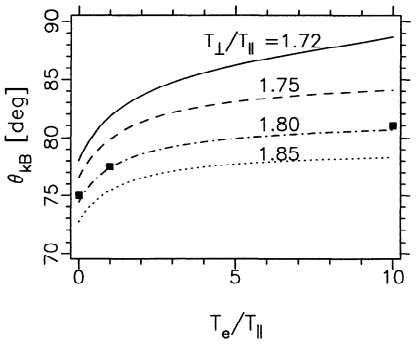

Figure 4. Curves showing the dependence of the angle θ_{kB} between the wave vector of the most unstable mode and the background magnetic field $\mathbf{B}_0$ as a function of $T_e/T_\parallel$ for different values of $T_\perp/T_\parallel$ in the case of $\beta_\parallel = 1$ (equation (16)). As in Figure 3, squares denote values of θ_{kB} for the fastest growing mode found by numerically solving the full Vlasov dispersion relation for three different values of $T_e/T_\parallel$ in the case $T_\perp/T_\parallel = 1.8$ and $\beta_\parallel = 1$.

sure balance condition is only a good approximation as long as the Larmor radius of a protons is small compared to the perpendicular scale length of the wave and as long as in one gyroperiod a proton guiding center sees a nearly uniform field, namely,

$$\frac{v_{T\perp}}{\Omega_p} \ll \frac{1}{k_\perp} \tag{19a}$$

$$\frac{v_{T\parallel}}{\Omega_p} \ll \frac{1}{k_\parallel} \tag{19b}$$

with $\Omega_p \equiv eB/mc$ being the proton cyclotron frequency. Thus for $k_\perp$ ($k_\parallel$) larger than some value, which is of order $\Omega_p/v_{T\perp}$ ($\Omega_p/v_{T\parallel}$), finite Larmor radius effects become important, damping takes over, and the growth rate isn't well approximated by (15) any more.

The instability threshold for the proton mirror mode in the presence of hot electrons can be deduced from (15) and (16) and reads

$$\beta_\perp^{-1} + \left(1 - \frac{T_\perp}{T_\parallel}\right)\left[1 - \frac{1}{2}\left(1 - \frac{T_\parallel}{T_\perp}\right)\frac{T_e}{T_e + T_\parallel}\right] = 0 \tag{20}$$

a result which has been obtained, in less explicit forms, by *Barnes* [1966], *Tajiri* [1967], and *Belmont et al.* [1992]. Curves of the instability threshold for three different values of $\beta_\parallel$ are shown in Figure 5. The curves show that the sensitivity of the instability threshold on the electron temperature is rather weak unless $\beta_\parallel$ is small. Under such conditions, instability is only possible for high anisotropies $T_\perp/T_\parallel \gg 1$ in which case the last term in (20) eventually becomes important.

Although the instability threshold is only slightly modified by the hot electrons, this is not true for the growth rate. Figure 6 shows the growth rate of the fastest growing mode as a function of $T_e/T_\parallel$ for $\beta_\parallel = 1$ and three different values of $T_\perp/T_\parallel$. The growth rate is

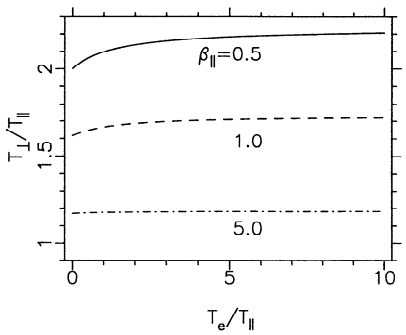

Figure 5. Instability threshold predicted by the model (equation (20)) as a function of $T_e/T_\parallel$ for three different values of $\beta_\parallel$. The unstable regions are located above the respective curves. Note the weakly stabilizing effect of an increasing T_e, particularly visible at low $\beta_\parallel$.

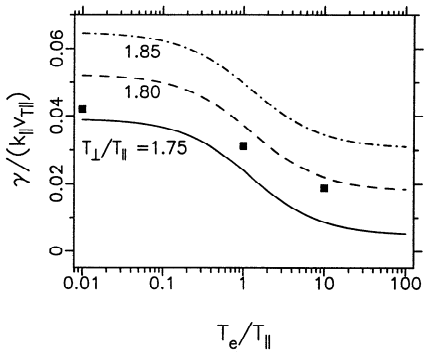

Figure 6. Growth rate of the most unstable mode for three different values of proton temperature anisotropy $T_\perp/T_\parallel$ (equation (15)). Unlike the instability threshold, which is only weakly dependent on T_e, the growth rate is seen to depend significantly on the electron temperature for $T_e/T_\parallel = O(1)$. Again, squares indicate the results for the fastest growing mode from the full Vlasov dispersion relation for the case $T_\perp/T_\parallel = 1.8$ and $\beta_\parallel = 1$.

naturally seen to increase with increasing $T_\perp/T_\parallel$, and the curves are found to depend strongly on T_e over a rather broad range around $T_e/T_\parallel = O(1)$. Note that at some value of $T_\perp/T_\parallel$ the curves eventually cross the $\gamma = 0$ axis, as the instability threshold, given by equation (20), depends on T_e.

The reason for the squares in Figure 6, indicating the results from the full Vlasov dispersion relation, being systematically below the $T_\perp/T_\parallel$ curve is mainly due to finite Larmor radius effects. The discrepancies between the theory and the numerical results vanish in the long-wavelength limit as the temperature anisotropy approaches the stability threshold given by (20).

2.3. Polarization

Concerning the mirror mode's polarization, we note that combining Faraday's equation $\gamma\delta B_\parallel = -ick_\perp\delta E_y$ (with $k_\perp$ pointing in the x direction, and c denoting the speed of light) and (9) we can explicitly evaluate $\delta\epsilon_\parallel$ defined as

$$\begin{aligned}\delta\epsilon_\parallel &\equiv \frac{\delta E_\parallel}{\delta E_y}\left(\frac{\Omega_p}{k_\perp v_{T\parallel}}\right) \\ &= \frac{k_\parallel v_{T\parallel}}{2\gamma}\left(\frac{T_\perp - T_\parallel}{T_e + T_\parallel}\right)\frac{T_e}{T_\parallel}\end{aligned} \tag{21}$$

where γ is given by (15). The quantity $\delta\epsilon_\parallel$ has the advantage over the usual ratio $\delta E_\parallel/\delta E_y$ that it is independent of $k_\perp$ (which can't be computed from the model). The dependence of the effective polarization $\delta E_\parallel/\delta E_y$ on T_e is obviously not the same as the dependence of $\delta\epsilon_\parallel$ on T_e since $k_\perp$ itself is generally a function of T_e. However, as we will show below, the T_e depen-

dence of the polarization is extremely strong, while it is heuristically clear that $k_\perp$ of the fastest growing mode is roughly determined by the appearance of finite proton Larmor radius effects so that $k_\perp \sim \Omega_p/v_{T\perp}$ independent of the electron temperature. In an example which will be discussed in section 3 we show, by solving numerically the full Vlasov dispersion relation (see Table 1), that increasing the electron temperature by a factor of 1000 (from $T_e/T_\parallel = 0.01$ to 10) only reduces by 66% the value of $k_\perp$ for the fastest growing mode. On the other hand, (21) applied to the same example shows that, taken over the same temperature range, $\delta\epsilon_\parallel$ rises by 2 orders of magnitude (see the lower solid line in Figure 7).

As pointed out by *Hasegawa* [1969] in the cold electron limit, only the y component of the electric field fluctuation is finite. In fact, (9) reveals that in the limit $T_e \to 0$ one has that $\delta E_\parallel \to 0$, and since no charge separation can occur in this limit, Poisson's equation reduces to $k_\perp \delta E_x + k_\parallel \delta E_\parallel = 0$ which also implies $\delta E_x = 0$. On the other hand, the mirror mode must satisfy $\delta B_y = 0$ in order to prevent the mode from acquiring characteristics associated with the transverse Alfvén mode (the y component of the magnetic field fluctuation never appears in the model since for a given $\delta B_\parallel$, only δB_x is fixed by the condition $\nabla \cdot \delta\mathbf{B} = 0$). Thus we have $(\nabla \times \delta\mathbf{E})_y = 0$, i.e.,

$$\frac{\delta E_x}{\delta E_\parallel} = \frac{k_\perp}{k_\parallel} \tag{22}$$

which at maximum growth can be computed from (16). Finally, combining (21) and (22), we obtain

$$\delta\epsilon_x \equiv \frac{\delta E_x}{\delta E_y}\left(\frac{\Omega_p}{k_\perp v_{T\parallel}}\right) = \frac{k_\perp}{k_\parallel}\delta\epsilon_\parallel. \tag{23}$$

From (21) and (23) we deduce that both $\delta\epsilon_x$ and $\delta\epsilon_\parallel$ increase with T_e. Thus the effect of increasing the electron temperature is to switch the electric field from the y direction into the plane perpendicular to it. The quantities $\delta\epsilon_\parallel$ and $\delta\epsilon_x$ are reproduced in Figure 7 for the fastest growing mode, in the case $\beta_\parallel = 1$ and $T_\perp/T_\parallel = 1.8$ (solid curves) and $T_\perp/T_\parallel = 1.85$ (dashed curves). The dependence of the polarization on the electron temperature is very strong for $T_e/T_\parallel \lesssim 1$, while both $\delta\epsilon_\parallel$ and $\delta\epsilon_x$ saturate at some value as $T_e \gg T_\parallel$ (note that one has always $\delta\epsilon_x/\delta\epsilon_\parallel = k_\perp/k_\parallel$). The differences between the solid and dashed curves indicate that as $T_\perp/T_\parallel$ is increased, the mirror component of the electric field δE_y is also increased relative to the components in the $(\mathbf{k}, \mathbf{B}_0)$ plane. Figure 7 also shows that polarization measurements in linear mirror waves are an extremely sensitive measure of the electron temperature.

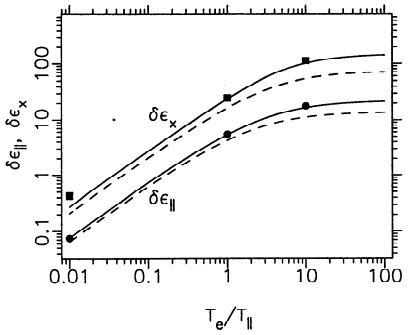

Figure 7. Normalized polarizations $\delta\epsilon_\parallel$ and $\delta\epsilon_x$ for the case $\beta_\parallel = 1$ and $T_\perp/T_\parallel = 1.8$ and 1.85 (solid and dashed curves, respectively). Squares (denoting $\delta\epsilon_x$) and circles (denoting $\delta\epsilon_\parallel$) correspond to the fastest growing mode determined from the full Vlasov dispersion relation in the case $T_\perp/T_\parallel = 1.8$ and $\beta_\parallel = 1$.

2.4. The Parallel Compressibility

In the case of a nonzero T_e the accumulation of electrons in regions of low parallel magnetic field density increases the electron pressure there. As expressed by (8) the electron pressure gradient between low and high parallel magnetic field has to be compensated by a longitudinal electric field. How strongly T_e, through $\delta E_\parallel$, acts against the development of the characteristic magnetic field-density anticorrelation can be quantified by computing the parallel compressibility $C_\parallel$ [cf. *Lacombe*

Table 1. Full Vlasov Dispersion Relation

Case	β_e	γ/Ω_p	$kv_{T\perp}/\Omega_p$	$\gamma/(k_\parallel v_{T\parallel})$	θ_{kB}	$Re(C_\parallel)$	$\delta\epsilon_\parallel$	$\delta\epsilon_x$
A	0.01	2.99×10^{-3}	0.369	4.20×10^{-2}	75°	−0.607	0.075	0.429
B	1	1.57×10^{-3}	0.313	3.11×10^{-2}	77.5°	−0.340	5.49	25.0
C	10	5.34×10^{-4}	0.243	1.88×10^{-2}	81°	−0.067	17.8	112.4

Properties of the most unstable modes for three different values of the ratio of the electron pressure to the magnetic field pressure β_e. Listed quantities are γ/Ω_p, the growth rate normalized to the proton cyclotron frequency; $kv_{T\perp}/\Omega_p$, the length of the wave vector normalized to the Larmor radius of a thermal proton; $\gamma/(k_\parallel v_{T\parallel})$, the width of the resonance normalized to the parallel proton thermal velocity; θ_{kB}, the angle between the wave vector and the magnetic field; $Re(C_\parallel)$, the real component of the parallel compressibility. Both $\delta\epsilon_\parallel$ and $\delta\epsilon_x$ are a measure of the the electric polarization of the mode (see section 2.3). The complete dispersion relation has been solved using WHAMP [*Rönnmark*, 1983]. Other plasma paramcters are $T_\perp/T_\parallel = 1.8$, $\beta_\parallel = 1$ and $\omega_p/\Omega_p = 3.3 \times 10^3$.

Table 2. Model of Section 2

Case	β_e	$\gamma/(k_\parallel v_{T\parallel})$	θ_{kB}	$Re(C_\parallel)$	$\delta\epsilon_\parallel$	$\delta\epsilon_x$	$v_{\perp,\mathrm{crit}}/v_{T\perp}$
A	0.01	5.21×10^{-2}	74.1°	−0.80	0.078	0.275	0.099
B	1	3.72×10^{-2}	77.2°	−0.40	6.15	27.0	0.707
C	10	2.19×10^{-2}	80.6°	−0.073	21.0	126.4	0.953

Properties of the most unstable modes for the same cases as in Table 1. Listed quantities have same meaning as in Table 1 with $v_{\perp,\mathrm{crit}}/v_{T\perp}$ denoting the temperature-dependent critical velocity given by equation (12). All quantities have been calculated using the model presented in section 2. Note the good agreement with the corresponding quantities listed in Table 1.

et al., 1992] explicitly. $C_\parallel$ has a vanishing imaginary part because δN_p and δN_e are out of phase by 180° with respect to $\delta B_\parallel$ and is easily found from (8) and (9) to be given by

$$C_\parallel = \frac{\delta N_p}{N_0}\frac{B_0}{\delta B_\parallel} = \frac{\delta N_e}{N_0}\frac{B_0}{\delta B_\parallel} = \frac{T_\parallel - T_\perp}{T_e + T_\parallel} < 0 \qquad (24)$$

which goes to 0 as $T_e \to \infty$ and to the cold electron limit as $T_e \to 0$. Also note that the cold electron limit obtained by *Hasegawa* [1969] is identical to the result found by *Belmont et al.* [1992] since near to the instability threshold, one has $C_\parallel = \beta_\perp^{-1} = (1 - T_\perp/T_\parallel)$. From (24) it appears that whenever T_e is of the same order or larger than $T_\parallel$, the compressibility strongly differs from the cold electron limit as illustrated by the solid curve in Figure 3. This has to do with the fact that as $v_{\perp,\mathrm{crit}}$ becomes of the same order of $v_{T\perp}$, a significant fraction of circulating (i.e., nonresonant) protons are being dominated by the longitudinal electric field rather than by the mirror force. The fact that even for very hot electrons, one always has $v_{\perp,\mathrm{crit}} < v_{T\perp}$ ensures that the mirror force always overcomes the electrostatic force for protons with $v_\perp \geq v_{T\perp}$ and thus $C_\parallel < 0$ even for $T_e \gg T_\parallel$. Other transport ratios can obviously be calculated using (10) and (11).

It has to be pointed out at this stage that most of the conclusions in the above model and, in particular, the ones for $C_\parallel$, are based on the critical assumption that the contributions of the resonant protons to the moments is negligible except for determining the growth rate (i.e., (15)). Taking the zeroth order moment of (10), we find that the contribution to the density perturbation δN_p from the resonant protons is small provided the following inequality holds

$$\frac{|\gamma|}{k_\parallel v_{T\parallel}} \ll \frac{1}{\sqrt{\pi}}\frac{T_\perp - T_\parallel}{T_e + T_\perp}. \qquad (25)$$

This is a necessary condition for the above estimates of $C_\parallel$ to be valid. If (25) is violated, the contribution of the resonant protons to δN_p has then to be retained in the theory in order to get the correct expressions.

3. Testing the Model

In order to test the validity of the model presented in section 2, we compare its results with the results from the full Vlasov dispersion relation. We use the program WHAMP (Waves in Homogeneous Anisotropic Multicomponent Plasmas) [*Rönnmark*, 1983] to solve the dispersion relation for three different electron temperatures such that $\beta_e = 0.01, 1, 10$ (cases A, B, and C) with all other plasma parameters being the same for the three cases. These are $T_\perp/T_\parallel = 1.8$, $\beta_\parallel = 1$, and the ratio of the proton plasma frequency to the proton cyclotron frequency $\omega_p/\Omega_p = 3.3 \times 10^3$ which is of the order of solar wind values. Note that the actual value of ω_p/Ω_p is irrelevant here as long as it is $\gg 1$ which is an implicit assumption of the above nonrelativistic model. The characteristics of the most unstable modes in the three cases are given in Table 1. As required by the model, the growth rates are small compared to the proton cyclotron frequency Ω_p and $(k_\parallel/k_\perp)^2 \ll 1$. It appears from Table 1 that the wavelength of the most unstable mode only increases by a factor of about 1.5 between case A and C, while the absolute value of the parallel compressibility drops by as much as 1 order of magnitude. The values of $C_\parallel$ from Table 1 are also reported in Figure 3 (solid squares) showing a good agreement with the curve from the model.

In Table 2 the results of the model applied to the three above cases are shown. For all listed quantities the agreement between the results from the full Vlasov dispersion relation and the model is quite satisfactory. Even the wave vector angle θ_{kB} and the polarization computed in section 2 (see figures 4 and 7) agree well with the corresponding quantities from WHAMP listed in Table 1 suggesting that the model takes into account most of the relevant features of the instability in a nonzero electron temperature plasma. The reason why the model systematically overestimates the growth rates from WHAMP stems from the fact that finite Larmor radius effects, which have a damping effect on the mirror mode, have not been retained in our calculations. Finite Larmor radius effects are, of course, the reason for the growth rate $\gamma(k)$ computed from WHAMP, to peak at values of k which are of the order of $\Omega_p/v_{T\perp}$ (see Table 1).

Figure 8 shows the distribution function $\delta f(v_\parallel, v_\perp)$ for cases A, B, and C at a position corresponding to a maximum of the parallel magnetic field flux $|B_0 + \delta B_\parallel|$. The δf_p has been obtained by numerically following proton phase space trajectories through the field of the

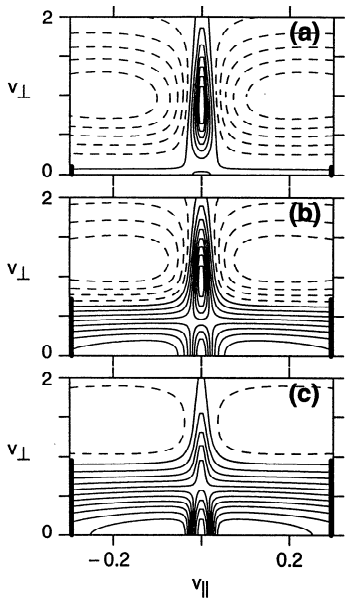

Figure 8. The perturbation of the distribution function $\delta f_p(v_\parallel, v_\perp)$ calculated from complete linear theory at a maximum of $|B_0 + \delta B_\parallel|$ for the (a) case A, (b) case B, and (c) case C in Table 1. Solid (dashed) lines denote positive (negative) equidistant contours. The black stripes denote $v_\perp < v_{\perp,\mathrm{crit}}$, where $v_{\perp,crit}$ is given by equation (12). This figure should be compared with the schematic picture in Figure 2.

growing linear waves given in Table 2 and by applying the Liouville theorem starting from the unperturbed distribution function $f_p(v_\parallel, v_\perp)$ (details of the method are given by *Pantellini et al.* [1994]). The results of Figure 8, of course, depend on the final amplitude of the wave. However, as long as $\delta B_\parallel / B_0 \ll 1$ (in figure 8 the final amplitudes are $\lesssim 0.01$), δf scales with $\delta B_\parallel / B_0$ apart from negligible small corrections proportional to $(\delta B_\parallel / B_0)^2$. Since the wave field seen by a proton varies slowly in space and time (see above), the drift equations [cf. *Morozov and Solov'ev*, 1966)] have been used in place of the full equations of motion.

The thick solid bars in Figure 8 indicate the region $v_\perp < v_{\perp,\mathrm{crit}}$ as given by (12) (compare Table 2). From Figure 8 it appears that $v_{\perp,\mathrm{crit}}$ gives an excellent estimate of the position of sign reversal in f_p, suggesting that δf_p as given by (10) is a good approximation to the linear perturbation of the proton distribution function. Note that for Figure 8a the region $v_\perp < v_{\perp,\mathrm{crit}}$ is negligibly small; in this case the cold electron model applies and only the circulating (dashed contours) as well as the resonant protons (solid contours centered around $|v_\parallel| \lesssim |\gamma / k_\parallel| \ll v_{T\parallel}$), are important. Figure 8b shows that as T_e becomes of the same order of $T_\parallel$, a non-negligible number of protons with small perpendicular velocity ($\lesssim v_{\perp,\mathrm{crit}}$) become dominated by the longitudinal electric field. For $T_e \gg T_\parallel$ (Figure 8c), protons dominated by longitudinal electric field cover nearly the whole region with $v_\perp < v_{T\perp}$. In this case the proton distribution function bears little resemblance to the cold electron limit distribution of panel Figure 8a. Owing to the fact that the compressibilities calculated from the model and from the full Vlasov dispersion relation are in excellent agreement (compare Figure 3 and both Tables 1 and 2), it is not surprising that values for $v_{\perp,\mathrm{crit}}$, estimated from (12), are a good estimate of the position of sign reversal of δf_p as shown in Figure 8 for all three cases. A final comment on Figure 8 is that as the spatial dependence of the linear response δf_p is given by $\exp[i(k_\perp x + k_\parallel z)]$, one has that at a minimum of the parallel magnetic field flux, δf_p is just the negative of δf_p at a maximum of the parallel magnetic field flux.

It should also be emphasized that the discrepancies between the numerical solutions and the model tend to shrink as one approaches the stability threshold given by (20) and if one takes the long-wavelength limit $k \to 0$. However, here we show that the model gives good estimates of the characteristics, including the T_e dependencies, of the most unstable mode even in the case of fairly oblique (i.e., relatively fast growing) instabilities. From this detailed comparison of the analytical results derived in section 2 with the results from WHAMP we conclude that the model presented in section 2 gives a good description of the slowly growing proton mirror instability in a proton-electron plasma with $T_e \neq 0$.

4. Conclusion

We have presented a model for the long-wavelength proton mirror instability when a nonzero temperature electron population is included. The model shows that as expected, the nonzero temperature of the electrons decreases the growth rate and modifies the instability threshold, as well as θ_{kB}, of the fastest growing mode. Apart from causing a significant reduction in the values of the parallel compressibility $C_\parallel$, the hot electrons strongly modify the mode's polarization causing the electric field fluctuations to turn into the $(\mathbf{k}, \mathbf{B}_0)$ plane. All these effects are ultimately due to a longitudinal field which arises because an electron pressure gradient builds up as the electrons are dragged by the circulating protons from the high into the low parallel magnetic field flux regions. The longitudinal electric field, which for positively charged particles acts against the mirror force, prevents protons with $v_\perp < v_{\perp,\mathrm{crit}}$ from responding in the usual way to the magnetic field perturbations.

The effects of the nonzero electron temperature are seen to be important whenever $T_e / T_\parallel = O(1)$. This is a value which is easily encountered in the solar wind and even in magnetospheric plasmas where, as a result, the cold electron model by *Southwood and Kivelson* [1993]

may not be applicable. The effect of a nonzero electron temperature on the proton distribution function at a maximum of the parallel magnetic field flux is shown in Figures 2 and 8. Figure 2 and Figures 8b and 8c differ from *Southwood and Kivelson* [1993, Figure 2] in that the density of protons with $v_\perp < v_{\perp,\mathrm{crit}}$ is increasing and not decreasing as the instability develops. The fact that these protons are not mirror accelerated as are the ones with $v_\perp \geq v_{\perp,\mathrm{crit}}$, added to the fact that their number is a sensitive function of $T_e/T_\parallel$, is the reason most of the characteristics of the proton mirror mode are strongly dependent on the electron temperature.

Acknowledgments. This work has been supported by SERC (UK) grant GR/H09454 and the Commission of the European Community under contract SCI0468-M. The authors express their thanks to K. Rönnmark for kindly supplying the WHAMP program.

The Editor thanks M. Kivelson and S.P. Gary for their assistance in evaluating this paper.

References

Anderson, B.J., and S.A. Fuselier, Magnetic pulsations from 0.1 to 0.4 Hz and associated plasma properties in the Earth's subsolar magnetosheath and plasma depletion layer, *J. Geophys. Res.*, *98*, 1461, 1993.

Anderson, B.J., S.A. Fuselier, S.P. Gary, and R.E. Denton, Magnetic spectral signatures in the Earth's magnetosheath and plasma depletion layer, *J. Geophys. Res.*, *99*, 5877, 1994.

Barnes, A., Collisionless damping of hydromagnetic waves, *Phys. Fluids, 9*, 1483, 1966.

Belmont, G., D. Hubert, C. Lacombe, and F. Pantellini, Mirror mode and other compressive ULF modes, in Proceedings of the 26th ESLAB Symposium on the Study of the Solar-Terrestrial System, *Eur. Space Agency Spec. Publ. ESA SP-346*, 263, 1992.

Chandrasekhar, S., A.N. Kaufman, and K.M. Watson, The stability of the pinch, *Proc. R. Soc. London, A, 245*, 435, 1958.

Davidson, R.C., and J.M. Ogden, Electromagnetic ion cyclotron instability driven by ion energy anisotropy in high-beta plasmas, *Phys. Fluids, 18*, 1045, 1975.

Gary, S.P., The mirror and ion cyclotron anisotropy instabilities, *J. Geophys. Res.*, *97*, 8519, 1992.

Hasegawa A., Drift mirror instability in the magnetosphere, *Phys. Fluids, 12*, 2642, 1969.

Hubert, D., C. Perche, C.C. Harvey, C. Lacombe, and C.T. Russell, Observation of mirror waves downstream of a quasi-perpendicular shock, *Geophys. Res. Lett.*, *16*, 159, 1989.

Jeffrey, A., and T. Taniuti, *Magnetohydrodynamic Stability and Thermonuclear Containment*, Academic, San Diego, Calif., 1966.

Kaufmann, R.L, J.T. Horng, and A. Wolfe, Large amplitude hydromagnetic waves in the inner magnetosheath, *J. Geophys. Res.*, *75*, 4666, 1970.

Krall, N.A., and A.W. Trivelpiece, *Principles of Plasma Physics*, McGraw-Hill, New York, 1973.

Lacombe, C., F.G.E. Pantellini, D. Hubert, C.C. Harvey, A. Mangeney, G. Belmont, and C.T. Russell, Mirror and Alfvénic waves observed by ISEE1-2 during crossing of the Earth's bow shock, *Ann. Geophysicae, 10*, 772, 1992.

McKean, M.E., D. Winske, and S.P. Gary, Mirror and ion cyclotron anisotropy instabilities in the magnetosheath, *J. Geophys. Res.*, *97*, 19,421, 1992.

McKean, M.E., S.P. Gary, and D. Winske, Kinetic physics of the mirror instability, *J. Geophys. Res.*, *98*, 21,313, 1993.

Morozov, A.I, and L.S. Solov'ev, Motion of charged particles in electromagnetic fields, in *Reviews of Plasma Physics, vol. 2*, Consultants Bureau, New York, 1966.

Northrop, T.G., *The Adiabatic Motion of Charged Particles*, p. 12, Wiley Interscience, New York, 1963.

Pantellini, F.G.E., D. Burgess, and S.J. Schwartz, Phase space evolution in linear instabilities, *Phys. Plasmas, 1*, 3784, 1994.

Pantellini, F.G.E., D. Burgess, and S.J. Schwartz, On the non linear mirror instability, *Adv. Space Res.*, in press, 1995.

Price, C.P., D.W. Swift, and L.C. Lee, Numerical simulation of nonoscillatory mirror waves at the Earth's magnetosheath, *J. Geophys. Res.*, *91*, 101, 1986.

Rönnmark, K., Computation of the dielectric tensor of a Maxwellian plasma, *Plasma Phys. Controlled Fusion, 25*, 699, 1983.

Rose, D.J., General criterion for mirror instability of a plasma, *Phys. Fluids, 8*, 951, 1965.

Russell, C.T., W. Riedler, K. Schwingenshuh, and Ye. Yeroshenko, Mirror instability in the magnetosphere of Comet Halley, *Geophys. Res. Lett.*, *14*, 664, 1987.

Southwood, D.J., and M.G. Kivelson, Mirror instability, 1, The physical mechanism of linear instability, *J. Geophys. Res.*, *98*, 9181, 1993.

Tajiri, M., Propagation of hydromagnetic waves in collisionless plasma, 2, Kinetic approach, *J. Phys. Soc. Jpn.*, *22*, 1482, 1967.

Tsurutani, B.T., D.J. Southwood, E.J. Smith, and A. Balogh, Nonlinear magnetosonic waves and mirror mode structures in the March 1991 Ulysses interplanetary event, *Geophys. Res. Lett.*, *19*, 1267, 1992.

Winske, D., and K.B. Quest, Magnetic field and density fluctuations at perpendicular supercritical collisionless shocks, *J. Geophys. Res.*, *93*, 9681, 1988.

F.G.E. Pantellini, Observatoire de Paris, Département de Recherche Spatiale, 92195 Meudon Cédex, France. (e-mail: pantellini@megasx.obspm.fr)

S.J. Schwartz, Astronomy Unit, Queen Mary and Westfield College, Mile End Road, London E1 4NS, England, United Kingdom. (e-mail: S.J.Schwartz@qmw.ac.uk)

(Received June 17, 1994; revised September 23, 1994; accepted September 23, 1994.)

4 Une théorie pour la formation des trous magnétiques

JGR 103, 4789-4798 (1998)

JOURNAL OF GEOPHYSICAL RESEARCH, VOL. 103, NO. A3, PAGES 4789–4798, MARCH 1, 1998

A model of the formation of stable nonpropagating magnetic structures in the solar wind based on the nonlinear mirror instability

Filippo G. E. Pantellini

Département de Recherche Spatiale, Observatoire de Paris–Meudon, Meudon, France

Abstract. A simple model for the formation of stable nonpropagating structures in a magnetized collisionless plasma is presented. The model describes the evolution of an electron-proton plasma from an initially spatially uniform, but unstable, configuration toward a final nonuniform and nonpropagating stable configuration. The model is based on the following hypothesis: (1) one-dimensionality and spatial periodicity, (2) cold electrons, (3) bi-Maxwellian protons as initial condition, (4) conservation of magnetic moment for all protons, (5) conservation of energy for magnetically non trapped protons, (6) spatial pressure balance, (7) evolved structure has a crenellated shape, (8) slow growth of the structure. Given these assumptions all the macroscopic properties of the plasma (density, pressure, and magnetic field) in the saturated state can be computed explicitly. The model shows that a spatially uniform and homogeneous plasma that is unstable against the linear mirror mode can form stable non propagating structures. Thus one can consider the model as a model for the nonlinear mirror instability where the magnetic trapping of protons in the low magnetic field region is the important saturation mechanism. A simple expression for the magnetic field saturation amplitude is found. The pressure balance, between high and low magnetic field regions, which is needed for the evolved structure to be a stable one, is obtained solely through betatron cooling of the trapped protons. Modification of the trapped protons energy due to the Fermi effect seems to be of secondary importance. The model predicts that the evolved structures are characterized by narrow and deep magnetic wells except in the case of very low magnetic pressure (ratio of thermal to magnetic pressure $\beta \gtrsim 10$) where the opposite situation becomes possible. This enforces the idea according to which the proton mirror instability is the driving mechanism for the formation of magnetic holes in high β ($\gtrsim 1$) plasmas.

1. Introduction

On a timescale of a minute or less, magnetic holes are the most commonly observed stable and nonpropagating structure in the solar wind. Even though a rigorous definition of magnetic hole has not yet been given, such structures are generally identified as more or less deep dropouts of the magnetic field. The magnetic field intensity within a hole can be as low as 10% of the out of hole magnetic field. Typical durations are in the interval ranging from a few seconds up to 1 or 2 min [*Winterhalter et al.*, 1994]. Magnetic holes have been observed in the Earth magnetosheath [e.g., *Kaufmann et al.*, 1970; *Tsurutani et al.*, 1982], in the free solar wind [*Turner et al.*, 1977; *Fitzenreiter and Burlaga*, 1978; *Klein and Burlaga*, 1980; *Winterhalter et al.*, 1994], mostly in the vicinity of stream interfaces, and at comets [*Russell et al.*, 1987; *Glassmeier et al.*, 1993]. The total pressure (particle + field) inside a magnetic hole is generally believed to be balanced by the pressure of the surrounding plasma even though observations do not seem to be very conclusive on that point. However, it is clear that if the pressure of a nonpropagating magnetic hole is not balanced by the pressure of the surrounding plasma, it must be unstable and either collapse or explode. As we are only concerned with stable structures, we shall consider the case of nonpropagating magnetic holes that are in pressure balance with the surrounding plasma.

Magnetic holes are mainly observed in high β (the ratio of thermal pressure to magnetic pressure) plasmas with $\beta \gtrsim 1$. Thus, soon after the very first observations of magnetic holes, the proton mirror instability, which is driven by an anisotropic thermal pressure of the protons such that $p_\perp/p_\parallel > 1$ (subscripts $\perp$ and $\parallel$ refer to the local magnetic field direction), has been proposed to be the basic mechanism leading to their formation. In fact, in a high β plasma, the proton temperature anisotropy required for instability is rather weak, that is $T_\perp/T_\parallel > 1 + 1/\beta_\perp$ [e.g., *Southwood and Kivelson*, 1993]. The mirror instability has some other particularities that make it a privileged candidate to fit into

Paper number 97JA02384.
0148-0227/98/97JA-032384$09.00

a scenario of magnetic holes formation, the nonpropagating nature of the mode and the anticorrelation of density and magnetic field being two other important reasons.

Since the late 1950s the theory of the linear proton mirror instability has been discussed by a large number of authors [see *Pantellini and Schwartz*, 1995, and references therein]. However, the underlying physical processes, implicit in the early treatments of the instability [e.g., *Barnes*, 1966; *Tajiri*, 1967], have been elucidated only recently by *Southwood and Kivelson* [1993]. The new important aspect which has been pointed out in the *Southwood and Kivelson* [1993] theory is that the mirror instability is one where the resonant particles, that is, particles with small velocities parallel to the magnetic field, play an important role. This has been the strongest demonstration of the fact that the mirror instability is based on essential kinetic effects and that, as a consequence, fluid theories do not lead to a correct understanding of the instability.

The rather speculative hypothesis according to which the mirror instability is responsible for the formation of magnetic holes has been consolidated after the identification of mirror mode waves in planetary magnetosheaths [e.g., *Tsurutani et al.*, 1982; *Hubert et al.*, 1989; *Lacombe et al.*, 1992; *Anderson and Fuselier*, 1993; *Violante et al.*, 1995]. The hypothesis has become even less speculative since *Winterhalter et al.* [1994] could show that trains of closely spaced magnetic holes are often observed in marginally mirror mode stable plasmas and also that proton distribution functions observed within holes are sometimes similar to distributions seen in numerical simulations of mirror mode waves [e.g., *McKean et al.*, 1993]. From the theoretical point of view the most stringent proof of the causal relationship between mirror instability and magnetic holes has been given recently in a paper on the nonlinear mirror instability by *Kivelson and Southwood* [1996]. The theory of *Kivelson and Southwood* [1996] indicates that if one admits that particles trapped in the magnetic wells, created by the instability, do undergo a mixture of both betatron deceleration, due to the locally decreasing field intensity, and Fermi acceleration, due to the relative motion of the mirror points, then the mirror instability may evolve toward a saturated state characterized by deep and narrow holes in the magnetic field profile. The *Kivelson and Southwood* [1996] theory is based on the fact that the evolved structure must satisfy the pressure balance condition. This is only possible if one allows for substantial cooling of the trapped proton population. However, the amount of cooling needed to saturate the instability depends on the spatial and temporal evolution of the magnetic field. Unfortunately, the spatial and temporal dependence of the magnetic field is not given by the *Kivelson and Southwood* [1996]theory.

Our approach is similar to the one of *Kivelson and Southwood* [1996] with the important difference that we restrict the analysis to a particularly simple profile of the evolved spatial structure which we expect to be a rough approximation of the real structure of the saturated nonlinear mirror instability (see Figure 1). Following *Kivelson and Southwood* [1996], our model is based on a spatial pressure balance condition between the high and low magnetic field regions. The pressure balance condition includes the contribution from both magnetically trapped and nontrapped (circulating) protons. The advantage of restricting the evolved magnetic field profile to the simple shape shown in Figure 1 is that the model can be calculated easily throughout. In particular, we will show that for one given initial plasma condition, which is fully specified by two parameters (the proton pressure anisotropy and the plasma β), there is at most one final stable plasma configuration. This is completely different than in the *Kivelson and Southwood* [1996] theory where the emphasis is put on the qualitative description of the cooling of the trapped proton population needed to reach a given final state which may be taken from observations. The main problem with that stems from the fact that it is extremely difficult, not to say impossible, to specify a plasma equilibrium consistent with an observed non uniform magnetic field profile. Given the strong uncertainties on the final state, it is virtually hopeless to determine how such a state has been obtained from an initially unstable (and a priori unknown) configuration.

In our approach we start from an easy to define initial state and compute the final state using a number of assumptions that make the problem simpler than the one addressed by *Kivelson and Southwood* [1996] at the expense of a loss of generality. We shall see that even in the framework of this simplified theory a final stable configuration can be obtained in most cases. We shall argue that the detailed motion of the trapped particles is unimportant in the saturation process. We shall also show that the model leads naturally to the formation of deep and narrow magnetic holes (observed) rather than the opposite situation characterized by large and shallow holes (rarely observed). In the latter case one would no longer define these structures as magnetic holes but rather as "magnetic monoliths"The qualitative agreement between the results of our model and the observations suggests that the former includes most of the important physics necessary to generate the observed nonpropagating structures.

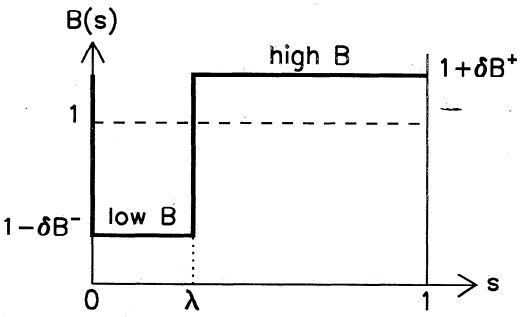

Figure 1. Magnetic field profile for $t > 0$. At $t = 0$ the field is a constant $B_0 = 1$ over the whole domain $s \in [0, 1]$. The model is spatially periodic with period 1. Together with Faraday's equation, periodicity implies that the average magnetic field is equal to B_0 at any time. Thus λ, δB^- and δB^+ are related through (2). Note that all other quantities appearing in the model (number density, pressure, etc.) are always taken to be constant in the intervals $[0, \lambda]$ (low-B field) and $[\lambda, 1]$ (high-B field).

We conclude by noting that the first attempt to describe the nonlinear evolution of the mirror instability has been proposed, long ago, by *Shapiro and Shevchenko* [1964]. Their approach was based on quasi-linear theory. However, as pointed out by *Kivelson and Southwood* [1996], quasi-linear theory is most probably inappropriate in the treatment of the mirror instability except in the case of very weak growth. The main reason is that quasi-linear theory predicts a spatially uniform final state while simulations [e.g., *McKean et al.*, 1992; *McKean et al.*, 1993], as well as the above cited observations, indicate that the evolved state of the mirror instability is generally characterized by strong spatial variations.

2. Basic Assumptions of the Model

We start from the postulate that both the particle trapping and a spatial pressure balance condition are the main ingredients in a theory of the evolution of the nonlinear mirror instability. Based on these two main assumptions, we construct a simple model for the nonlinear evolution of the mirror instability.

We consider a model where, at any given time t, all quantities (e.g., density, pressure, magnetic field, ...) depend on one spatial dimension only. As in linear theory, it is the motion of the particles along the magnetic field lines which controls the evolution of the system [*Kivelson and Southwood*, 1996] so that the relevant spatial dimension is along the field line. We restrict the model to a two species proton-electron plasma. This restriction is a minor one as heavy ions, which are present in the solar wind, do not affect significantly the mirror instability [*Price et al.*, 1986]. For simplicity we assume that the electrons are cold so that they do not produce any longitudinal electric field [cf. *Pantellini and Schwartz*, 1995]. Our purpose is to predict the final state of the plasma given an unstable uniform initial equilibrium. Thus at $t = 0$ the plasma is taken to be spatially uniform, the protons being distributed according to a bi-Maxwellian

$$f_0 = \frac{n_0 \pi^{-3/2}}{v_{T\perp}^2 v_{T\parallel}} \exp\left[-\frac{v_{0\parallel}}{v_{T\parallel}^2} - \frac{v_{0\perp}}{v_{T\perp}^2}\right] \tag{1}$$

where $v_{T_\perp} \equiv (2k_B T_\perp/m)^{1/2}$ and $v_{T_\parallel} \equiv (2k_B T_\parallel/m)^{1/2}$ designate the proton thermal velocity perpendicular and parallel to the uniform magnetic field B_0. Here m is the proton mass, k_B is the Boltzmann constant and n_0 is the proton number density.

Hereinafter we adopt the following normalizations: $n_0 = 1$, $B_0 = 1$ and $v_{T\parallel} = 1$ the plasma at $t = 0$ being completely specified by the dimensionless parameters $\beta_\parallel \equiv 2\mu_0 k_B n_0 T_\parallel/B_0^2$ and the ratio $R \equiv T_\parallel/T_\perp$. We further assume that the system is spatially periodic, with period 1, and that at any time $t > 0$ the magnetic field is constant in the intervals $[0, \lambda]$ and $[\lambda, 1]$ (see Figure 1). We shall denote quantities characterizing the high magnetic field region by a plus superscript and quantities characterizing the low magnetic field region by a minus superscript. Subscript 0 denotes time level $t = 0$ whenever this indication is needed to avoid ambiguity. We also note that the scale of length of the system does not need to be specified as only relative dimensions will be used. Moreover, since the model is one dimensional and periodic, from Faraday's equation $\partial \mathbf{B}/\partial t = -\nabla \times \mathbf{E}$ it follows that the average magnetic field must be constant in time. Thus from Figure 1 one deduces that λ, δB^+ and δB^- are related to each other through

$$(1 - \lambda)\delta B^+ = \lambda \delta B^- . \tag{2}$$

Hereinafter we will sometimes use the notation $B^\pm \equiv 1 \pm \delta B^\pm$.

3. Density and Pressure in the High Magnetic Field Region

In order to compute the number density n^+ and the perpendicular particle pressure $p_\perp^+$ in the high magnetic field region, we note that in a slowly growing magnetic structure nearly all particles do conserve energy. Only a small number of particles for which the time needed to cross the whole system is longer than the typical growth time of the magnetic structure do not conserve energy. These particles, called resonant particles in linear theory, gain or lose energy depending on whether the local field is growing or decreasing (betatron effect) and have been described in detail by *Southwood and Kivelson* [1993]. Using the fact that the particles' energy $m(v_\perp^2 + v_\parallel^2)/2$ and the particles' first adiabatic invariant $\mu = mv_\perp^2/(2B)$ are both conserved one finds that only particles satisfying the condition

$$v_{0\parallel}/v_{0\perp} > \sqrt{\delta B^+} \tag{3}$$

can reach the high magnetic field region corresponding to the interval $[\lambda, 1]$. Thus we call circulating particles those particles which do satisfy to the inequality (3) and trapped particles those which do not. The two populations are separated by the trapping boundary, or separatrix, defined by $v_{0\parallel}/v_{0\perp} = \sqrt{\delta B^+}$. It is obvious that trapped particles are located in the interval $[0, \lambda]$, whereas the circulating particles are distributed over the whole available space $[0, 1]$.

Taking into account that f is constant along particle trajectories and that energy and magnetic moment of the circulating particles are both conserved, it is easy to compute the number density n^+ and the particle pressure $p_\perp^+$ in the high magnetic field region. Thus for n^+ we have

$$\begin{aligned}
n^+ &= \int_{D_t^+} f^+(v_\parallel, v_\perp, t)\, dv^3 \\
n^+ &= \int_{D_t^+} f^+(v_\parallel, v_\perp, t)\, J^+\, dv_0^3 \\
n^+ &= \int_{D_0} f_0(v_{0\parallel}, v_{0\perp})\, J^+\, dv_0^3 \\
n^+ &= \int_0^\infty 2\pi v_{0\perp} dv_{0\perp} \int_{|v_{0\parallel}| > v_{0\perp}\sqrt{\delta B^+}} f_0(v_{0\parallel}, v_{0\perp}) \cdot \\
&\quad J^+(B^+, v_{0\parallel}, v_{0\perp})\, dv_{0\parallel} \\
n^+ &= \frac{RB^+}{R + \delta B^+}
\end{aligned} \tag{4}$$

where D_t^+ denotes the domain in velocity space occupied by the circulating particles spatially located in the high magnetic field region at time t, while D_0 denotes the domain in velocity space occupied by the same particles at $t = 0$. J^+ represents the Jacobian giving the variation of the velocity space volume element $dv_0^3 = 2\pi v_{0\perp} dv_{0\perp} dv_{0\parallel}$ during the time interval t. The Jacobian can be computed from the equations of conservation for energy and magnetic moment. This leads to

$$J^+(B^+, v_{0\parallel}, v_{0\perp}) = \frac{|v_{0\parallel}| B^+}{(v_{0\parallel}^2 - v_{0\perp}^2 \delta B^+)^{1/2}}. \quad (5)$$

Equation (4) shows that the density in the high-field region is always smaller than the initial density value $n_0 = 1$, and that for small amplitudes $\delta B^+ \ll 1$, the result $n^+ = 1 + \delta B^+ (1 - 1/R)$, known from the linear theory of the mirror instability, is recovered [*Southwood and Kivelson*, 1993]. This makes clear that our model is effectively a model for the nonlinear mirror instability.

The mappings of D_0 resulting from the motion of the circulating particles to both high and low magnetic field regions are illustrated in Figure 2. As D_0 extends to infinity, only the mapping of a part of the distribution function f_0 (shaded region), delimited by an arbitrary contour level, is actually shown in the figure. The fact that for $\delta B^+ \to \infty$ one obtains a nonvanishing asymptotic density value $n^+ \to R$ can be easily understood from Figure 2b. Since by definition the energy of the circulating particles is conserved, particles do move on circles in velocity space when being mapped from the initial contour, corresponding to the distribution at $t = 0$ to the new contour at time $t > 0$. Thus in the limit $\delta B^+ \to \infty$ the major half-axis of the half-ellipse D_t^+ shrinks to the same values as the minor half-axis, that is D_t^+ becomes a nonvanishing half circle. It is also clear from the figure that in the same way $f^+(v_\parallel, v_\perp, t)$ must tend toward an isotropic Maxwellian distribution with temperature $T = T_\parallel$ since it results from the mapping, along circles, of the points $f_0(v_{0\parallel}, 0)$. The integration over the resulting isotropic distribution leads to the above asymptotic result $n^+ = R$.

The question mark in Figure 2c illustrates the fact that, as we shall show below, the motion of the trapped particles in velocity space does not have to be known in order to compute the model throughout. The only assumption concerning the trapped particles is that their magnetic moment is conserved. However, the energy of a particle trapped near the separatrix has to be conserved if one asks for the distribution f to be continuous there. We shall point out that this has not to be true (and is certainly not true in general!) for all other trapped particles. The complicated behavior of the trapped particles, which is implicit in our model, is schematically illustrated in Figure 3. The top panel (Figure 3a) shows that circulating particles are thought to be energy conserving since the time these particles spend in the low, or high, field region is assumed to be small compared to the typical growth time of the magnetic structure. Similarly, a particle that has just been trapped, that is, a particle with mirror points at a magnetic field strength close to B^+, has spent most of the time as circulating particle, so that its energy did not have time to depart significantly from the initial value. Particles that have mirror points corresponding to a field strength significantly less than B^+ have been trapped during a time which is comparable to the typical growth time. Two effects can affect the energy of these particles. (1) The particle loses energy due to fact that it sees a decreasing magnetic field (Figure 3b). This is the so-called be-

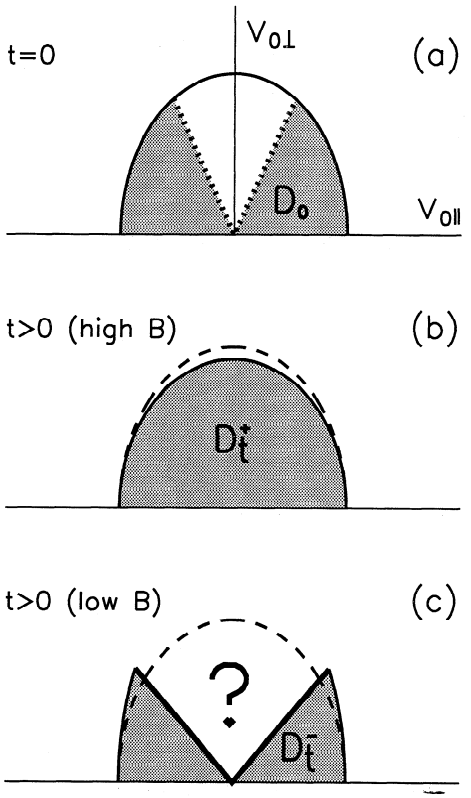

Figure 2. Mapping of the velocity distribution function of circulating particles to both high- and low-B field regions. (a) A particular contour level c_l of the distribution function $f_0(v_{0\parallel}, v_{0\perp})$ is shown. The interior of the half-ellipse corresponds to the domain with $f_0 > c_l$. The shadowed domain corresponds to the circulating particles for which the inequality (3) is true, given a certain δB^+. The remaining sector of the ellipse corresponds to the particles which are trapped for this same δB^+. (b, c) Mapping of the circulating particles to high- and low-field regions with the original contour being represented by the dashed line. Obviously, there are no trapped particles at magnetic field maximum (Figure 2b). As the model only requires that trapped particles conserve magnetic moment μ, but not energy, their velocity distribution is not known for $t > 0$, thus the question mark in Figure 2c.

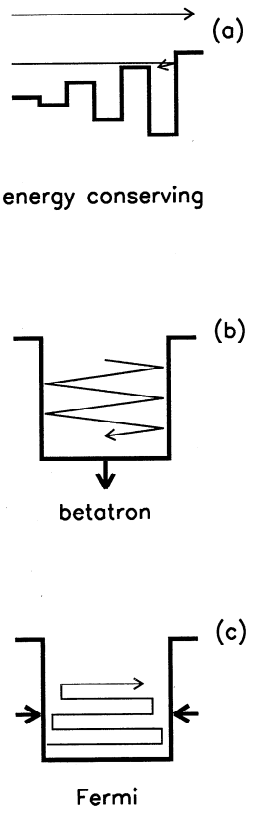

Figure 3. Time dependence of the energy for particles in the model. (a) A circulating and a freshly trapped particle are shown. Both particles do approximately conserve energy since the average magnetic field the particles see during the typical growth time of the structure is roughly constant. A particle that is trapped during a time which is comparable to the time of evolution of the magnetic field may change its energy due to two distinct mechanisms illustrated in Figures 3b and 3c. (b) The trapped particle loses energy at the rate $\mu\partial B/\partial t$ as it experiences a constantly decreasing magnetic field (betatron deceleration), while (c) the trapped particle gains energy as the magnetic hole contracts and the magnetic mirror points move toward each other (Fermi acceleration).

tatron deceleration. It affects the perpendicular velocity of the particle. (2) The particle gains (loses) energy because of the converging (diverging) mirror points (Figure 3c). This is the so-called Fermi acceleration (deceleration). It affects the particle's parallel velocity. We shall show below that only the betatron effect does play a role in our model and that the Fermi effect is of secondary importance in the saturation of the mirror instability.

As announced, we may now compute the particle pressure p^+ at magnetic field maximum in the same way as we did for the number density n^+. Keeping in mind that $v_\perp^2 = v_{0\perp}^2 B^+$ for the particles circulating in the high-field region, we obtain

$$p_\perp^+ = \int_{D_0} f_0(v_{0\|}, v_{0\perp})\, v_{0\perp}^2 B^+ J^+ \, dv_0^3$$

$$p_\perp^+ = R\left(\frac{B^+}{R+\delta B^+}\right)^2. \tag{6}$$

It should be noted that n^+ and $p_\perp^+$ do not depend on δB^- and λ. This is a consequence of the fact that the equations of motion for particles reaching the high-field region only depends on δB^+. This is not true for particles located in the magnetic wells. For example, circulating particles in the low-field region do satisfy to the same inequality (3) as do the circulating particles in the high magnetic field region, but their perpendicular velocity depends on B^- since $v_\perp^2 = v_{0\perp}^2 B^-$. Thus their contribution to the density and pressure depend on both B^+ and B^-.

4. High-Field Saturation Level

In the previous section we have computed the density and the particle pressure in the high magnetic field region for a given magnetic field amplitude δB^+. In this section we shall compute the saturation amplitude $\delta B_{\rm sat}^+$ in the case of an unstable plasma.

Now from the previous section we already know that, for a given value of the field perturbation δB^+ the total perpendicular plasma pressure is given (in normalized units) by

$$p_{\perp,\rm tot}^+ = R\left(\frac{B^+}{R+\delta B^+}\right)^2 + \frac{(B^+)^2}{\beta_\|}. \tag{7}$$

The important fact about this expression is that it does not depend on the characteristics of the low magnetic field region. It is therefore clear that the saturation amplitude $\delta B_{\rm sat}^+$ must depend on the initial plasma parameters $\beta_\|$ and R only. Another important point about (7) is that for small values of δB^+ the total pressure and the magnetic pressure vary in antiphase provided $R^{-1} - 1 - R/\beta_\| > 0$, which is precisely the instability condition for the linear mirror instability. In fact, (7) is the finite amplitude equivalent of the magnetohydrodynamic response of a bi-Maxwellian plasma to a small, and slowly varying, compressional perturbation δB^+, which reads

$$\delta p_{\perp,\rm tot}^+ = 2p_{0\perp,\rm tot}^+(1 - R^{-1})\delta B^+/B_0$$

and is the base of any theory of the linear mirror instability [e.g., *Hasegawa*, 1969; *Southwood and Kivelson*, 1993]. We now postulate that even in the nonlinear regime the instability keeps on growing as long as the total pressure and the magnetic field pressure vary in antiphase. By setting $\partial p_{\perp,\rm tot}^+/\partial B^+ = 0$ one computes directly the limiting value $\delta B_{\rm sat}^+$ beyond which the total pressure and the magnetic field pressure are both growing. This leads to a simple expression for the saturation amplitude

$$\frac{\delta B_{\rm sat}^+}{B_0} = [\beta_\| R(1-R)]^{1/3} - R. \tag{8}$$

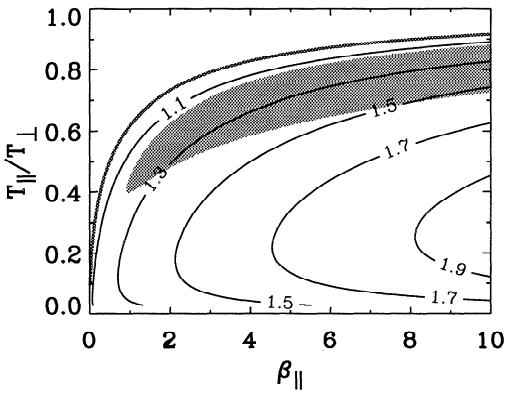

Figure 4. Contours of $B^+_{\rm sat}$ computed from (8). The upper thick contour corresponds to the stability threshold for the linear mirror mode. The meaning of the shaded region will be discussed in relation to Figure 5.

We note that (8) gives the saturation peak value for an arbitrary magnetic field profile which may be different from the one shown in Figure 1. This is a consequence of the fact that no reference to the actual magnetic field profile has been made in deriving equation (8). An example: for $\beta_\parallel = 1$ and $R = 0.5$, (8) predicts a saturation amplitude $\delta B^+_{\rm sat} = 0.13$. The same value has been obtained numerically by Kivelson and Southwoo using a sinusoidal field profile (compare Figure 3 of *Kivelson and Southwood* [1996]).

A contour plot for $B^+_{\rm sat}(\beta_\parallel, R)$ is shown in Figure 4. The thick curve corresponds to the value $B^+_{\rm sat} = 1$ which separates the mirror stable (above the curve) from the mirror unstable domain. The figure shows that for reasonably weak anisotropies of the proton distribution the saturation amplitude increases with $\beta_\parallel$ and $T_\perp/T_\parallel$. For strong anisotropies $R \to 0$ we do not expect the model to be valid any longer as the growth rate would then be so strong that most of the circulating particles would not conserve energy which, of course, is against one of the basic assumptions of the model.

5. Saturation in the Low-Field Region and Overall Structure at Saturation

The explicit shape of the magnetic field profile has to be considered in the derivation of the plasma conditions in the low magnetic field region. Our purpose is to determine δB^- and λ, which are defined in Figure 1, such that the resulting structure is a stable equilibrium. Stability of the structure requires that the total pressure is the same at field minimum and field maximum [*Kivelson and Southwood*, 1996]. In this section we shall use a pressure balance condition in order to compute the complete macroscopic state of the plasma at saturation.

The density ratio $\eta \equiv n^-/n^+$ (where the density n^- includes both trapped and circulating particles) is, besides the magnetic field profile, one of the most easy to measure quantity that characterizes a magnetic hole [e.g., *Winterhalter et al.*, 1994]. Given n^+ from (4) and λ which will be determined later using the pressure balance condition (12), η must necessarily satisfy to the following condition

$$\eta \equiv n^-/n^+ = [1 - (1-\lambda)n^+]\lambda/n^+. \tag{9}$$

In fact, this expression is consistent with the requirement $n^-\lambda + n^+(1-\lambda) = 1$ which ensures that the total number of particles in the system is conserved. Let us now compute the total number of particles that are trapped for a given field strength δB^+. This number, denoted $N_{\rm tr}$, includes all particles that do not verify the inequality (3). Thus

$$\frac{N_{\rm tr}}{N_0} = \int\limits_{|v_{0\parallel}|<v_{0\perp}\sqrt{\delta B^+}} f_0\, dv_0^3 = \left(\frac{\delta B^+}{R+\delta B^+}\right)^{1/2} \tag{10}$$

where N_0 is the total number of particles in the system. The total number of circulating particles is then simply given by

$$N_{\rm circ} = N_0 - N_{\rm tr}. \tag{11}$$

Let us now come to the determination of λ. We start by writing the pressure balance condition for our system. Given the simplicity of the configuration, we are considering here the latter reduces to a balance between the pressure (particle + field) in the high magnetic field region and the pressure in the low magnetic field region. Using the above normalization, this can be written in the following way

$$p^+_{\perp,\rm tot} = p^-_{\perp,\rm circ} + p^-_{\perp,\rm tr} + (B^-)^2/\beta_\parallel \tag{12}$$

where $p^-_{\perp,\rm circ}$ and $p^-_{\perp,\rm tr}$ are the pressure of the circulating and the trapped particles in the magnetic wells, respectively. In reality, since B^- is related to λ through (2), (12) is nothing else but an equation for λ. However, in order to solve (12) we need to determine the dependence on λ of $p^-_{\perp,\rm circ}$ and $p^-_{\perp,\rm tr}$. For this purpose we observe that the contribution to the pressure coming from one single particle is proportional to B so that $p^-_{\perp,\rm circ}$ and $p^-_{\perp,\rm tr}$ are both proportional to B^-. On the other hand, the pressure of a given population changes proportionally to the spatial size of the domain occupied by the population. In order to make things simple we suppose that all the populations we are going to consider below are distributed uniformly at $t = 0$. This is reasonable for two reasons. First, at $t = 0$ the distribution of the sum of all proton populations is given by the distribution function (1). Second, the growth of the instability is slow compared to the time it takes for a particle to cross the system. The latter means that two particles with nearly the same velocity and the same position at time t originate, in general, from two completely different positions at $t = 0$; that is, the memory of the initial position is lost. Stated differently, one can say that a particle located near a given position at time t was with the same probability located in the vicinity of any of the points in the interval $[0, 1]$ at $t = 0$. As a consequence, we

may assume that the population of trapped particles covers uniformly the whole domain $[0, 1]$ at $t = 0$ but that this same population is confined to the domain $[0, \lambda]$ at time t. Summarizing these considerations, we conclude that the pressure contribution due to the trapped particles at time t must be given by

$$p^-_{\perp,\mathrm{tr}} = p_{0\perp,\mathrm{tr}}\, B^-/\lambda \tag{13}$$

where $p_{0\perp,\mathrm{tr}}$ is the trapped particles' pressure at $t = 0$, that is,

$$\begin{aligned} p_{0\perp,\mathrm{tr}} &= \int_{|v_{0\parallel}|<v_{0\perp}\sqrt{\delta B^+}} v_{0\perp}^2\, f_0\, 2\pi v_{0\perp} dv_{0\perp} dv_{0\parallel} \\ p_{0\perp,\mathrm{tr}} &= \left(\frac{\delta B^+}{R+\delta B^+}\right)^{1/2} \left[\frac{3R+2\delta B^+}{2R(R+\delta B^+)}\right]. \end{aligned} \tag{14}$$

An argument, similar to the one for trapped particles, applies to the circulating particles. Suppose that the circulating particles, located in the low magnetic field region at time t, cover a fraction α of the domain $[0, 1]$ at $t = 0$. According to the above discussion, α must be the same as the ratio of the number of circulating particles located in the magnetic well at time t to the total number of circulating particles. Since the total number of particles which are located in the high-field region at time t is $n^+(1-\lambda)$, one has $\alpha = [N_{\mathrm{circ}} - n^+(1-\lambda)]/N_{\mathrm{circ}}$ which leads to

$$\begin{aligned} p^-_{\perp,\mathrm{circ}} &= p_{0\perp,\mathrm{circ}}\, \alpha B^-/\lambda \\ p^-_{\perp,\mathrm{circ}} &= \left(\frac{1}{R} - p_{0\perp,\mathrm{tr}}\right)\frac{\alpha B^-}{\lambda}. \end{aligned} \tag{15}$$

We can now express (12) as a function of the known quantities $\beta_\parallel$, R, $\delta B^+_{\mathrm{sat}}$ and the remaining unknown parameter λ. This leads to a polynomial equation of degree three for λ. Physically acceptable solutions must be real and in the interval $[0, 1]$. Only two solutions, shown in Figure 5, satisfy these requirements in the domain in parameter space $(\beta_\parallel, R)$ below the mirror instability threshold curve and outside the shaded domain. Elsewhere (above the mirror instability threshold curve and in the shaded domain) the two solutions are complex so that no equilibrium solution exists there. In the domain where the two roots are real their value is generally smaller then 0.5, suggesting that the mirror instability tends to form narrow low magnetic field regions rather than the opposite. This is in qualitative agreement with most observations [*Winterhalter et al.*, 1994]. However, even though observations seem to indicate that the nonlinear evolution of the mirror instability leads to narrow and deep holes in the magnetic field, it sometimes happens that the opposite situation is observed. One such case is illustrated by Figure 2a in the *Leckband et al.* [1995] paper. The figure shows large nonlinear fluctuations of the magnetic field observed in the Earth's magnetosheath. The fluctuations can be described as a more or less irregular sequence of narrow magnetic field spikes. Even this particular episode is consistent with the results of the model. In fact, the plasma β, measured by Leckband et al., was exceptionally large ($\beta \approx 30$). If we put the value $\beta_\parallel = 20$ in our model we find that the stable solution, shown in Figure 5a for the domain $\beta_\parallel < 10$ predicts that λ is larger than 0.5, provided the initial temperature anisotropy is not too weak, that is $R \lesssim 0.5$.

Let us come back to the discussion of (12). Even though the two physically acceptable solutions of (12) correspond to possible equilibrium solutions, only one is a stable solution (Figure 5a). Figure 5b corresponds to a solution with $\partial p^-_{\perp,\mathrm{tot}}/\partial B^- < 0$ (at saturation), that is, the total pressure and the magnetic pressure vary in antiphase in the low-field region. Thus only Figure 5a corresponds to a totally stable equilibrium for the final configuration. We note, however, that the two solutions become identical on the border of the shaded region and that they become both vanishing small as one approaches the instability threshold from below.

Figure 6 is a contour plot of the density ratio η of the low to high magnetic field region densities (equation (9)). The figure shows that for reasonable anisotropies $R \gtrsim 0.4$ the values for η do not exceed 2.5 which is consistent with

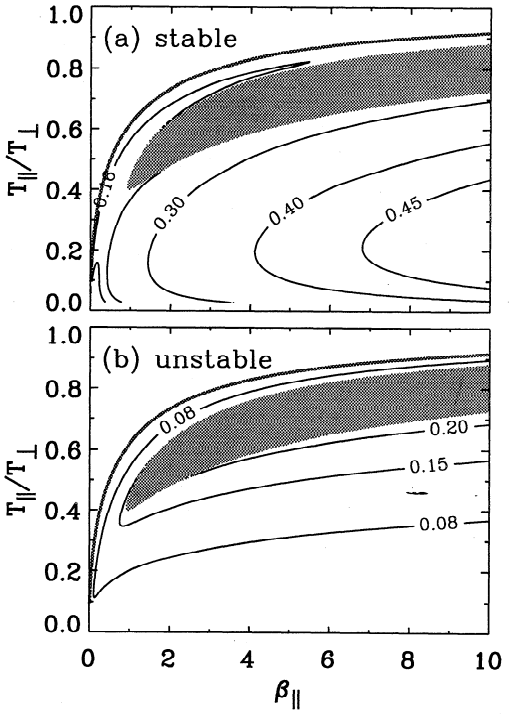

Figure 5. Contours for the two positive solutions λ of (12). The solutions become complex conjugate above the mirror mode stability threshold and in the shaded region where no stable solutions exist. (a) Stable solution with $\partial p^-_{\perp,\mathrm{tot}}/\partial B^- < 0$. (b) Unstable solution with $\partial p^-_{\perp,\mathrm{tot}}/\partial B^- > 0$.

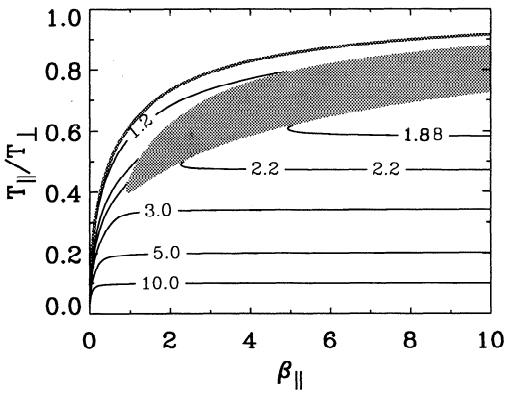

Figure 6. Contours of the density ratio n^-/n^+ computed using (9) for the case where λ is the stable solution of Figure 5a.

the typical values observed in the solar wind by *Winterhalter et al.* [1994]. Concerning the fact that observed values for η seem to be closer to unity than what may eventually suggest our model, it should be pointed out here that all the above results are valid in the case of a cold electron population such that its temperature T_e is much smaller than the parallel proton temperature, that is, $T_e \ll T_{\parallel}$. Electron temperature effects have been shown to play an important role in the linear mirror instability [*Pantellini and Schwartz*, 1995]. In particular, a hot electron population significantly reduces the absolute value of the parallel compressibility (a measure of the density fluctuations compared to the magnetic field fluctuations) in a plasma with $T_e \gtrsim T_{\parallel}$. We therefore expect the electron temperature effects to act in the sense of reducing the value of η shown in Figure 6. Still, it should be noted that even in the cold electrons framework it is possible to obtain relatively small values of η associated with narrow and deep holes. For example, the case $\beta_{\parallel} = 2$ and $R = 0.65$ (weakly unstable) leads to the stable asymptotic state characterized by $\lambda_{\rm sat} = 0.17$, $\delta B^+_{\rm sat} = 0.12$ and $\delta B^-_{\rm sat} = 0.59$, which represents a noticeable magnetic hole, while the associated density ratio $\eta = 1.34$ is rather small.

Let us conclude this section with a comment concerning the validity of the presented model. The most important restriction comes from the fact that the circulating particles are supposed to conserve energy. As already stated above, this cannot be true for particles located near the velocity space trapping boundary. Thus in cases where the number of circulating particles that do not conserve energy is large (e.g., in the case of fast growth of the instability), the model is certainly inappropriate. In order to estimate the domain of validity of the model, let us suppose that during the time of growth of the instability the maximum growth rate is $\gamma = 2\pi/t_{\rm growth}$. This growth rate is likely to be the growth rate predicted by linear theory, as in the nonlinear phase of the instability growth tends to become smaller as the instability saturates. On the other hand, at saturation, in the high-field region, a circulating particle that conserves energy has a field-aligned velocity given by $v_{\parallel} = \sqrt{v_{0\parallel}^2 - v_{0\perp}^2 \delta B^+_{\rm sat}}$. If $v_{\parallel}$ is large enough, so that the time it takes for the particles to cross the high-field region is shorter than the typical growth time $t_{\rm growth}$, the assumption of energy conservation is a good approximation. This leads immediately to the condition $v_{\parallel} > \gamma(1-\lambda)/(2\pi)$. Since linear theory provides a value for γ, but not for λ, we may use the more restrictive condition $\sqrt{v_{0\parallel}^2 - v_{0\perp}^2 \delta B^+_{\rm sat}} > \gamma/(2\pi)$ which states that only particles with an initial parallel velocity within $\gamma/(2\pi)$ from the separatrix do not conserve energy. Note that for small $\delta B^+_{\rm sat}$ the above condition is the same condition that distinguishes circulating from resonant particles in the linear mirror instability [*Southwood and Kivelson*, 1993].

6. Discussion

We have presented a model for the formation of stable nonpropagating structures in a collisionless magnetized plasma. The model is based on the fact that in a plasma with cold electrons and a bi-Maxwellian proton distribution with $T_{\perp} > T_{\parallel}$ the total pressure responds in antiphase to a low-frequency compressional perturbation of the magnetic field provided the criterion for the mirror instability is satisfied. Saturation is assumed to occur when the magnetic pressure and the total pressure of the plasma start varying in phase. The model is in fact a model of the nonlinear mirror instability where saturation is the consequence of particle trapping in the low magnetic field regions of the evolved structure.

The model is similar to the one proposed by *Kivelson and Southwood* [1996] in that the saturated state is one where the total pressure is the same for both the high and the low magnetic field region. The main difference stems from the fact that in our model a particular magnetic field profile, shown in Figure 1, has been chosen. Compared to the more general, but essentially qualitative, model of Kivelson and Southwood, our model has the advantage of providing quantitative estimates of the characteristics of the evolved structure (Figures 4 to 6).

The basic conclusion of the Kivelson and Southwood analysis is that cooling of the trapped particles, which is needed to reach pressure equilibrium, is likely to result from a mixture of betatron and Fermi deceleration. A quantitative estimate of the final state is not possible in their case as the evolution of the instability does in general depend on the unknown temporal and spatial variations of the magnetic field profile. The simplifications in our model are such that the temporal evolution of the field becomes unimportant and the final structure can in general be computed unambiguously as a function of the initial plasma conditions only. Moreover, the detailed behavior of the trapped particles, which may be rather complicated, does not need to be known.

The main results can be summarized as follows. First of all, a simple expression for the saturation level of the nonlinear mirror instability is found. As shown in Figure 4, the saturation level generally increases with both $\beta_{\parallel}$ and the temperature anisotropy $T_{\perp}/T_{\parallel}$. We also observe that a stable final solution can nearly always be found in the linearly un-

stable domain except in the narrow shadowed domain shown in Figures 4-6. A more general treatment of the instability (allowing for structures other than the one shown in Figure 1) as the one discussed by *Kivelson and Southwood* [1996] may probably lead to a stable final state even in the shadowed domain shown in our figures. We have argued that finite electron temperature effects, that have been shown to be important in linear theory, may also significantly modify the final equilibrium configuration. As suggested by *Kivelson and Southwood* [1996], we observe that substantial cooling of the particles in the magnetic wells is generally necessary in order to reach the final equilibrium solution. Thus the evolved structure tends to be one where the low magnetic field regions are narrower than the high magnetic field regions unless the plasma β is very high (i.e., $\beta \gtrsim 10$). Narrow wells also mean deep wells which seems to agree with the majority of the observed magnetic holes wherein magnetic field intensities as low as 10% of the out of hole value are not unusual [e.g., *Winterhalter et al.*, 1994]. The model suggests that the holes are narrowest in plasma that are marginally unstable and predicts that the particle density is always higher in the magnetic holes than in surrounding plasma, which is consistent with observation. Finally, since our results are independent of the amount of Fermi acceleration (or deceleration) that affects the trapped particles, we conclude that the most important mechanism leading to saturation is the betatron cooling of the trapped protons.

Further improvements of the model may be obtained rather easily by including electron temperature effects. The treatment of more general field profiles, compared to the one used here, may not be possible without making the model considerably more complicated. Particle simulations of the type published by *McKean et al.* [1992, 1993] may help in better understanding the details of the formation of magnetic holes whereas full particle simulations (including the electron dynamics) would be extremely useful in order to determine whether or not the high-frequency waves (for example, the so-called lion roars [*Tsurutani et al.*, 1982]), frequently observed in magnetic holes, are effectively due to the electron cyclotron instability as suggested by *Lee et al.* [1987]. Particle simulations will also be needed to understand the effects on the formation of stable structure due to finite Larmor radius effects. Our model as well as the *Kivelson and Southwood* [1996] one are both based on the hypothesis of magnetic moment conservation for all particles. It is clear that such an approximation will fail in the case of strong instabilities where the most unstable wavelength becomes of the order of the proton Larmor radius with a typical growth rate comparable to the Larmor frequency. The complexity of the particles' motion in a field where the typical spatial and temporal scales are of the order of the Larmor scales is such that only numerical simulations may help farther under these conditions.

Acknowledgments. I thank R. J. MacDowall for useful comments. The Editor thanks D. Winterhalter and another referee for their assistance in evaluating this paper.

References

Anderson, B.J., and S.A. Fuselier, Magnetic pulsations from 0.1 to 40 Hz and associated plasma properties in the Earth's subsolar magnetosheath and depletion layer, *J. Geophys. Res., 98*, 1461, 1993.

Barnes, A., Collisionless damping of hydromagnetic waves, *Phys. Fluids, 9*, 1483, 1966.

Fitzenreiter, R.J., and L.F. Burlaga, Structure of current sheets in magnetic holes at 1 AU, *J. Geophys. Res., 83*, 5579, 1978.

Glassmeier, K.-H., U. Motschmann, C. Mazelle, F.M. Neubauer, K. Sauer, S.A. Fuselier, and M.H. Acuna, Mirror modes and fast magnetoacoustic waves near the magnetic pileup boundary of comet P/Halley, *J. Geophys. Res., 98*, 20955, 1993.

Hasegawa, A., Drift mirror instability in the magnetosphere, *Phys. Fluids, 12*, 2642, 1969.

Hubert, D., C. Perche, C.C. Harvey, C. Lacombe, and C.T. Russell, Observation of mirror waves downstream of a quasi–perpendicular shock, *Geophys. Res. Lett., 16*, 159, 1989.

Kaufmann, R.L., J.T. Horng, and A. Wolfe, Large-amplitude hydromagnetic waves in the inner magnetosheath, *J. Geophys. Res., 75*, 4666, 1970.

Kivelson, M.G., and D.J. Southwood, Mirror instability, 2, The mechanism of nonlinear saturation, *J. Geophys. Res., 101*, 17365, 1996.

Klein, L., and L.F. Burlaga, Interplanetary sector boundaries 1971-1973, *J. Geophys. Res., 85*, 2269, 1980.

Lacombe, C., F.G.E. Pantellini, D. Hubert, C.C. Harvey, A. Mangeney, G. Belmont, and C.T. Russell, Mirror and Alfvénic waves observed by ISEE1–2 during crossing of the Earth's bow shock, *Ann. Geophys., 10*, 772, 1992.

Leckband, J.A., D. Burgess, F.G.E. Pantellini, and S.J. Schwartz, Ion distributions associated with mirror waves in the Earth's magnetosheath, *Adv. Space Res., 15*, 345, 1995.

Lee, L.C., C.S. Wu, and C.P. Price, On the generation of magnetosheath lion roars, *J. Geophys. Res., 92*, 2343, 1987.

McKean, M.E., D. Winske, and S.P. Gary, Mirror and ion cyclotron anisotropy instabilities in the magnetosheath, *J. Geophys. Res., 97*, 19421, 1992.

McKean, M.E., S.P. Gary, and D. Winske, Kinetic physics of the mirror instability, *J. Geophys. Res., 98*, 21313, 1993.

Pantellini, F.G.E., and S.J. Schwartz, Electron temperature effects in the linear proton mirror instability, *J. Geophys. Res., 100*, 3539, 1995.

Price, C.P., D.W. Swift, and L.C. Lee, Numerical simulation of nonoscillatory mirror waves at the Earth's magnetosheath, *J. Geophys. Res., 91*, 101, 1986.

Russell, C.T., W. Riedler, K. Schwingenshuh, and Y. Yeroshenko, Mirror instability in the magnetosphere of Comet Halley, *Geophys. Res. Lett., 14*, 664, 1987.

Shapiro, V.D., and V.I. Shevchenko, Quasilinear theory of instability of a plasma with an anisotropic ion velocity distribution, *Sov. Phys. JETP, Engl. Transl., 18*, 1109, 1964.

Southwood, D.J., and M.G. Kivelson, Mirror instability, 1, The physical mechanism of linear instability, *J. Geophys. Res., 98*, 9181, 1993.

Tajiri, M., Propagation of hydromagnetic waves in collisionless plasma, 2, Kinetic approach, *J. Phys. Soc. Jpn., 22*, 1482, 1967.

Tsurutani, B.T., E.J. Smith, R.R. Anderson, K.W. Ogilvie, J.D. Scudder, D.N. Baker, and S.J. Bame, Lion roars and nonoscillatory drift mirror waves in the magnetosheath, *J. Geophys. Res., 87*, 6060, 1982.

Tsurutani, B.T., D.J. Southwood, E.J. Smith, and A. Balogh, Nonlinear magnetosonic waves and mirror mode structures in the March 1991 Ulysses interplanetary event, *Geophys. Res. Lett., 19*, 1267, 1992.

Turner, J.M., L.F. Burlaga, N.F. Ness, and J.F. Lemaire, Magnetic holes in the solar wind, *J. Geophys. Res., 82*, 1921, 1977.

Violante, L., M.B. Bavassano Cattaneo, G. Moreno, and J.D. Ri-

chardson, Observations of mirror waves and plasma depletion layer upstream of Saturn's magnetopause, *J. Geophys. Res., 100*, 12047, 1995.

Winterhalter, D., M. Neugebauer, B.E. Goldstein, E.J. Smith, S.J. Bame, and A. Balogh, Ulysses field and plasma observations of magnetic holes in the solar wind and their relation to mirror-mode structures, *J. Geophys. Res., 99*, 23371, 1994.

Filippo Pantellini, Département de Recherche Spatiale, Observatoire de Paris–Meudon, 5 Place Jules Janssen, 92195 Meudon Cedex, France. (e-mail: Filippo.Pantellini@obspm.fr)

(Received February 17, 1997; revised August 15, 1997; accepted August 18, 1997.)

5 Un modèle didactique pour simuler un gaz dans un champ gravitationnel

AjP 61-68, 4789-4798 (1998)

A simple numerical model to simulate a gas in a constant gravitational field

Filippo G. E. Pantellini
Département de Recherche Spatiale, Observatoire de Paris-Meudon, Meudon, France

(Received 24 August 1998; accepted 29 April 1999)

The equilibrium pressure of a perfect gas in a constant gravitational field decreases exponentially with height. This result, known as the barometric formula, can be observed in a one-dimensional numerical simulation where the gas molecules are represented by colliding massive points. © *2000 American Association of Physics Teachers.*

I. INTRODUCTION

It was in 1686 that the English astronomer Edmund Halley[1] first recognized that the pressure p of the Earth's atmosphere decreases exponentially with height z in good agreement with the so-called barometric formula

$$p(z)=p(0)\exp\left(-\frac{z}{H}\right), \tag{1}$$

where the constant H is the scale height of the atmosphere. A number of derivations of the barometric formula and its amazing history, from antiquity to the twentieth century, have already been discussed in another paper[2] and shall not be repeated here. Still, a short discussion of the main ingredients that go into most derivations of the barometric formula may be welcome here. The standard derivations based on fluid theories[3] postulate the existence of a particular equation of state relating the pressure p and the mass density ϱ of the fluid atmosphere. For gaseous atmospheres it is quite natural to invoke the perfect gas equation,

$$p=\varrho\frac{kT}{m}, \tag{2}$$

where m is the mass of the gas molecules, k the Boltzmann constant, and T the temperature. This equation on its own still doesn't allow the derivation of the barometric formula, as one needs a second equation in order to fully specify the thermodynamic state of the system. In the absence of any external energy source, the second equation that imposes itself quite naturally is

$$T=\text{constant}, \tag{3}$$

which states that the temperature is the same everywhere in the atmosphere. But why should a stratified fluid, say a perfect gas for simplicity, be isothermal whereas the pressure, the density, and even the entropy depend on z? For instance it is extremely well known that Eq. (3) is not true for the low Earth atmosphere (the troposphere) where the temperature typically decreases with height at a rate of 10^{-2} K/m. Of course, the temperature gradients in the Earth atmosphere are a consequence of the fact that the system is not a closed one due to the energy input through radiation from both the Sun and the Earth surface. It is possible to make (3) a plausible assumption at least in the case where the collisional mean free path of the molecules (i.e., the average distance that particles travel between two successive collisions) is small compared to the scale of variation of the macroscopic quantities such as the density or the pressure. In this case the local particle velocity distribution must be very nearly a Maxwellian with zero mean velocity which, for a local number density $n(z)=\varrho(z)/m$, reads

$$f(z,v)=n(z)\left(\frac{m}{2\pi kT}\right)^{3/2}\exp\left(-\frac{mv^2}{2kT}\right), \tag{4}$$

i.e., the atmosphere must be static. The requirement that the mean velocity be zero is easily justified since a nonzero mean velocity implies a mass flux that cannot be compatible with a stationary solution. For example, the density near the ground would be increasing or decreasing depending on whether a downward or an upward net flow is present in the atmosphere. As we will show below, if the distribution is Maxwellian at a given height, it must be Maxwellian, with the same temperature, at any other height, provided the atmosphere is a static one. This is the justification of the isothermal hypothesis from the kinetic point of view.

From a fluid point of view, one can justify the choice of a constant temperature by noting that if there were a temperature gradient somewhere in the atmosphere, there would inevitably be an energy flux (or heat flux) from the higher temperature to the lower temperature region and the system could neither be static nor stationary. However, this explanation does not seem to be consistent with our everyday experience of the Earth atmosphere, which is essentially static but never, not even nearly, isothermal.

If we accept the isothermal hypothesis as a plausible one, it is easy to derive the barometric formula using a fluid approach. In a static atmosphere, subject to a constant gravitational field $g>0$, the pressure p at a given height z is just the force exerted by the mass of gas above that height per square unit, i.e.,

$$p(z)=-g\int_z^\infty \varrho(z)dz, \tag{5}$$

where the minus sign comes from the fact that gravity is taken to be oriented toward the negative z direction. It then follows that the pressure difference $dp(z)$ between two points at height z and $z+dz$ is simply given by

$$dp(z)=p(z)-p(z+dz)=-g\varrho(z)dz, \tag{6}$$

which clearly indicates that pressure cannot be uniform in the system unless $g=0$. From the perfect gas equation of state (2) and Eq. (3), the barometric formula (1) with a scale height

$$H=\frac{kT}{mg} \tag{7}$$

is readily obtained by integrating the differential equation (6).

Besides the fluid derivations of the barometric formula, there are a number of derivations called kinetic. The latter are characterized by the fact that the physical state of the system (the atmosphere) is specified by the distribution function $f(t,\mathbf{r},\mathbf{v})$ of the gas molecules, $\mathbf{r}\equiv(x,y,z)$ and $\mathbf{v}\equiv(v_x,v_y,v_z)$ being the three-dimensional position and velocity vectors, respectively. In a kinetic description, $f(t,\mathbf{r},\mathbf{v})\,d^3r d^3v \equiv f(t,\mathbf{r},\mathbf{v})dx\,dy\,dz\,dv_x\,dv_y\,dv_z$ represents the number of particles that at time t are located in the six-dimensional phase space volume $d^3r d^3v$ centered on the phase space point ($\mathbf{r}$, $\mathbf{v}$). An elegant kinetic derivation of the barometric formula, which has not been discussed by Berberan-Santos *et al.*,[2] has been given by Becker in his classical book on thermodynamics.[4] The derivation is based on the fact that the number of particles in a volume $d^3r_0 d^3v_0$ at time t_0 is the same as the number of particles in the same volume (transported along particles' trajectories in phase space) $d^3r d^3v$ at a later time $t>t_0$, formally

$$f(t_0,\mathbf{r}_0,\mathbf{v}_0)d^3r_0 d^3v_0 = f(t,\mathbf{r},\mathbf{v})d^3r d^3v. \tag{8}$$

In the case of a constant gravitational field, the equations of motion, $dz/dt=v_z$ and $dv_z/dt=-g$, can be integrated for a small time interval τ leading to

$$z = z_0 + v_{0z}\tau, \tag{9}$$

$$v_z = v_{0z} - g\tau. \tag{10}$$

These equations show that the infinitesimal phase space volumes $dz\,dv_z$ and $dz_0\,dv_{0z}$ are identical. On the other hand, since gravity doesn't affect the velocity components perpendicular to the z axis, one has $dx\,dy\,dv_x\,dv_y = dx_0\,dy_0\,dv_{0x}\,dv_{0y}$, meaning that the phase space volume $d^3r d^3v$ is not modified during its motion along particles' trajectories in phase space. As a consequence, and because we assume that the system only depends on z, we can write a linearized form of Eq. (8), for small time intervals τ,

$$\begin{aligned} F(t,z,v_z) &= F(t_0+\tau, z_0+v_{0z}\tau, v_{0z}-g\tau) \\ &\simeq F(t_0,z_0,v_{0z}) + \frac{\partial F}{\partial t}\tau + \frac{\partial F}{\partial z}v_{0z}\tau - \frac{\partial F}{\partial v_z}g\tau, \end{aligned} \tag{11}$$

where F represents the reduced distribution that is obtained after integration of f over both velocity components v_x and v_y. Since, according to (8) and the ensuing discussion, $F(t,z,v_z)$ and $F(t_0,z_0,v_{0z})$ must be equal and since we are seeking stationary solutions, such that $\partial F/\partial t=0$, Eq. (11) reduces to a simple differential equation involving partial derivatives of z and v_z only,

$$\frac{\partial F}{\partial z}v_z - \frac{\partial F}{\partial v_z}g = 0. \tag{12}$$

The general solution of this differential equation is an arbitrary function of energy (gravitational energy+kinetic energy), i.e.,

$$F(z,v_z) = F(gz + \tfrac{1}{2}v_z^2). \tag{13}$$

This solution clearly shows that if the velocity distribution function is Maxwellian at a given height z_0, it must be Maxwellian, with the same temperature, at any other height, i.e.,

$$F(z,v_z) = n_0\left(\frac{m}{2\pi kT}\right)^{1/2}\exp\left(-\frac{mgz+mv_z^2/2}{kT}\right), \tag{14}$$

where n_0 is the particle number density at $z=0$. As expected, integration in velocity space of (14) leads to the exponentially decreasing density profile

$$n(z) = n_0\exp\left(-\frac{mgz}{kT}\right), \tag{15}$$

which is nothing else but the barometric formula for an isothermal perfect gas. The main assumption of this derivation of the barometric formula is that the particles' velocity distribution is Maxwellian at some height. As already stated, this is a reasonable assumption for a static atmosphere, at least as long as the mean free path is small compared to the scale height H.

II. THE NUMERICAL MODEL

Numerical simulations do often offer the best illustration of the behavior of a physical system. The aim of Sec. II is precisely the description and the discussion of a simple numerical model describing the evolution of a sort of hard sphere gas under the influence of a constant gravitational field. As we will see below, the model allows for an ''experimental'' derivation of the barometric formula thus completing the discussion of Sec. I.

Again we consider the case of a constant gravitational field pointing toward the negative z direction. We model the static atmosphere by considering the statistical properties of N identical free falling massive point particles. We use a one-dimensional approximation so that the position of each particle is fully specified by its height z above the ground level located at $z=0$. Two particles are supposed to interact via an elastic collision if they are simultaneously located at the same height. A particle hitting the ground simply rebounds elastically. Despite the fact that the particles' motion is restricted to one spatial dimension and in order to introduce ergodicity in the system (see below), we allow the particles to have three-dimensional velocities. One can regard the system as being spatially three dimensional with periodic x and y directions, the periodicity length being vanishingly small.

Similar numerical models, involving colliding spheres or discs instead of points, have already been used some 20 years ago, though not in the case of a gas in a gravitational field.[5–9]

A. Ergodicity

In 1887 L. Boltzmann formulated his famous ''Ergodenhypothese.''[10] Boltzmann's hypothesis, which has been put into a mathematically rigorous form by P. and T. Ehrenfest,[11] states that the phase space trajectory of a closed thermodynamical system covers densely and uniformly the subspace (a hypersurface in phase space) defined by the condition that the energy E of the system is constant. A classical dynamical system, e.g., a system of N particles governed by Hamilton's equations of motion (which is generally called a thermodynamical system in the limit $N\to\infty$), that has this property is said to be ergodic. Later, starting in 1922, G. D. Birkhoff[12] proved the important theorem according to which ergodicity implies that the long time average over an arbitrary function of the phase space coordinates is equal to the average of the same function taken over all possible, and (as can be shown[4])

equally probable, states that the system can go through. Possible functions of the phase space coordinates one may want to take averages of are the number density $n(z)$, the pressure $p(z)$, or any other macroscopic quantity. The average over the collection of all states on the energy hypersurface is called the average over the microcanonical ensemble.[4] It should be noted that the time average and the average over the microcanonical ensemble may be considered to be equal for practical purposes only if the time of averaging is long enough for the system's trajectory to cover densely the hypersurface of constant energy E. In practice, one has just to wait long enough for the functions that describe the macroscopic state of the system (we are not interested in the trajectories of individual particles) to become independent of the time interval used in the averaging process. One may then say that the system has reached equilibrium.

In general, one can estimate the minimum time of averaging needed for the system to cover uniformly the surface of constant energy to be of the order of a macroscopic relaxation time. For example, in the case of a large number N of molecules with mean energy $3kT/2$ restricted to a three-dimensional cubic box of dimension L^3, the relaxation time can be estimated to be of the order of the box scale length L divided by the sound velocity $c \sim \sqrt{kT/m}$.

The justification of Boltzmann's ''Ergodenhypothese'' may now become clear if one asks what happens to a system that is nonergodic. By definition in such a case the system's phase space trajectory does not cover the whole hypersurface of constant energy. This means that for two different initial conditions the system's trajectory generally covers different parts of the energy surface leading to different temporal averages even if one lets the time of averaging become infinitely long. In such a system there is no longer a unique equilibrium state since different initial conditions will lead to different equilibrium states. It is now intuitively clear that a nonergodic dynamical system is not a good model for a thermodynamic system, as the latter should evolve toward a unique equilibrium that is independent of the initial conditions. This is of course what we expect a thermodynamic system to do based on the second principle according to which the system must evolve toward a unique state that maximizes entropy.[7,8,13]

Let's come back to our model of the atmosphere and let's suppose first that the trajectory of the N particles is strictly one-dimensional, i.e., position and velocity are both one-dimensional vectors. In this case the time evolution of the system is represented by a curve in a $2N$-dimensional phase space. Now, in the case of one-dimensional velocities, the result of an elastic collision between two particles j and k is nothing else but the exchange of velocities $v_k \leftrightarrow v_j$. This configuration is of the type depicted in Fig. 1(a), where the balls, within an infinite vertical tube of the same diameter as the balls, are not allowed to have a velocity component in the horizontal direction. In this case the net result of a collision is the same as if the particles would simply go through each other without any interaction. One may consider the system as being made of N noninteracting particles just bouncing periodically off the ground. In that particular case each particle conserves energy separately and the system is therefore characterized by N constants (or integrals) of motion, meaning that its trajectory in phase space is bounded to a $2N-N=N$-dimensional subspace. Thus, if $N>1$, the dimension of the subspace covered by the system's trajectory is smaller than the $2N-1$ dimensions of the hypersurface of constant energy. The conclusion is that not all points of the latter can be approached by the system's trajectory in phase space so that the ergodic condition cannot be satisfied.

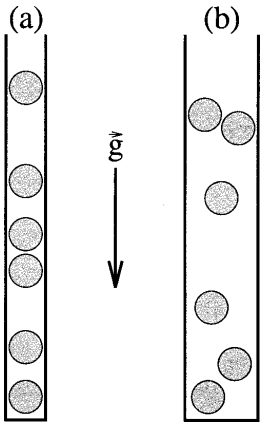

Fig. 1. System of hard balls in an infinitely long tube under the influence of gravity. (a) The balls' diameter and the tube diameter are identical: The system is nonergodic. (b) The balls' diameter is less than half the tube's diameter so that the balls can pass each other and can have horizontal velocities: The system is ergodic and is analogous to the model presented in Sec. II.

In the case of three-dimensional velocities, it is no longer possible to consider that each particle in the system separately conserves energy. This situation is similar to Fig. 1(b), where the balls are contained in a tube of cross section large enough for the balls to pass each other and where the balls can therefore have nonzero velocity components in the horizontal direction.[14] The only integral of motion in that case is the energy E, and the system is reminiscent of the hard sphere Boltzmann gas that has been shown to be ergodic, and approaching equilibrium, for as few as two particles.[15] The fact that the system is already ergodic for two particles shows that one does not need to approach the thermodynamic limit $N \to \infty$ in order to model a gas in a box. This is the main reason for choosing a small number of particles in the example in Sec. II E. A convincing illustration of the ergodicity of a low dimensional dynamical system, which is similar to the one presented in this paper, is the case of the motion of disks in a stadium-shaped billiard table.[9]

We shall conclude this section by noting that the nonergodicity of the system depicted in Fig. 1(a) is primarily due to the fact that all the balls in the system are of equal mass. Thus, as pointed out by Sauer,[6] it is possible to make the system in Fig. 1(a) ergodic by simply choosing the mass to be different for neighboring balls and for a number of balls larger than two.[16] The consequence is that collisions no longer reduce to a simple interchange of velocities and one may no longer consider the system as being made of N noninteracting particles just going through each other and individually conserving energy. Again there is only one (the total energy) and not N integrals of the motion and the system is ergodic.

The interested reader may find the historical bibliography

along with the proofs of the major theorems on the subject of this section in the review article by D. Ter Haar[17] and in Becker's course.[4]

B. Equations of motion

During the time interval between collisions (see Sec. II C) the particles are free falling. Their trajectories are thus determined by the integrated equations of motion for a particle in a constant gravitational field,

$$z(t)=z_0+v_{0z}t-gt^2/2, \tag{16}$$

$$v_z(t)=v_{0z}-gt, \tag{17}$$

$$\mathbf{v}_\perp(t)=\text{constant}, \tag{18}$$

where t indicates the time interval since the last collision and where $\mathbf{v}_\perp$ is the velocity of the particle perpendicular to the z axis.

C. Collisions

In order to make the model as simple at possible, we consider the atmosphere to be made of particles of equal mass m.[18] Two particles are supposed to interact (collide) when their respective world lines in space–time intersect each other. The collisions are elastic, i.e., both energy and momentum of the two-particle system are conserved.

One important difference between our model, where phase space has one spatial and three velocity dimensions, and the two ''Gedankenexperiments'' shown in Fig. 1 is that in the latter the particles' trajectories are fully deterministic while in the former they are not. The reason that the collisions in our model are nondeterministic is that there are six unknowns (the velocity components of the two particles after the collision) and only four equations (the energy conservation equation plus the three components of the momentum conservation equation). Thus, we need two more equations in order to fully specify the post-collision trajectories of the particles.

It is simplest to represent the collision using a spherical coordinate system in velocity space centered on center of mass velocity $\mathbf{v}_{\text{c.m.}}\equiv(\mathbf{v}_1+\mathbf{v}_2)/2$, where $\mathbf{v}_1$ and $\mathbf{v}_2$ are the velocities of the two colliding particles in the frame of reference of the static atmosphere. We define θ to be the angle with respect to the vertical direction (the z axis), ϕ the longitudinal angle (in the horizontal plane), and $u=|\mathbf{v}_1-\mathbf{v}_{\text{c.m.}}|=|\mathbf{v}_2-\mathbf{v}_{\text{c.m.}}|$ the particles' speed with respect to the center of mass. Figure 2 illustrates how the velocities $\mathbf{u}_{1,2}=\mathbf{v}_{1,2}-\mathbf{v}_{\text{c.m.}}$ of two colliding particles must change during the collision in order to preserve energy and momentum. Two parameters remain undetermined: the post-collision angles ϕ' and θ'. Since the model is rotationally invariant with respect to the vertical direction, we choose ϕ' at random in the interval $[0, 2\pi]$ so that the only parameter one really has to care about is θ'.

In order to get a physical insight into the problem of wisely choosing θ' in our model, let us come back to Fig. 1(b) and let us suppose that at any time both the height z and the velocity $\mathbf{v}$, but not the horizontal position, are known for all the balls in the tube. Given such an hypothesis, the post-collision angle θ' is undetermined exactly as in our model. For example, if we take the balls to be initially aligned vertically and having no horizontal velocity component, they must rebound vertically and the post-collision angle is therefore $\theta'=0$. On the other hand, if the same two balls are not aligned vertically, θ' can take any value >0 and $\leqslant\pi/2$ depending on the relative initial horizontal displacement of the two balls.

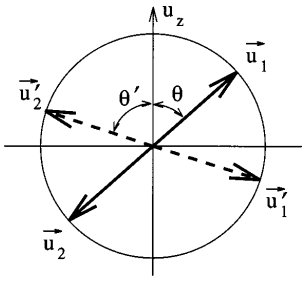

Fig. 2. Energy and momentum conserving collision of two particles of equal mass in the center-of-mass frame. Arrows denote velocities before (full arrow bodies) and after (dashed arrow bodies) the collision. Post-collision quantities are primed. Note that because of the axial symmetry of the model, the choice of the post-collision longitudinal angle ϕ' is arbitrary. The angle θ' is chosen according to Eq. (24).

The important point is that neither in the experiment depicted in Fig. 1(b) nor in our model are we actually interested in the kinematics of individual collisions. For this reason we shall base our strategy for choosing θ' on statistical considerations only. For example, we shall suppose that under the effect of a large number of collisions, our system relaxes toward a stationary state, i.e., toward a thermodynamic equilibrium. Given that such a state is by definition invariant under time reversal, we conclude that the differential probability distribution $dP(\theta)$ of observing a collision with a pre-collision angle θ in the angular range $[\theta,\theta+d\theta]$ must be equal to the differential probability distribution $dP(\theta')$ of observing a collision with a post-collision angle θ' in the same angular range.

Let us suppose that after some time the system has become stationary under the effect of collisions and let us concentrate on a small interval on the z axis. Let $f_R(\mathbf{v})$ be the particles' velocity distribution function within that interval. Now, since in our one-dimensional model $f_R(\mathbf{v})$ depends on the (not yet specified) angular distribution dP, we may choose f_R in order to constrain dP. Quite naturally we choose f_R to be an isotropic function of velocity in the center-of-mass frame of reference. Because this assumption implies that there are no privileged directions in velocity space, it follows that the distribution of the particles' relative velocity $\boldsymbol{\mu}$ given by

$$\tilde{f}_R(\boldsymbol{\mu})\equiv\frac{1}{n}\int f_R(\mathbf{v})f_R(\mathbf{v}-\boldsymbol{\mu})d^3v, \tag{19}$$

is also isotropic, i.e., $\tilde{f}_R=\tilde{f}_R(\mu)$, with $\mu=|\boldsymbol{\mu}|$. Now that we have chosen f_R we can compute the associated angular distribution $dP(\theta)$. In order to do so, we make the experiment of following a particle during a sufficiently long time that we can draw a complete histogram in the angle θ of the number of collisions experienced by the particle. Of course this histogram is nothing but the representation of the distribution $dP(\theta)$ we are seeking. Strictly speaking we can't perform this experiment since the scattering law has not yet been

specified. However, if after each collision we select the post-collision velocity of the test particle according to the distribution f_R, as if we were following a different particle after each collision, we ensure that its trajectory in velocity space is statistically representative of the trajectories of all other particles, i.e., its motion is ergodic and the relative velocities of all other particles are distributed according to $\tilde{f}_R(\mu)$. Now, since particles have to move relative to each other along the z axis in order to collide, it follows that the average number of collisions per time unit ν_c experienced by the test particle is given by the sum of the downward and the upward fluxes measured in the frame of reference of the test particle, i.e.,

$$\nu_c = \int \tilde{f}_R(\mu)|\mu_z| d^3\mu. \tag{20}$$

If we write Eq. (20) in spherical coordinates,

$$\nu_c = 4\pi \int_0^\infty \tilde{f}_R(\mu)\mu^3 d\mu \int_0^{\pi/2} \cos\theta \sin\theta \, d\theta, \tag{21}$$

it appears that the average number of collisions $d\nu_c(\theta)$ experienced by the test particle in the angular range $[\theta, \theta + d\theta]$ is given by

$$d\nu_c(\theta) = \left(4\pi \int_0^\infty \tilde{f}_R(\mu)\mu^3 d\mu \right) \cos\theta \sin\theta \, d\theta$$
$$= \text{constant} \times \cos\theta \sin\theta \, d\theta. \tag{22}$$

The important conclusion one draws from Eq. (22) is that the condition of isotropy for $\tilde{f}_R(\mu)$ implies that the angular probability distribution dP of observing a collision in the interval $[\theta, \theta + d\theta]$ is given by the relatively simple expression

$$dP(\theta) \propto \cos\theta \sin\theta \, d\theta. \tag{23}$$

We shall remember that this result is quite general as it is based on only two assumptions: (1) the system has one spatial and three velocity dimensions and (2) the relaxed velocity distribution is isotropic.

The probability $P(\theta)$ of observing a collision with an initial angle with respect to the vertical direction $\leqslant\theta$ is easily found by integrating Eq. (23). With the appropriate normalizations one obtains

$$P(\theta) = 1 - \cos^2\theta. \tag{24}$$

Since in the relaxed state the probability distributions for θ and θ' have to be identical, Eq. (24) provides the rule for choosing θ'. Thus, choose a random number P in the range $[0,1]$ and determine $\theta' \in [0, \pi/2]$ from Eq. (24) using this same P.

The essence of the whole discussion in this section resides in the conclusion that for the particles' velocity distribution function to relax toward an isotropic distribution, one has to choose the post-collision velocity of two interacting particles according to

$$|\mathbf{u}'_{1,2}| = |\mathbf{u}_{1,2}|, \tag{25}$$

$$\theta' = \arccos(\sqrt{P}) \quad \text{with} \quad P = \text{random number} \in [0,1], \tag{26}$$

$$\phi' = \text{random number} \in [0, 2\pi]. \tag{27}$$

D. The algorithm

We have now assembled all the elements that enter the algorithm, which goes as follows:

(1) Initiate the velocities $\{\mathbf{v}_0^i\}$ and the positions $\{z_0^i\}$ of N particles. Order the particles according to their height such that $z_0^1 < z_0^2 < \cdots < z_0^N$.

(2) Determine for each pair of neighboring particles, with indices i and $i-1$, the time interval t^i until their next collision, i.e., [according to (17)]

$$t^i = \frac{z_0^i - z_0^{i-1}}{v_{0z}^{i-1} - v_{0z}^i}, \quad i > 1,$$

where one should better set t^i to a very large number if the denominator becomes too small for t^i to be computed correctly. Particle $i=1$ is special in that its neighbor is in fact the ground level at $z=0$. That particle hits the ground after a time

$$t^1 = \frac{v_{0z}^1 + \sqrt{(v_{0z}^1)^2 + 2g z_0^1}}{g}.$$

(3) Find the shortest time interval $t_{\min}$ in the set $\{t^i > 0\}$ (i.e., the time interval until the next collision in the system) and store the index $I = i$ of the particle corresponding to that minimum.

(4) Advance all particles in the system using the equations of motion (16)–(18) through the time interval $t = t_{\min}$.

(5) Perform the collision between particle I and particle $I-1$ according to Eqs. (25)–(27). After the collision, choose particle I to be the one that has an upward directed velocity in the center-of-mass frame, so that the spatial ordering of the N particles remains unchanged. The case $I=1$ means that particle number 1 hits the ground. In this case we choose to make the particle rebound and simply change the sign of its vertical velocity component, i.e., $v_z \rightarrow -v_z$.

(6) Repeat steps (2)–(5) using the newly computed positions and velocities of the N particles until a given number of collisions or a given time level has been reached.

This algorithm corresponds to the simulations of an ergodic system similar to the one shown in Fig. 1(b). It is a simple and instructive matter to simulate the nonergodic equivalent of the system shown in Fig. 1(a) by choosing the initial particle velocities to have vanishing horizontal components and by performing strictly one-dimensional interparticle collisions, such that particles simply exchange their velocity as if they were going through each other. This system does not lead to a static atmosphere stratified according to the barometric formula unless very special initial conditions are selected for the particles.[2]

E. The choice of the number of particles

The choice of the number N of particles that one wants to put in the system is a crucial one and is dictated by the fact that an arbitrary initial distribution of particles will evolve toward a static atmosphere (characterized by a scale height H) in a time that is much longer than the characteristic free fall time $t_f \equiv (H/g)^{1/2}$. In order to keep the computation time at a reasonable level, one must require t_f to be not too large a number of times $t_{\min}$, the latter being roughly the interval between two collisions in the most dense region of the system, i.e., close to the ground level at $z=0$. An estimate of the

typical collision time $t_{\min}$ is easily found by first noting that the total number of particles in the system is directly related to the number density $n(z)$ given by Eq. (15) via

$$N=\int_0^\infty n(z)dz=n_0H, \tag{28}$$

which means that the average distance between particles near the ground, at $z=0$, is $l(0)=H/N$. Given that the average velocity of particles in a Maxwellian gas can be estimated to be of order $(kT/m)^{1/2}$, it follows that $t_{\min}$ is of the order of $H/[N(kT/m)^{1/2}]$ and thus

$$\frac{t_f}{t_{\min}}\sim\left(\frac{H}{g}\right)^{1/2}\frac{N(kT/m)^{1/2}}{H}=N, \tag{29}$$

which means that computation time is roughly proportional to N^2 for a given total physical simulation time. From (29) one also learns that even though after N collisions a physical time of order t_f can be reached, the system may still be far from thermodynamic equilibrium (if it was out of equilibrium at the beginning of the simulation), since on average the particles in the system have experienced only one collision during that same time period. Experiments in uniform systems show that five collisions per particle are needed for thermalization to be practically complete[7,8] so that one may estimate that after $10N$ collisions the system will generally be thermalized. However, one should remember that in our nonuniform system the collision frequency of the uppermost particle (particle $i=N$) is much smaller than the collision frequency of the particle close to the ground (particle $i=1$) so that $10N$ collisions may not be enough in some cases.

III. THE VIRIAL THEOREM

It is easy to compute the statistical relation between the mean kinetic and the mean potential energy per particle in our one-dimensional system.

From the identity

$$\frac{d}{dt}(z\dot z)=z\ddot z+\dot z^2, \tag{30}$$

where the dot represents the usual total time derivative d/dt, and the equation of motion

$$\dot v_z=\ddot z=-g, \tag{31}$$

it follows that the average of the squared vertical velocity of all particles in the system,

$$\langle v_z^2\rangle\equiv\frac{1}{N}\sum_{i=1}^{N}(v_z^i)^2, \tag{32}$$

is given by

$$\langle v_z^2\rangle=\left\langle\frac{d}{dt}(z\dot z)\right\rangle+\langle zg\rangle. \tag{33}$$

It is easy to convince oneself that in a static system the time average of the first term on the right in Eq. (33) must vanish as the time interval used in the averaging process goes to infinity. This leads to the following relation for the mean kinetic and the mean potential energy per particle:

$$\overline{\langle E_z\rangle}\equiv\tfrac{1}{2}m\overline{\langle v_z^2\rangle}=\tfrac{1}{2}m\overline{\langle zg\rangle}\equiv\tfrac{1}{2}\overline{\langle E_{\rm pot}\rangle}, \tag{34}$$

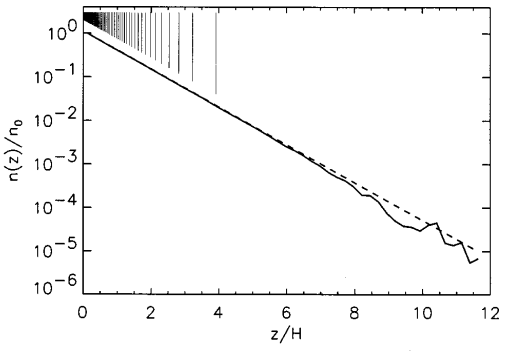

Fig. 3. The solid line corresponds to the density profile from a simulation of an atmosphere using $N=50$ particles that have been allowed to collide some 10^7 times. The dashed line corresponds to the prediction based on the virial theorem. The density has been obtained by counting all particles' positions every 50 collisions. Bin size is $\Delta z=0.245H$. The vertical lines in the upper part inform on the theoretical average position of the 50 particles in the system. For example, the lowest 49 particles are located most of the time below level $z=3.9$ while the lowest 48 particles are mostly located below $z=3.2$, etc. One can also say that the average position of particle $i=49$ lies somewhere between $z=3.2$ and $z=3.9$, etc. The separation between the vertical lines also gives a measure of the local mean free path.

where overlining means that the temporal average of the corresponding quantity must be taken. If collisions are frequent enough and if the number N of particles is large enough (see below), the velocity distribution is Maxwellian with a temperature T, which is independent of height [see the discussion leading to Eq. (14)]. The mean kinetic energy per particle $\langle E_{\rm kin}\rangle$ is therefore independent of height and can be computed easily by weighting $mv^2/2$ with the Maxwell velocity distribution (4):

$$\langle E_x\rangle=\langle E_y\rangle=\langle E_z\rangle=\tfrac{1}{3}\langle E_{\rm kin}\rangle=\tfrac{1}{2}kT. \tag{35}$$

We can thus conclude that if the number N of particles in the system is large enough and if one lets the system evolve long enough, it will reach a stationary state where the mean total energy per particle $\epsilon\equiv E/N$ is related to the temperature T via

$$\epsilon=\overline{\langle E_{\rm kin}\rangle}+\overline{\langle E_{\rm pot}\rangle}=\tfrac{3}{2}kT+kT=\tfrac{5}{2}kT, \tag{36}$$

where the time averages that appear in Eq. (34) have been evaluated using the velocity distribution function weighted quantities in (35). Using the same procedure, one shows that in a system with s spatial dimensions the average potential energy per particle must be skT.

IV. AN EXAMPLE

We start a simulation by distributing a set of N particles uniformly between the ground level and an arbitrary height h. The particles have zero initial velocity, so that the average total energy per particle is simply $\epsilon=mh/2$. Using Eq. (36) we can immediately predict that the scale height of the atmosphere will be $H=kT/(mg)=h/5$. Figure 3 shows the density profile of a simulated atmosphere using $N=50$ particles that have been let collide some 10^7 times during a total simulation time $t_{\rm end}=1.43\times10^4t_f$. The density profile has been obtained by counting the particles' positions every 50

collisions within bins of size $\Delta z = 0.245H$. However, no positions have been retained during the first 5×10^4 collisions, to ensure that the memory of the initial condition is lost.[19] Thus the density profile results from averaging over the different possible states visited by the system (a subset of the microcanonical ensemble). However, the averaging can also be interpreted as the time average over the density profiles recorded at different times. Note that since the system is ergodic, the entire microcanonical ensemble will be visited by the system within a lapse of time that depends on how densely one requires the energy surface to be covered by the system's phase space trajectory. In practice we expect that time to be longer than the longest correlation time in the system. The latter is most likely the time separating two successive collisions of the uppermost particle, that is, a time of the order of $\langle v_z^2\rangle^{1/2}/g = t_f$. As already stated, the total physical simulation time leading to the density profile in Fig. 3 is $1.43\times10^4 t_f$, so that we may consider that temporal averages are already a good approximation of the microcanonical averages.

Figure 3 shows that the simulation is in good agreement with the prediction of the virial theorem up to level $z \approx 5H = h$. Above that level, the measured curve departs more and more from the theoretical prediction based on the virial theorem. However, even with only 50 particles in the system, the barometric formula is extremely well reproduced up to a height corresponding to a falloff of the density, with respect to the ground level, by more than three orders of magnitude. Of course the fact that the simulated density profile departs from the barometric formula for high z values is not an artifact. Indeed, besides the statistical departures due to the small count rates at large altitudes (count rate is of the order 10^2 per bin at $z/H = 10$), the differences between the measured and the barometric density profile are a consequence of the fact that the total energy is finite so that the phase space domain that is accessible for the particle trajectories shrinks with increasing height, until it vanishes completely above a critical height that depends on the total energy of the system. Naturally, the difference of the measured density profile from the barometric formula is also due to the finite integration time. If a region in phase space is ''visited'' on a typical time scale that is much larger than the integration time and if the contribution of that region to the barometric distribution function (14) is important, the measured density profile will of course differ from the barometric formula.

Figure 4 shows two things. The first noticeable thing is that the clouds of dots representing the positions of two particles in a space–time plot clearly show that, as expected, there is no temporal correlation between the subsequent positions of a given particle after a time interval of the order of the total simulations time $\approx 2\times10^4 t_f$, consistent with the fact that the longest expected correlation time is of order t_f only. Thus the two probability histograms shown on top of both scatter plots in Fig. 4 won't change significantly after further increasing the simulation time. The second striking aspect in Fig. 4 is that the probability distribution of a particle in the highly collisional domain of the atmosphere, defined as the domain where the mean free path is such that $l(z) \ll H$, is roughly symmetric about the particles' average height. This is the case for particle $i = 25$ shown in panel (a) for which the mean free path is roughly given by the separation between the two vertical lines going through the cloud of dots. The situation is completely different for the uppermost particle in the simulation shown in Fig. 4(b). For this particle the mean free path is strongly anisotropic, being of order H in the downward direction and ∞ in the upward direction. Of course, the large and anisotropic mean free path is the reason for the strong asymmetry in the probability distribution. However, despite the fact that the domain $z/H \lesssim 5$ is essentially explored by the uppermost particle in the simulation alone and despite the strong asymmetry of its probability distribution, the barometric formula is reasonably well approximated up to a level $z/H \approx 10$, which is a clear demonstration of the (well known?) fact that in the case of the static atmosphere the ratio of the local mean free path to the scale height H is not a critical parameter of the problem, as the collision time is always small compared to the infinitely long time scale of a static system. This is generally not so in the case of nonstatic atmospheres, like stationary stellar winds, since in that case the relevant time scale, which is the typical time it takes for the flow to travel one scale height, is finite and may not be long compared to the collision time. This is precisely the case of the solar wind problem.[20]

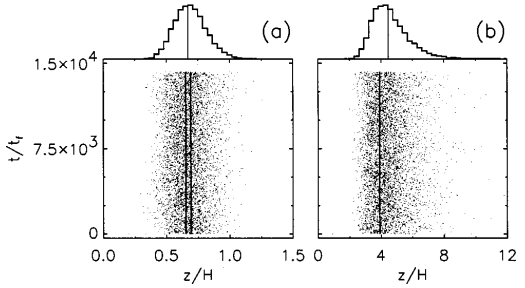

Fig. 4. Time and position for two different particles registered every 1000 collisions, i.e., roughly every $1.4t_f$: (a) corresponds to particle $i = 25$ and (b) to particle $i = N = 50$. Note the different spatial scales used for the two plots. The vertical lines through the clouds of dots are the ones discussed in Fig. 3 even though only the ones that are of interest for the given particle are plotted here. The histograms thus represent the observed probability of finding the associated particle at a given height, with the vertical line going through the histogram indicating the average measured position of the corresponding particle.

V. CONCLUSION

We have presented a simple one-dimensional kinetic simulation that shows the formation of a gaseous atmosphere stratified according to the barometric formula. The interest of the model resides essentially in its coding simplicity and in its didactical aspects, as it addresses various subjects at a time, including interparticle collisions, phase space trajectories, the problem of ergodicity, and the virial theorem. It is possible, though much more complicated, to generalize the model to the astrophysically interesting case of a spherical body of mass M and radius R_0 surrounded by a gas. It is well known[2] that in such case a static equilibrium is not possible because of the finite value of the escape velocity from the body surface, which allows for the high energy particles in the Maxwellian distribution (4) to escape to large radial distances causing the body to lose its atmosphere sooner or later.[21] However, if one compensates for the escaping particles by injecting new particles coming from below the surface R_0, it is possible to sustain a stationary flow.[22] Depend-

ing on the number density and the temperature at R_0, the flow can become supersonic at some distance above R_0 in very much the same way as in Parker's fluid theory of the solar wind.[20]

ACKNOWLEDGMENTS

I would like to thank the referees and many colleagues (in particular F. Cametti, R. Grappin, S. Landi, F. Leblanc, and F. Lignières) for useful comments, especially on Sec. II C.

[1]E. Halley, ''A Discourse of the Rule of the Decrease of the Height of the Mercury in the Barometer, According as Places are Elevated above the Surface of the Earth, with an Attempt to Discover the True Reason of the Rising and Falling of the Mercury, upon Change of Weather,'' Philos. Trans. R. Soc. London **16**, 104–116 (1686–1692).

[2]M. N. Berberan-Santos, E. N. Bodunov, and L. Pogliani, ''On the barometric formula,'' Am. J. Phys. **65** (5), 404–412 (1997).

[3]In fluid theories the thermodynamic state of a system is specified by the spatial distribution of at least two macroscopic quantities like the pressure, the density, etc.

[4]R. Becker, *Theorie der Wärme* (Springer-Verlag, Berlin, 1978), 2nd ed. In particular Chaps. 25–28 and 31–33. There is also an English version of the book: R. Becker, and G. Leibfried, *Theory of Heat* (Springer-Verlag, Berlin, 1967).

[5]W. W. Wood, ''Computer studies on fluid systems of hard-core particles,'' in *Fundamental Problems in Statistical Mechanics III* (North-Holland, Amsterdam, 1975), pp. 331–388.

[6]G. Sauer, ''Teaching classical statistical mechanics: A simulation approach,'' Am. J. Phys. **49** (1), 13–19 (1981).

[7]M. Eger and M. Kress, ''Simulation of the Boltzmann Process: An Energy Space Model,'' Am. J. Phys. **50** (2), 120–124 (1982).

[8]R. P. Bonomo and F. Riggi, ''The evolution of the speed distribution for a two-dimensional ideal gas: A computer simulation,'' Am. J. Phys. **52** (1), 54–55 (1984).

[9]R. M. Sperandeo-Mineo and A. Falsone, ''Computer simulation of ergodicity and mixing in dynamical systems,'' Am. J. Phys. **58** (11), 1073–1078 (1990).

[10]L. Boltzmann, ''Über die mechanische Analogien des zweiten Hauptsatzes der Thermodynamik,'' J. für reine und angew. Mathematik **100**, 201 (1887).

[11]P. Ehrenfest and T. Ehrenfest, ''Begriffliche Grundlagen der statistischen Auffassung in der Mechanik,'' Encyclopaedie der mathematischen Wissenschaften, Vol. 4, Part 32 (Teubner Verlag, Leipzig, 1911).

[12]G. D. Birkhoff, ''Proof of a Recurrence Theorem for Strongly Transitive systems,'' Proceedings of the National Academy of Sciences of the USA **17**, 650 (1931); ''Proof of the Ergodic Theorem,'' Proceedings of the National Academy of Sciences of the USA **17**, 656 (1931). It may be easier to find the two volumes with Birkhoff's collected works: G. D. Birkhoff, *Collected Works* (American Mathematical Society, Providence, 1960).

[13]L. Boltzmann, ''Weitere Studien über das Wärmegleichgewicht unter Gasmolekülen (*H*-Theorem),'' Wien. Ber. **66**, 275 (1972). The article where Boltzmann proves his famous *H*-theorem.

[14]Despite the analogy between our model and the physical representation of Fig. 1(b) it should be noted that our model is not ergodic on the whole hypersurface of constant energy. The reason is that there are no vertical walls in our model so that the total horizontal momentum is necessarily conserved. The system's phase space trajectory is therefore restricted to a subspace of the energy surface defined by the conservation of the two components of the total horizontal momentum. Thus, the dimension of the subspace is equal to the dimension of the energy surface minus two. One could make the model fully ergodic by stochastically reversing the particles' horizontal velocity in order to mimic the effect of the walls of the tube in Fig. 1(b). However, in a stationary system with a large number of particles the total horizontal momentum is approximately constant with strong departures from the average being extremely rare and therefore statistically insignificant. In order to appreciate quantitatively the constancy of total horizontal momentum, let us consider a system of N particles and let us suppose, for simplicity, that the v_x component of the particles' velocity can only take two values $v_x=\pm v_T$. The velocity v_T represents a typical velocity of the particles in the x direction and is reminiscent of the thermal velocity $\sqrt{2kT/m}$ for a Maxwellian gas. If we assume that the system is ergodic we can easily compute the probability $w(n)$ of observing exactly n particles with a speed $v_x=+v_T$:

$$w(n)=\frac{N!}{n!(N-n)!}\frac{1}{2^N}, \tag{37}$$

where 2^N is the total number of possible states and $N!/[n!(N-n)!]$ the number of possibilities of selecting n particles out of N. For large values of N, n, and $N-n$ one can use Stirling's formula $N!\approx\sqrt{2\pi N}\,N^N e^{-N}$ in Eq. (37). Thus, for small departures $\nu\equiv n-N/2$ of n from the mean value $\langle n\rangle=N/2$, and after some calculations (see Sec. 23 in Becker's book—Ref. 4—for the details), Eq. (37) can be transformed into

$$w(\nu)=\frac{1}{\sqrt{\pi N/2}}\exp\left(-\frac{\nu^2}{N/2}\right). \tag{38}$$

The probability for the system's average velocity $|\langle v_x\rangle|=v_T\,\nu/N$ to be smaller than an arbitrary fraction α is readily obtained by integrating Eq. (38),

$$w(|\langle v_x\rangle|<\alpha v_T)=\frac{1}{\sqrt{\pi N/2}}\int_{-\alpha N}^{\alpha N}\exp\left(-\frac{\nu^2}{N/2}\right)d\nu$$

$$=\frac{2}{\sqrt{\pi}}\int_0^{\alpha\sqrt{2N}}e^{-x^2}\,dx=\mathrm{erf}(\alpha\sqrt{2N}). \tag{39}$$

This equation shows that there is a 4.7×10^{-3} probability for the mean velocity $|\langle v_x\rangle|$ to be larger than $v_T\sqrt{2/N}$. The probability falls to an already ridiculously small 1.5×10^{-8} for $|\langle v_x\rangle>|v_T\sqrt{8/N}$, which shows how insignificant the departures from the average behavior are. This is the justification for ignoring such departures in our model.

[15]Ya. G. Sinai, *Introduction to Ergodic Theory* (Princeton U.P., Princeton, NJ, 1976).

[16]The case of only two balls of different mass m_1 and m_2 in a one-dimensional closed system is not ergodic. The numerical integration of the equations of motion on a computer shows that the momentum p of each particle can only take a finite number of values. Although the exact number of accessible states depends on both the mass ratio m_1/m_2 and the initial conditions, it is clear that the ellipse of constant energy $E=(p_1^2/m_1+p_2^2/m_2)/2$ cannot be densely covered. Thus a minimum of three particles and two species is probably needed for such a system to be an ergodic one.

[17]D. Ter Haar, ''Foundations of Statistical Mechanics,'' Rev. Mod. Phys. **27**, 289–338 (1955).

[18]If there were two, or more, different species of particles, collisions would thermalize all species to the same temperature T. Since in our model the particles can pass each other, every species j would separately produce a pressure profile of the barometric type [cf. Eq. (1)] with scale height $H_j=kT/m_jg$. The result is that the relative concentration of light to heavy particles increases with height. In Sauer's model—Ref. 6 [cf. Fig. 1(a)], where particles cannot pass each other, things are quite different. In that case a sequence of particles, alternatively of mass m_1 and m_2, lead to an atmosphere profile of the type given in Eq. (1) with an intermediate scale height $H=kT/(\bar{m}g)$ with $\bar{m}=(m_1+m_2)/2$. It is therefore clear that Sauer's model does not provide a good description of a real atmosphere where species are distributed independently from each other following their respective scale heights H_j. On the other hand, Sauer's model provides a good description of ionized atmospheres (e.g., stars' atmospheres) where the Coulomb force prevents positive and negative charged particles (for example, protons and electrons) from separating.

[19]According to the discussion at the end of Sec. II E a number of collisions larger than $10N=500$ generally suffice for the system to become thermalized.

[20]E. N. Parker, ''Dynamics of interplanetary gas and magnetic field,'' Astrophys. J. **128**, 664–676 (1958).

[21]See J. H. Jeans, *The Dynamical Theory of Gases* (Cambridge U.P., Cambridge, 1925), in particular the chapter on planetary atmospheres. There are numerous editions and translations of this classical book, e.g. (Dover, New York, 1954).

[22]In stars there is not a well-defined surface R_0, as in the case of nongaseous planets like the Earth, separating the planet's body from the atmosphere. Of course, in the case of a star like the Sun, which is entirely made of gas, the choice of the reference level R_0 is arbitrary. In a stationary situation the net amount of gas crossing the spherical surface $R=R_0$ per time unit is the same as the mass loss rate of the star. In the case of the Sun the loss rate is of the order of 10^{-14} solar mass/yr only.

6 Une méthode de simulation originale pour les plasmas faiblement collisionnels

Ap&SS 277,149-152 (2001)

A Simulation Method for Semicollisional Plasmas

Filippo Pantellini and Simone Landi
Observatoire de Paris, France

May 25, 2000

Abstract. We present a one dimensional kinetic simulation model which can be used to simulate the stationary state of a semicollisional plasma. Results of a simple simulation are presented and compared to Fokker–Planck calculations. The model is particularly well suited for the diluted solar atmosphere.

Keywords: Simulation, collisions, plasma, kinetic

1. Introduction

It is sometimes impossible to conveniently simulate a plasma using either fluid (i.e. fully collisional) or collisionless model. The solar atmosphere beyond the upper chromosphere and out to heliocentric distances of the order of an astronomical unit is an example of such a plasma. The method we present in this paper is suited for stationary configurations where the collisional mean free path for a thermal particle is not too small compared to the typical gradients of macroscopic quantities (e.g. temperature, density, etc.) and can be seen as alternative to Fokker–Planck and Monte Carlo simulations. Most basic aspects of the model have been discussed elsewhere (Pantellini, 2000) for the case of identical particles undergoing hard–sphere type collisions and shall not be repeated here. Only the extension of the model to the case of charged particles undergoing Coulomb type collisions is briefly discussed here.

2. The model

A qualitative sketch of the model is shown in Figure 1. The model is based on the numerical integration of the one dimensional motion (along the z axis) of N protons and N electrons plunged in a z aligned gravitational field g and an external self–consistent charge neutralizing constant electric field E which is determined experimentally by trying a number of different values. Particles are vanishing small, have non zero mass and three dimensional velocities. Whenever the world lines of any two particles encounter they may make an elastic collision according to a prescribed velocity dependent probability distribution P. The choice

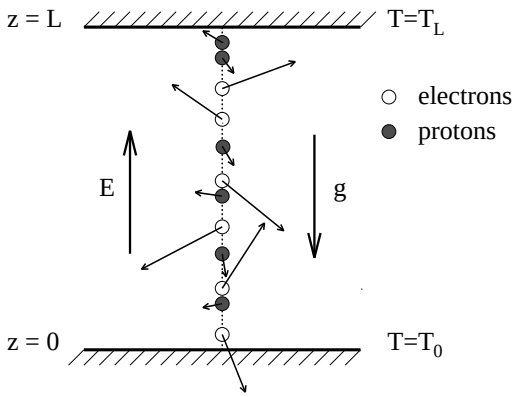

Figure 1. Schematic illustration of the model for a proton–electron plasma. Note that the particles' velocity is 3D even though the model is spatially 1D.

of P specifies the character of the interaction. A probability distribution $P \propto u^{-4}$, where u is the relative velocity of the two particles, mimics a Coulomb type collision whereas a velocity independent P mimics a hard sphere type collision. Given the low velocity divergency of the probability distribution for Coulomb collisions we set $P(u) = 1$ for relative velocities $u < u_0$ where u_0 is typically of the order, or smaller, than half the typical relative velocities between the colliding particles. A particle hitting one of the boundaries at $z = 0$ or $z = L$ is instantly reinjected into simulation domain following a not yet specified velocity distribution function.

3. An example: the thermoelectric field

We simulate a plasma in a $g = 0$ gravitational field using 80 electrons and 80 protons. A proton to electron mass ratio of 100 has been used to speed–up the simulation. Particles reaching the boundaries are reinjected into the simulation domain according to Maxwellian velocity distribution functions with temperatures $T(0) = T_0$ and $T(L) = T_L$, respectively. For moderate temperature gradients a constant electric field is generally good enough to ensure local charge neutrality everywhere in the system. Now, if the plasma is sufficiently collisional such that the electron temperature $T_e(z)$ and the proton temperature $T_p(z)$ are equal we expect the electric field to be related to the temperature gradient

via (e.g. Chapter 7.9 in Golant, Zhilinsky and Sakharov (1980))

$$eE = -\alpha \frac{\partial}{\partial z}(kT_e) \tag{1}$$

where k is the Boltzmann constant and e the proton charge. This field is called the thermoelectric field as it is solely due to the temperature gradient in the plasma slab. It is reminiscent of the Seebeck effect in metals (first described by Seebeck in the early 1820s) which makes the familiar thermocouple thermometer to work. The field is ultimately due to the unbalanced frictional force exerted by the heavy protons on the electrons flowing from the hot to the cold boundary and vice versa so that the appearance of the numerical constant α is primarily an effect of proton–electron collisions. Figure 2 shows electron num-

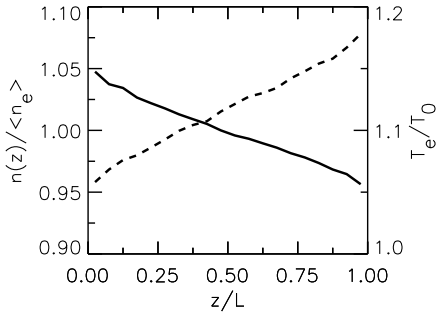

Figure 2. Simulation of a plasma slab with imposed temperature gradient. The electron temperature (dashed profile) and the electron density have been obtained by periodically sampling the position and the velocity of all electrons in the system.

ber density n_e (normalized to the average electrons density $\langle n_e \rangle$) and electron temperature T_e (in units of T_0) profiles for a simulation based on our model. The reason for the normalized temperature profile to differ from the theoretical profile $T_e(z) = 1 + 0.2\ z/L$ one would expect based on the imposed temperatures at the boundaries is due to the fact that the typical collisional mean free path is finite. As expected both the proton and electron pressures are equal and constant so that the only contribution to the charge neutralizing electric field is the thermoelectric field which we find to be $E = -0.0895$ (in units of kT_0/eL). On the other hand the temperature gradient, which can be measured on the figure, is $\partial T_e/\partial z = 0.116/L$. Using Eq. (1) we find $\alpha_{sim} = 0.77$ which compares quite well with the Fokker–Planck result $\alpha_{FP} = 0.71$ found by Spitzer and Härm(1953).

Unlike the thermoelectric field, which depends on the electron–proton collisions, the electron heat flux is mainly supported by electron–electron collisions. Accurate Fokker–Planck calculations lead to the following expression for the total electron heat flux (e.g. Chapter 7.10 in Golant, Zhilinsky and Sakharov (1980))

$$q^e_{FP} = -3.16\,\frac{n_e k T_e}{\nu_{ep} m_e}\,\frac{\partial k T_e}{\partial z} \tag{2}$$

where ν_{ep} is the collision frequency of an electron with the protons in system. Replacing the collision frequency measured in the simulation and the temperature gradient of Fig. 2 into Eq. (2) one obtains a heat flux $q^e_{FP} = -0.075$ (in units of $\langle n_e \rangle m_e (kT_0/m_e)^{3/2}$) which, again, compares quite well with the heat flux $q^e_{sim} = -0.087$ measured in the simulation. This value differs substantially from hard sphere type collisional heat flux, which for the observed temperature gradient can be estimated (cf. most books on statistical physics) to be $q^e_{HS} = -0.027$. Even though a collisionless plasma is unable to support a temperature gradient it can support a strong heat flux. The latter is due to the fact that the upward and downward traveling particles have different temperatures given by the injection temperature T_0 and T_L, respectively. In that case the temperature is constant $T_e(z) = \sqrt{T_0 T_L}$ but the heat flux is roughly twice the Fokker–Planck value, i.e. $q^e_{NC} = -0.167$. We conclude by noting that the Fokker–Planck results Eqs. (1) and (2) are valid in the limit of small values of the thermal Knudsen number $K_T = (\partial T_e/\partial z)\lambda_{ee}/T_e$ where λ_{ee} is the average collisional mean free path for an electron–electron collision. In the simulation of Fig. 2 we find $\lambda_{ee} = 0.19\,L$ and $K_T \approx 0.02$ which justifies comparing our simulation with results from Fokker–Planck calculations. We note that increasing the number of particles by roughly a factor 10 leads to $K_T = O(10^{-3})$ which is a typical value in the solar corona or the solar transition region. Simulations in this regime of the Knudsen number, including gravitational effects, will be published elsewhere.

References

F. G. E. Pantellini. A simple numerical model to simulate a gas in a constant gravitational field *Am. J. Phys.*, 68(1):61–68, January 2000.

V. Golant, A. Zhilinsky, and I. Sakharov. *Fundamentals of Plasma Physics*. John Wiley & Sons, New York, 1980.

L. Spitzer, and R. Härm. Transport Phenomena in a Completely Ionized Gas *Phys. Rev.*, 89:372–380, May 1953.

7 Sur le flux de chaleur dans la couronne

A&A 372, 686-701 (2001)

A&A 372, 686–701 (2001)
DOI: 10.1051/0004-6361:20010552

Astronomy & Astrophysics

On the temperature profile and heat flux in the solar corona: Kinetic simulations

S. Landi and F. G. E. Pantellini

Département de Recherche Spatiale, Observatoire de Paris–Meudon, 92195 Meudon Cedex, France

Received 29 January 2001 / Accepted 26 March 2001

Abstract. In the solar corona the collisional mean free path λ for a thermal particle (electrons or protons) is of the order of 10^{-2} to 10^{-4} times the typical scale of variation H of macroscopic quantities like the density or the temperature. Despite the relative smallness of the ratio λ/H, an increasingly large number of authors have become convinced that the heat flux in such a plasma cannot be described satisfactorily by theories which suppose that the local particle velocity distribution functions are close to Maxwellian. We address this question through kinetic simulations of the low solar corona by assuming that non thermal velocity distribution functions are present at the base of the corona. In particular, we show that if one assumes that the electron velocity distribution functions at the base of the corona have sufficiently strong suprathermal power law tails, the heat flux may flow upwards, i.e. in the direction of increasing temperature. Using kappa velocity distribution functions as prototypes for non thermal velocity distributions, we find that the heat conduction can be properly described by the classical Spitzer & Härm (1953) law provided the kappa index is $\gtrsim 5$. This value is much smaller than the value previously found by Dorelli & Scudder (1999). In addition we show that, unless extremely strong power law tails are assumed near the base of the corona (i.e. $\kappa < 4$), a local heating mechanism (e.g. waves) is needed to sustain the temperature gradient between the base of the corona and the coronal temperature maximum.

Key words. Sun: corona – methods: numerical – plasmas – conduction

1. Introduction

In this paper we present results from a one dimensional kinetic model of a semicollisional electron–proton plasma plunged in a gravitational field. The model is especially suited for stationary (not necessarily static) flows and for Knudsen numbers $K = \lambda/H \gtrsim 10^{-4}$, where H is a typical scale of variation of a macroscopic quantity, such as the density or the temperature and λ the distance between two successive collisions of a typical particle in the system. A simplified version of the model has previously been used by Pantellini (2000) to simulate a one-species atmosphere in a constant gravitational field. As expected, the result was the formation of a stratified isothermal atmosphere with an exponentially decreasing density known as the barometric law. The fact that the barometric law could be recovered was the first confirmation of the fact that, despite being one dimensional, the model could correctly reproduce known results. More recently, we implemented a more sophisticated version of the model to simulate an electron–proton plasma confined to the space between two conducting plates held at different temperatures and not subject to any external force (Pantellini & Landi 2000). We could show that the thermoelectric field needed to ensure quasi–neutrality in our simulation compares quite well with results of Fokker-Planck calculations with all possible interspecies collisions included (Spitzer & Härm 1953). These encouraging results motivated us to use the model to address the question of the heat flux in the solar corona.

The motivation for applying the model to the solar corona stems from the fact that observations suggest that above the transition region the typical thermal Knudsen number $K_{\mathrm{T}} \equiv \lambda\, \partial \ln T/\partial z$ is of the order 10^{-3} or larger (e.g. Dupree 1972; Ko et al. 1997; David et al. 1998; Fludra et al. 1999). It has been demonstrated that such a value, despite being much smaller than unity, is large enough for the classical transport coefficients (obtained by applying the Chapmann-Enskog formalism to the Fokker-Planck equation) to become substantially modified because of the presence of high non thermal energy tails in the electron velocity distribution functions (e.g. Shoub 1983; Scudder 1992b). Whence the necessity of using a numerical model appropriate for the solar atmosphere above the chromosphere-corona transition region where high values of the thermal Knudsen number $\gtrsim 10^{-3}$ are commonplace. The difficulty with the coronal plasma (and even for the solar wind plasma out to distances of the

Send offprint requests to: F. G. E. Pantellini,
e-mail: landi@despace.obspm.fr

order of astronomical units) is that neither a collisionless model based on the Vlasov equation nor a fluid model with Spitzer-Härm transport coefficients provide a convenient framework for investigation. Unfortunately, acceptance of the postulate of the existence of non thermal electron velocity distributions in the solar corona introduces an infinite number of additional free parameters required to define the distributions at the boundaries of the system. However, it is common practice to generalize the standard Maxwell-Boltzmann velocity distribution function using kappa distributions (see Eq. (18) below) which have the substantial advantage of requiring one additional free parameter only (the κ index). Depending on the value of the parameter κ the distribution departs more or less significantly from a Maxwell-Boltzmann distribution due to the presence of a more or less large excess of high energy particles. At least two studies have already discussed the fate of electron kappa distributions in the solar corona under the action of collisions. Anderson (1994) shows that collisions do strongly affect density and temperature profiles obtained using Scudder's (1992b) collisionless approach. After assuming that collisions do merely introduce first order perturbations to the collisionless distribution function he finds that the actual perturbations are of order unity or larger showing that collisions need to be treated self-consistently. To a certain extent this has been done by Dorelli & Scudder (1999) who let collisions affect the first order term of the Legendre polynomial expansion of the electron distribution function without assuming that this term was small but with the assumption of all higher order terms being zero. However, as we shall demonstrate below, higher order Legendre terms cannot be neglected. For example we find that collisions substantially modify the collisionless temperature profile (this has been observed by Anderson 1994, as well) indicating that at least the second order Legendre term must be retained in the expansion. The approach of Lie-Svendsen et al. (1999) is not substantially different from that of Dorelli & Scudder (1999) since they also use a first order truncated Legendre expansions for the electron distribution function. According to Chapman & Cowling (1970), such a truncation is valid for $K_{\mathrm{T}} \ll 1$ (weak inhomogeneity assumption) but, as pointed out by Shoub (1983) and Anderson (1994), $K_{\mathrm{T}} \lesssim 10^{-3}$ is probably a more appropriate condition for the first order truncated Legendre expansion to remain a justified approximation, especially in the case of non-thermal boundary conditions. Unfortunately, 10^{-3} is a typical value for the thermal Knudsen number K_{T} in the corona and the weak inhomogeneity assumption may be regarded as questionable. Assuming much stronger temperature gradients than the ones assumed in both the Dorelli & Scudder (1999) paper and in the present work, Lie-Svendsen et al. (1999) argue that the classical Spitzer & Härm (1953) heat flux adequately describes the heat flux in the lower solar corona if Maxwellian boundary conditions are chosen at both ends of the simulated plasma slab. All these Fokker-Planck based models eventually are affected by additional limitations. For example, Dorelli & Scudder (1999) use the standard hydrostatic equilibrium equation as a closure whereas, following Shoub (1983), Lie-Svendsen et al. (1999) use a contestable zero-gravity pressure equilibrium condition. We do not need such a fluid closure equation nor do we require the velocity distribution functions to be of any particular form. However, the principal advantage of our model stems from the fact that collisions are included self-consistently, even though their treatment is strongly simplified with respect to the complexity of collisions in a real plasma. We are unable to evaluate precisely the importance of the simplified treatment of the collisions on our results. However, the very fact that the transport properties measured in test simulations compare well with those predicted by Fokker-Planck calculations suggests that our simplified way of handling collisions allows us to retain most of the essential physics occurring in a non-magnetized plasma.

Since the simulation model we use has never been described in full, we shall devote the next section to doing so. Non-essential details of the algorithm are presented in Appendix A. A brief discussion of the differences and similarities between our model and conventional Fokker–Planck models is given in Appendix B. The derivation of some relevant quantities (density, temperature and heat flux) for a collisionless plasma is given in Appendix C.

2. The model

A qualitative sketch of the model is shown in Fig. 1. The model is based on the numerical integration of the one dimensional motion (one space and three velocity components) of N protons and N electrons plunged in a constant gravitational field and an electric field which is generally needed to ensure quasi–neutrality everywhere in the system. Particles are confined to the interval $z \in [0, L]$ by two conducting plates. Each time a particle hits one of the plates, it is instantly reinjected into the system according to a user defined prescription (e.g. elastic reflection, contact with a heat bath, etc.). Whenever the world lines of any two particles meet they may (or not) make an elastic collision depending on the magnitude of their relative velocity. The functional form of the velocity-dependent collision probability strongly influences the macroscopic behavior of the plasma (cf. 2.3).

2.1. Equation of motion

Both the gravitational field acceleration $\boldsymbol{g}$ and the electric field $\boldsymbol{E}(z) = [E_0 + \delta E(z)]\hat{\boldsymbol{z}}$ are directed along the z axis so that the equation of motion for a particle of species α can be written as

$$\mathrm{d}v_z/\mathrm{d}t = -g + q_\alpha E(z)/m_\alpha \tag{1}$$

$$v_z = \mathrm{d}z/\mathrm{d}t, \quad v_x = \text{const.}, \quad v_y = \text{const.} \tag{2}$$

where q_α and m_α are the charge and the mass of the particles of species α (electrons or protons). As can be seen on the left hand side of Fig. 1, we assume that the electric field

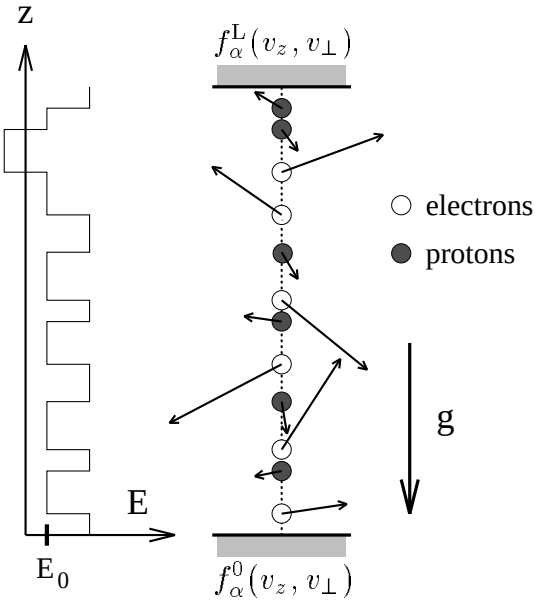

Fig. 1. Schematic illustration of the model for a proton-electron plasma plunged in a z aligned constant gravitational field. The particles' velocities are 3D even though the model is spatially 1D. E_0 is a z aligned external electric field which is generally needed to ensure local quasi-neutrality. In some cases a constant electric field does not suffice for the system to be neutral everywhere. In this case an additional small interparticle electric field is introduced (as shown on the left hand side of the figure) to compensate for these polarization effects. When two particles encounter each other, they may collide as described in Sect. 2.3. If a particle of species α hits one of the two boundaries at $z = 0, L$ it is injected back into the system according to prescribed velocity distributions $f_\alpha^{0,\mathrm{L}}(v_z, v_\perp)$ (cf. Sect. 2.4) where v_z is the particle's velocity along the z axis and $v_\perp$ the absolute value of the particle's velocity in a plane perpendicular to z.

between adjacent particles is constant, eventually increasing (decreasing) discontinuously by an arbitrary amount ϵ at the position of each proton (electron) in the system as if the particles where a succession of condensator plates attracting or repulsing each other depending on the charges on each plate. We then take the electrostatic field felt by a given particle (or condensator plate) to be the mean of the electrostatic field on either side of the particle. Thus, if we number all the particles in the system from 1 (bottom particle) to $2N$ (top particle) it follows that particle i feels the electrostatic field $E = \bar{E}_i \equiv (E_i + E_{i+1})/2$ during the whole time interval δt_i until the earliest of the three possible collisions between i and $i \pm 1$ and between $i - 1$ and $i - 2$. Note that only a collision between particles of different charges may modify the topology of the electrostatic field in the system, provided the interacting particles exchange their relative position during the collision. Since the electrostatic field is piecewise constant, we always integrate Eq. (1) using a constant E field.

2.2. The electric field

It is often possible to ensure a satisfactory charge neutrality in the system without the need for an interparticle electrostatic field ϵ. In these cases, the same constant external electric field E_0 can be used for all particles in the system. Particles do not feel each other. However, in the general case, a constant electric field is not good enough, as the plasma may behave like a dielectric medium, where polarization effects are no longer negligible. In that case, the Poisson equation must be written in the form

$$\frac{\partial \boldsymbol{D}}{\partial z} \equiv \frac{\partial}{\partial z}(\varepsilon_0 \boldsymbol{E} + \boldsymbol{P}) = \rho \tag{3}$$

where ρ is the charge density, ε_0 the permittivity of the vacuum, $\boldsymbol{D}$ the electric displacement and $\boldsymbol{P}$ the polarization. If $\boldsymbol{P}$ is negligible or (and) independent of z Eq. (3) implies that the electric field $\boldsymbol{E}$ needed to ensure charge neutrality ($\rho = 0$) is a constant $\boldsymbol{E} = E_0 \hat{\boldsymbol{z}}$. This may be the case when the density or temperature gradients in the system are small (Pantellini & Landi 2000). In cases where polarization effects are not negligible, a better charge neutrality can be obtained by introducing a moderately strong interparticle electric field ϵ as shown in Fig. 1. Let E_i denote the electric field between particles i and $i - 1$ and let E_0 be an external electric field, for example the gravitoelectric field (Rosseland 1924). Let us suppose that the boundaries at $z = 0$ and $z = L$ are conducting. It is well known that in this case a charged particle is attracted by the boundary as if there was a particle of opposite charge in the symmetric position behind the conductor. In this case, it is easy to see that the electric field E_1 between the conducting wall at $z = 0$ and particle number 1 as well as the field E_{i+1} above particle i must be given by

$$E_1 = E_0 + (q_{2\mathrm{N}} - q_1)\epsilon/2 \tag{4}$$

$$E_{i+1} = E_i + q_i \epsilon, \quad i \in \{1, 2, ..., 2N\}. \tag{5}$$

We emphasize that to simulate a plasma, ϵ should be taken to be small enough for the electrostatic energy between neighboring particles $|q_i q_{i-1}\, \epsilon \delta z|$ (δz is a typical interparticle distance) to be much smaller than the typical kinetic energy of the particles. Otherwise particles of opposite charge become bounded and form atoms.

2.3. Collisions

A particle of the system shown in Fig. 1 can either collide with another particle or with one of the two conducting walls at $z = 0, L$. The former is elastic, i.e. both total momentum and total energy of the colliding particles are conserved while the latter is not, as the walls reflect particles according to a prescribed velocity distribution function regardless of the particles' velocities before the collision. Let us discuss the case of a particle-particle collision first; we shall come back to the particle-wall collision in Sect. 2.4.

Two particles may collide if they simultaneously occupy the same position along the z-axis. During an elastic collision between two particles (labeled 1 and 2) the velocity changes according to the well-known rules (e.g. Landau & Lifshitz 1960)

$$\boldsymbol{v}_1' = \frac{m_1\boldsymbol{v}_1 + m_2\boldsymbol{v}_2}{m_1+m_2} + \frac{m_2}{m_1+m_2} u\,\boldsymbol{n}(u) \quad (6)$$

$$\boldsymbol{v}_2' = \frac{m_1\boldsymbol{v}_1 + m_2\boldsymbol{v}_2}{m_1+m_2} - \frac{m_1}{m_1+m_2} u\,\boldsymbol{n}(u) \quad (7)$$

where primed and unprimed velocities represent pre- and post-collision velocities, respectively and $u \equiv |\boldsymbol{v}_2 - \boldsymbol{v}_1|$. We note that the orientation of the unity vector $\boldsymbol{n}$ in velocity space is not specified by the requirement of the total energy (1 equation) and total momentum (3 equations) to be conserved during the collision, as the number of unknowns is 6 (the three velocity components for both particles). Let us use spherical coordinates to define the orientation of $\boldsymbol{n}$ in velocity space with θ' being the angle between $\boldsymbol{n}$ and the z-axis and ϕ' the angle between the projection of $\boldsymbol{n}$ in the (x, y) plane and the x axis. The question is: how shall we choose the angles θ' and ϕ' for any given collision in the system? Given the rotational symmetry of our system around the z axis, it is quite natural to choose ϕ' according to a uniform probability distribution in the interval $[0, 2\pi[$. The answer is not as obvious concerning the angle θ' since the system is not spherically symmetric. In the case of particles of equal mass (Pantellini 2000) the probability distribution for θ' is specified by the requirement that the system (in its most simple configuration, e.g. without external forces and with elastic boundary conditions) must relax towards a stationary state where the particle velocity distribution function is isotropic. This condition implies the post-collision angle θ' should be chosen according to (see Sect. II C in Pantellini 2000)

$$\theta' = \arccos(\sqrt{P}), \text{ with } P = \text{random number} \in [-1, 1]. \quad (8)$$

It is straightforward to convince oneself that the same result holds in the case of particles of unequal mass.

Now, even though the orientation of the $\boldsymbol{n}$ in Eqs. (6) and (7) must be chosen according to the above probability distributions if one requires the relaxed particle velocities to become distribute isotropically, one is still free to decide whether or not two particles which encounter each other effectively make a collision. If one decides that there isn't a collision, the two particles just go through each other without changing their velocities. If one decides that there is a collision, we compute the new velocities of the particles using Eqs. (6)–(8) to determine $\boldsymbol{n}$. In general, one is allowed to decide if two encountering particles collide depending on the magnitude u of their relative velocity only. The collision probability cannot depend on the orientation of $\boldsymbol{n}$ as the relaxed state would no longer be characterized by an isotropic velocity distribution.

Figure 2 shows two choices for the velocity dependence of the collision probability R on the relative velocity u. One may interpret R as the collisional cross-section.

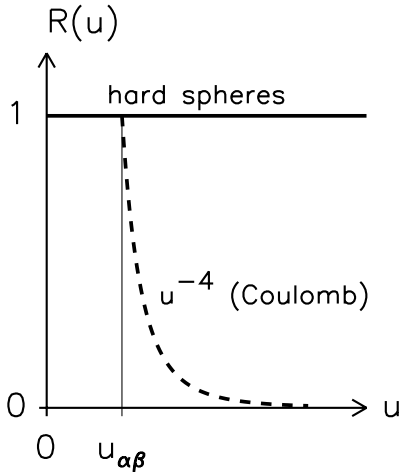

Fig. 2. Collision probability R for hard sphere type collisions (solid line) and for Coulomb type collisions (dashed line) as a function of the relative velocity u.

Accordingly, we call the case $R = 1$, where particles collide at each encounter, the "hard spheres" case and

$$R_{\alpha\beta}(u) = \begin{cases} 1 & \text{if } u < u_{\alpha\beta} \\ (u_{\alpha\beta}/u)^4 & \text{otherwise} \end{cases} \quad (9)$$

the "Coulomb" case. In Eq. (9) the indices α and β indicate that one is considering collisions between a particle of species α and a particle of species β (e.g. electron-electron, proton-electron, proton-proton).

A detailed comparison of the present model with other numerical models based on the Fokker-Planck or the Boltzmann equation (e.g. Shoub 1992) is beyond the scope of the present paper. Qualitatively speaking, the justification of the model stems from the fact that the scattering cross-section due to the cumulated effect of distant encounters in a near-equilibrium plasma is proportional to $\propto u^{-4}$ (e.g. Chandrasekhar 1943). Accordingly, one may interpret one collision in our model as representing the cumulated effect of a large number of distant encounters in a real plasma. Given that the most widely used (and best justified) numerical model to simulate distant encounter dominated plasma are Fokker-Planck models, we discuss more thoroughly the relation between our model and Fokker-Planck models in Appendix B. In the paper by Pantellini & Landi (2000) we show that using cut-off velocities $u_{\alpha\beta}$ of the order of, or smaller than, the typical relative velocity between α particles and β particles, our model gives results that compare well with results from Fokker-Planck calculations.

2.4. Boundary conditions

There are several ways of treating the problem of a particle hitting one of the boundaries at $z = 0$ and $z = L$.

One may, for example, let the particle rebound elastically by simply changing the sign of the z component of its velocity. In this case, total energy is exactly conserved. However, neither temperature gradients nor non-Maxwellian distribution functions can be simulated in such a system. Given that we are interested in situations where both temperature gradients and non-Maxwellian distributions are present, we shall use more sophisticated boundary conditions allowing the injection of an arbitrary velocity distribution function. The prescription is as follows. Each time a particle of species α hits one of the boundaries, it is reinjected into the system following a specified velocity distribution function $f_\alpha^{0,\mathrm{L}}(\boldsymbol{v})$. This implies that in a stationary state, and apart from statistical fluctuations, the bulk velocity along z must be zero everywhere. We further assume that particles are injected following isotropic velocity distribution functions, i.e. $f_\alpha^{0,\mathrm{L}}(\boldsymbol{v}) = f_\alpha^{0,\mathrm{L}}(v)$, where $v = |\boldsymbol{v}|$ is the magnitude of the velocity of the injected particle. Accordingly, the theoretical flux of particles coming from the boundary with velocity $\boldsymbol{v}$ in the magnitude interval $[v, v+\mathrm{d}v]$ and orientation with respect to the z axis in the range $[\theta, \theta+\mathrm{d}\theta]$ is given by

$$\mathrm{d}F_\alpha^{0,\mathrm{L}}(v,\theta) = v\cos\theta\, f_\alpha^{0,\mathrm{L}}(v)\, 2\pi\, v^2\, \sin\theta \mathrm{d}\theta\, \mathrm{d}v.$$

This expression can be integrated separately for both the velocity v and the angle θ, leading to the probability distributions P_v and P_θ of observing a particle entering the system from the boundary at $z = 0$ with velocity $V < v$ and θ in in the range $[0, \theta]$

$$P_\theta(\theta) = A_\vartheta \int_0^\theta \cos\vartheta\, \sin\vartheta\, \mathrm{d}\vartheta = \sin^2\theta \tag{10}$$

$$P_v(v) = A_v \int_0^v f(V)\, V^3\, \mathrm{d}V \tag{11}$$

where we have suppressed the species index α for readability and where A_v and A_θ are normalization constants such that $P_\theta(\pi/2) = P_v(\infty) = 1$. Thus, each time a particle hits the boundary at $z = 0$ it is reinjected following the probability distributions (10) and (11). This requires that the expressions (10) and (11) be solved for θ and v . For example, the angle θ is obtained by computing $\theta = \arccos(\sqrt{P})$ where P is a random number in the range $[0, 1]$. Similarly $v = P_v^{-1}(P)$ where P is again a random number in the range $[0, 1]$ and where the function P_v^{-1} is obtained by inverting (in most cases numerically) Eq. (11). Of course this procedure applies for both boundaries and all species.

3. Results

In the present simulations we consider a thin layer of a fully ionized electron-proton plasma plunged in a uniform gravitational field $g = GM_\odot/R_\odot^2$ where $M_\odot$ and $R_\odot$ are the solar mass and the solar radius, respectively while G is the universal constant of gravitation.

Following the reference paper by Dorelli & Scudder (1999), we assume typical temperatures and densities at the $z = 0$ boundary to be $T_0^{\mathrm{M}} \equiv 5 \times 10^5$ K and $n_\mathrm{e}(0) = n_0^{\mathrm{M}} \equiv 10^8$ cm^{-3} (we shall use these quantities for normalization in the remaining of the paper). The typical temperature gradient between the two boundaries at $z = 0$ and $z = L$ is of the order of 1.4×10^6 K$/R_\odot$. For a system length $L = 0.1\ R_\odot$ this leads to an upper boundary temperature $T_\mathrm{L} = 6.4 \times 10^5$ K. These parameters correspond to a thermal Knundsen number $K_\mathrm{T} \equiv \lambda_\mathrm{ee}(\partial T/\partial z)/T$ (T is the temperature and λ_ee the mean free path for electron-electron collisions) of the order 10^{-4} to 10^{-3}, which is typical for the low solar corona in coronal holes (e.g. Ko et al. 1997; David et al. 1998; Fludra et al. 1999). The Fokker-Planck electron-proton collision frequency for such a plasma is given by Eq. (B.11). The same collision frequency is obtained in our simulation model if the number of electrons (or protons) N is of the order $N \simeq 1000$ (cf. Appendix B), which is therefore a typical value for all the simulations presented in the paper.

In order to reduce computational time a proton-to-electron mass ratio $m_\mathrm{p}/m_\mathrm{e} = 100$ has been chosen for all simulations. This can be done provided the relevant dimensionless parameter

$$\gamma \equiv \frac{g(m_\mathrm{p}+m_\mathrm{e})R_\odot}{2k_\mathrm{B}T} \approx \frac{gm_\mathrm{p}R_\odot}{2k_\mathrm{B}T_0^{\mathrm{M}}} \tag{12}$$

is chosen to be the same as in the real world, i.e. $\gamma \approx 23$. We note that γ is the length $R_\odot$ expressed in units of the isothermal scale height of the atmosphere. Thus if one assumes protons to be less massive than in the real world, one has to assume gravity g to be stronger than in the real world (i.e. a fictitious Sun more massive then the real Sun), so as to ensure γ remains unchanged. On the other hand, as we shall see below, a thermoelectric field E_T is needed to ensure quasi-neutrality in a plasma with an imposed temperature gradient (cf. Eq. (17)). Since E_T does not depend on the mass of the particles, at least as long as $m_\mathrm{e}/m_\mathrm{p} \ll 1$, there is no reason to use the real mass ratio in the simulation, the only requirement being the condition $m_\mathrm{e}/m_\mathrm{p} \ll 1$.

In simulations it is generally convenient to suitably normalize all physical quantities. Thus, throughout the remainder of the paper, we shall assume that velocities are normalized to $v_0^{\mathrm{M}} \equiv \sqrt{2k_\mathrm{B}T_0^{\mathrm{M}}/m_\mathrm{e}}$, distances to the slab thickness L, time intervals to $t_0^{\mathrm{M}} \equiv L/v_0^{\mathrm{M}}$, electric fields to $E_0^{\mathrm{M}} \equiv m_\mathrm{e}(v_0^{\mathrm{M}})^2/(eL)$ and heat fluxes to $q_0^{\mathrm{M}} \equiv m_\mathrm{e}n_0^{\mathrm{M}}(v_0^{\mathrm{M}})^3$.

Distribution functions and moments are constructed by regularly sampling positions and velocities of the particles in the system. In practice, we sample positions in bins of width $0.03125L$ and velocities in bins of width of the order of 0.4 times the thermal velocity of the given population. In a typical simulation, 10^3 particles encounter some 10^{10} times and the distribution functions are obtained by sampling positions and velocities every 10^4 encounters. This sampling interval is roughly the time it takes for a thermal proton to cross the plasma slab, which is also an estimate of the time memory of the system.

The just described procedure allows the construction of density or heat flux profiles which are not yet

normalized. In order to do so one has to determine the "real" number density (in cm^{-3}) somewhere in the system, for example at $z = 0$. This is impossible in a collisionless stationnary and quasi-neutral system where the absolute density is an arbitrary parameter which can be eliminated from the equations (e.g. from the Vlasov equation). In a collisional system, however, the number density is no longer an arbitrary parameter given its intimate (roughly linear) connection with, for example, the electron-proton collision frequency. Thus, by recording the electron-proton collision frequency somewhere in the system (in units of $1/t_0^{\mathrm{M}}$ and thus in s^{-1}), say at $z = 0$, one can determine the absolute density there, provided a relationship between density and collision frequency has been previously established in some way. Such a relationship may have been established experimentally by measuring the collision frequency in a real Maxwellian plasma as a function of temperature and density. As we shall discuss below, and in Appendix B, we much more pragmatically adopt the relationship provided by a Fokker-Planck model. In brief, our strategy goes as follows: we choose a number of simulation particles N such that the recorded collision frequency near $z = 0$ corresponds to a typical Fokker-Planck collision frequency for a plasma with an electron (or proton) number density $n(0)$ of about $n_0^{\mathrm{M}} = 10^8\ \mathrm{cm}^{-3}$. In practice we just ensure that the Knudsen number in our simulation and in the solar corona are the same, despite the fact that the number of particles N in our system is ridiculously small compared to the number of particles which populate the solar corona. Fortunately, only 10^3 to 10^4 particles are required to simulate the corona. A number $N \sim 10^5$ would already require a computational power well beyond present day computer capabilities.

In the following subsections we shall discuss the behavior of a slab of solar corona for three different kinds of boundary conditions. The thickness of the slab L is taken to be either 0.1 $R_\odot$ or 0.2 $R_\odot$. The temperatures (based on the second moment of the velocity distribution function) of the boundaries are adjusted to make the mean temperature and the temperature gradient of the system compatible with the previously prescribed plasma conditions. No energy sources or sinks are present in the system. Energy is injected at the boundaries in the form of kinetic energy of the particles. The only way of transporting energy in the system is through a collisional (or collisionless) heat flux which means that all other means (e.g. radiation, waves, internal energy of the particles) are excluded.

The first subsection is devoted to the simulation of the "classical" case with thermalized (Maxwellian) boundary conditions. We shall see that even in this case the Spitzer and Härm heat flux (Spitzer & Härm 1953) is not able to sustain the prescribed temperature gradient over a distance larger than 0.1 $R_\odot$ or so. In the second subsection we shall discuss the case of non thermal velocity distribution functions at the lower boundary. These simulations show that the prescribed temperature gradient can be sustained without local heating provided the number of suprathermal particles is high enough. This number turns out to be much higher than suggested in previous works (e.g. Dorelli & Scudder 1999). In the last subsection we briefly discuss the case of both boundary conditions being non thermal. We consider this case as rather unphysical as it supposes a source of suprathermal particles somewhere above the base depending on the position of the upper boundary. We discuss this case mainly because in the collisionless studies (e.g. Scudder 1992b) and in the reference paper by Dorelli & Scudder (1999) the nonthermal distributions "survive", by construction, across the entire slab of plasma.

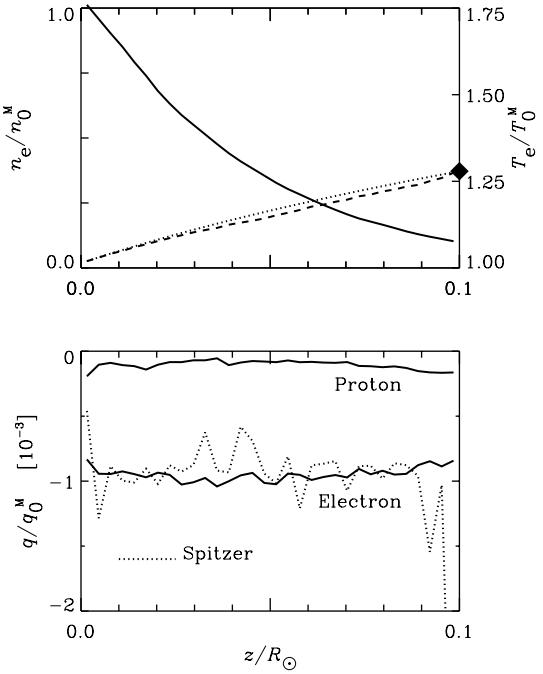

Fig. 3. Maxwell-Maxwell boundaries: in the top panel the electron density (solid line) and the temperature (dashed line) profiles are plotted. The dotted profile in the top panel represents the Spitzer-Härm temperature profile assuming a spatially constant electron heat flux. The dark square on the right indicates the temperature of the upper thermostat, i.e. the temperature of the boundary at $z = 0.1\ R_\odot$. The bottom panel shows the proton and electron heat flux. As expected, their relative strength is of the order $\sqrt{m_\mathrm{p}/m_\mathrm{e}}$. The Spitzer labeled profile in the bottom panel has been computed via Eq. (14) using the measured electron temperature and density profiles.

3.1. Maxwell–Maxwell boundaries

For the simulations in this section we impose Maxwellian distribution functions at the boundaries, i.e.

$$f_\alpha^{0,\mathrm{L}}(v) \propto \left(\frac{m_\alpha}{2\pi k_\mathrm{B} T_{0,\mathrm{L}}}\right)^{3/2} \mathrm{e}^{-\frac{m_\alpha v^2}{2k_\mathrm{B}T_{0,\mathrm{L}}}}. \qquad (13)$$

The normalized temperature and density profiles as well as both the electron and proton heat flux profiles are shown in Fig. 3. As expected, the electron to proton heat flux ratio is roughly equal to $\sqrt{m_\mathrm{p}/m_\mathrm{e}}$, which means that the energy is predominantly transported by the electrons. The dotted temperature profile in the upper panel has been obtained by assuming that the electron heat flux q_e between the two boundaries is constant and that the heat flux is given by the Spitzer & Härm formula (Spitzer & Härm 1953), which under the above conditions can be approximated by $q_\mathrm{e} \propto T_\mathrm{e}^{5/2}\partial T_\mathrm{e}/\partial z$ (cf. Eq. (14) and Appendix B). From the figure, it appears that if the upper thermostat is located at a distance of 0.1 $R_\odot$ from the surface, the measured profiles are in good agreement with the Spitzer-Härm predicted profiles, which seems to indicate that a classical Spitzer-Härm heat flux can sustain the given temperature profile up to a height of 0.1 $R_\odot$ without the need for some sort of local heating mechanism (e.g. dissipation of MHD waves). However, before accepting this statement as definitive, we have to ensure that the simulated plasma has the characteristics of the coronal plasma. In order to do so, we have to compute the "real" density of the simulated plasma and compare it to the density of the lower solar corona.

In a collisional plasma, the collision frequencies depend on the density (the higher the density the higher is the rate at which a particle undergoes collisions). On the other hand, the gravitational timescale $\sqrt{L/g}$ does not depend on density, which means that density is not just a free parameter as in the collisionless case (cf. Appendix C). We may then estimate the "real" density of the simulated system from the measured electron-proton collision frequency. The measured electron-proton collision frequency in the simulation is approximately $\nu_\mathrm{ep} = 717/t_0^\mathrm{M}$ near the bottom at $z = 0$. This means that in the average an electron collides 717 times with a proton during the time interval t_0^M. Based on the measured collision frequency we may now determine the (unknown) number density n of the simulated plasma. In order to do so we make a slight detour in the field of Fokker-Planck models by observing that in Fokker-Planck models of a close to equilibrium plasma, with temperature T, collision frequency $\overline{\nu}_\mathrm{ep}^\mathrm{FP}$ and density n are intimately connected through Eq. (B.11) (cf. Appendix B). Thus, by using Eq. (B.10) with $\nu_\mathrm{ep} = 717/t_0^\mathrm{M}$ and setting $\overline{\nu}_\mathrm{ep}^\mathrm{FP} = \overline{\nu}_\mathrm{ep}$ in Eq. (B.11) we can estimate the density at the bottom of our simulation region to be $n_0 = 1.01 n_0^\mathrm{M} \approx 10^8$ cm^{-3} which is an acceptable value for the low solar corona.

Similarly, we may compare the electron heat flux observed in our simulation with the Fokker-Planck heat flux for a fully ionized electron-proton plasma (e.g. Spitzer & Härm 1953)

$$q_\mathrm{SH} = -3.19 \times 10^{-3}\, \frac{n_\mathrm{e} k_\mathrm{B}^2 T}{m_\mathrm{e}\overline{\nu}_\mathrm{ep}^\mathrm{FP}} \nabla T \quad \text{(SI units)}. \tag{14}$$

Assuming, as above, that $\overline{\nu}_\mathrm{ep}^\mathrm{FP} = \overline{\nu}_\mathrm{ep}$ with $\overline{\nu}_\mathrm{ep}$ given by Eq. (B.10) and taking the temperature gradient measured in Fig. 3, one finds $q_\mathrm{SH} = -1.0 \times 10^{-3} q_0^\mathrm{M}$, which is in good agreement with the heat flux $q_\mathrm{obs} = -0.9 \times 10^{-3} q_0^\mathrm{M}$ measured in the simulation.

We emphasize that even in the collisionless case there is a heat flux flowing from the hot (upper) to the cold (lower) boundary. The collisionless heat flux q_NC can be computed analytically by applying Liouville's theorem (e.g. Landau & Lifshitz 1960) to the electron and proton distributions in constant gravitational and electric fields and subject to the above-specified boundary conditions, i.e. $T_\mathrm{L} = 1.28 T_0$ with $T_0 = T_0^\mathrm{M}$. Given that the net particle flux is zero, the neutralizing electric field is nothing but the familiar gravitoelectric field (Rosseland 1924)

$$E_\mathrm{g} = \frac{g\, m_\mathrm{p}}{2e}\left(1 - \frac{m_\mathrm{e}}{m_\mathrm{p}}\right). \tag{15}$$

In general, for Maxwell-Maxwell boundaries the collisionless electron heat flux is given by (see Appendix C)

$$q_\mathrm{NC} = \sqrt{\frac{8}{\pi}}\, \frac{n_\mathrm{L} k_\mathrm{B}^{3/2}}{m_\mathrm{e}^{1/2}} \left(T_0 T_\mathrm{L}^{1/2} - T_\mathrm{L} T_0^{1/2}\right) \tag{16}$$

where the electron density at the upper boundary n_L is a complicated function of all other parameters, which turns out to be $n_\mathrm{L} = 0.085 n_0$ for the present case. In the particular case shown in Fig. 3 we have $n_\mathrm{L} \approx 0.1 n_0$ from which we obtain a theoretical collisionless heat flux $q_\mathrm{NC} = -8.9 \times 10^{-3} q_0^\mathrm{M}$ which is much stronger a flux than either q_SH or q_obs. The collisionless heat flux is an upper limit for the electron transported energy flux.

As already stated, in the collisionless regime E_g is the charge neutralizing field. However, in the collisional regime the total electric field is generally made of the sum of E_g and the thermoelectric field (see e.g. Golant et al. 1980; Hinton 1983)

$$E_\mathrm{T} = -\frac{\alpha}{e}\,\frac{\partial}{\partial z}(k_\mathrm{B} T) \tag{17}$$

where α is a constant of order unity. In our simulations, α lies in the range 0.7 to 0.9 when $u_{\alpha\beta}$ in Eq. (9) is smaller than the typical relative velocity between particles of species α and particles of species β (Pantellini & Landi 2000). Fokker-Planck models including all kind of collisions (electron-electron, electron-proton and proton-proton) predict $\alpha = 0.71$ (Spitzer & Härm 1953). The thermoelectric field required to ensure quasi-neutrality in the simulation of Fig. 3 is $E_\mathrm{T} = -0.11$, which is small (but not negligible) compared to the gravitoelectric field $E_\mathrm{g} = 1.17$. The question one may now ask is whether the above results depend on the position of the upper boundary or not. Even if the exact position of the temperature maximum is unknown it is likewise located somewhere between 0.2 and 1 $R_\odot$ above the solar surface (e.g. Ko et al. 1997; David et al. 1998). Without going up to such heights where the zero mass flux hypothesis may no longer be valid, we may just ask the question of what happens if the upper boundary is located at twice the distance, i.e.

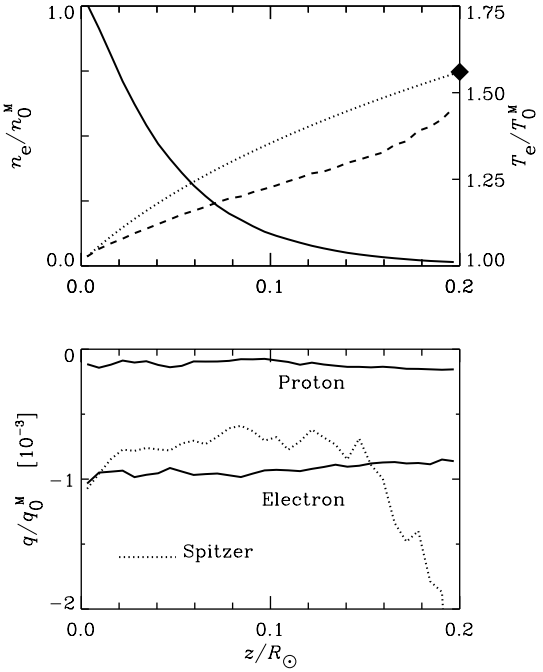

Fig. 4. Maxwell-Maxwell boundaries: Same format as Fig. 3.

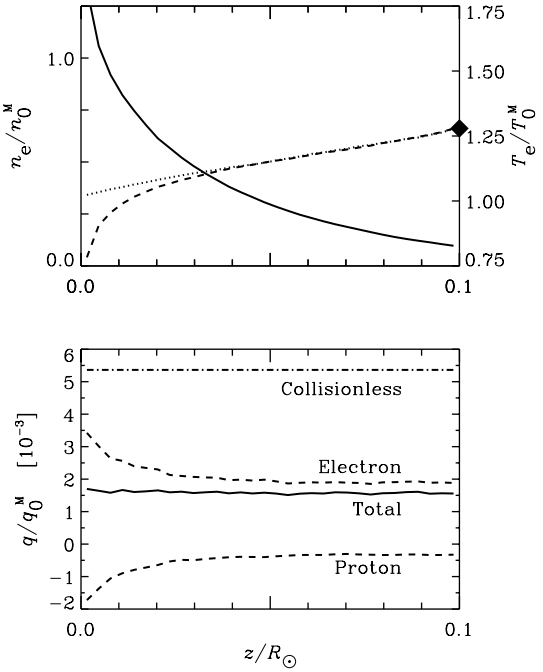

Fig. 5. Kappa-Maxwell boundaries with $\kappa = 4$. The top panel shows the density (solid line) and the temperature (dashed line). Note that the temperature of the left boundary is only $0.49T_0^{\rm M}$ (instead of $T_0^{\rm M}$ used in the Maxwellian case of Fig. 3) to compensate for the strong collisional heating of the plasma with height. The dashed line reproduces the temperature profile of the thermal boundaries case shown in Fig. 3. The lower panel shows the heat flux profiles for electrons and protons as well as the total heat flux (protons + electrons). The collisionless electron heat flux has been computed using Eq. (20). Note that while the proton heat flows down the temperature gradient (the "classical" behavior), the opposite is true for the electrons.

$L = 0.2\ R_\odot$. For coherence, the temperature of the upper thermostat has been chosen to be such that the temperature difference between the two thermostats is twice the value in the first simulation. The results are shown in Fig. 4. Interestingly enough, they are not quite the same as for the smaller system of Fig. 3. One observes that the electron temperature gradient is too weak to smoothly connect to the temperature of the upper thermostat (dark square). The heat that flows from the upper to the lower boundary is simply too weak to sustain the prescribed temperature profile: a local heating mechanism (waves?) is required in this case. The lower panel also shows that the observed electron heat flux is rather badly approximated by the Spitzer-Härm heat flux formula Eq. (14), suggesting that even in the most favorable case of Maxwellian boundary conditions, Eq. (14) does not provide a sufficiently reliable estimate of the thermal heat flux in the lower solar corona.

3.2. Kappa–Maxwell boundaries

In this section we discuss a run with Maxwellian boundary conditions at $z = L$ (as in the previous section) and kappa velocity distribution functions

$$f_\kappa(v) = A_\kappa \left[1 + \frac{v^2}{(\kappa - 3/2)\, v_0^2}\right]^{-\kappa-1} \tag{18}$$

with

$$A_\kappa = \frac{n_0}{2\pi\,(\kappa-3/2)^{3/2}\, v_0^3}\ \frac{\Gamma\,(\kappa+1)}{\Gamma\,(3/2)\,\Gamma\,(\kappa-1/2)}$$

as boundary condition at $z = 0$. In order to ensure energy equipartition among species, we use the same κ index for both protons and electrons and a velocity v_0 (reminiscent of the thermal velocity in a Maxwellian distribution) $\sqrt{m_{\rm p}/m_{\rm e}}$ smaller for protons than for electrons. The density and temperature profiles as well the v_z distribution profiles for electron and protons are shown in Fig. 5 for the case $\kappa = 4$. The upper panel shows that the temperature profile increases very rapidly away from the lower boundary. The rapid rise in temperature is not the manifestation of the collisionless gravitational velocity filtration mechanism first described by Scudder (1992a) but is essentially due to collisional effects. This can be demonstrated easily by estimating the temperature gradient due

to the velocity filtration mechanism. According to Scudder (1992a) the latter is given by

$$T^*(z) = T_0\left[1+\frac{\psi(z)}{(\kappa-3/2)k_{\rm B}T_0}\right] = T_0\left[1+\frac{gz/v_0^2}{\kappa-3/2}\frac{m_{\rm p}+m_{\rm e}}{m_{\rm e}}\right] \quad (19)$$

where $\psi(z)=m_{\rm p}gz+e\phi_{\rm g}(z)=m_{\rm e}gz-e\phi_{\rm g}(z)$ is the total potential energy of a particle with $e\phi_{\rm g}(z)=(m_{\rm e}-m_{\rm p})gz/2$ being the gravitoelectric potential energy (cf. Eq. (15)). According to Eq. (19), the temperature rises linearly with height provided $3/2<\kappa<\infty$. For $\kappa=4$ and $T_0=0.49T_0^{\rm M}$ one has $T^*(z)=T_0(1+1.95z)$ and at $z=0.3$ the temperature should be $T^*(0.3)=1.59T_0=0.78T_0^{\rm M}$ only. Such a temperature is well below the temperature $T(0.3)\approx 1.1T_0^{\rm M}$ observed in the simulation (see Fig. 5) from where we conclude that velocity filtration is not the principal reason for the rapid rise of the temperature profile inward from the $z=0$ boundary. Indeed, the strong inward heating of the plasma is neither due to the gravitational field nor to the temperature gradient imposed by the boundary conditions. The heating is essentially due to the effect of collisions on the κ velocity distribution injected from the $z=0$ boundary. Of course the heating effect decreases with increasing κ and in the limit $\kappa\to\infty$ (the Maxwellian case) it disappears completely, as shown in Fig. 5. Let us give a qualitative physical interpretation of the strong temperature gradient near the kappa boundary. If there were no collisions in the system, a collisionless electron heat flux would flow from the lower to the upper boundary (see Eq. (20)). However, the system is collisional and collisions do always act in the sense of a reduction of the heat flux. This is clearly visible in Fig. 5, where the electron heat flux is seen to decreases inwards from the right hand boundary over a distance of the order of $0.3L$, inducing a strong heating of the plasma over this very same distance. Since protons become thermalized much more rapidly than electrons, the former carry energy in a "classical" way, i.e. protons transport heat down the temperature gradient against the electron heat flux. We note that the total (proton + electron) heat flux is constant despite the fact that this is not so for individual species. Thus energy is transferred from electrons to protons and vice versa.

This peculiar behavior of the plasma near a kappa boundary does not show on the temperature profiles in Fig. 2 of Dorelli & Scudder (1999). The difference is due to the restrictions imposed upon the general shape of the electron velocity distribution functions by Dorelli and Scudder. In their paper, the general form of the electron velocity distribution function is a first order truncated Legendre polynomial expansion. Thus, at any given height z, the electron velocity distribution is a superposition of an isotropic kappa distribution function and an odd function of v_z (the first order correction) which does not affect the even moments of the velocity distribution function so that the temperature is by construction determined by the zero order distribution only, i.e. by the isotropic kappa distribution. Our simulation shows that restricting the Legendre expansion to the first order term only does not allow for a correct description of the temperature profiles especially for boundary conditions with low κ indices. However, as we shall see in the remainder of this section, and in the next section, the unusual behavior of the heat flux (unusual from a fluid point of view) described by Dorelli & Scudder (1999), remains qualitatively valid for small values of κ.

The average total heat flux observed in our simulation is $q_{\rm obs}\approx 1.6\times10^{-3}q_0^{\rm M}$ and is mainly carried by the electrons (cf. Fig. 5). The very fact that $q_{\rm obs}>0$ means that energy flows upwards, i.e. from the cold to the hot thermostat. This may appear to be a surprising result as it seems to contradict the second law of thermodynamics (cf. the Introduction in Scudder 1992b). However, the behavior of our system can be described by the Boltzmann equation with a particular scattering operator, defined by the rules outlined in Sect. 2.3, and must therefore obey Boltzmann's H-theorem (Boltzmann 1872) and all fundamental laws of thermodynamics.

As a guiding reference for future discussion, we compute the collisionless electron heat flux $q_{\rm NC}$ by applying Liouville's theorem to the proton and electron velocity distribution functions imposed by the boundary conditions at $z=0,L$ and the constraint of zero bulk velocity. Under these conditions, the charge-neutralizing electric field is precisely the gravitoelectric field $E_{\rm g}$ given by Eq. (15). Straightforward application of Liouville's theorem then leads to

$$q_{\rm NC} = \sqrt{\frac{8}{\pi}}\frac{n_{\rm L}k_{\rm B}^{3/2}}{m_{\rm e}^{1/2}}\frac{\sqrt{T_{\rm L}^*T_{\rm L}}}{\sqrt{T_{\rm L}^*}+B_\kappa\sqrt{T_{\rm L}}}\left[\left(\frac{\kappa-3/2}{\kappa-2}\right)T_{\rm L}^*-T_{\rm L}\right] \quad (20)$$

where the density $n_{\rm L}=n(L)$ is a complicated function of the other parameters of the problem (cf. Appendix C), $T_{\rm L}^*\equiv T^*(L)$ and B_κ is a κ dependent constant

$$B_\kappa\equiv\frac{\Gamma(\kappa-1/2)}{(\kappa-3/2)^{1/2}\Gamma(\kappa-1)}. \quad (21)$$

With the parameters of the present simulation (i.e. $\kappa=4$, $T_{\rm L}=1.28T_0^{\rm M}$) one finds $n_{\rm L}=0.1n_0^{\rm M}$, and $q_{\rm NC}=5.4\times10^{-3}q_0^{\rm M}$ which, as expected, is stronger than the observed collisional electron heat flux observed in the simulation (Fig. 5). However, the general behavior of the system is neither that of a strongly collisional plasma with a Spitzer & Härm heat flux (1953) nor that of a collisionless plasma since the electron heat flux intensity is both spatially variable and substantially smaller than the collisionless value $q_{\rm NC}$.

The v_z velocity distributions for both electrons and protons at $z=0.5L$ are shown in Fig. 6. From the figure it appears that while the proton distribution is essentially Maxwellian, the electron distribution has still substantial

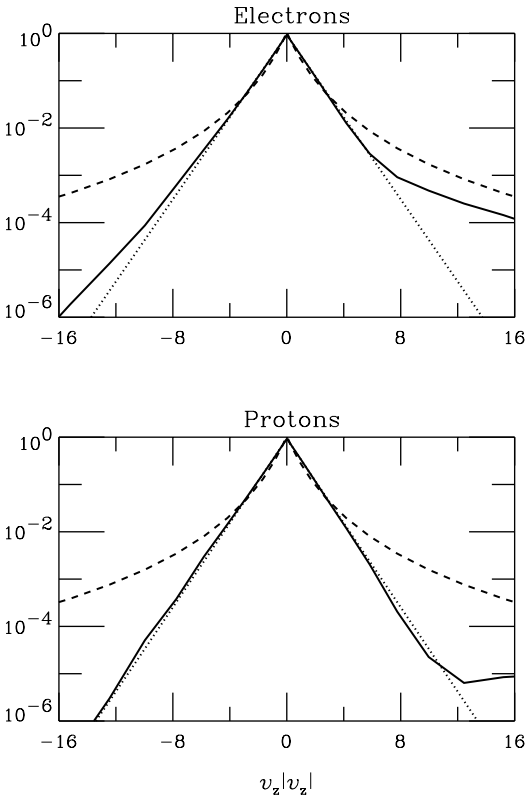

Fig. 6. Velocity distribution functions for kappa-Maxwell boundary conditions ($\kappa = 4$) at height $z = 0.5L$ for the case $L = 0.1\ R_\odot$ shown in Fig. 5. Velocities have been normalized to the local thermal velocity $v_T \equiv \sqrt{2k_\mathrm{B}T/m}$ of the relevant species. The dotted curves are Maxwellians normalized to the local temperature and density. The dashed curves are kappa distributions with $\kappa = 4$ where n_0 and v_0 are determined by the local density and temperature (cf. Eq. (18)).

suprathermal tails, particularly for large positive velocities $v_z \gtrsim 2.5$. The obvious reason is that the collisional cross section for a suprathermal proton vs. thermal electron collision is only weakly velocity dependent given that the relative velocity is always approximately v_e, independent of the proton's velocity. Thus suprathermal protons are efficiently thermalized by collisions with thermal electrons. This is not so for a suprathermal electron since its velocity with respect to either a thermal proton or a thermal electron is, by definition, larger than v_e. Given that the collisional cross section decreases as the forth power of the relative velocity it then follows that the thermalization of the suprathermal electrons is much less efficient than the thermalization of the suprathermal protons.

Let us conclude this section with a short discussion of the simulation in the light of the Dorelli & Scudder (1999) model (we shall call it the DS model). As already stated, there are some qualitative similarities between the behavior of the plasma observed in our simulations and the behavior of the plasma in their model. However, the very particular form of the distribution function in the DS model implies that their temperature profiles do differ significantly from ours. As already stated, the difference stems from the fact that in the DS model the just described collisional heating near a kappa boundary is missing, essentially because by construction the temperature in the DS model is that of a κ distribution function with the same κ index throughout the whole plasma slab. The reason for the DS temperature profile not being the collisionless temperature profile is due to the fact that their electric field (which has not been computed explicitly by the authors) is not Rosseland's gravitoelectric field (cf. Eq. (15)), which happens to be charge neutralizing in the collisionless case only. Despite these substantial differences, we do observe an upward-directed heat flux for the $\kappa = 4$ in accordance with the DS model which predicts an upward directed heat flux for $\kappa \lesssim 10$.

How sensitive are the above results on the rather arbitrary position of the upper boundary? Figure 7 shows that doubling the size of the system and changing the temperature of the upper thermostat accordingly does not change the conclusions in a very substantial way. The main difference is that the average temperature gradient is slightly reduced with respect to the shorter system. As a consequence, the temperature of the plasma near the upper boundary is clearly below the prescribed temperature of the boundary (dark square on the figure). Thus, even with a kappa index as small as $\kappa = 4$ one has to invoke a local heating mechanism to sustain the prescribed temperature gradient up to the $z = 0.2$ level. For comparison, if the system was entirely collisionless, the temperature near the upper boundary would be as high as $1.7T_0^\mathrm{M}$, i.e. above the temperature of the boundary.

The temperature profiles for different kappa indices of the $z = 0$ boundary distribution functions are plotted in Figs. 8 and 9. For each run the temperature of the $z = 0$ boundary has been adjusted to obtain equal mid-box temperatures and temperature gradients. The collisional heating near the $z = 0$ boundary is clearly visible on all plotted profiles except the $\kappa = \infty$ case. Figure 8 shows that if the upper boundary (the source of energy) is located at $z = 0.1\ R_\odot$ the system is able to sustain the prescribed temperature profile independently of the κ index. On the other hand, Fig. 9 shows that if the upper boundary is located at a height $z = 0.2\ R_\odot$ the system is no longer able to sustain the $1.4 \times 10^6\ \mathrm{K}/R_\odot$ temperature gradient unless some local heating is at work. Indeed, all temperature profiles reach the $z = 0.2\ R_\odot$ level with a temperature which is clearly below the value imposed by the boundary. We note in passing that the steepening of the temperature profiles above $z \approx 0.17\ R_\odot$ is not due solely to the vicinity of the hot boundary but also to the collisionless gravitational velocity filtration. The reason for the collisionless filtration to become more efficient above $z \approx 0.17\ R_\odot$ is

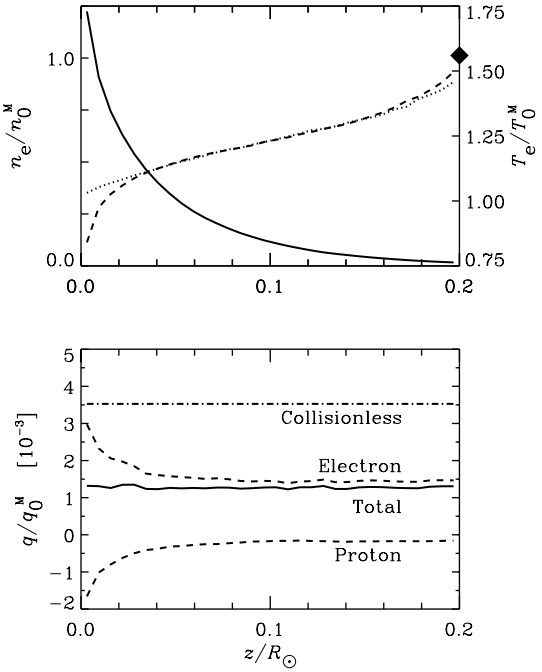

Fig. 7. Kappa-Maxwell boundaries with $\kappa = 4$. The format of the figure is the same as in Fig. 5. Note that the upper boundary is located at $z = 0.2\ R_\odot$ and the temperature of the upper thermostat is the same as for the Maxwell-Maxwell case of Fig. 4. Again, the temperature of the lower thermostat is $0.49T_0^{\rm M}$, as in Fig. 5. The dashed line in the top panel reproduces the temperature profile for the thermal boundary case of Fig. 4. As in the shorter system of Fig. 5, heat flows upward in the temperature gradient.

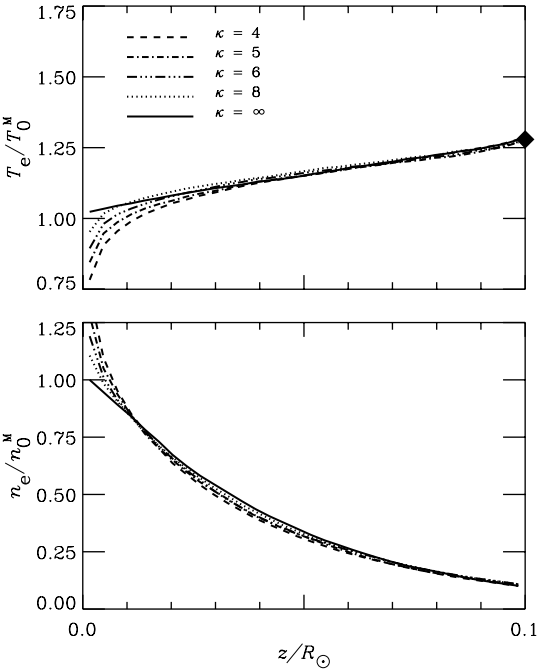

Fig. 8. Temperature and density profiles for kappa-Maxwell boundary conditions. Each profile corresponds to a different kappa index ranging from $\kappa = 4$ (dotted line) to $\kappa = \infty$ (solid line). The heat flux associated with each profile are shown in Fig. 10.

that at such heights the density has become extremely low (of the order 10^{-2} times the density at $z = 0$) and collisions much less effective in thermalizing the electron distribution function which still have suprathermal tails at a non negligible level (cf. Fig. 6) going into the heating via the collisionless gravitational velocity filtration mechanism. Of course gravitational filtration does not work in the Maxwellian case, which is the reason for the temperature to grow more slowly for $z \gtrsim 1.7\ R_\odot$ in the Maxwellian case than in the $\kappa = 4$ case (cf. Fig. 7).

Even though the temperature and density profiles appear to be quite similar over the major part of the simulation domain for all cases shown in Figs. 8 and 9, the transport properties are different. This is particularly evident for the heat flux. In Fig. 10 are plotted the values of the total heat flux observed in the simulations for different values of the kappa index. The horizontal solid line represents the total heat flux for the Maxwell–Maxwell boundaries case, i.e. the classical Spitzer & Härm (1953) heat flux for the given temperature gradient and plasma parameters. For the kappa–Maxwell simulations, the energy flows depend sensitively on κ; for $\kappa \lesssim 4$ the heat flux is positive and flows from the cold to the hot boundary. For $\kappa = 5$ the heat flux is negative but its intensity is still significantly smaller than the classical Spitzer-Härm value. For $\kappa \gtrsim 6$ the heat flux is essentially Spitzer-Härm. The index $\kappa_{\rm o}$ below which the energy flows in the upward direction can be determined in the collisionless limit using Eq. (20) and the condition $q_{\rm NC} \geq 0$ from where one obtains

$$\kappa \leq \kappa_{\rm o} = \frac{1}{2}\frac{T_{\rm L}}{T_{\rm L} - T_0}\left(1 + 2\frac{\psi_{\rm L}}{k_{\rm B}T_{\rm L}} + 3\frac{T_{\rm L} - T_0}{T_{\rm L}}\right). \qquad (22)$$

Plugging the parameters of the above simulations into Eq. (22) one finds $\kappa_{\rm o} \approx 12$ which is significantly larger than the value we find in Fig. 10. We conclude by noting that in the DS model, reversal occurs for $\kappa \approx 10$ which is also the value for which the collisionless heat flux reverses in the kappa-kappa case (see Eq. (24) below). Our simulations indicate that the effect of collisions on both the heat flux and the temperature profile is much stronger than suggested by the DS model.

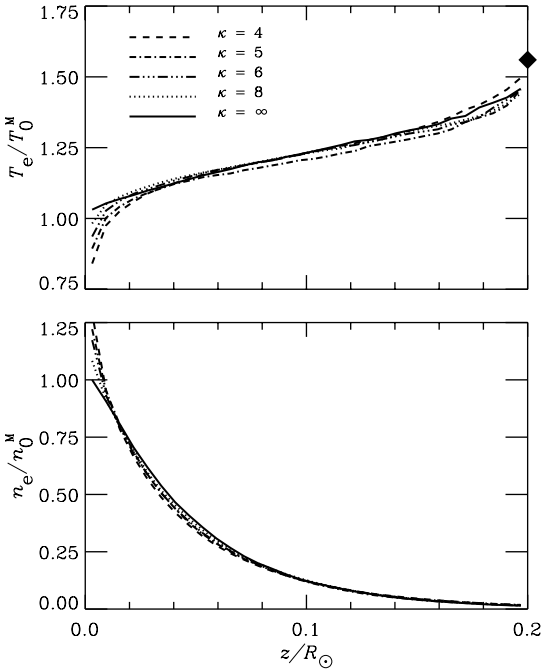

Fig. 9. Same as Fig. 8 for the case extending up to 0.2 $R_\odot$.

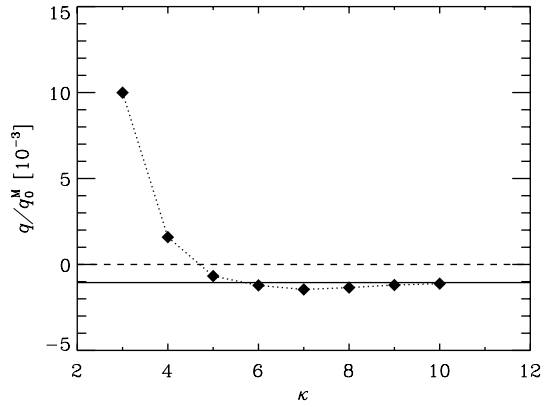

Fig. 10. Heat flux measured in the simulations for kappa-Maxwell boundaries shown in Fig. 8. Solid line represents the Spitzer-Härm value for the Maxwell-Maxwell case (cf. Fig. 3).

3.3. Kappa–kappa boundaries

In this section we briefly discuss the case where the velocity distribution functions are kappa at both boundaries $z = 0$ and $z = L$. The collisionless electron heat flux $q_{\rm NC}$ can be computed analytically using the general expressions given in Appendix C

$$q_{\rm NC} = \sqrt{\frac{8}{\pi}}\frac{n_{\rm L}k_{\rm B}^{3/2}}{m_{\rm e}^{1/2}}\frac{1}{B_\kappa}\frac{\kappa-3/2}{\kappa-2}\cdot \sqrt{T_{\rm L}^* T_{\rm L}}\left(\sqrt{T_{\rm L}^*}-\sqrt{T_{\rm L}}\right). \quad (23)$$

As for the kappa-Maxwell case, one can determine the limiting value $\kappa_{\rm r}$ below which heat flows in the direction of the temperature gradient by setting $q_{\rm NC} \geq 0$ in Eq. (23). The result is

$$\kappa \leq \kappa_{\rm r} = \frac{3}{2} + \frac{\psi_{\rm L}}{k_{\rm B}(T_{\rm L}-T_0)}. \quad (24)$$

For the parameters we use (which are the same as in the Dorelli & Scudder 1999, paper) one finds $\kappa_{\rm r} \approx 10$ which, of course, is precisely the value predicted by the DS model. Indeed, the main effect of collisions in the DS model is to reduce the intensity of the heat flux, not its sign. We note that $\kappa_{\rm r}$ is always smaller than the heat flux reversal value $\kappa_{\rm o}$ found in the kappa-Maxwell case by an amount $T_{\rm L}/2(T_{\rm L}-T_0)$. This difference is due to the fact that heat flows more easily up the temperature gradient if there is no downward-directed suprathermal tail due to the kappa boundary condition at $z = L$.

We have opted not to present simulations with kappa-kappa boundary conditions for two reasons. The main reason is that from a conceptual point of view it does not make much sense to suppose that there is a generator of kappa distributions located at an arbitrary height L above the coronal base. How shall one choose this point? What is the most appropriate value of the kappa index there? Our approach consists of assuming that there is a mechanism (e.g. shocks) capable of generating suprathermal tails at the base of the corona, i.e. at a natural boundary of the solar atmosphere. This is not so for the fictitious upper boundary we suppose to be located at 0.1 $R_\odot$ (following Dorelli & Scudder 1999) or 0.2 $R_\odot$, given that the solar corona extends out to distances of the order of many tens of AU. Also, given the strong collisionality of the system, we found the choice of the Maxwellian distribution to be the most natural one (or the less artificial one).

Simulations with a kappa boundary located at much larger distances, where the wind is supersonic and essentially collisionless, may be realistic as non thermal distributions are systematically observed there. Such simulations may become possible in the near future.

We conclude this section by noting that in the DS model the lower and the upper boundary conditions are not independent of each other, as the zero order distribution function is supposed to be a kappa distribution, with the same index κ, in all points of the system. The constant kappa index assumption in the DS model finds its justification in the fact that the kappa index is known to remain unchanged in the collisionless case (Scudder 1992a). As a consequence, the above discussion on the choice of the upper boundary condition for our simulation is irrelevant in the DS model where the two boundaries cannot be treated

separately due to the constant constant kappa index assumption.

4. Conclusion

There we summarize the most important aspects arising from our simulations. First of all, as already suggested by other authors, it appears that due to their rapid thermalization, on a scale much shorter than the density or temperature scale of height, proton velocity distributions are close to Maxwellian in the solar corona. Unless some non-thermal local ion acceleration mechanism (e.g. some kind of magnetic turbulence) is at work, the Spitzer & Härm (1953) theory provides a good description of the proton transport properties in the corona. This seems not to be the case for the electron velocity distributions which, if not Maxwellian at a given height (at $z = 0$ in the simulation), remain non Maxwellian over distances greater than the scale of height of macroscopic quantities. More specifically, if the electron velocity distributions have suprathermal tails, there is no hope for the Spitzer-Härm theory to provide the correct value of the electron heat flux. On the other hand, heat flux density and temperature profiles cannot be described by Scudder's collisionless model either (Scudder 1992a). This has been demonstrated by Anderson (1994), who also showed that the effect of collisions on the velocity filtration model is not a minor effect, which means that linearized collisional operators are inadequate for the description of the transport properties in the corona. Dorelli & Scudder (1999) tried to overcome this difficulty by expanding kappa distributions in terms of Legendre polynomials. This approach has the advantage of not requiring the first order Legendre term f_1 to be small compared to the zero order term f_0. However, the limitation of the development to the first order term only turns out to be too restrictive because of the strong up-down anisotropy of the problem. In particular, the temperature profiles cannot be conveniently described using a Legendre expansion truncated after the first order term, given that the latter does not directly contribute to the temperature. This is not very surprising. Anderson (1994) already suggested that the collisionless temperature profile is strongly modified by collisions (see Fig. 4 in his paper). Here we show that the collisionless temperature profiles of kappa distributions are strongly modified by collisions and that the effect is strongest close to the boundaries where the kappa distributions are artificially maintained (the $z = 0$ boundary in our simulations). The simulations show that the collisional heating of the plasma near a kappa boundary increases with decreasing kappa index. The scale height of the collisional heating is determined by the relaxation length of the electron velocity distribution function, which for coronal plasma conditions is much shorter than the assumed temperature scale height $[(\partial T/\partial z)/T]^{-1} \approx 0.4\ R_\odot$. The heating of a plasma near a kappa boundary could not be observed by Dorelli & Scudder (1999) due to the limited impact on the temperature that collisions are allowed to have in their model. One of the key points of the DS model was to show that the predictions of the collisionless gravitational velocity filtration model (Scudder 1992a) for the corona are only weakly modified by collisions. For example, for a given coronal temperature gradient, heat flux reversal occurs at the same kappa value whether collisions are included or not, the only effect of collisions being a reduction of the heat flux intensity. In reality, the effect of collisions on the collisionless results happens to be much more destructive than suggested by the DS model. We find that in the coronal plasma, heat flux reversal already occurs at $\kappa \approx 4$. For $\kappa = 5$, the heat flux is already of the Spitzer-Härm type whereas the DS model predicts strong departures from the classical heat conduction even for $\kappa \gtrsim 10$. Our simulations also suggest that velocity filtration alone is not capable of sustaining the assumed coronal temperature gradient of 1.4×10^6 K$/R_\odot$ unless $\kappa < 4$. This means that unless some extremely intense source of suprathermal electrons exists near the base of the corona some local heating mechanism (e.g. waves) has to be at work between the base of the corona and the coronal temperature maximum, which we assume to be at a height $z \gtrsim 0.2\ R_\odot$. Thus, gravitational velocity filtration may be capable of sustaining the observed temperature gradient without substantial heating, provided electron distributions near the coronal base have strong suprathermal tails. Even if present observations of the corona do not allow us to exclude the presence of strongly non thermal electron distributions at low altitudes, it seems hard to imagine a mechanism (e.g. Fermi acceleration, Fermi 1954) capable of sustaining such distributions given the high collisionality of the plasma. The conclusion would eventually be different if kappa distributions were injected into the system from the top, i.e. from the solar wind where non thermal electron velocity distributions are commonplace. However, this is much more general problem which cannot be treated in zero mass flux and plane parallel approximation used in this paper.

Appendix A: The algorithm

The structure of the algorithm for advancing the particles of the system of Fig. 1 during a given time interval is very similar to the algorithm described in Pantellini (2000) for the case of hard sphere particles of equal mass and no charge. The main difference is that the presence of an electric field makes the integration of the equations of motion slightly more complicated (not all particles feel the same acceleration). In addition, a non negligible fraction of the simulation time must be spent in computing the charge-neutralizing electric field.

The algorithm can be summarized as follows:

1. Initialize the velocities $\{\boldsymbol{v}_i(t = 0)\}$ and the positions $\{z_i(t = 0)\}$ of N protons and N electrons. Order the particles based on their height such that $0 < z_1 < z_2 < ... < z_{2N} < L$. Make an initial guess for the external electric field E_0 and eventually choose a non zero value

for the variable ϵ (cf. Eqs. (4) and (5)) if polarization effects are expected to be important;
2. Determine for each pair of neighboring particles, with indices i and $i-1$ and for $i = 2, 3, ...\, 2N$, the time interval δt_i until their next collision. If particle i and $i-1$ do not collide in the future, we shall set $\delta t_i = \infty$. Also compute the time δt_1 and δt_{2N+1} until the next collision of the first and last particle with one of the boundaries. The equations of motion to be solved are Eqs. (1) and (2) with the electric field felt by the particle i being $E_i + q_i\,\epsilon/2$, where E_i is recursively given by Eqs. (4) and (5);
3. Determine the time interval $\delta t_{\min} = \min\{\delta t_i\}$ until the next collision in the system. Let $I \in \{1, 2, ..., 2N+1\}$ be the index of the particle making this collision;
4. Advance all particles through the time interval $\delta t_{\min}$;
5. Make the collision between particle I and particle $I-1$ if $I \in \{2, 3, ..., 2N\}$ according to the prescriptions given in Sect. 2.3. If $I = 1$ or $I = 2N+1$ (particle-wall collision), draw a new velocity vector for the particle using, in particular, Eqs. (10) and (11);
6. If the system's charge neutrality is not satisfactory, increase or decrease E_0 in order to reduce departures from neutrality. E_0 should not be corrected too often. Ideally one should not update E_0 before the system has become stationary. This can be a very long time since it is of the order of the longest macroscopic relaxation time. For a Maxwellian plasma, the characteristic timescales could be $\sqrt{L/g}$ or L/c, where c is the sound speed. This step is rarely performed;
7. Repeat steps 2–5 until a given time level has been reached.

The computational time needed to go through one cycle is proportional to N. A more sophisticated version of the algorithm allows us to make the computational time be proportional to $\sqrt{N}$ instead.

Appendix B: Comparison with Fokker–Planck model

Let's consider a relaxed system where N particles of species α and N particles of species β are uniformly distributed in a box of dimension L. Let's consider particles which have relative velocities in the spherically geometric velocity-space element $2\pi u^2 \mathrm{d}u\mathrm{d}\mu$, where $\mu \equiv \cos\theta$ (θ being the angle between $\boldsymbol{u}$ and the z direction). The number of collisions per time unit experienced by a particle of species α with particles of species β with relative velocities near $\boldsymbol{u}$ is then given by

$$\mathrm{d}\nu_{\alpha\beta} = u\,|\mu|\,R_{\alpha\beta}(u) f_{\alpha\beta}(u,\mu)\,2\pi u^2 \mathrm{d}u\mathrm{d}\mu \tag{B.1}$$

where $R_{\alpha\beta}$ is the collision probability function defined in Eq. (9) and $f_{\alpha\beta}$ is the distribution function for the relative velocities between α and β particles. If the distribution functions for both species are Maxwellians with thermal velocities $v_\alpha = \sqrt{2k_\mathrm{B}T_\alpha/m_\alpha}$ and $v_\beta = \sqrt{2k_\mathrm{B}T_\beta/m_\beta}$, respectively, one has

$$f_{\alpha\beta}(u) = \frac{1}{\pi^{\frac{3}{2}} v_{\alpha\beta}^3} \frac{N}{L}\,\mathrm{e}^{-u^2/v_{\alpha\beta}^2} \tag{B.2}$$

with $v_{\alpha\beta}^2 \equiv v_\alpha^2 + v_\beta^2$. Integration of Eq. (B.1) over all velocities and directions then gives the total collision frequency

$$\nu_{\alpha\beta} = \frac{4}{\sqrt{\pi}} \frac{N}{L} \frac{1}{v_{\alpha\beta}^3} \int_0^1 \mu \mathrm{d}\mu \int_0^\infty R_{\alpha\beta}(u) u^3 \mathrm{e}^{-u^2/v_{\alpha\beta}^2} \mathrm{d}u \tag{B.3}$$

i.e.

$$\nu_{\alpha\beta} = \frac{1}{\sqrt{\pi}} \frac{N}{L} v_{\alpha\beta} \Psi(\tilde{u}_{\alpha\beta}^2) \tag{B.4}$$

where $\tilde{u}_{\alpha\beta}^2 \equiv u_{\alpha\beta}^2/v_{\alpha\beta}^2$ and Ψ is the function

$$\Psi(x) \equiv \left[1 - (1+x)\mathrm{e}^{-x} + x^2 \Gamma\,(0, x)\right] \tag{B.5}$$

with

$$\Gamma(0, x) = \int_x^\infty \mathrm{e}^{-t} t^{-1} \mathrm{d}t$$

being the incomplete gamma function of order 0. Sample values for the function $\Psi(x)$ are given in Table B.1.

Table B.1. Sample values for the function defined in Eq. (B.5); $x = \infty$ correspond to hard spheres collision.

x	0.125	0.25	0.5	1	∞
$\Psi(x)$	0.03256	0.0918	0.230	0.484	1

Let us now consider the case of a thermalized and fully ionized electron-proton plasma and let's choose $u_{\alpha\beta}$ in Eq. (9) by setting

$$u_{\alpha\beta} = v_{\alpha\beta}/\sqrt{2} \tag{B.6}$$

so that the dependency on Ψ is the same for all kind of collisions (i.e. proton-proton, electron-proton, electron-electron). For $m_\mathrm{p} \gg m_\mathrm{e}$, we then have $v_\mathrm{ee} = \sqrt{2} v_\mathrm{e}$, $v_\mathrm{ep} \simeq v_\mathrm{e}$ and $v_\mathrm{pp} = \sqrt{m_\mathrm{e}/m_\mathrm{p}}\, v_\mathrm{ee}$ which leads to the familiar relationship between the collision frequencies

$$\nu_\mathrm{ee} = \sqrt{2}\nu_\mathrm{ep} = \sqrt{\frac{m_\mathrm{p}}{m_\mathrm{e}}}\nu_\mathrm{pp}. \tag{B.7}$$

It is common practice to define the collision frequency $\overline{\nu}_{\alpha\beta}$ as the rate of momentum exchange between particles of species α and particles of species β. For isotropic distribution functions and elastic collisions one has (Golant et al. 1980)

$$\overline{\nu}_{\alpha\beta} = \left\langle \frac{\partial}{\partial u_\mathrm{k}} \left[u_\mathrm{k} \nu_{\alpha\beta}^*(u)\right] \right\rangle \tag{B.8}$$

where $\langle ... \rangle$ means averaging over the relative velocities distribution Eq. (B.2) and $\nu_{\alpha\beta}^* \equiv (N/L) u |\mu| R_{\alpha\beta}(u)$ is the collision frequency for the particles in the velocity-space

element $2\pi u^2 \mathrm{d}u\mathrm{d}\mu$. Carring out the integration, using the collision frequency Eq. (B.4), leads to

$$\overline{\nu}_{\alpha\beta} = \frac{2}{\sqrt{\pi}}\frac{N}{L}v_{\alpha\beta}[1-(1+\tilde{u}_{\alpha\beta}^2)\mathrm{e}^{-\tilde{u}_{\alpha\beta}^2}] \quad \text{(B.9)}$$

$$= \nu_{\alpha\beta}\frac{2}{\Psi(\tilde{u}_{\alpha\beta}^2)}\left[1-(1+\tilde{u}_{\alpha\beta}^2)\mathrm{e}^{-\tilde{u}_{\alpha\beta}^2}\right]. \quad \text{(B.10)}$$

On the other hand, the Fokker-Planck electron-proton transport collision frequency for a plasma with an electron density n and temperature T is known to be (e.g. Golant et al. 1980)

$$\overline{\nu}_{\mathrm{ep}}^{\mathrm{FP}} = \frac{ne^4}{3\varepsilon_0^2 m_{\mathrm{e}}^{1/2}(2\pi k_{\mathrm{B}}T)^{3/2}}\ln\Lambda \quad \text{(B.11)}$$

where

$$\ln\Lambda = \ln\left[\frac{12\pi(\varepsilon_0 k_{\mathrm{B}}T)^{3/2}}{n^{1/2}e^3}\right]$$

is the Coulomb logarithm. We emphasize that the collision rate given in Eq. (B.11) is based on the time interval it takes for a thermal electron's trajectory to become strongly deflected by the protons in the system. After setting $\overline{\nu}_{\mathrm{ep}}^{\mathrm{FP}} = \overline{\nu}_{\alpha\beta}$ we find the number of electrons N needed to simulate a plasma with a given Fokker-Planck collision frequency $\overline{\nu}_{\mathrm{ep}}^{\mathrm{FP}}$ to be

$$N = \frac{1}{24\pi}\frac{ne^4\ln\Lambda}{\varepsilon_0^2 k_{\mathrm{B}}^2 T^2}\frac{L}{\left[1-\left(1+\tilde{u}_{\mathrm{ep}}^2\right)\mathrm{e}^{-\tilde{u}_{\mathrm{ep}}^2}\right]}. \quad \text{(B.12)}$$

For typical coronal conditions, e.g. $n = 10^8$ cm^{-3} and $T = 5\times10^5$ K one has $\overline{\nu}_{\mathrm{ep}}^{\mathrm{FP}} = 20.4$ s^{-1}. Thus, in order to simulate a plasma slab of thickness $L = 0.1\ R_\odot$ some $N \simeq 4000$ particles are required. We note that the number of particles needed to simulate a given plasma strongly depends on the choice of $u_{\alpha\beta}$ in Eq. (B.6): the smaller the ratio $u_{\alpha\beta}/v_{\alpha\beta}$ the larger N and the heavier the simulation. One should therefore choose $u_{\alpha\beta}/v_{\alpha\beta}$ as large as possible remembering that when $u_{\alpha\beta}/v_{\alpha\beta} \gtrsim 1$ the macroscopic characteristics of the plasma (e.g. heat conduction, thermoelectric coefficient, etc.) are no longer those of a Coulomb collision dominated plasma because of the large number of hard-sphere type collisions involving all particles moving at relative velocities $u < u_{\alpha\beta}$. The properties of such a plasma may differ substantially from the properties of a real electron-proton plasma!

Appendix C: The collisionless limit

Let us consider a collisionless electron-proton plasma plunged in a gravitational field $g(z) = -\partial\phi_{\mathrm{G}}/\partial z$, which is not necessarily constant. At the boundaries, $z = 0$ and $z = L$, particles are injected with kappa type velocity distributions with temperatures T_0 and T_{L} and kappa indices κ_0 and κ_{L}, respectively. Due to the unequal mass of electrons and protons, an electric field $E(z) = -\partial\phi_{\mathrm{E}}/\partial z$ is needed to ensure local charge neutrality. The stationary distribution function $f(v,z)$ for particles of mass m and charge q with a monotonical potential energy

$$\psi(z) = m\phi_{\mathrm{G}}(z) + q\phi_{\mathrm{E}}(z) \quad \text{(C.1)}$$

can be computed using Liouville's theorem, viz.

$$f(v,z) = \begin{cases} f_0(v,z) & v_z > -w \\ f_0^*(v,z) & v_z < -w \end{cases} \quad \text{(C.2)}$$

where $w^2 \equiv 2\left[\psi_{\mathrm{L}} - \psi(z)\right]/m$ and

$$f_0 = \left(\frac{m}{2\pi k_{\mathrm{B}}T_0}\right)^{3/2}\frac{A_0\Gamma(\kappa_0+1)}{(\kappa_0-3/2)^{\frac{3}{2}}\Gamma(\kappa_0-1/2)}\left[1+\frac{mv^2+2\psi}{(\kappa_0-3/2)2k_{\mathrm{B}}T_0}\right]^{-\kappa_0-1} \quad \text{(C.3)}$$

$$f_0^* = \left(\frac{m}{2\pi k_{\mathrm{B}}T_0^*}\right)^{3/2}\frac{A_{\mathrm{L}}\Gamma(\kappa_{\mathrm{L}}+1)}{(\kappa_{\mathrm{L}}-3/2)^{\frac{3}{2}}\Gamma(\kappa_{\mathrm{L}}-1/2)}\left[1+\frac{mv^2+2\psi}{(\kappa_{\mathrm{L}}-3/2)2k_{\mathrm{B}}T_0^*}\right]^{-\kappa_{\mathrm{L}}-1} \quad \text{(C.4)}$$

and where we have set $\psi(0) = 0$ and $\psi(L) = \psi_{\mathrm{L}}$. In Eq. (C.4) T_0^* is the temperature of the downward-traveling kappa distribution at $z = 0$ which is linked to the temperature $T_{\mathrm{L}} = T(z)$ via (Scudder 1992a)

$$T_0^* = T_{\mathrm{L}}\left[1-\frac{\psi_{\mathrm{L}}}{(\kappa_{\mathrm{L}}-3/2)\,k_{\mathrm{B}}T_{\mathrm{L}}}\right]. \quad \text{(C.5)}$$

The problem has two unknown parameters, A_0 and A_{L}, which are determined by the condition of zero bulk velocity and $n_{\mathrm{L}} = n(L)$. The electric field profile is obtained by imposing local charge neutrality. We shall show that this field corresponds to the field required to make the potential energy of protons and electrons to be equal (cf. Eq. (C.14)).

Let $\chi(v,\mu)$ be an arbitrary function of the absolute velocity v and $\mu = \cos\theta$, where θ is the angle between z direction and the velocity. The mean value of this function is then given by

$$\langle\chi\rangle = 2\pi\int_0^w\int_{-1}^1 \mathrm{d}\mu v^2\mathrm{d}v\chi f_0 + 2\pi\int_w^\infty\int_{-w/v}^1 \mathrm{d}\mu v^2\mathrm{d}v\chi f_0 + 2\pi\int_w^\infty\int_{-1}^{-w/v} \mathrm{d}\mu v^2\mathrm{d}v\chi f_0^*. \quad \text{(C.6)}$$

For example, the density is obtained by integrating of Eq. (C.6) with $\chi = 1$:

$$n(z) = \frac{A_0}{2}\left[1+\frac{\psi}{k_{\mathrm{B}}T_0(\kappa_0-3/2)}\right]^{-\kappa_0+1/2}\left[1+\mathcal{K}(\kappa_0-1,\xi_0)\right] + \frac{A_{\mathrm{L}}}{2}\left[1+\frac{\psi}{k_{\mathrm{B}}T_0^*(\kappa_{\mathrm{L}}-3/2)}\right]^{-\kappa_{\mathrm{L}}+1/2}\left[1-\mathcal{K}(\kappa_{\mathrm{L}}-1,\xi_{\mathrm{L}})\right] \quad \text{(C.7)}$$

where

$$\mathcal{K}(\kappa,\xi) \equiv \frac{2}{\sqrt{\pi}} \frac{\Gamma(\kappa+1)}{\Gamma(\kappa+1/2)} \int_0^{\xi} \frac{\mathrm{d}x}{(1+x^2)^{\kappa+1}} \tag{C.8}$$

and

$$\xi_0 \equiv \sqrt{\frac{\psi_{\mathrm{L}}-\psi}{(\kappa_0-3/2)(k_{\mathrm{B}}T_0+\psi)}} \tag{C.9}$$

$$\xi_{\mathrm{L}} \equiv \sqrt{\frac{\psi_{\mathrm{L}}-\psi}{(\kappa_{\mathrm{L}}-3/2)(k_{\mathrm{B}}T_0^*+\psi)}}. \tag{C.10}$$

In the limit $k \to \infty$ we have $\xi \to \sqrt{(\psi_{\mathrm{L}}-\psi)/k_{\mathrm{B}}T}$ and $\mathcal{K} \to \mathcal{G}$, the standard error function

$$\mathcal{G} \equiv \frac{2}{\sqrt{\pi}} \int_0^{\xi} \mathrm{e}^{-x^2} \mathrm{d}x. \tag{C.11}$$

On the other hand the zero bulk velocity condition $\langle v_z \rangle = 0$ leads to

$$A_0 = A \left[\frac{(\kappa_0-1)\kappa_0\Gamma(\kappa_0-1/2)}{(\kappa_0-3/2)^{\frac{1}{2}}\Gamma(\kappa_0+1)}\right] \left[1+\frac{\psi_{\mathrm{L}}}{(\kappa_0-3/2)k_{\mathrm{B}}T_0}\right]^{\kappa_0-1} \tag{C.12}$$

$$A_{\mathrm{L}} = A \left[\frac{(\kappa_{\mathrm{L}}-1)\kappa_{\mathrm{L}}\Gamma(\kappa_{\mathrm{L}}-1/2)}{(\kappa_{\mathrm{L}}-3/2)^{\frac{1}{2}}\Gamma(\kappa_{\mathrm{L}}+1)}\right] \left[1+\frac{\psi_{\mathrm{L}}}{(\kappa_{\mathrm{L}}-3/2)k_{\mathrm{B}}T_0^*}\right]^{\kappa_{\mathrm{L}}-1} \left(\frac{T_0}{T_0^*}\right)^{1/2}. \tag{C.13}$$

All the above calculations indicate that the density $n(z)$ only depends on the charge and mass of the particles via the potential energy $\psi(z)$. Thus, if we use the same κ and same boundary temperatures T_0 and T_{L} for both electrons and protons the charge neutrality condition reduces to

$$m_{\mathrm{p}}\phi_{\mathrm{G}} + e\phi_{\mathrm{E}} = m_{\mathrm{e}}\phi_{\mathrm{G}} - e\phi_{\mathrm{E}} \tag{C.14}$$

which arises from where one easily computes the classical gravitoelectric field (Rosseland 1924)

$$\phi_{\mathrm{E}} = \frac{1}{2}(m_{\mathrm{p}}-m_{\mathrm{e}})\phi_{\mathrm{G}}. \tag{C.15}$$

The constant parameter A in Eqs. (C.12) and (C.13) is determined by the condition $n(L) = n_{\mathrm{L}}$, i.e.

$$A = \frac{2n_{\mathrm{L}}}{\sqrt{T_0}} \frac{1}{(B_{\kappa_0}/\sqrt{T_{\mathrm{L}}^*}) + (B_{\kappa_{\mathrm{L}}}/\sqrt{T_{\mathrm{L}}})} \tag{C.16}$$

with

$$B_{\kappa_0} \equiv \frac{\Gamma(\kappa_0-1/2)}{(\kappa_0-3/2)^{\frac{1}{2}}\Gamma(\kappa_0-1)} \tag{C.17}$$

$$B_{\kappa_{\mathrm{L}}} \equiv \frac{\Gamma(\kappa_{\mathrm{L}}-1/2)}{(\kappa_{\mathrm{L}}-3/2)^{\frac{1}{2}}\Gamma(\kappa_{\mathrm{L}}-1)} \tag{C.18}$$

and where the quantity

$$T_{\mathrm{L}}^* = T_0\left[1+\frac{\psi_{\mathrm{L}}}{(\kappa_0-3/2)k_{\mathrm{B}}T_0}\right] \tag{C.19}$$

has been introduced.

We can now compute explicitly the higher moments for the velocity distribution function Eq. (C.2). For example, the parallel pressure (with respect to z) turns out to be

$$P(z) = \frac{A_0 k_{\mathrm{B}} T_0}{2}\left[1+\frac{\psi(z)}{(\kappa_0-3/2)k_{\mathrm{B}}T_0}\right]^{-\kappa_0+3/2} [1+\mathcal{K}(\kappa_0-2,\xi_0)] + \frac{A_{\mathrm{L}} k_{\mathrm{B}} T_0^*}{2}\left[1+\frac{\psi(z)}{(\kappa_{\mathrm{L}}-3/2)k_{\mathrm{B}}T_0^*}\right]^{-\kappa_{\mathrm{L}}+3/2} [1-\mathcal{K}(\kappa_{\mathrm{L}}-2,\xi_{\mathrm{L}})]. \tag{C.20}$$

If we impose $\kappa_{\mathrm{L}} = \kappa_0$ and $T_0^* = T_0$, using Eq. (C.7) and Eq. (C.20), we obtain the well known result (Scudder 1992a)

$$T^*(z) = T_0\left[1+\frac{\psi(z)}{(\kappa-3/2)k_{\mathrm{B}}T_0}\right]. \tag{C.21}$$

Similarly we find the collisionless heat flux by setting $\chi = 0.5mv^3\mu$ in Eq. (C.6), whence

$$q = \sqrt{\frac{8}{\pi}} \frac{n_{\mathrm{L}} k_{\mathrm{B}}^{3/2}}{m_{\mathrm{e}}^{1/2}} \frac{\sqrt{T_{\mathrm{L}}^* T_{\mathrm{L}}}}{B_{\kappa_0}\sqrt{T_L} + B_{\kappa_{\mathrm{L}}}\sqrt{T_{\mathrm{L}}}} \left[\left(\frac{\kappa_0-3/2}{\kappa_0-2}\right)T_{\mathrm{L}}^* - \left(\frac{\kappa_{\mathrm{L}}-3/2}{\kappa_{\mathrm{L}}-2}\right)T_{\mathrm{L}}\right]. \tag{C.22}$$

The heat flux for the Maxwellian case given in Eq. (16) can be obtained in the limit $\kappa_0 \to \infty$ and $\kappa_{\mathrm{L}} \to \infty$. Equation (20) is obtained in the limit $\kappa_{\mathrm{L}} \to \infty$ and Eq. (23) by imposing $\kappa_0 = \kappa_{\mathrm{L}}$.

References

Anderson, S. W. 1994, ApJ, 437, 860
Boltzmann, L. 1872, Wien. Ber., 275
Chandrasekhar, S. 1943, Rev. Mod. Phys., 15, 1
Chapman, S., & Cowling, T. 1970, The mathematical theory of non-uniform gases, 3 edition (Cambridge University Press, Cambridge, England)
David, C., Gabriel, A. H., Bely-Dubau, F., et al. 1998, A&A, 336, L90
Dorelli, J. C., & Scudder, J. D. 1999, Geophys. Res. Lett., 26, 3537
Dupree, A. K. 1972, ApJ, 178, 527
Fermi, E. 1954, ApJ, 119, 1
Fludra, A., del Zanna, G., Alexander, D., & Bromage, B. J. I. 1999, J. Geophys. Res., 104, 9709
Golant, V., Zhilinsky, A., & Sakharov, I. 1980, Fundamantals of plasma physics (John Wiley & Sons, New York)
Hinton, F. 1983, in Basic Plasma Physics, ed. A. Galeev, & R. Sudan, vol. 1 (North-Holland, Amsterdam), 147–197
Ko, Y., Fisk, L. A., Geiss, J., et al. 1997, Sol. Phys., 171, 345
Landau, L., & Lifshitz, E. 1960, Course of Theoretical Physics, vol. 1, 1st edition (Pergamon Press, Oxford, England)
Lie-Svendsen, Ø., Holzer, T. E., & Leer, E. 1999, ApJ, 525, 1056
Pantellini, F., & Landi, S. 2000, Ap&SS, in press
Pantellini, F. G. E. 2000, Am. J. Phys., 67, 60
Rosseland, S. 1924, MNRAS, 84, 720
Scudder, J. D. 1992a, ApJ, 398, 299
Scudder, J. D. 1992b, ApJ, 398, 319
Shoub, E. C. 1983, ApJ, 266, 339
Shoub, E. C. 1992, ApJ, 389, 558
Spitzer, L., & Härm, R. 1953, Phys. Rev. A, 89, 372

8 Une simulation cinétique du vent solaire

A&A 400, 769-778 (2003)

A&A 400, 769–778 (2003)
DOI: 10.1051/0004-6361:20021822

Astronomy & Astrophysics

Kinetic simulations of the solar wind from the subsonic to the supersonic regime

S. Landi[1] and F. Pantellini[2]

[1] Dipartimento di Astronomia e Scienza dello Spazio, Largo Enrico Fermi 2, 50125 Firenze, Italy
e-mail: slandi@arcetri.astro.it
[2] Observatoire de Paris, LESIA, 5 Place Jules Janssen, 92195 Meudon, France

Received 30 August 2001 / Accepted 9 December 2002

Abstract. We present and discuss a completely self-consistent kinetic simulation of a steady state transonic solar type wind. The equations of motion of an equal number of protons and electrons plunged in a central gravitational field and a self-consistent electric field are integrated numerically. Particles are allowed to make binary collisions with a Coulombian scattering cross-section. The velocity distributions of the particles injected at the boundaries of the simulation domain are taken to be Maxwellian. As anticipated by previous authors we find that the transonic solution implies the existence of a peak in the proton equivalent potential at some distance above the sonic critical point. Collisions appear to be the fundamental ingredient in the process of accelerating the wind to supersonic velocities. For a given temperature at the base of the simulation domain the acceleration efficiency decreases with decreasing density. The reason is that the plasma has to be sufficiently collisional for the heat flux to be converted efficiently into plasma bulk velocity. Concerning the heat flux we find that even when in the vicinity of the sonic point the collisional mean free path of a thermal particle is significantly smaller than the typical scales of variation of the density or the temperature, the electron heat flux cannot be described conveniently by the classical Spitzer-Härm conduction law; not even in most of the subsonic region. Indeed, in the simulations where a transonic wind forms the heat flux has been found to strongly exceed the Spitzer-Härm flux, in opposition to recently published results from multi-moment models. We emphasize that given the high coronal temperatures we use in our simulations (3 times the typical solar values) we do not expect the results presented in this report to be uncritically transposable to the case of the "real" solar wind. In particular, the quantitative aspects of our results must be handled with some care.

Key words. Sun: solar wind – stars: winds, outflows – plasmas – conduction – methods: numerical

1. Introduction

At all heights, from the bottom of the corona up into the interplanetary space, the solar atmosphere is a permanently expanding, out of thermodynamic equilibrium and fully ionized plasma. During the 1950's the recognition of the weak collisionality of the solar wind conveyed some doubts concerning the ability of fluid models to describe the solar atmosphere conveniently. As a consequence Chamberlain (1960), largely influenced by the theories on gas evaporation from planetary atmospheres, published the first kinetic model of the solar wind. In Chamberlain's evaporation model the wind is subsonic at the Earth's orbit in clear opposition with the supersonic solution of the fluid equations proposed a few years earlier by Parker (1958). During the early 1960's in situ measurements confirmed the supersonic nature of the solar wind and kinetic models just fell in disuse for some time. In the early 1970's it became clear that Chamberlain's erroneous prediction of a subsonic wind was the consequence of having mistakenly assumed that the charge neutralizing electric field was the Pannekoek-Rosseland field (e.g., Rosseland 1924). The latter is based on the assumption of a static solar atmosphere which has been a privileged working hypothesis since Laplace's *Traité de mécanique céleste*, published in the early years of the nineteenth century, but has been shown to be completely at odds with observations. After the definitive relaxation of the static approximation for the electric field, kinetic models of the solar wind were back on stage again (Jockers 1970).

The simplest, and most widely used kinetic models are the so called exospheric models (e.g., Lemaire & Sherer 1971). In these models the solar atmosphere is assumed to change from fully collisional to collisionless at a sharply defined level called the exobase. Above the exobase, conventional exospheric models assume a monotonically decreasing equivalent proton potential Ψ_p (cf. Eq. (4)) and no protons coming into the system from infinity, so that, by construction, all protons have anti sunward directed velocities. For non pathological distribution functions this means that the plasma bulk velocity at the exobase is of the order of the proton thermal velocity, i.e. of the order of the sound velocity. For example, $\langle v \rangle = v_p/\sqrt{\pi}$

Send offprint requests to: F. Pantellini,
e-mail: Filippo.Pantellini@obspm.fr

is the mean velocity of a proton population with Maxwellian velocity distribution $f_M = n_0(\pi v_p^2)^{-3/2} \exp[(v_\parallel^2 + v_\perp^2)/v_p^2]$ truncated for $v_\parallel < 0$ (subscripts $\parallel$ and $\perp$ refer to the radial direction with respect to the center of the Sun). Since the typical velocity of a proton at the exobase is by construction of the order of the radial bulk velocity, it follows that the exobase is located at a heliocentric distance comparable to the distance r_* where the subsonic-supersonic transition is located (the sonic critical point). However, as demonstrated graphically by Jockers (1970), the proton potential cannot be monotonic from deep inside the corona, where the bulk velocity is supposed to be small compared to sound speed and where static approximation may apply, out to infinity, where the wind is supersonic. Jockers anticipated that on its way from the corona to infinity a transonic wind must overcome a maximum in the proton potential Ψ_p such that $\Psi_p(r_\psi) > \Psi_p(\infty)$, where r_ψ is the location of the maximum. In two recent papers Scudder (Scudder 1996a,b) pushes a step farther by identifying the critical point of Parker's fluid model with the location of the maximum of the proton potential energy Ψ_p. Based on that assumption he derives a number of constraints on the possible radial variations of both the proton and the electron temperatures near the sonic point. However, even though the existence of a transonic wind seems to be intimately related to the existence of a peak of the potential Ψ_p, there is no reason for r_ψ to coincide with the sonic point of fluid theories unless very special, and therefore unlikely, conditions are met there. For example, in the simulations presented in this paper we do always find $r_\psi > r_*$. It can be shown analytically that this is indeed the normal case for radially decreasing temperature profiles provided T decreases more slowly than r^{-1} (Meyer-Vernet et al. 2002).

In this paper we present self-consistent kinetic simulations of a stationary solar type wind, where we concentrate on those aspects which cannot be addressed by fluid theories such as the electric field, the heat flux and the collisionality of the plasma. We deliberately treat only the most simple case of Maxwellian boundary conditions for the particles' velocity distribution function. The effects of plasma instabilities and waves are also not included in the model. Such additional "complications" may hide part of the fundamental physics of the acceleration process and shall be discussed elsewhere. In this respect we do merely mention that the effect of resonant waves on a hybrid (fluid + kinetic) solar wind model has been discussed by Tam & Chang (1999) who conclude that ions may well be accelerated more efficiently by resonant waves rather than by the radial electric field. A similar model has been used by Lie-Svendsen & Leer (2000) to show that the two temperature electron velocity distribution functions often observed in the solar wind can be generated by Coulomb collisions without the need of assuming the presence of non-Maxwellain distribution in the corona. Olsen & Leer (1999) and Li (1999) use a closed system of transport equations based on an anisotropic bi-Maxwellian approximation for the velocity distribution functions to simulate the solar wind from the lower corona outward. Lie-Svendsen et al. (2001) extend the model down to the chromosphere based on the argument that chromosphere, transition region, corona and solar wind constitute a coupled system. The system of equations used by these authors is known as the 16-moment approximation (e.g., Demars & Schunk 1979) is a fluid-type model including transport effects such as heat flow and viscosity and even Coulomb collisions between interacting species. The main purpose of the above authors was to reproduce as good as possible the characteristics of the coronal plasma by including ad-hoc heating functions supposed to mimic the local deposit of energy due to plasma waves. If suitably chosen the heating functions can reproduce the temperature profile and temperature anisotropies which observations suggest to prevail in the solar corona (e.g., Esser et al. 1999). In many respects, our model is much more limited than the above multi-moment models which include most of the ingredients (e.g. radiation, plasma heating through waves, collisions, etc.). However, these models are fundamentally fluid models and many ingredients are not self-consistent. Our model is kinetic and fully self-consistent, but neither waves nor radiation and not even the lower layers of the corona are taken into account. In addition, because of computational limitations, we use an artificially low proton to electron mass ratio, and an exceedingly high coronal temperature, so that transposition of our results to the case of the real Sun must be done critically. One substantial difference between our results and the results from the mentioned multi-moment models is that we find that the electron heat flux in the corona is one order of magnitude larger than the classical value predicted by the Spitzer-Härm formula (Spitzer & Härm 1953), whereas the multi-moment models find it to be of the same order. Of course, both models are subject to their own limitations so that the question of whether the heat flux in the solar wind is classical or not appears to remain an open question.

Even though the physical parameters characterizing the wind simulated in the following section do not correspond exactly to those observed for the Sun, we shall refer to the simulated wind as the solar wind and to the central star as the Sun.

2. The model

Details of the simulation model have been given in two previous papers (Pantellini 2000; Landi & Pantellini 2001) and shall not be repeated here to full extent. The model is spatially one dimensional, i.e. all fields depend on the heliocentric distance r only. An equal number of protons and electrons are allowed to move freely in the domain $r_0 < r < r_{max}$, where r_0 is the solar radius and r_{max} is the outer boundary of the system located several solar radii beyond the sonic point. The equations of motion are those of a particle of mass m and charge q in a central gravitational field produced by a star of mass M and a radial, charge neutralizing electric field, $\mathcal{E}(r)$, i.e.

$$\frac{d^2r}{dt^2} = -\frac{GM}{r^2} + \frac{L^2}{m^2r^3} + \frac{q}{m}\mathcal{E}(r). \quad (1)$$

$$\boldsymbol{L} \equiv m\boldsymbol{r} \times \boldsymbol{v}_\perp = \text{constant} \quad (2)$$

where G is gravitational constant, $\boldsymbol{L}$ the angular momentum of the particle and $\boldsymbol{v}_\perp$ its velocity component perpendicular to the radial direction. Two particles finding themselves simultaneously at the same radial distance r do either make an isotropic elastic collision with a probability $\propto u^{-4}r^{-2}$ or just go through each other as if they were transparent. The u^{-4} dependence

of the collision probability mimics velocity dependence of the scattering cross section for Coulomb collisions whereas the r^{-2} dependence accounts for the spherical geometry of the problem. The transport properties of such a plasma have been shown to be very much the same as those of a Fokker-Planck plasma (Pantellini & Landi 2001; Landi & Pantellini 2001).

3. Defining the simulation

The physical state of the solar corona at heliocentric distance r_0 (the lower boundary of our simulation domain) is characterized by the dimensionless parameter γ defined as (k_B is the Boltzmann constant)

$$\gamma \equiv \frac{GM}{r_0}\frac{m_p + m_e}{2k_B T_0} \approx \frac{GM}{r_0}\frac{m_p}{2k_B T_0} \equiv \gamma_p. \quad (3)$$

The parameter γ is half the ratio of the escape velocity squared to the protons thermal velocity squared $v_{p0}^2 \equiv 2k_B T_0/m_p$. For a typical solar coronal temperature $T_0 = 10^6$ K one has $\gamma = 11.6$. The fact that γ is larger than unity means that a typical coronal proton is too slow to escape to infinity. On the other hand, for coronal electrons at the same temperature one has $\gamma_e = 6.3 \times 10^{-3} \ll 1$, meaning that the vast majority of the electrons would easily escape to infinity if gravity was the only force field. The solar corona is thus characterized by $\gamma \gtrsim 1$ and $\gamma_e \ll 1$. In order to reduce the required computational time to an acceptable level we choose $\gamma_p = 4$ and $\gamma_e = 10^{-2}$, instead of the above values of the real Sun. This, means that we adopt a rather high coronal temperature of 2.9×10^6 K and an artificially low proton to electron mass ratio $m_p/m_e = 400$. However, since the two important constraints for a solar type atmosphere $\gamma_p \gtrsim 1$, $\gamma_e \ll 1$ are satisfied we expect the simulations to provide a fair approximation of the solar case.

The equations of motion Eqs. (1) and (2) are integrated for N protons, and an N electrons in the radial distance range between $r = r_0$ and $r = r_{top} \equiv 51 r_0$. The number N is determined by the requirement of the collision frequency of an electron in the system (near $r = r_0$) being roughly equal to the Fokker-Planck collision frequency of a plasma with an electron number density $n_e \approx 10^8$ cm^{-3}, which is a typical figure in the solar corona. The so calculated number N turns out to be of the order 10^3 (Landi & Pantellini 2001). Each time a proton or an electron hits the boundary at $r = r_0$ it is injected back into the system according to a non drifting isotropic Maxwellian velocity distributions with a temperature T_0. Given that the protons reaching the top boundary at $r = r_{top}$ are generally either supersonic or nearly supersonic most of it must be re-injected into the system at $r = r_0$. On the other hand, electrons reaching the $r = r_{top}$ boundary are injected back into the system either at $r = r_0$ or at $r = r_{top}$ depending on what is needed to make the electron flux to be equal to the proton flux (zero charge current condition). The injection method ensures that there are always N protons and N electrons in the system. The velocity distribution of the electrons injected at the top boundary is chosen to be a drifting bi-Maxwellian with radial and perpendicular temperatures equal to the radial and perpendicular temperature of the outgoing electrons. Finally, the drift velocity of the electrons at $r = r_{top}$ is taken to be equal to the drift velocity of the protons measured at $r = r_{top}$. In case of a supersonic wind this is just the average velocity of the protons escaping from the top of the system. In a subsonic wind some protons have to be re-injected into the system from the top. The temperature and the number of the re-injected protons is then adjusted iteratively until a coherent solution is obtained, in a manner similar to the one used by Landi & Pantellini (2001) to simulate the static corona. The electric field profile is adjusted iteratively, during an initialization phase, until zero charge flux and local charge neutrality is achieved in all points of the system.

4. Results

4.1. Effect of varying the coronal density

The number density n and the collisionality of the simulated plasma is dependent on the number of particles N used in the model. Figure 1 shows the results of 4 simulations which only differ in the number N of simulated particles, i.e. $N = 400, 784, 1600, 6400$, the $N = 400$ run being the one with the most tenuous (i.e. less collisional) atmosphere. The corresponding number densities at the base of the system are $n_0[10^8\ \text{cm}^{-3}] = 0.8, 1.5, 3.6$ and 13.4, respectively. The differences between the 4 simulations are substantial in many respects. The most evident difference is that the wind acceleration is much more efficient in the high density case, even though the thermal Knudsen number $K_T \equiv \overline{\lambda}_{ep}|\partial \ln T_{e\|}(r)/\partial r|$ (where $\overline{\lambda}_{ep} \equiv v_{e\|}/\overline{\nu}_{ep}$ is the electron-proton collisional mean free path based on the electron-proton rate of momentum exchange $\overline{\nu}_{ep}$ (Landi & Pantellini 2001, Appendix B), and where $v_{e\|} \equiv (2k_B T_{e\|}/m_e)^{1/2}$ is the radial thermal electron velocity) is much smaller than unity for all runs, ranging from 10^{-3}, for the densest case, to 10^{-2} for the most tenuous case. From the figure it appears that the two more tenuous cases do not even become supersonic with respect to radial proton thermal velocity $v_{p\|} \equiv (2k_B T_{p\|}/m_p)^{1/2}$ (which coincides with the fluid isothermal sound speed when $T_{p\|} = T_{e\|}$). The curves on the bottom panel of Fig. 1 illustrate the effect of collisions on the proton potential energy Ψ_p. The latter results from the sum of the gravitational potential and a charge neutralizing electrostatic potential ϕ:

$$\Psi_p = -\frac{GMm_p}{r_0}\left(\frac{r_0}{r} - 1\right) + e\phi(r) \quad (4)$$

where e is the absolute value of the electron charge and where, because of the finite extent of the simulation domain we choose the level $r = r_0$ to be the reference level for both the gravitational potential and the electrostatic potential, rather than $r = \infty$. Thus $\Psi_j(r_0) = 0$ by construction. The decreasing height of the potential barrier the protons have to overcome as the plasma collisionality increases is evident. In the least collisional case (dash-dot profiles in Fig. 1) the potential Ψ_p is a monotonically growing function of r. However, increasing the system's collisionality beyond a given threshold makes the potential Ψ_p become non monotonic, with the peculiar formation of a maximum a few solar radii above the bottom boundary at $r = r_\psi$. As already stated in the introduction the existence of a maximum in the proton potential has been suggested

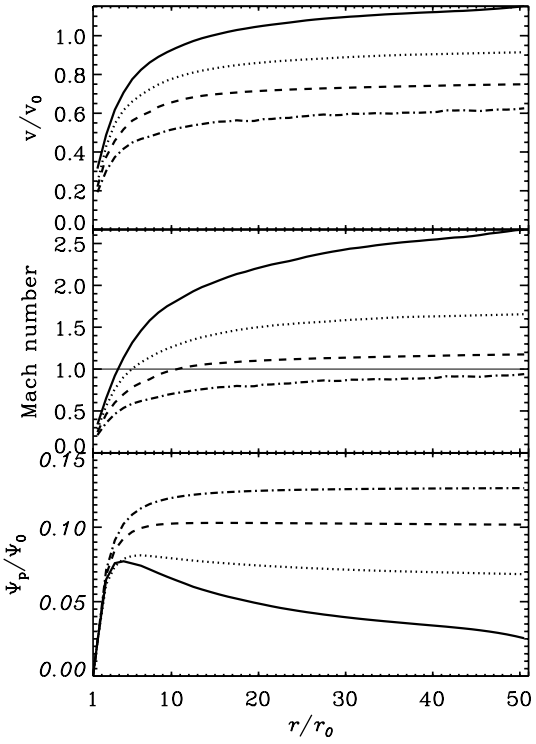

Fig. 1. Flow velocity, Mach number and proton potential energy profiles for four different values of the number of particles N in the system. From bottom to top the velocity profiles correspond to N = 400, 784, 1600, 6400, respectively. In all runs $\gamma = 4$ and $m_p/m_e = 400$. The normalizing velocity v_0 is the proton thermal velocity $v_p(r_0)$. The Mach number is defined as the ratio of the radial bulk velocity of the plasma divided by the proton thermal speed $v_{p\|} \equiv (2k_B T_{p\|}/m_p)^{1/2}$. The normalizing energy Ψ_0 is given by $\Psi_0 = GMm_p/r_0$. Thus, as a reference, if the charge and current neutralizing electric field was the Pannekoek-Rosseland potential $\Psi_p/\Psi_0 \approx 0.5$ for $r \gg r_0$.

some time ago by Jockers (1970). Scudder (1996a) pushed a step farther by postulating r_ψ to coincide with the position of the isothermal sonic point of Parker's fluid theory. Figure 1 shows that when a maximum of Ψ_p exists, it is located above the sonic point, in agreement with the theoretical predictions (Meyer-Vernet et al. 2002). Figure 1 also shows that the low density cases do neither produce a maximum in the proton potential nor a supersonic wind, at least if terms of the parallel temperature based Mach number. One may suspect that if the Mach number was defined with respect to the mean temperature $T \equiv (T_\| + 2T_\perp)/3$ the flow would more easily become supersonic at large distances because of the $T_\perp \propto r^{-2}$ dependence implied by the conservation of angular momentum in a collisionless plasma with negligible heat flux. In the end, however, given that in the collisionless limit and for $r \to \infty$, one has $T_\| \to$ const. (e.g., Meyer-Vernet & Issautier 1998), so that $T \to T_\|$, asymptotically. As a consequence, the distant Mach number does not depend on which of the two above definitions has been used.

In summary, the main consequence of increasing the plasma density beyond some threshold appears to be a reduction of the potential barrier the protons have to overcome in order to escape to infinity, accompanied by the formation of a local maximum in the $\Psi_p(r)$ profile. As we shall see below the formation of the maximum in the proton potential energy is intimately related to the existence of both an outward directed, and radially decreasing heat flux, and a radially decreasing temperature profile. Both contribute in strengthening the outward directed electric field $\mathcal{E} = -\partial\phi/\partial r$, thus facilitating the extraction of the protons. In this context we shall remember that if the plasma was static (impermeable boundaries) with equal electron and proton temperatures, the charge neutralizing potential ϕ would be the celebrated Pannekoek-Rosseland potential (e.g., Rosseland 1924)

$$\phi(r) = \phi_{PR}(r) \equiv \frac{GM}{r_0}\frac{m_p}{2e}\left(1 - \frac{m_e}{m_p}\right)\left(\frac{r_0}{r} - 1\right) \tag{5}$$

and the total potential energy of a proton would be a monotonically increasing function of r

$$\Psi_p = -\frac{GM}{r_0}\frac{m_p}{2}\left(1 + \frac{m_e}{m_p}\right)\left(\frac{r_0}{r} - 1\right) \quad \text{(static limit)}$$

asymptotically reaching the value $GMm_p/(2r_0)$ which is much higher than the values observed in the simulations (cf. bottom panel of Fig. 1).

4.2. Wind acceleration

Let us now address the question of the wind acceleration mechanism. In order to do so we write the energy equation for the species j for the case of a steady state and purely radial wind. Indeed, the second moment of Boltzmann's equation (e.g., Endeve & Leer 2001) leads to the following expression

$$E_j = \frac{1}{2}m_j v_j^2 + h_j(r) + \Psi_j + \frac{q_j}{n_j v_j} \tag{6}$$

where q_j, n_j, v_j are the heat flux, density and bulk velocity of the corresponding species and where we have defined the enthalpy per particle of the species j

$$h_j(r) \equiv \frac{3}{2}k_B T_{j\|} + k_B T_{j\perp}. \tag{7}$$

We note in passing that the first moment of Boltzmann's equation leads to Jockers's Eq. (1.1) (Jockers 1970)

$$m_j v_j \frac{\partial v_j}{\partial r} = -\frac{1}{n}\frac{\partial\left(nk_B T_{j\|}\right)}{\partial r} - \frac{2k_B}{r}\left(T_{j\|} - T_{j\perp}\right) - \frac{\partial\Psi_j}{\partial r}. \tag{8}$$

When applied to the electrons one may neglect the small terms proportional to the electron mass m_e in Eq. (8) which then reduces to the usual expression for the electric field $\mathcal{E}$

$$e\mathcal{E} = -\frac{1}{n_e}\frac{\partial}{\partial r}\left(n_e k_B T_{e\|}\right) - \frac{2}{r}k_B\left(T_{e\|} - T_{e\perp}\right). \tag{9}$$

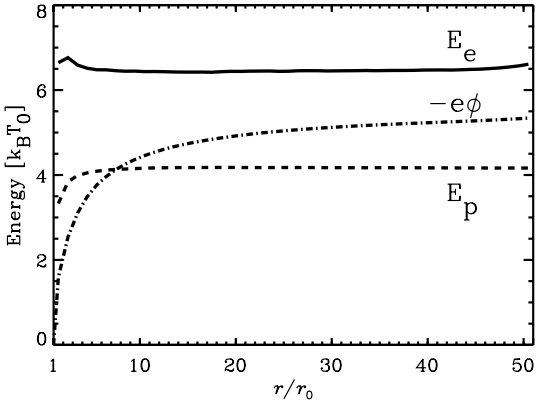

Fig. 2. Proton and electron energy profiles obtained by evaluating Eq. (6) for the $N = 6400$ simulation. Note how both, E_e and E_p are separately constant over most of the simulation domain. The electrostatic profile $-e\phi$ is plotted as a reference.

But let us come back to Eq. (6). In all simulations E_e and E_p are separately approximately constant over the whole simulation domain (excepted for a small region near the $r = r_0$ boundary). This is shown in Fig. 2 for the $N = 6400$ case. At first, this seems to indicate that the net energy exchanges between protons and electrons are quantitatively small. This is not necessarily correct. Indeed, it appears that the system does merely organize itself in order to ensure a spatially constant proton to electron energy density ratio throughout the system. The ratio can be constant even if interspecies energy exchanges via collisions are strong. A simple example of such a system consists of a collisional proton-electron plasma under the effect a constant gravitational acceleration field g. In this case the temperatures of both, electrons and protons, must be equal, isotropic and spatially constant. Further, the heat flux must vanish and the charge neutralizing electric field is just the Pannekoek-Rosseland field $g(m_p - m_e)/(2e)$ so that $E_p = E_e = (5/2)k_B T + g(m_p + m_e)z/2$, i.e. $E_p/E_e = 1$, independently of the height z. On the other hand, as we shall see below, in the spherically symmetric case the heat flux (mainly conveyed by the electrons) is the dominant source of energy for the acceleration of the wind. In order to proof this affirmation it is useful to evaluate the mean energy per particle $\langle E\rangle$ as a function of r. Averaging the contribution of electrons and protons according to Eq. (6) leads to

$$\langle E\rangle \approx \frac{1}{2}\left[\frac{1}{2}m_p v^2 + h(r) + \frac{GMm_p}{r_0}\left(1 - \frac{r_0}{r}\right) + \frac{q}{nv}\right] \qquad (10)$$

where the enthalpy term $h(r)$ includes the temperature terms from all species (electrons and protons). In order to obtain Eq. (10) we made use of the fact that $m_p \gg m_e$ and that the proton and electron number fluxes are equal, i.e. $n_p v_p = n_e v_e \equiv nv$. As a reference, the number flux nv has been found to be of the order $10^{-2} v_{e0} n_0$ in all runs. In particular for the $N = 6400$ case we find $nv = 1.2 \times 10^{-2}\, n_0 v_{e0}$. The energy flux F_E conveyed by the wind through the spherical shell located at a distance r is the product of the particles mean energy at that distance (after deduction of their gravitational energy) times the number of particles crossing the shell per time unit. Since the total number density is equal to twice the number density of either species the particle flux is a constant given by $8\pi r^2 nv$ and the energy flux becomes

$$F_E(r) = 8\pi r^2 nv\left[\langle E\rangle - \frac{GMm_p}{2r_0}\left(1 - \frac{r_0}{r}\right)\right]. \qquad (11)$$

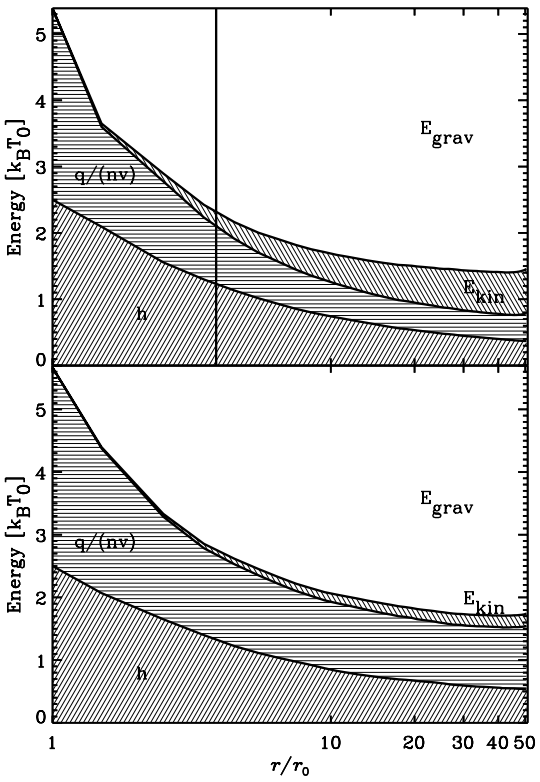

Fig. 3. Relative importance of each term in Eq. (10) for the most dense case $N = 6400$ (top panel) and the most tenuous case $N = 400$ (lower panel). The dense case supports a transonic wind (the vertical line in the top panel gives the position of the sonic point r_*) while the tenuous case does not. From the comparison of the two figures it appears that the wind acceleration is primarily driven by the heat flux term $q/(nv)$.

Figure 3 illustrates the relative importance of each of the 4 terms in Eq. (10) as a function of the radial distance r for the $N = 6400$ (top) and the $N = 400$ (bottom) run. Since the gravity term vanishes at $r = r_0$ and the bulk velocity v is much smaller than the sound speed, only the enthalpy and the heat flux term contribute to the total energy there. The reason for the total energy being slightly larger in the low density case arises from the heat flux term $q/(nv)$ being stronger in that case. This is because at $r = r_0$ we do not have control over this term as we do for the enthalpy, which only depends on the temperature imposed at the boundary. Interestingly the run characterized by the largest heat flux term $q/(nv)$ (which

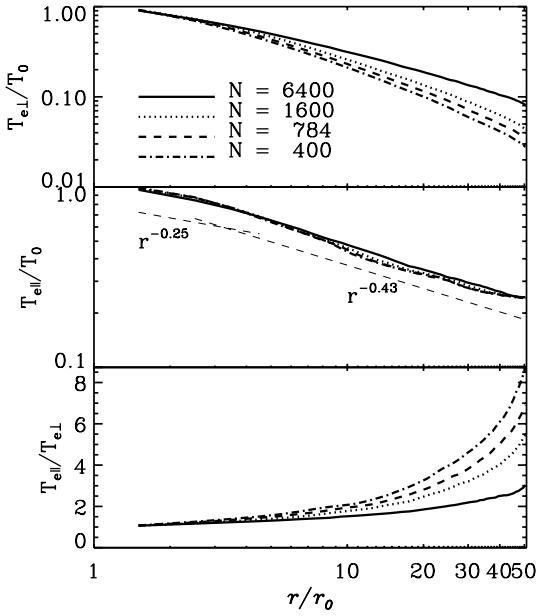

Fig. 4. Radial and perpendicular temperature profiles for 4 different values of the N. Note the log-log axis of the top two panels.

does not necessarily mean that the heat flux q, or the specific heat flux q/n are largest) is precisely the one where the wind remains subsonic. This is particularly surprising in the light of the fact that the velocity of the wind is clearly boosted by the heat flux term given that the enthalpy profile is seemingly identical for the two cases. However, a strong heat flux term near the bottom does not guarantee that the wind will be accelerated to supersonic velocities. A sufficient amount of collisions is needed to efficiently transform the energy transported outward by the electron heat flux into bulk plasma kinetic energy.

Figure 4 shows that the radial electron temperature profile $T_{e\parallel}$ is essentially insensitive to the density while $T_{e\perp}$ is not. Indeed, in the collisionless limit the parallel and perpendicular temperatures are independent of each other and one should observe $T_{e\perp} \propto r^{-2}$ in order to satisfy to the angular momentum conservation law of individual particles (cf. Eq. (2)). As a consequence, in the rigorously collisionless case, $T_{e\perp}$ should decrease by a factor 50^2 from bottom to top of the simulation domain. Collisions do significantly contribute in limiting this bottom to top perpendicular electron temperature gradient which ranges from 10 to 30 depending on the value of N. On the other hand, for all four cases the parallel temperature only drops by a factor 3 from bottom to top, leading to strong temperature anisotropies $T_{e\parallel}/T_{e\perp}$ (bottom panel in Fig. 4). This is not particularly surprising as in the collisionless limit the parallel temperature of a plasma plunged in a potential field is constant as long as the velocity distribution function is close to Maxwellian.

We can now summarize the wind acceleration scenario from a kinetic point of view. The natural decrease of the temperature with distance (essentially due to the fact that in the collisionless limit $T_\perp \propto r^{-2}$) implies the existence of a radial heat flux predominantly conveyed by the electrons. The heat flux is transfered from the electrons to the protons which become accelerated in the outward direction. Since the momentum of the wind is mainly carried by the heavy protons (rather than by the light electrons) the plasma as a whole becomes accelerated in this way. This mechanism must be particularly efficient in the region located inside the spherical shell $r = r_\Psi$ (location of the maximum of Ψ_p) where the protons have to climb uphill in order to escape from the potential energy well (cf. Fig. 1). As already stated above, collisions contribute in increasing the electric field strength. Since the electric field is directed outward, increasing the electric field favors the extraction of the protons from the gravitational well by reducing the height of the maximum in the proton potential Ψ_p. The fluid estimate of the macroscopic electric field $\mathcal{E}$ for a spherically symmetric electro-proton plasma can be obtained by differentiating Eq. (6) for the electrons. Neglecting the small terms proportional to m_e and taking advantage of the fact that E_e is approximately constant (in particular if one compares it to the $\phi(r)$ profile shown in Fig. 2) we then obtain

$$e\mathcal{E} \approx -k_B \frac{\partial}{\partial r}\left(\frac{3}{2}T_{e\parallel} + T_{e\perp}\right) - \frac{\partial}{\partial r}\left(\frac{q}{nv}\right). \tag{12}$$

This estimate is not as rigorous as the standard estimate based on Eq. (8) since it is based on the assumption of a constant $E_e(r)$ profile. The equation has the advantage of highlighting the role of the heat flux in the shaping of the electric field profile. For radially decreasing temperature profiles the first two terms on the right hand side of Eq. (12) are positive and favor the outward acceleration of the protons. They are reminiscent of the thermoelectric effect (e.g., Pantellini & Landi 2001). Given that q/nv has been seen to decrease with distance for the two extreme cases shown in Fig. 3 it follows that the third term on the right hand side of Eq. (12) is also positive for all simulation. However, the contribution of the latter to the acceleration is significantly stronger in the $N = 6400$ case than in the $N = 400$ case, where the radial dependence of q/nv is seemingly weak.

It is instructive to apply Eq. (12) to a a weakly collisional system. In such a case the parallel temperature $T_{e\parallel}$ is roughly constant and the perpendicular temperature $T_{e\perp} \propto r^{-2}$. This leads to the collisionless approximation

$$e\mathcal{E} \propto \frac{\text{constant}}{r^3} - \frac{\partial}{\partial r}\left(\frac{q}{nv}\right) \tag{13}$$

where the constant is positive. From Eq. (13) it appears that when the heat flux term is constant, or only weakly spatially dependent, such that the first term on the right hand side of the equation dominates over the second term, the electric field decreases faster than the gravitational field (i.e. $\mathcal{E} \propto r^{-3}$). This is the reason for the proton potential energy Ψ_p to be a monotonically growing function of distance r in the $N = 400$ case shown in Fig. 1. Increasing the number of particles in the system makes the plasma more collisional and forces the perpendicular temperature $T_{e\perp}$ to fall off more slowly than r^{-2} (see Fig. 4)

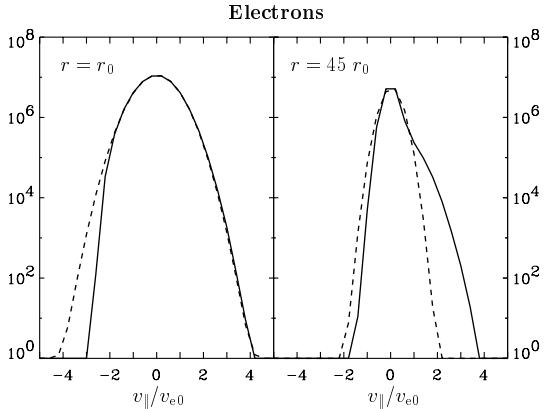

Fig. 5. Parallel electron velocity distribution functions (solid lines) in arbitrary units at two different positions in the system, near the base and in the supersonic region. Shown are results of the $N = 6400$ simulation. The dashed lines represent Maxwellian distributions for which the first three moments (density, mean velocity and temperature) are those of the measured distributions. Velocities are normalized to the electron thermal velocity $v_{e0} = v_e(r_0)$.

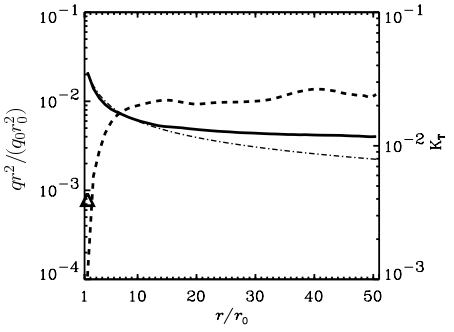

Fig. 6. Electron heat flux profile (solid line) and thermal Knudsen number $K_T \equiv \overline{\lambda}_{ep}|\partial \ln T_{e\parallel}(r)/\partial r|$ (dashed line) for the most strongly collisional case $N = 6400$ normalized to $q_0 \equiv n_0 m_e v_{e0}^3$, where v_{e0} is the electron thermal velocity at the base of the system at $r = r_0$. The triangle on the heat flux axis indicates the heat flux expected near the base of the system using the Spitzer-Härm formula (Spitzer & Härm 1953). The dot-dash line shows the $-T_{e\parallel}^{5/2}\partial T_{e\parallel}/\partial r$ law normalized to the measured flux at $r = r_0$.

making it harder for the gravitational force acting on a proton to overcome the electric force. Eventually, if $T_{e\perp}$ decreases more slowly than r^{-1}, there must be a minimum distance beyond which the electric force on a proton overcomes the gravitational force and Ψ_p has a maximum. This is clearly the case for the $N = 6400$ case shown in Fig. 4 where $T_{e\perp} \propto r^{-0.6}$. For the $N = 400$ case the temperature profile is steeper, with an average radial dependence given by $T_{e\perp} \propto r^{-0.9}$. Thus, even though all profiles can be described by a power law which decreases more slowly than r^{-1} (on average over the simulation domain) all profiles tend to steepen at large distances because of the plasma tendency to become less collisional. Eventually beyond some N-dependent threshold distance the $T_{e\perp}$ profiles becomes steeper than r^{-1} so that the formation of a maximum of Ψ_p becomes impossible beyond this point. This is the case for the $N = 400$ run. In the other three runs a maximum forms below the point where the $T_{e\perp}$ profile becomes steeper than r^{-1}. We can now reexamine Fig. 3 in the light of Eq. (12). Figure 3 already told us that the enthalpy profile is not very sensitive on the plasma collisionality even though it contributes significantly in strengthening the electric field according to Eq. (12). The determinant contribution in accelerating the wind to supersonic velocities comes from the heat flux term $q/(nv)$ which has been seen to be much more sensitive on the plasma collisionality. As demonstrated by Eq. (12), the heat flux term contributes to the strengthening of the outward directed electric field, provided it decrease with distance. Figure 3 shows that the heat flux term decreases for both simulations represented on the figure with the steepest profile being associated with the high density case which therefore produces the strongest electric field, according to the last term on the right-hand side of Eq. (12).

For the $N = 6400$ simulation the parallel electron velocity distribution functions at the base of the system at $r = r_0$, and in the supersonic region at $r = 45\,r_0$ are shown in Fig. 5. Since the collisional mean free path λ is proportional to v^4 high energy electrons are nearly unaffected by collisions on their journey through the system. Thus, the velocity distribution of the high energy electrons flowing downward is the imprint of the upper boundary condition whereas the velocity distribution of the high energy electrons flowing upward is the imprint of the lower boundary at $r = r_0$. On the other hand, the low energy electrons, which populate the core of the velocity distribution function, are strongly affected by collisions. As a consequence, at low velocities, the electron velocity distributions are approximately isotropic Maxwellians which do not carry any heat flux. Instead, the heat flux is carried by the high energy electrons which are responsible for the asymmetry of the distribution function. As illustrated by the profiles in Fig. 5 the heat flux is due to a deficiency of downward flowing high energy electrons near the lower boundary and to an excess of upward flowing particles in the supersonic region.

4.3. Comments on the electron heat flux

Figure 6 shows the heat flux and the thermal Knudsen number K_T measured in the $N = 6400$ run. One observes that while it remains approximately constant in the supersonic region above the $r \approx 10r_0$ level, K_T grows steeply in the subsonic region, where it increases from 10^{-3} to 10^{-2}. Since $K_T \lesssim 2 \times 10^{-2}$ in whole simulation domain, it is not particularly surprising that the heat flux closely follows a $T_{e\parallel}^{5/2}\partial T_{e\parallel}/\partial r$ dependence (dot-dash curve) as in the case of the classical Spitzer-Härm heat conduction formula (Spitzer & Härm 1953). This conclusion is misleading, since, despite the smallness of the Knudsen number, the heat flux is strongly non classical. As already pointed out by several authors in the past the classical heat conduction formulation breaks down either because the heat flux intensity exceeds a value of the order $10^{-2}q_0$

(Gray & Kilkenny 1980), or because the Knudsen number is larger than 10^{-3} (Shoub 1983), or because the flow velocity is a significant fraction of the sound speed (Hollweg 1974; Alexander 1993), or even because the electric field in the system is of the order of the Dreicer field $\mathcal{E}_D \equiv kT_e/(e\overline{\lambda}_{ep})$ (Scudder 1996b). Indeed, in the $N = 6400$ simulation the electric field at the sonic point is $\mathcal{E} \approx \mathcal{E}_D$, reaching an intensity $\mathcal{E} \approx 8\mathcal{E}_D$ in the $N = 1600$ case. Concerning the heat flux intensity, Fig. 6 shows that it is small enough for the the low heat flux intensity condition established by Gray & Kilkenny (1980) to be satisfied. One can therefore conclude that the heat flux intensity is low enough for the plasma to be capable to support a Spitzer-Härm flux. Let us now address the problem of the heat flux in a flowing, and weakly collisional plasma. As discussed by Hollweg (1974) and Alexander (1993) a non negligible fraction of the of the energy is carried by a collisionless term of the form $q_{NC} = (3/2)\alpha n v k_B T_e$ where α is a positive numerical factor of order unity (note that the electron temperature has been supposed to be isotropic by these authors). Given that collisions are still relatively important in our simulations we make the ansatz that the observed electron heat flux is made of the sum of a classical (collisional) term (e.g., Braginskii 1965) q_{SH} and a collisionless term q_{NC}

$$q_e = q_{SH} + q_{NC} = -3.16 \frac{nk_B^2 T_e}{m_e \overline{\nu}_{ep}} \frac{\partial T_e}{\partial r} + \frac{3}{2} \alpha\, n v k_B T_e \qquad (14)$$

where α is a positive constant of order unity whose numerical value depends on the assumptions of the specific heat flux model (Hollweg 1974; Alexander 1993). As a guide, Hollweg's estimate of α for the solar wind are in the range 2.0 to 7.0 (Hollweg 1974). Equation (14) shows that the two heat conduction terms have an extremely different dependence on the macroscopic moments of the plasma. The Spitzer-Härm heat conduction does only depend on the temperature, and its radial variation, while the collisionless term q_{NC} depends on both the electron number flux and the temperature (but not on the temperature gradient). This situation is reminiscent of the heat conduction in a plasma confined to the space between two parallel plates separated by a distance L at temperatures T_0 and T_L, respectively (Landi & Pantellini 2001). If the plasma is dominated by collisions the heat conduction between the two plates just equal to q_{SH}. However, if the plasma is sufficiently diluted for a non negligible number of electrons to be able to proceed from one plate to the other without colliding with other particles in the system, the heat flux is best described by the collisionless approximation $q_{NC} \propto n(T_0 T_L^{1/2} - T_L T_0^{1/2})$ which (unlike q_{SH}) is a function of the number density n. Figure 7 compares the Spitzer-Härm estimate and the collisionless estimates of the electron heat flux with the observed heat flux for the four simulations. All profiles in the figure have been obtained using $T_{e\|}$ in place of the temperature T_e which appears in Eq. (14). Even though Hollweg's collisionless approximation is not expected to provide an accurate approximation of the heat flux in the simulated systems, it appears that the measured heat flux varies significantly from one simulation to the other, in good qualitative agreement with the non collisional flux q_{NC}

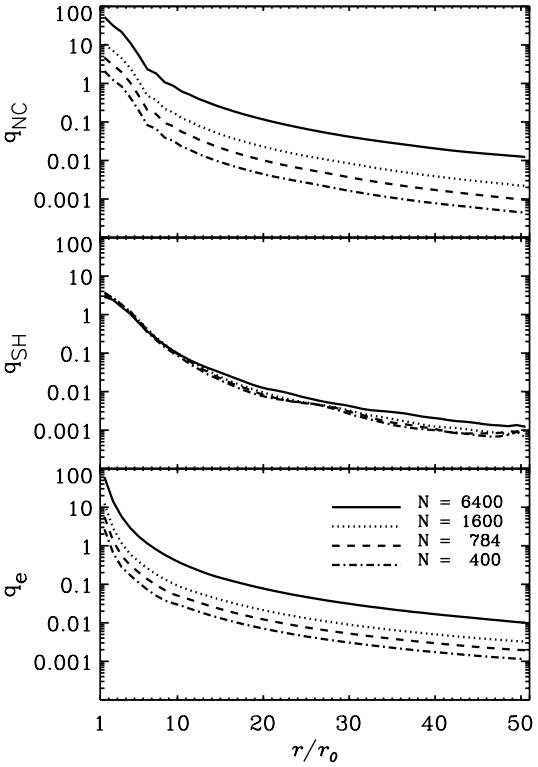

Fig. 7. Electron heat flux calculated using the collisionless approximation $q_{NC} = (3/2)\alpha n v T_{e\|}$ (top panel), the classical Spitzer-Härm approximation $q_{SH} = -\text{constant} \times T_{e\|}^{5/2} \partial T_{e\|}/\partial r$ (middle panel). The lower panel shows the heat flux profiles effectively measured in the simulations. Fluxes are in arbitrary units, but the same normalization has been used for all simulations.

obtained using Alexander's model (Alexander 1993) to compute α in Eq. (14) after replacing T_e by $T_{e\|}$. The Spitzer-Härm prediction of an equal heat flux intensity for all four simulations (based on the fact that the radial profiles of $T_{e\|}$ are very similar cf. Fig. 4) is completely at odds with the measured intensities. But why is this so, despite the smallness of the Knudsen number? The answer is hidden in Eq. (14). Indeed, from Eq. (14), after replacing T_e by $T_{e\|}$, it follows that the ratio of the two contributions to the total heat flux is given by

$$\frac{q_{NC}}{q_{SH}} = \frac{3\alpha}{3.16} \frac{v}{v_{e\|}} \frac{1}{K_T}. \qquad (15)$$

From Eq. (15) it follows that the condition for the heat flux in the system to be dominated by the classical term q_{SH} one must have $K_T \gg \alpha v/v_{e\|}$. For example, at the sonic point one has $v/v_{e\|} = (m_e/m_p)^{1/2} = 1/20$ and $K_T \approx 10^{-2}$ from where one can estimate $q_{NC}/q_{SH} \approx 5\alpha$, which is substantially larger that unity for any reasonable value of α. Thus, for the heat flux to be of the Spitzer-Härm type in the vicinity the sonic point requires the thermal Knudsen number to be larger than $(m_e/m_p)^{1/2}$. The simulations suggest that this is not easily achievable because

the driving of the wind to supersonic velocities does precisely requires the plasma to be sufficiently collisional at the sonic point. As already stated, the way around this restriction may be the presence of an additional scattering mechanism (e.g. waves) in the plasma. However, in that case the Spitzer-Härm formulation of the heat transport would not be the relevant one anyway. As already pointed out in the introduction recent multi-moment simulations of the solar wind yield a close to classical electron heat flux (e.g. Olsen & Leer 1999; Li 1999; Lie-Svendsen et al. 2001). The discrepancy may be due to the fact that physical conditions of the wind we simulate are quite different from those used in these multi-moment simulations or, eventually, to the fact that the heat flow equations in the multi-moment models are affected by the closure scheme. The simplified version of the Coulomb collision operator used in our model or even the one-dimensionality of the model may also contribute to the observed discrepancy. The reason for the radial dependence of the heat flux measured in the simulation (cf. Fig. 6) to be roughly of the Spitzer-Härm type stems from the fact that the radial dependences of both terms in Eq. (14) are quite similar for the given temperature profiles. Indeed, if we replace T_e by $T_{e\|}$ in Eq. (14) and use the fair approximation $T_e \propto r^{-0.4}$ (from Fig. 4) it follows that both q_{SH} and q_{NC} vary approximately as $r^{-2.4}$.

4.4. Effects of varying the proton to electron mass ratio

Given the artificially low mass ratio in our simulations there is a concern about the sensitivity of the results on the value of m_p/m_e. In order to address this question we show the same simulation for two different values of m_p/m_e in Fig. 8. The other parameters are identical for both simulations , i.e. $\gamma_p = 4$ and $N = 6400$. In both cases the formation of a transonic wind occurs, in association with the formation of a maximum in the proton potential. However, the maximum's amplitude is substantially higher, and less peaked, in the low mass ratio simulation. The discrepancy is likely due to the fact that in the high mass ratio case the scattering of the electrons in velocity space by the protons is more efficient than in the low mass ratio case. Indeed, the temperature ratio $T_{e\|}/T_{e\perp}$ reaches a value of 3 at the upper boundary in the $m_p/m_e = 400$ case (cf. Fig. 4) and a value of 4 in the $m_p/m_e = 100$ case. As a result the absolute value of second term on the right hand side of Eq. (9) is significantly smaller in the high mass ratio case than in the low mass ratio case. Since the sign of this term is negative it contributes in reducing the the strength of the overall positive electric field. From Fig. 4 one may argue that a similar argument applies to the observation that the electric field strength increases with increasing plasma density (i.e. with increasing collisionality) as does effectively show Fig. 1.

Extrapolating these observations to $m_p/m_e = 1836$ and $N = 6400$ one therefore expects the maximum of the proton potential to drop to an even lower level. The peak is expected to be at least as marked as for the $m_p/m_e = 400$ case.

5. Conclusion

From self-consistent kinetic simulation of a solar type wind we find that, unless an efficient isotropization mechanism for the electron velocity distribution (e.g. wave-particle interaction), or some source of suprathermal electron distributions are invoked (e.g. shock produced), the formation of a transonic wind is only compatible with a sufficiently high collisionality in the vicinity of the sonic point $r = r_*$. In oder words, the coronal density must exceed a threshold density for the wind acceleration to be sufficiently strong to become supersonic. Given the admittedly oversimplifications in our model, combined with the fact that the parameters we use are rather unrealistic (excessively high coronal temperature and low m_p/m_e ratio) makes it impossible for us to specify an upper limit for the thermal Knudsen number at the sonic point r_*. We do merely show that the number cannot be arbitrarily large, the limiting value most likely being of the order unity, or less. As already stated, non Maxwellian boundary conditions, feeding an excess of suprathermal particles into the system (e.g. kappa distributions) may help overcoming the low Knudsen number condition. However, the existence of non thermal particle distributions rises the question of their origin. We chose not to address this question and assume Maxwellian boundary conditions which have the advantage of not requiring the introduction of additional ad hoc parameters into the model. Thus, in the absence of any electron scattering

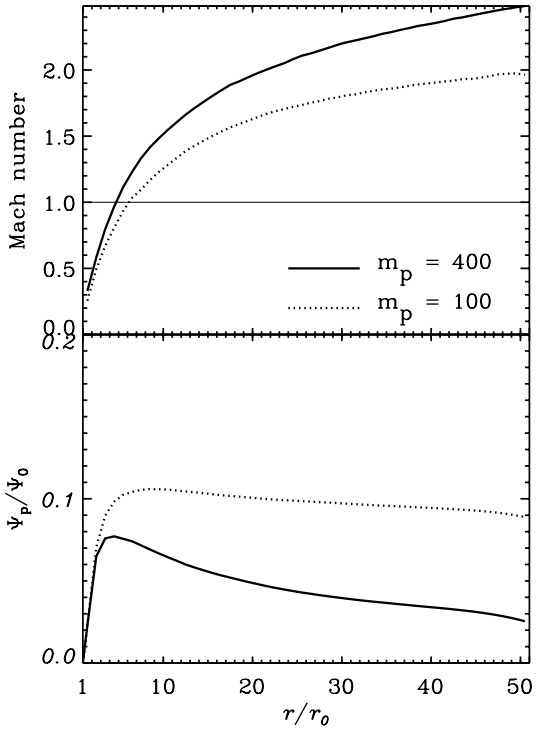

Fig. 8. Dependence of the Mach number and the proton potential energy on the proton to electron mass ratio for the simulation with $N = 6400$. Even though the qualitative behavior is similar it appears that a high mass ratio is in favor of a stronger acceleration of the wind. The definitions for the Mach number and the normalizing energy Ψ_0 are the same as in Fig. 1.

mechanism (apart from collisions), and unless special boundary conditions are imposed at the base of the simulation domain, collisions appear to be the essential ingredient for the wind to become accelerated to supersonic velocities, mainly because collisions are necessary to convert the electron heat flux into bulk energy of the plasma. The enthalpy gradient does also contribute to the acceleration of the wind. However, the acceleration associated with the radially decreasing enthalpy is found to be weakly dependent on the plasma collisionality and doesn't seem to be the discriminating factor in the acceleration of the wind to supersonic velocities.

In simulations where a transonic wind forms we find that the proton potential has a maximum near (but above) the sonic point. Typical values of the electric field near the sonic point r_* are found to be of the order of Dreicer's field, or larger. The presence of such strong electric field intensities may contribute in making the electron heat flux depart from the classical Spitzer-Härm formula (which requires the electric field being much weaker than Dreicer) but the main reason for the observed heat flux to depart from the Spitzer-Härm prediction is due to the presence of a strong "non collisional" heat flux $q_{\rm NC} \propto nvT_{\rm e}$. The latter appears to contribute significantly to the total electron heat flux, even in the region where the wind velocity is much smaller than the sound speed. We are aware of the fact that extrapolating the above results to the "real" Sun is a perilous exercise. However, we do not expect the qualitative behavior of a system with real coronal temperature and real proton to electron mass-ratio to behave in a substantially different way from the high density case discussed in this paper. In particular, increasing the proton to electron mass ratio from 400 to 1836 implies a factor two increase in the electron thermal velocity, only. Given that the electron thermal velocity at the base of the system is already one order of magnitude larger than the escape velocity for the $m_{\rm p}/m_{\rm e} = 400$ case, not much difference is expected in a system with twice this thermal velocity. The skeptical reader may also argue that using a realistic mass ratio would substantially modify the transport properties of the plasma. This is certainly true, but we expect the modifications to be small, essentially because neither the classical electron heat flux $q_{\rm SH}$ nor the collisionless heat flux $q_{\rm NC}$ depend on the mass ratio, at least as long as $m_{\rm p}/m_{\rm e} \gg 1$. We expect the excessively high coronal temperature used in our simulations to be a more crucial limitation in the process of transposing the above results to the solar case just because the proton thermal velocity and the escape velocity are of the same order, i.e. $\sqrt{\gamma_{\rm p}} = O(1)$. Indeed, the coronal temperature of the real Sun is roughly 3 times smaller that the value we use here. This implies a factor $\sqrt{3}$ difference for the order unity quantity $\gamma_{\rm p}$. The impact is certainly non negligible from a quantitative point of view but there aren't any reasons for us to believe that the qualitative aspects of our results do not apply to the solar case. For instance, whether or not the collisionless heat flux near the solar sonic point is really one order of magnitude stronger that the classical Spitzer-Härm flux remains an open question since this finding discords with recent results from multi-moment models.

Acknowledgements. We thank the referee for the detailed comments which very much helped us during the revision of the paper.

References

Alexander, P. 1993, ApJ, 414, 372
Braginskii, S. 1965, in Reviews of Plasma Physics, ed. M. Leontovich (New York: Consultants Bureau), 1, 205–311
Chamberlain, J. W. 1960, ApJ, 131, 47
Demars, H. G., & Schunk, R. W. 1979, J. Phys. D Appl. Phys., 12, 1051
Endeve, E., & Leer, E. 2001, Sol. Phys., 200, 235
Esser, R., Fineschi, S., Dobrzycka, D., et al. 1999, ApJ, 510, L63
Gray, D. R., & Kilkenny, J. D. 1980, Plasma Phys., 22, 81
Hollweg, J. V. 1974, J. Geophys. Res., 79, 3845
Jockers, K. 1970, A&A, 6, 219
Landi, S., & Pantellini, F. 2001, A&A, 372, 686
Lemaire, J., & Sherer, M. 1971, J. Geophys. Res., 76, 7479
Li, X. 1999, J. Geophys. Res., 104, 19773
Lie-Svendsen, Ø., & Leer, E. 2000, J. Geophys. Res., 105, 35
Lie-Svendsen, Ø., Leer, E., & Hansteen, V. H. 2001, J. Geophys. Res., 106, 8217
Meyer-Vernet, N., & Issautier, K. 1998, J. Geophys. Res., 103, 29705
Meyer-Vernet, N., Mangeney, A., Maksimovic, M., Pantellini, F., & Issautier, K. 2002, in Proceedings of the Tenth International Solar Wind Conference (American Institute of Physics), submitted
Olsen, E. L., & Leer, E. 1999, J. Geophys. Res., 104, 9963
Pantellini, F., & Landi, S. 2001, Ap&SS, 277, 149
Pantellini, F. G. E. 2000, Am. J. Phys., 67, 60
Parker, E. N. 1958, ApJ, 128, 664
Rosseland, S. 1924, MNRAS, 84, 720
Scudder, J. D. 1996a, J. Geophys. Res., 101, 11039
Scudder, J. D. 1996b, J. Geophys. Res., 101, 13461
Shoub, E. C. 1983, ApJ, 266, 339
Spitzer, L., & Härm, R. 1953, Phys. Rep., 89, 977
Tam, S. W. Y., & Chang, T. 1999, Geophys. Res. Lett., 26, 3189

9 Simulations d'un système granulaire

Eur. Phys. J. E (Soft Matter) 25, 201-212, 2008

Eur. Phys. J. E **25**, 201-212 (2008)
DOI 10.1140/epje/i2007-10281-5

Species segregation in one-dimensional granular system simulations

Filippo Pantellini[1] and Simone Landi[2]

[1] LESIA, Observatoire de Paris, CNRS, UPMC, Université Paris Diderot, 5 Place Jules Janssen, 92195 Meudon, France
[2] Dipartimento di Astronomia e Scienza dello Spazio, Largo Enrico Fermi 2, 50125 Firenze, Italy

Received 9 july 2007 and Received in finale form 16 November 2007

Abstract. We present one dimensional molecular dynamics simulations of a two species, initially uniform, freely evolving granular system. Colliding particles swap their relative position with a 50% probability allowing for the initial spatial ordering of the particles to evolve in time and frictional forces to operate. Unlike one dimensional systems of identical particles, two species one dimensional systems of quasi-elastic particles are ergodic and the particles' velocity distributions tend to evolve towards Maxwell-Boltzmann distributions. Under such conditions, standard fluid equations with merely an additional sink term in the energy equation, reflecting the non elasticity of the interparticle collisions, provide an excellent means to investigate the system's evolution. According to the predictions of fluid theory we find that the clustering instability is dominated by a non propagating mode at a wavelength of the order $10\pi L/N\varepsilon$, where N is the total number of particles, L the spatial extent of the system and ε the inelasticity coefficient. The typical fluid velocities at the time of inelastic collapse are seen to be supersonic, unless $N\varepsilon \lesssim 10\pi$. Species segregation, driven by the frictional force occurs as a result of the strong temperature gradients within clusters which pushes the light particles towards the clusters' edges and the heavy particles towards the center. Segregation within clusters is complete at the time of inelastic collapse.

PACS. 45.70.Mg Granular flow: mixing, segregation and stratification – 45.50.Tn Collisions – 02.70.Ns Molecular dynamics and particle methods

1 Introduction

Granular materials are ubiquitous in the macroscopic world [1]. The consequence of the inelasticity of the collisions between grains is that the standard fluid equations used to describe a gas of atoms or molecules need to be modified. Even for the simplest systems, the mathematical expressions for the transport coefficients turn out to be much more involved than the expressions for a system of elastic particles. In addition, granular materials are often polydisperse. For example sand grains are generally characterized by a broad range of particle sizes and shapes. Thus, theoretical models and numerical simulations based on granular systems of identical particles may be too limited to describe a real system, even on a purely qualitative level. On the other hand, systems of identical particles have the non negligible advantage of being mathematically simple while retaining many important features of real dissipative systems.

One of the most spectacular consequences of the inelastic nature of collisions in a granular system is the so called inelastic collapse. In the absence of energy injection statistical fluctuations in an initially uniform system can lead some regions to cool faster than others producing linearly growing density fluctuations which can be described in the frame of continuum model theories [2, 3, 4]. In the non linear regime the high density regions collapse producing clumps of particles where the collision frequency grows to infinity[5, 6]. The instability is a long wavelength instability which is hardly avoidable in freely evolving systems provided the number of particles in the system exceeds some minimum value which very much depends on the system's characteristics [6, 3]

It is often acceptable to describe granular systems by means of fluid equations derived from the inelastic Boltzmann equation using the Chapman-Enskog procedure [7, 8, 9]. Hydrodynamic models have been applied to the case of inelastic particles in a constant gravitational field [10, 11, 12]. These systems often behave non intuitively. Hence, it is shown in [12] that a collection of inelastic particles confined to a vertical box with permanent injection of energy from the base (e.g. by shaking the base of the box vertically) the granular temperature profile is a non monotonic function of height. The temperature decreases near the bottom, goes through a minimum, and finally rises indefinitely with height above the minimum.

It has been recently shown in [13] that during the homogeneous regime of the temporal evolution of a one dimensional system of identical particles the spatial ordering of the particles appears to play a crucial role in

shaping the particles' velocity distribution. Thus, works [14], based on the so-called pseudo-Maxwell model, a homogeneous model where no spatial ordering is assumed by construction, have been found to be unable to describe the evolution of a system of inelastically interacting particles, even during the homogeneous regime. The late evolution of systems of identically spatially ordered particles has been shown to be strongly affected by the development of spatial correlations between the particles' velocities eventually leading to an inelastic collapse [e.g. 2, 13].

One dimensional systems of identical particles behave in a very peculiar way. Thus, in the elastic limit, the overall velocity distribution of the particles' is not modified by collisions. Colliding particles do merely exchange their velocities and the system is not ergodic. Adjunction of just one anomalous particle forces the velocity distribution to relax towards a Maxwell-Boltzmann distribution.

In this paper we use molecular dynamics (MD) simulations to investigate the evolution of a two species one-dimensional, periodic, system of N point particles. $N/2$ particles have mass $m_1 = 1$ (species 1) and $N/2$ particles have mass $m_2 = 4$ (species 2). The system is a prototype for more complex systems with broader mass distributions. One important ingredient of the model is that colliding particles swap their relative position with a 50% probability allowing for the initial spatial ordering of the particles to evolve in time. This introduces the possibility of species to stream with respect to eachother giving frictional forces the opportunity to operate.

The restitution coefficient r, appearing in the collision rules (12) and (13), is close to elastic such that the thermalization time is always much shorter than the cooling time. As a consequence, the velocity distribution function of both species are always close to Maxwellian, at least as long as the species do not segregate. Such dissipative systems are always linearly unstable with respect to the so-called clustering instability. In one dimension the clustering instability is a fluid instability which is found to triggers the formation of non propagating spatial density inhomogeneities at scales of the order $10\pi L/N\varepsilon$, where $\varepsilon \equiv 1 - r^2$ and L is the size of the system. The clusters of particles which form due to the clustering instability are characterized by a temperature profile which increases exponentially as a function of the particle index l away from the center of the cluster (cf e.g. Figure 6). These strong temperature gradients within clusters drive the light particles away from their centers towards the edges of the clusters while the opposite happens to the heavy particles which tend to become concentrated in a very small region near the center of the cluster. (cf Figures 4 and 5). The species segregation is driven by the frictional force (7) which points in opposite directions for the light and heavy particles. At the time of inelastic collapse, fluid motions may or may not be supersonic depending on whether or not the number of particles N exceeds a critical number of order $10\pi/\varepsilon$. In order to avoid confusion, we do loosely define the time of inelastic collapse in our simulations as the time for which the molecular dynamic simulation is essentially "frozen". By "frozen" we mean that the total energy and, consequently the fluid velocity profiles of the system do not change significantly by doubling the number of collisions.

The paper is organized as follows. In Section 2 we introduce the set of fluid equations whereon we base our analysis of the simulation results. The numerical model is presented in Section 3. Simulations with $N = 19600$ particles and 3 different values of the restitution coefficient r are presented in Section 4, In Appendix A we develop the linear theory of the clustering instability for a two-species, one dimensional system. The collision frequency for such a system in the homogeneous limit and close to the thermodynamic equilibrium, is given in Appendix B.

2 Fluid equations for a mixture of two species

In the general case [see e.g. 15], the expressions for the hydrodynamic transport coefficients describing a granular gas with two species of inelastically interacting particles are so involved that they are of little practical use to describe real systems. It is not even clear under which conditions fluid equations are relevant for real granular systems. However, over the years it has been shown that fluid equations are extremely useful to help understand results from granular system simulations. Over the few last decades, explicit expressions for the transport coefficients in 2 and 3 spatial dimensions have been published by various authors. To our knowledge, expressions for the 1d case have not been published until now, certainly because of the non-ergodicity of most 1d systems. Yet, in the case of a mixture of unequal particles, collisions among particles of different mass do inevitably drive the velocity distribution functions for all species towards Maxwell-Boltzmann. The tendency to thermalization in such one dimensional mixtures indicates that "standard" fluid equations may apply to such systems as well.

The fluid equations of this section all stem from a Chapman-Enskog type treatment of the Boltzmann equation by various authors [7, 8, 15, 9] which implies that their validity is at best limited by the assumptions on which the Chapman-Enskog procedure is based on. One of the most stringent conditions, in a system characterized by a mean free path l_{mfp} and a spatially varying temperature $T(x)$, is the requirement of the Knudsen number $K \equiv l_{\mathrm{mfp}}\, \partial \log T/\partial x$ being much smaller than unity. The $K \ll 1$ condition means that the particles' distribution functions do not vary substantially over distances of the order of the mean free path l_{mfp} and that the velocity distributions are close to Maxwellian. A related condition is that fluid time scales must be long compared to the collisional time scale, i.e. the time between successive collisions of a thermal particle.

We write the continuity equation for two species $\alpha = 1, 2$ in terms of the species mean velocities u_α and mass densities $\varrho_\alpha = m_\alpha n_\alpha$:

$$\frac{\partial \varrho_\alpha}{\partial t} + \frac{\partial}{\partial x}\left(\varrho_\alpha u_\alpha\right) = 0. \tag{1}$$

Defining the total density $\varrho \equiv \varrho_1 + \varrho_2$ and the center of mass flow velocity $u \equiv (u_1\varrho_1+u_2\varrho_2)/\varrho$ one can add the two continuity equations (1) and write a one fluid continuity equation:

$$\frac{\partial \varrho}{\partial t} + \frac{\partial}{\partial x}(\varrho u) = 0. \tag{2}$$

According to [16] we write the momentum equation for both species in the form

$$\varrho_\alpha \left(\frac{\partial u_\alpha}{\partial t} + u_\alpha \frac{u_\alpha}{\partial x} \right) = -\frac{\partial [p_\alpha (1 + K_\alpha)]}{\partial x} + \phi_\alpha \tag{3}$$

where ϕ_α represents the frictional force on the species α due to the collisions with the other species in the system and where K_α is the contribution to the pressure tensor from collisions with all species (shear and bulk viscosity). Momentum conservation implies $\phi_1 = -\phi_2$. The sign difference between ϕ_1 and ϕ_2 indicates that if the frictional force is dominant, it can act as a species filter. The partial pressures p_α in equation (3) are defined with respect to the center of mass flow velocity u, i.e.

$$p_\alpha \equiv \int m_\alpha (v-u)^2 f_\alpha(v) dv = n_\alpha T_\alpha. \tag{4}$$

For the remaining of this section, and throughout the paper, we assume that collisions are efficient enough to ensure energy equipartition among species, i.e. $T = T_1 = T_2$. This restriction implies the characteristic cooling time for each species being long with respect to the thermalization time. The energy equation for the mixture in the one-dimensional case is then given by [15]

$$\frac{\partial p}{\partial t} + u\frac{\partial p}{\partial x} + 3p\frac{\partial u}{\partial x} + 2\frac{\partial q}{\partial x} - \frac{8}{3}\eta \left(\frac{\partial u}{\partial x} \right)^2 = -\zeta p \tag{5}$$

where $p \equiv p_1+p_2$ is the total pressure, q the total heat flux, η the shear viscosity and ζ the cooling rate due to inelastic collisions. The bulk viscosity is zero by construction [see 9]. Similarly, the momentum equation for the mixture can be written in the conventional form [15]

$$\frac{\partial u}{\partial t} + u\frac{\partial u}{\partial x} = -\frac{1}{\varrho}\frac{\partial}{\partial x}\left(p - \frac{4}{3}\eta \frac{\partial u}{\partial x} \right). \tag{6}$$

We note that this equation is equivalent to equations (3) up to terms which are quadratic in the species relative drift velocity $\delta u_1 \equiv (u_1 - u)$.

In the quasi-elastic limit, for small relative drift velocities, and assuming energy equipartition among species the following relations do conveniently close the above set of fluid equations. According to [16] the frictional force may be cast into the form

$$\phi_1 = a(n_1, n_2)\, 2T\, \frac{n_1 n_2}{n} \frac{\partial}{\partial x}\left[\ln\left(\frac{n_1}{n_2} T^{\,m_{12}} \right) \right] \tag{7}$$

with $m_{12} \equiv (m_2 - m_1)/m$, $m \equiv m_1 + m_2$ and $n \equiv n_1 + n_2$. In equation (7) a is a dimensionless function of n_1 and n_2 which takes into account the species volume fraction and the radial distribution function of the contacting pairs. Explicit forms have been given for the 2 and 3 dimensional case [16]. In this paper we do not care about the exact form of equation 7. We are just interested in the qualitative dependence of ϕ_1 on the temperature T and on the relative species concentration n_1/n_2. Following [9, 15] we write the constitutive relation for the heat flux as

$$q = -\frac{nT}{\nu_0\sqrt{m_1 m_2}} \frac{\partial T}{\partial x} \left[b_1 \frac{n_1}{n}\sqrt{\frac{m}{m_1}} + b_2 \frac{n_2}{n}\sqrt{\frac{m}{m_2}} \right] \tag{8}$$

where we have defined the frequency $\nu_0 \equiv V_{12} n \sigma$ and the characteristic velocity $V_{12}^2 = 2Tm/(m_1 m_2)$, which, for species with Maxwellian distributions, is just the thermal velocity for the relative velocities between the two species (cf Appendix B). Again, both, b_1 and b_2, are rather involved functions of n_1/n, m_1, m_2 and even V_{12}, which we do not need to care about in this paper. In the above equation σ has the dimension of a surface and may be interpreted as a collisional cross section. Formally, we express σ in terms of the total number of particles N, the box length L and the mean number density $\overline{n}$:

$$\sigma = \frac{N}{\overline{n} L}. \tag{9}$$

With this definition, in a uniform system one has $\nu_0 = V_{12} N/L$. Starting from equation (27) of Jenkins and Mancini [7] we find that ζ must depend on the species densities via an expression of the kind

$$\zeta = \varepsilon \nu_0 \left[c_{11}\frac{n_1^2}{n^2}\sqrt{\frac{m_2}{m}} + c_{22}\frac{n_2^2}{n^2}\sqrt{\frac{m_1}{m}} + c_{12}\frac{n_1 n_2}{n^2} \right] \tag{10}$$

where the numerical coefficients c_{11}, c_{12}, and c_{22} are unknown for the 1d case and where ε is the fractional energy loss per collision (see Section 3). Equation (10) is correct up to terms of order two in the gradients of hydrodynamic quantities[8, 15]. Following Garzo et al [15] we write the shear viscosity coefficient η as

$$\eta = \frac{nT}{\nu_0}\left[d_1 \frac{n_1}{n}\sqrt{\frac{m}{m_2}} + d_2 \frac{n_2}{n}\sqrt{\frac{m}{m_1}} \right] \tag{11}$$

where, once more, d_1, and d_2 are order unity coefficients for which we do not care about the exact form. As a final remark, we note that in the set of fluid equations (2),(5) and (6) the inelasticity coefficient ε does only appear in the energy equation (5) through the cooling rate $\zeta \propto \varepsilon\nu_0$. In particular, neither the friction ϕ_1, nor the heat flux q depend on ε, which is only acceptable in the quasi-elastic limit $\varepsilon \ll 1$ [15].

3 Simulation model

We use a one-dimensional model which is close to the traditional point-like hard particles on a ring model [13] with the notable difference that $N/2$ particles have mass m_1 and $N/2$ particles have mass m_2. In the strict one dimensional case the post collision velocities v_i' and v_j' for two

Table 1. Basic parameters for the 3 simulations discussed in the paper. The total number of particles in each simulation is $N = 19600$ with half of the particles with mass $m_1 = 1$ and the other half with mass $m_2 = 4$.

Run	ε	r^2	$N\varepsilon$
1	5×10^{-4}	0.9995	9.8
2	2×10^{-3}	0.998	39.2
3	2×10^{-2}	0.98	392

colliding particles i and $j = i + 1$ of mass m_i and m_j and center of mass velocity $v_{0ij} = (m_i v_i + m_j v_j)/(m_i + m_j)$ are given by

$$v_i' = \pm \frac{m_j v_{ij}}{m_i + m_j} r + v_{0ij} \quad (12)$$

$$v_j' = \mp \frac{m_i v_{ij}}{m_i + m_j} r + v_{0ij} \quad (13)$$

where r is the restitution coefficient ($r = 1$ for elastic collisions), v_k the velocity of particle $k = i, j$ before the collision and $v_{ij} \equiv v_j - v_i < 0$ (we implicitly suppose a one dimensional axis x with coordinates increasing from left to right $x_i < x_j$). With this definition of the restitution coefficient r the kinetic energy of two colliding particles is reduced by a factor $\varepsilon \equiv 1 - r^2$ in the center of mass frame. The + sign in (12) and the − sign in (13) correspond to the normal case where particle i and j do not exchange their relative positions during collision. The − sign in (12) and the + sign in (13) correspond to the case where particles i and j swap their relative positions during collision. In the latter case, taking $r = 1$, one has $v_i' = v_i$ and $v_j' = v_j$, i.e. particles just ignore each other. In principle one should reject this possibility as it is a non physical event for the case of a system of beads on a ring. We shall take advantage of this possibility as it allows for the different particles to become distributed spatially independently of the initial ordering with the possibility of species segregation to operate as in 2 and 3 dimensional systems.

4 Simulation results

In all simulations N particles are initially distributed uniformly over the spatial domain $[0, L[$. We consider a simple two species system of $N/2$ particles with mass $m_1 = 1$ and $N/2$ particles with mass $m_2 = 4$. Particles of both species are initially disposed in alternating order. The initial velocity of a particle with mass m_α is randomly selected in the interval $[-0.5, 0.5]/m_\alpha^{1/2}$ following a uniform probability distribution as in the [13] where the reference case of N identical particles is discussed. The mean energy per particle is therefore the same for all species. Bulk velocities of all species are initially set to zero. The parameters for the 3 runs which will be discussed in the paper are listed in Table 1. The somewhat arbitrary mass ratio $m_2/m_1 = 4$, which will be used throughout the paper, is sufficiently small to ensure efficient interspecies energy thermalization, so that we can assume $T_1 = T_2$, and sufficiently large for the frictional force ϕ_1 (see equation (7)) to play a non negligible role.

4.1 Homogeneous phase

The evolution of a one-dimensional system with not all particles having the same mass is very different from that of a one dimensional system of identical particles [e.g 6, 2, 13]. The difference is substantial, even in the elastic limit $r = 1$. Indeed, while in the case of elastically interacting identical particles the velocity distribution does not change in time, the asymptotic velocity distribution is a Maxwell-Boltzmann velocity distribution when different species coexist in the system. The global thermalization rate strongly depends on the particles' mass distribution, each species α thermalizing at different rates depending on the species number density N_α and on the mass m_α of the species particles. For example in the case of a system with $N \gg 1$ and just one anomalous particle, the evolution towards a Maxwell-Boltzmann distribution is much slower than in the case of a two species system with $N/2$ particles for each species, since only collisions among unequal particles can modify the velocity distribution functions in one dimensional systems.

In Figure 1 a snapshot of the velocity distribution function of both species are shown for Run 1 after a total number of 8×10^7 collisions . The distribution for both, light and heavy particles, which should be compared to the double peaked distribution of Figure 1 in [13] for the one species case, do closely follow a Maxwell-Boltzmann distribution disregarding of the fact that the initial distribution was strongly non thermal. This tendency of the velocity distributions to evolve towards Maxwell-Boltzmann

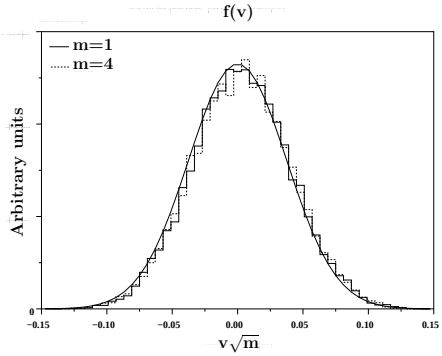

Fig. 1. Homogeneous regime for the case of $r^2 = 0.9995$ and $N = 19600$ particles half of which have mass $m_1 = 1$ and the other half $m_2 = 4$ (Run 1). Shown are the velocity distribution histograms for both species after 8×10^7 collisions. The solid line represents the Maxwell-Boltzmann distribution corresponding to the measured particles' mean energy.

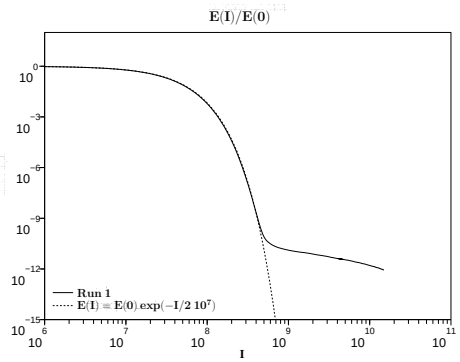

Fig. 2. Energy versus collision index I for Run 1. The exponential part of the profile closely follows the $E = E_0 \exp(-I/2 \times 10^7)$ profile of the fluid theory.

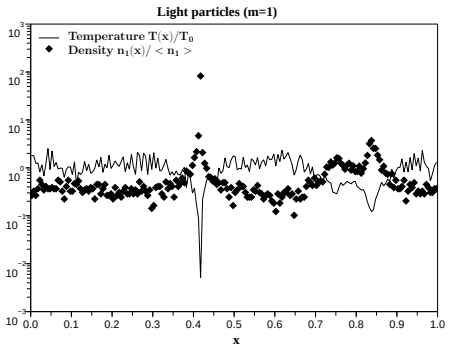

Fig. 3. Run 1: Temperature and density profiles for the light particles (i.e. $m = 1$) normalized to their average value at the end of the simulation. Note the high concentration and low temperature within the cluster near $x = 0.416$. Also note the presence of a second cluster forming near $x = 0.8$.

allows the use of standard fluid theories [7, 8, 15, 9] to analyze the system's behavior.

Figure 2 shows the evolution of the energy in Run 1. The energy decreases exponentially as a function of the number of collisions I during the first $5\,10^8$ collisions. We shall define this phase as the homogeneous phase as it is perfectly well described by the homogeneous version of the fluid energy equation (5) (see equation (A.7) together with the relation (B.7)) which predicts a per collision energy loss of

$$\frac{\overline{\delta E}}{E} = -2\frac{\varepsilon}{N} \tag{14}$$

Specifically, for $r^2 = 0.9995$ and $N = 19600$ one has $\overline{\delta E}/E \approx 5.1 \times 10^{-8}$ which corresponds to the value 2×10^7 observed in Figure 2.

4.2 Inhomogeneous phase

After the initial homogeneous phase the system enter a new, inhomogeneous, regime where cluster formation becomes the dominant effect. The transition between the homogeneous and the inhomogeneous regime is clearly visible as a departure from the exponential energy decay in Figure 2. In this section we discuss the cluster structures observed in the simulations in the light of the fluid equations exposed in Section 2.

4.2.1 Species segregation

As in the one species case, the inhomogeneous regime in the multi species case is characterized by the presence of clusters of particles. Given the smallness of the inelasticity coefficient ε and the initial homogeneity of the system, one expects the pressure to be spatially uniform for both species, except near the center of the collapsing cluster where the cooling rate ζ goes to infinity. Indeed, the temperature and density profiles, plotted for the light particles at the end of Run 1 are seen to vary in antiphase (cf Figure 3) ensuring an approximate pressure balance.

However, light and heavy particles are not evenly distributed within the cluster. The relative concentration of light particles as a function of the particle index l is shown in Figure 4 which clearly shows that the heavy particles are concentrated in the central part of the cluster, leaving an excess of light particles in the wings of the 6000 particles cluster.

In order to appreciate the spatial scales associated with the concentrations of light and heavy particles in the cluster we compute the integrated heavy particles excess func-

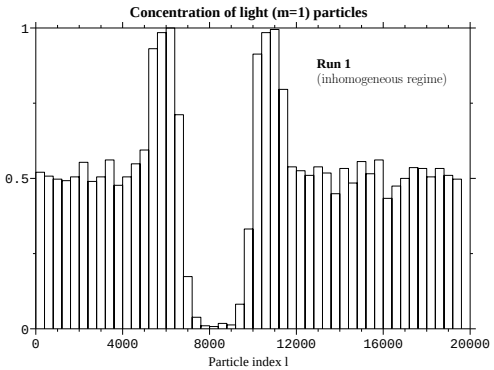

Fig. 4. Light particles histogram (m=1) at the end of Run 1. Bin values represent the fractional number of light particles n_1/n. Each bin contains 400 particles. The main cluster includes all particles with index l in the range 5000 to 11000.

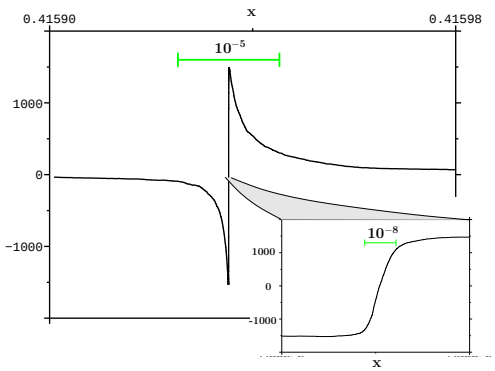

Fig. 5. Function $Y(x)$ (see equation (15)) for Run 1. The slope of the function Y is a measure of the heavy (positive slope) or light (negative slope) particle excess.

tion Y defined as

$$Y(x) = \sum_{l=1}^{N} (\delta_{m_l m_2} - \delta_{m_l m_1}) \int_0^x \delta(\xi - x_l) d\xi \qquad (15)$$

Contribution to the integral is -1 for light particles ($m_l = 1$) and +1 for heavy particle ($m_l = 4$).

The function $Y(x)$ is plotted in Figure 5 and illustrates how disparate the spatial repartition of light and heavy particles are in the system. The core of the cluster contains some 3×10^3 heavy particles concentrated in a region of size 10^{-8}. From Figure 4 we know that the 3×10^3 light particles of the cluster are largely excluded from this small central region dominated by the heavy particles but Figure 5 shows that the light particles dominate over a much larger region of size 10^{-5}, the characteristic size of the cluster at the end of the simulation. The species segregation is the visible effect of the frictional force ϕ_1 (cf equation (7)) of the two fluid momentum equations (6). In case of equal densities $n_1 = n_2$ and a spatially varying temperature profile $T(x)$ the frictional force $\phi_1 \propto (m_2 - m_1)\partial T/\partial x$ points up the temperature gradient for the light species m_1 and down the temperature gradient for the heavy species m_2. Segregation appears as a ineluctable consequence of the temperature gradients within clusters.

4.2.2 Temperature profiles in clusters

Figure 3 shows that the temperature in a cluster strongly decreases towards its center. Figure 6 shows the temperature profiles in the inhomogeneous regime for Run 1 and 2. The figure illustrates the fact that the temperature drops exponentially as a function of the particles index l towards the center of the cluster. In these particular cases the temperature decreases by several order of magnitudes from edge to center. As expected, the thermalization time being

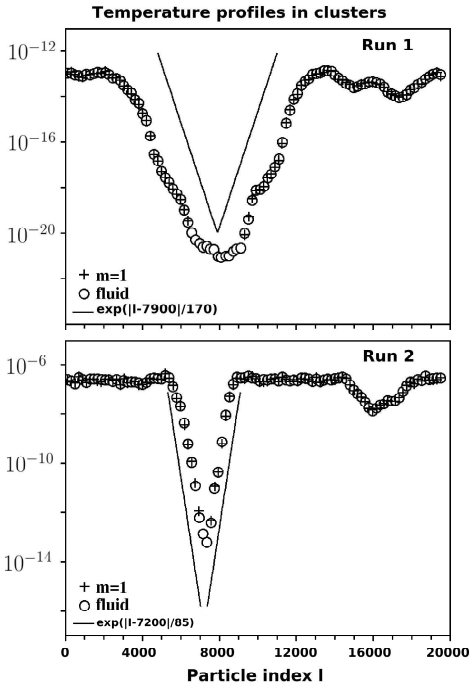

Fig. 6. Fluid temperature (circles) and light particles' temperature (plus) as function of the particle index for Run 1 (top panel) and Run 2 (bottom panel) during the inhomogeneous regime. In both simulations the temperature is found to decrease exponentially towards the center of the cluster according to a characteristic scale of order $\varepsilon^{-1/2}$.

much shorter than the cooling time, the fluid and light particle temperature profiles closely follow each other. The interesting point is that the granular temperature decreases exponentially towards the center of the cluster with a scale which seems to be of order $\varepsilon^{-1/2}$. Again, the $\varepsilon^{-1/2}$ scaling of the temperature profile in Fig. 6 can be deduced easily from the fluid equations. In order to do so, we evaluate the temperature profiles within clusters in the static limit. Using the energy equation (5) we can write

$$2\frac{\partial q}{\partial x} = -\zeta p \qquad (16)$$

Let us suppose that in a given region of the system species 1 is the dominating one, i.e. $n \approx n_1 \gg n_2$. In this case the heat flux reads (cf equation (8))

$$q = -\frac{b_1}{\sigma}\left(\frac{T}{2m_1}\right)^{1/2}\frac{\partial T}{\partial x} \qquad (17)$$

whereas the right hand side of Eq. (16) becomes

$$-\zeta p = -\varepsilon c_{11}\sigma\left(\frac{2T}{m_1}\right)^{1/2} T\, n^2 \qquad (18)$$

and the static energy equation (16) writes

$$\frac{\partial}{\partial x}\left(T^{1/2}\frac{\partial T}{\partial x}\right) = \varepsilon\,\frac{c_{11}}{b_1}\,\sigma^2 T^{-1/2} p_0^2 \tag{19}$$

where we have used the static limit $p = p_0 = const$ of the momentum equation (6). In order to compute the temperature profile as a function of the particle index l we have to introduce the transformation from the spatial coordinate x to the particle index l.

$$l(x) = A\int_0^x n(\xi)d\xi \tag{20}$$

where A is a surface such that $An(\xi)d\xi$ is the number of particles in the interval $[\xi, \xi + d\xi]$. Using the transformation (20) we write the energy equation (19) in terms of the particle index l

$$\frac{\partial}{\partial l}\left(T^{-1/2}\frac{\partial T}{\partial l}\right) = \frac{\varepsilon}{4}\,\frac{c_{11}}{b_1}T^{1/2} \tag{21}$$

where we have used the fact that the particles' cross section σ is equal to $A/2$ given the 50% swap probability for colliding particles. The solution of (21) is

$$T \propto \exp\left\{\pm l\,\left(\varepsilon\,\frac{c_{11}}{2b_1}\right)^{1/2}\right\} \tag{22}$$

If c_{11} and b_1 are numerical constants of order unity, it follows, as already suggested by Figure 6, that the typical scale of variation for the temperature profile is of order $\varepsilon^{-1/2}$.

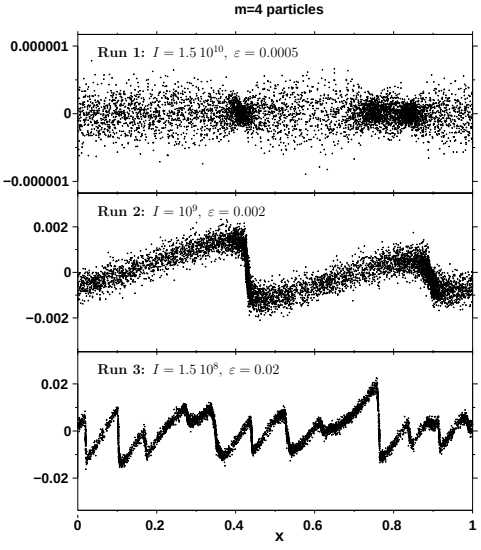

Fig. 7. Inhomogeneous regime: scatter plot for the $m = 4$ particles for all runs at the time of inelastic collapse.

4.3 Cluster formation and linear fluid theory

As in one species simulations [6], Figure 7 shows that at the time of inelastic collapse, the number of clusters is an increasing function of the $N\varepsilon$. Even the Mach number of the fluid motions is seen to depend on $N\varepsilon$, the simulation with the smallest value of $N\varepsilon$ being characterized by subsonic motions and the two other simulations being characterized by supersonic motions with the evident formation of shocks. As pointed out by Ben-Naim et al [17] the piecewise linear velocity profiles observed in Figure 7 are a direct consequence of the momentum equation (6). Indeed, as already discussed in the context of Figure 3, the pressure in the system is essentially constant everywhere except within clusters (shocks in the supersonic regime). In this case the momentum equation reduces to $\varrho(\partial u/\partial t + u\partial u/\partial x) = 0.75\eta\partial^2 u/\partial x^2$ with solutions of the type $u(x,t) = u_0 + (x - x_0)/t$, where u_0 and x_0 are integration constants.

The difference between the velocity profiles at the time of inelastic collapse for the three runs shown in Figure 7 can be explained on the basis of a linear analysis of the fluid equations of Section 2 developed in Appendix A. The linearized system of equations has three eigenmodes, two of which correspond to the right and left propagating sound wave and the non propagating (zero real frequency) entropy mode. The main difference with respect to classical gas dynamics is that all modes are unstable at long wave length. The other important prediction of linear theory is that in general, but more specifically for wave vectors k such that $\tilde{k} \equiv kL/(N\varepsilon) \lesssim 1$, the non propagating entropy mode grows substantially faster than the sound mode. Indeed, the growth rate of the entropy mode always peaks at $k = 0$ whereas the sound mode's growth rate vanishes as $k \to 0$. A careful analysis of the growth rates does actually shows that the entropy mode is always the fastest growing mode (see Appendix A).

4.3.1 The dominant mode

What determines the number of clusters in a one dimensional system at the time of inelastic collapse? Knowledge of the initial conditions for the velocity fluctuations of all modes makes it possible to estimate different characteristic time scales in terms of the dimensionless (pseudo) time variable τ (defined in A.5) using the approximations of linear theory.

Initially, in all systems, particles are distributed uniformly in the spatial interval $[0, 1[$ with $N/2$ particles of mass $m_1 = 1$ and $N/2$ particles of mass $m_2 = 4$. The velocity of a particle of mass m is sorted randomly in the velocity interval $[-0.5, 0.5]/m^{1/2}$ so that the average kinetic

energy per particle is the same for all species corresponding (formally) to an initial temperature $T_0 = 1/12$ and thermal velocity $v_0^2 = 2/(6\overline{m}) = 1/15$. Thermalization of such a system takes only a few collisions per particle so that all species can be assumed to be initially distributed according to a Maxwellian distribution at temperature $T_0 = 1/12$, ε being much smaller than unity. The initial amplitudes of the velocity fluctuations can be evaluated using the Wiener-Khintchine theorem which states that the power spectrum of the fluid velocity field for a set particles with uncorrelated velocities is flat (white noise). The immediate consequence of the Wiener-Khintchine theorem is that energy is evenly distributed among all Fourier modes, i.e. all modes have equal amplitude $|\delta u_0|$. Requiring the total kinetic energy of all particles in the system being $NT/2$ one must have

$$\delta u_0^2 = \frac{T}{\overline{m}} \frac{4}{N} = 2\frac{v_0^2}{N} \tag{23}$$

In all simulations, at $t = 0$, we have $T = 1/12$, $N = 19600$, $m_1 = 1$ and $m_2 = 4$. The initial amplitude of the velocity fluctuations are therefore of order $\delta u_0 = 2.6 \times 10^{-3}$ with $v_0 = 0.258$, which corresponds to $\delta U_0 = (2/N)^{1/2} = 1.01 \times 10^{-2}$.

From linear theory we know that at small values of the wave vector $\tilde{k} \lesssim 1/2$ the growth rate is approximately given by $\gamma N/\varepsilon = 1 - \tilde{k}^2/2$ indicating that the mode with the longest possible wavelength is always the fastest growing mode. It is then expected that clustering always occurs at the largest possible scale allowed by the system with only one cluster growing in the system. This is effectively the case in Run 1 only but not in Run 2 (with 2 clusters) and particularly in Run 3 where several clusters occur. This can be understood by noting that linear theory predicts that the density fluctuation of the entropy mode is proportional to the wave vector k:

$$\frac{\delta n_k}{n} = -i\tilde{k}\delta U_k \tag{24}$$

where $\delta U_k \equiv \delta u_k/v_0$ is essentially the fluctuation's Mach number. Thus, for two modes k_1 and k_2 with equal initial velocity fluctuation amplitude $\delta U_{k1} = \delta U_{k2}$, the one with the largest wave vector is the one with the largest associated density fluctuation and therefore a more likely candidate for triggering the inelastic collapse, provided the growth rate of the two modes are not too dissimilar. For example, in Run 3, there are some 10 visible density clusters corresponding to an average distance between clusters of the order $\lambda = L/10$. Therefore, the mode which triggers the inelastic collapse has $\tilde{k} = 0.16$ and a linear growth rate which is only roughly 1% less than the growth rate of the smallest possible wave vector $\tilde{k}_{\min} \equiv 2\pi/N\varepsilon$, but, according to equation 24, with a 10 times larger density fluctuation. Thus, as long as the velocity fluctuation amplitude of the mode $\tilde{k} = 0.16$ is not much smaller than the velocity fluctuation amplitude of the fastest growing mode, i.e. potentially during the first $100\gamma^{-1} \approx 100N/\varepsilon = 9.8 \times 10^7$ collisions, the strongest density fluctuations in the system are due to the mode with $\tilde{k} = 0.16$. Indeed, in Run 3 particle clustering and supersonic motions are already present after $I \approx 4 \times 10^6$ collisions, which, using the definition for τ given by (B.7) in Appendix B corresponds to $\tau = 2.06I \approx 8 \times 10^6$. This time is too short by more than one order of magnitude for the fastest growing mode to become dominant in terms of density fluctuations.

We conclude that, for quasi elastic restitution coefficients $\varepsilon \ll 1$, the mode which dominates the inelastic collapse has a wave vector $\tilde{k} \sim 1/5$ corresponding to a wavelength $\lambda \sim 10\pi L/N\varepsilon$. If such a long wavelength does not fit into the system, the dominant mode is simply the one with the longest possible wavelength, i.e. $\lambda = L$.

Table 2. Characteristic time scales of the entropy mode for the smallest possible wave vector $k = k_{\min} \equiv 2\pi/N\varepsilon$. The column labelled Supersonic indicates whether or not the fluid motions are supersonic at the time of inelastic collapse. γ refers is the linear growth rate of the mode, τ_s and τ_n are defined in equations (25) and (26), respectively. The parameters of the runs are given in Table 1.

Run	Supersonic	$\tilde{k}_{\min}$	γ^{-1}	τ_s	τ_n
1	no	0.64	4.9×10^7	2.3×10^8	2.5×10^8
2	yes	0.160	1.0×10^7	4.6×10^7	6.4×10^7
3	yes	0.016	1.0×10^6	4.5×10^6	8.6×10^6

4.3.2 Supersonic fluid motions

Let us now address the question of the magnitude of the characteristic fluid velocities at the time of the inelastic collapse. Velocities are subsonic in Run 1 and supersonic in Runs 2 and 3.

We introduce the sonic time scale τ_s, defined as the time for the amplitude of the velocity fluctuation δU_k to reach unity assuming linear growth, i.e.

$$\tau_s(\tilde{k}) = -\frac{\ln(\delta U_0)}{\gamma(\tilde{k})}. \tag{25}$$

For a system of uniformly distributed particles with uncorrelated velocities, the initial fluctuation amplitude is $\delta U_0 \approx (2/N)^{1/2}$. Similarly, using equation (24) we define τ_n as the time for the density fluctuation $\delta n(k)/n$ to reach an amplitude of order unity, i.e.

$$\tau_n = -\frac{\ln(\tilde{k}\ \delta U_0)}{\gamma(\tilde{k})}. \tag{26}$$

Both, τ_s and τ_n are listed in Table 2 for the mode with the longest wavelength $\tilde{k}_{\min}$.

In Run 1 the motions remain subsonic at the time of the inelastic collapse despite the simulation lasting significantly longer than τ_s, meaning that supersonic motions had enough time to develop. We conclude that an inelastic collapse is not necessarily associated with supersonic motions. The explanation at hand can be found in Table 2 which shows that in Run 1 the characteristic times τ_s

and τ_n are very much the same for the dominant mode $k = k_{min} \equiv 2\pi/N\varepsilon$ while the sonic time scale τ_s is significantly shorter than τ_n for the dominant mode in Runs 2 and 3. From Table 2 it follows that supersonic motions develop before the occurrence of an inelastic collapse provided $k_{min} \lesssim 1/5$, i.e. $10\pi \lesssim N\varepsilon$.

5 Conclusions

We have performed simulations of a one dimensional two species periodic system of N point particles undergoing inelastic collisions. In order to keep the possibility for the system to arrange particles independently of the initial configuration, particles are allowed to change their relative positions during collisions with a 50% probability. Initial velocities for particles of species α are selected randomly according to a constant distribution in the range $[-0.5, 0.5]/m_\alpha^{1/2}$. Unlike one dimensional systems of identical particles, where the homogeneous regime is characterized by double peaked velocity distributions [13, 18], one dimensional multi-species systems tend to evolve towards a Maxwell-Boltzmann distribution. This tendency justifies the use of "standard" fluid equations to describe such systems. As for one dimensional systems of identical particles, the inhomogeneous regime is characterized by the formation of clusters which eventually make an inelastic collapse. It has been shown in [2] that clustering in one species systems is driven by a beam instability. We show that in a two species system clustering is triggered by a fluid instability of the non propagating entropy mode, for which density and temperature fluctuations vary in antiphase ensuring spatial pressure balance. The sound mode is also found to be unstable but its growth rate is always substantially smaller than the growth rate of the entropy mode. Because of the non propagating nature of the entropy mode, the one dimensional system does evolve naturally towards a series of clusters with symmetric temperature and density profiles and antisymmetric velocity profiles.

The number of particles in the clusters is determined by the number of particles in one wavelength of the dominant mode of the clustering instability, i.e. the mode which first reaches a relative density fluctuation of order unity. The typical wavelength of this mode has been found to be of the order $\lambda \approx 10\pi L/N\varepsilon$ corresponding to $10\pi/\varepsilon$ particles per cluster. Clustering is generally characterized by supersonic fluid motions unless the total number of particles $N \lesssim 10\pi/\varepsilon$.

A peculiar aspect of the late evolution of a multi-species systems is the appearance of species segregation within the collapsing clusters, heavy particles becoming concentrated in an extremely small region around the center of the cluster and the light particles filling the space between the central region and the edges of the cluster. Segregation is driven by the temperature gradient inside the cluster [19] via the frictional force ϕ in the one-species fluid momentum equation (3).

We thank both referees for the many pertinent and helpful comments which strongly helped us to improve the original manuscript.

A Linear theory for a one-dimensional system

In this appendix we develop the linear theory for the clustering instability in a one-dimensional and spatially uniform system of inelastically colliding particles using the set of fluid equations of Section 2. Assuming particles of mean mass $\overline{m}$, we write the set of equations pertinent to the one-dimensional one-fluid case as

$$\frac{\partial n}{\partial t} + u\frac{\partial n}{\partial x} + n\frac{\partial u}{\partial x} = 0 \quad \text{(A.1)}$$

$$\overline{m}\left(n\frac{\partial u}{\partial t} + nu\frac{\partial u}{\partial x}\right) + \frac{\partial}{\partial x}\left(nT - \frac{4}{3}\eta\frac{\partial u}{\partial x}\right) = 0 \quad \text{(A.2)}$$

$$\frac{\partial}{\partial t}(nT) + u\frac{\partial}{\partial x}(nT) + 3nT\frac{\partial u}{\partial x} + 2\frac{\partial q}{\partial x} - \frac{8}{3}\eta\left(\frac{\partial u}{\partial x}\right)^2 + c\,\varepsilon\frac{N}{L}v_0 Tn = 0 \quad \text{(A.3)}$$

where c is a constant of order unity, which will be computed explicitly for a two species system in Appendix B. The other quantities in equation (A.3) are defined as

$$v_0 \equiv \left(\frac{2T}{\overline{m}}\right)^{1/2}$$

$$\eta \equiv d\,\frac{nT}{\nu_0} = d\,\frac{nT}{v_0}\,\frac{L}{N}$$

$$q \equiv -b\,\frac{nT}{\nu_0 m}\,\frac{\partial T}{\partial x} = -\frac{b}{2}nv_0\,\frac{L}{N}\,\frac{\partial T}{\partial x}$$

with b and d being two more constants of order unity. We note that for a two species system the normalization velocity v_0 is related to the thermal velocity V_{12} of the species relative velocity of Section 2 via

$$V_{12}^2 = 2\frac{\overline{m}}{m_1 m_2}v_0^2. \quad \text{(A.4)}$$

The linear analysis of the system is easier if performed in terms of the dimensionless variables τ and U:

$$d\tau = N^2\frac{v_0}{L}dt \quad \text{(A.5)}$$

$$U = \frac{u}{v_0}. \quad \text{(A.6)}$$

where $d\tau/dt$ is a measure of the number of collisions per time unit in the system during the homogeneous phase and U is essentially the flow's Mach number.

We assume a static equilibrium $u(x,\tau) = 0$ with a uniform density $n = n_0$, and temperature $T(x,\tau) = T_0(\tau)$ decreasing according to equation (A.3), i.e.

$$\frac{\partial T_0}{\partial \tau} = -c\frac{\varepsilon}{N}T_0 \rightarrow T_0(\tau) \propto e^{-c\varepsilon\tau/N}. \quad \text{(A.7)}$$

During the linear phase of the instability c is a constant which only depends on the species relative densities and on the species particle mass (see Appendix B). For example, if $N/2$ particles have mass $m_1 = 1$ and $N/2$ particles $m_2 = 4$, one has $c = 0.97$. Thus, $c = 0.97$ must be used for all runs discussed in the paper except Run 1, where all particles are identical and for which the linear theory presented here is not applicable.

Let us now investigate the response of the equilibrium characterized by $n = n_0$ and $T = T_0(\tau)$ to small perturbations δn, $\delta\theta$ and δU by setting

$$n = n_0 + \delta n \tag{A.8}$$
$$T = T_0(1 + \delta\theta) \tag{A.9}$$
$$U = \delta U. \tag{A.10}$$

The coefficients of the resulting linear system are independent of τ and x so that we can solve it using standard Fourier techniques. We therefore assume perturbations of the type $\delta n, \delta\theta, \delta U \propto \exp[i(kx-\omega\tau)]$ which, when plugged into the linearized system, lead to

$$\mathbf{M} \cdot \begin{pmatrix} \delta n/n_0 \\ \delta U \\ \delta\theta \end{pmatrix} = 0. \tag{A.11}$$

where $\mathbf{M}$ is the 3×3 matrix given by

$$\mathbf{M} \equiv \begin{pmatrix} -i\tilde{\omega} & i\tilde{k} & 0 \\ i\tilde{k} & \frac{4}{3}D\tilde{k}^2 - 2i\tilde{\omega} - 2 & i\tilde{k} \\ 2 - i\tilde{\omega} & 3i\tilde{k} & B\tilde{k}^2 - i\tilde{\omega} \end{pmatrix} \tag{A.12}$$

with $\tilde{k} \equiv kL/(N\varepsilon)$, $\tilde{\omega} \equiv \omega N/\varepsilon$, $B \equiv \varepsilon b$ and $D \equiv \varepsilon d$. Non trivial solutions of the system correspond to a vanishing determinant of the matrix $\mathbf{M}$. Splitting the complex frequency $\omega = \omega_r + i\gamma$ into real and imaginary parts ω_r and γ, and assuming real wave vectors k leads to two equations for the real and the imaginary part of the condition $\det \mathbf{M} = 0$ (in the remaining of this appendix we drop the tildes to ease readability):

$$\begin{aligned} &2\left(1 - Bk^2 - \frac{2}{3}Dk^2 - 3\gamma\right)\omega_r^2 \\ &+Bk^4 + 3\gamma k^2 - 2\gamma^2 + 2\gamma^3 - 2k^2 - 2B\gamma k^2 \\ &+2B\gamma^2 k^2 + \frac{4}{3}D\gamma^2 k^2 + \frac{4}{3}DB\gamma k^4 = 0 \end{aligned} \tag{A.13}$$

and either

$$\begin{aligned} \omega_r^2 = 3\ &\left(\gamma^2 + \frac{k^2}{2}\right) - 2\gamma\left(1 - Bk^2 - \frac{2}{3}Dk^2\right) \\ &- Bk^2 + \frac{2}{3}BDk^4. \end{aligned} \tag{A.14}$$

for the modified sound wave, or

$$\omega_r = 0 \tag{A.15}$$

for the modified, non propagating, entropy wave. The dispersion relation for sound waves, $\omega_r^2 = 3k^2/2$, is immediately obtained by setting $\gamma = B = D = 0$ in equation (A.14) (we shall remember that frequencies are measured in terms of the pseudo time τ and not the real time t). Switching back to real time using equation (A.5), the dispersion relation reduces to the more familiar relation $\omega_r^2 = 3Tk^2/\overline{m}$ for a one dimensional system. The growth rate $\gamma(k)$ for both, sound and entropy mode, can be obtained by substituting ω_r^2 from equation (A.14) or (A.15), respectively, into (A.13). After some juggling one ends up with

$$\begin{aligned} f_s(\gamma,\ k\ , B, D) = 16\gamma^3 &- 16\left(1 - \frac{2}{3}Dk^2 - Bk^2\right)\gamma^2 \\ &- \left(12Bk^2 - 8BDk^4 - 4B^2k^4 - \frac{16}{9}D^2k^4\right. \\ &+ \left.\frac{16}{3}Dk^2 - 6k^2 - 4\right)\gamma \\ &- 2B^2k^4 + \frac{4}{3}B^2Dk^6 + \frac{8}{9}BD^2k^6 - \frac{8}{3}BDk^4 \\ &+ 2Bk^4 + 2Bk^2 + 2Dk^4 - k^2 = 0 \end{aligned} \tag{A.16}$$

for the sound mode, and

$$\begin{aligned} f_e(\gamma,\ k\ , B, D) = 2\gamma^3 &+ \left(2Bk^2 + \frac{4}{3}Dk^2 - 2\right)\gamma^2 \\ &+ \left(3k^2 - 2Bk^2 + \frac{4}{3}BDk^4\right)\gamma \\ &+ Bk^4 - 2k^2 = 0 \end{aligned} \tag{A.17}$$

for the entropy mode. For small values of B and D, i.e. at sufficiently large spatial scales such that both thermal conduction time scale $1/Bk^2$ and the viscous time scale $1/Dk^2$ both exceed the linear time scale $1/\omega$, one may use the asymptotic expressions for the imaginary part of both the sound wave and the entropy wave, viz.

$$\begin{aligned} f_s(\gamma, k, 0, 0) = 16\gamma^3 &- 16\gamma^2 \\ &+ (6k^2 + 4)\gamma - k^2 = 0. \end{aligned} \tag{A.18}$$

and

$$\begin{aligned} f_e(\gamma, k, 0, 0) = 2\gamma^3 &- 2\gamma^2 \\ &+ 3k^2\gamma - 2k^2 = 0. \end{aligned} \tag{A.19}$$

We note that $f_{s,e}(0, k, 0, 0) < 0$ for all values of k. Since $f_{s,e}(\gamma \to \infty) = \infty$, a positive real solutions $\gamma > 0$ must exist for both equations (A.18) and (A.19). Thus, both the sound and the entropy mode are always unstable for $k \to 0$. There is indeed, only one real solution of (A.18) which goes as k^2 for $|k| \to 0$ and tends towards the asymptotic value $1/6$ for $|k| \to \infty$. Similarly, for $|k| \to \infty$, the entropy mode's growth rate tends towards $2/3$. Of course, for sufficiently large values of k both modes must be damped by diffusive effects. However, unlike the entropy mode, which is always unstable for $|k| \to 0$, the sound mode is completely stabilized for thermal diffusivity values $B > 1/2$.

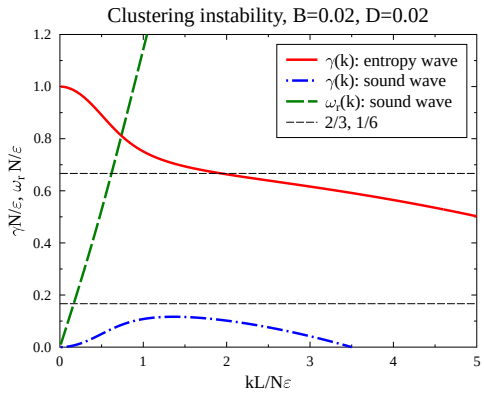

Fig. 8. Growth rate for the both the sound mode and the entropy mode for a particular value of the thermal diffusion coefficient B and the shear viscosity coefficient D. Plotted is also the real frequency of the sound mode $\omega(k)$ and the asymptotic values of the growth rates for both modes in the limit $k \gtrsim 1$, and $D = B = 0$.

The fact that the entropy mode is a non propagating mode implies that density and temperature fluctuations vary spatially in antiphase, ensuring pressure balance. Indeed, for $k \to 0$, one has $-i\omega = 1 - k^2/2$ (see Figure 8) from where, using the second line of the matrix in equation (A.11), one immediately deduces the linear pressure equilibrium condition $\delta n/n_0 = -\delta\theta$ which is valid up to order one in k. To same order in k, the first equation in (A.11) implies the $\delta n/n_0 = -ik\delta U$. This latter relation shows that in the entropy mode density and velocity fluctuations are out of phase by $\pi/2$ corresponding to the fluid flowing from the low density to the high density parts of the wave. These linear motions, eventually enforced by non linear effects (i.e. velocity profile steepening) at late times, ineluctably drive the system toward the final inelastic collapse.

B Collision frequency for Maxwellian distributions

The number of collisions per time unit of a particle of species α with the particles of species β for relative velocities in the range $[u, u + du]$ is given by

$$d\nu_{\alpha\beta} = |u| f_{\alpha\beta}(u) du, \quad u < 0. \tag{B.1}$$

In equation (B.1) $f_{\alpha\beta}(u)$ denotes the distribution of the relative velocities. If one assumes Maxwellian distributions for both species, the distribution of the relative velocities is also Maxwellian. In one dimensions, with N_β particles uniformly distributed in a system of length L it must be that

$$f_{\alpha\beta}(u) = \frac{1}{V_{\alpha\beta}\,\pi^{1/2}} \frac{N_\beta}{L} e^{-u^2/V_{\alpha\beta}^2} \tag{B.2}$$

where $V_{\alpha\beta}$ is the thermal velocity defined as

$$V_{\alpha\beta}^2 \equiv V_\alpha^2 + V_\beta^2 = 2\frac{T_\alpha}{m_\alpha} + 2\frac{T_\beta}{m_\beta}. \tag{B.3}$$

Integration of equation (B.1), assuming the Maxwellian distribution (B.2), gives the collision frequency of a particle α with the particles of species β:

$$\nu_{\alpha\beta} = \int_{-\infty}^{0} |u| f_{\alpha\beta}(u) du = \frac{N_\beta}{L} \frac{V_{\alpha\beta}}{2\pi^{1/2}}. \tag{B.4}$$

The total collision frequency ν in the system is obtained by adding the contributions from all kinds of collisions, i.e.

$$\nu = N_\alpha\, \nu_{\alpha\beta} + N_\beta \nu_{\beta\alpha} + N_\alpha \nu_{\alpha\alpha} + N_\beta \nu_{\beta\beta} = 2 \quad \frac{N_\alpha N_\beta}{L} \frac{V_{\alpha\beta}}{2\pi^{1/2}} + \frac{N_\alpha^2}{L} \frac{V_{\alpha\alpha}}{2\pi^{1/2}} + \frac{N_\beta^2}{L} \frac{V_{\beta\beta}}{2\pi^{1/2}} \tag{B.5}$$

Assuming energy equipartition $T = T_\alpha = T_\beta$ and an equal number of particles for both species $N_\alpha = N_\beta = N/2$, one ends up with

$$\nu(m_\alpha, m_\beta, T, N) = \frac{N^2}{4L} \frac{v_0}{\pi^{1/2}} \left[\left(\frac{\overline{m}}{m_\alpha} + \frac{\overline{m}}{m_\beta} \right)^{1/2} + \left(\frac{\overline{m}}{2m_\alpha} \right)^{1/2} + \left(\frac{\overline{m}}{2m_\beta} \right)^{1/2} \right] \tag{B.6}$$

where $\overline{m} \equiv (m_\alpha + m_\beta)/2$ and $v_0^2 \equiv 2T/\overline{m}$. Using the expression for the collision frequency given by (B.6) it becomes possible to specify the constant c which establishes a relation between the time variable t and the collision index I (cf equations (A.3) and (A.7)). Of course, given the above assumptions, the relation between t and I only holds as long as the inhomogeneities in the system are weak. By comparing (A.7) and (14) one obtains the following relation between the pseudo time variable τ and the collision index I:

$$2\delta I = c\delta\tau. \tag{B.7}$$

Given the relation between τ and the time variable t (see equation (A.5)) and using the fact that the collision frequency is just $\nu = \delta I/\delta t$ it follows that

$$c \equiv 2\nu \frac{L}{N^2 v_0} = \frac{1}{2\pi^{1/2}} \left[\left(\frac{\overline{m}}{m_\alpha} + \frac{\overline{m}}{m_\beta} \right)^{1/2} + \left(\frac{\overline{m}}{2m_\alpha} \right)^{1/2} + \left(\frac{\overline{m}}{2m_\beta} \right)^{1/2} \right] \tag{B.8}$$

We note that c does not depend on the temperature, as long as energy equipartition is a valid approximation.

References

1. H. M. Jaeger, S. R. Nagel, and R. P. Behringer. Granular solids, liquids, and gases. *Reviews of Modern Physics*, 68:1259–1273, October 1996.
2. S. McNamara and W. R. Young. Kinetics of a one-dimensional granular medium in the quasielastic limit. *Phys. Fl.*, 5:34–45, January 1993.
3. I. Goldhirsch and G. Zanetti. Clustering instability in dissipative gases. *Physical Review Letters*, 70:1619–1622, March 1993.
4. E. Efrati, E. Livne, and B. Meerson. Hydrodynamic Singularities and Clustering in a Freely Cooling Inelastic Gas. *Physical Review Letters*, 94(8):088001–+, March 2005.
5. B. Bernu and R. Mazighi. One-dimensional bounce of inelastically colliding marbles on a wall . *Journal of Physics A Mathematical General*, 23:5745–5754, December 1990.
6. S. McNamara and W. R. Young. Inelastic collapse and clumping in a one-dimensional granular medium. *Phys. Fluids*, 4:496–504, March 1992.
7. J. T. Jenkins and F. Mancini. Kinetic theory for binary mixtures of smooth, nearly elastic spheres. *Physics of Fluids*, 1:2050–2057, December 1989.
8. J. J. Brey, J. W. Dufty, C. S. Kim, and A. Santos. Hydrodynamics for granular flow at low density. *Phys. Rev. E*, 58:4638–4653, October 1998.
9. V. Garzó and J. W. Dufty. Hydrodynamics for a granular binary mixture at low density. *Phys. Fluids*, 14:1476–1490, April 2002.
10. J. Eggers. Sand as Maxwell's Demon. *Physical Review Letters*, 83:5322–5325, December 1999.
11. J. Javier Brey, F. Moreno, R. García-Rojo, and M. J. Ruiz-Montero. Hydrodynamic Maxwell demon in granular systems. *Phys. Rev. E*, 65(1):011305–+, January 2002.
12. R. Ramírez and R. Soto. Temperature inversion in granular fluids under gravity. *Physica A Statistical Mechanics and its Applications*, 322:73–80, May 2003.
13. A. Baldassarri, U. Marini Bettolo Marconi, and A. Puglisi. Influence of correlations on the velocity statistics of scalar granular gases. *Europhysics Letters*, 58:14–20, April 2002.
14. E. Ben-Naim and P. L. Krapivsky. Multiscaling in inelastic collisions. *Phys. Rev. E*, 61:5–+, January 2000.
15. V. Garzó, J. M. Montanero, and J. W. Dufty. Mass and heat fluxes for a binary granular mixture at low density. *Physics of Fluids*, 18:3305–+, August 2006.
16. J. T. Jenkins and D. K. Yoon. Segregation in Binary Mixtures under Gravity. *Physical Review Letters*, 88(19):194301–+, May 2002.
17. E. Ben-Naim, S. Y. Chen, G. D. Doolen, and S. Redner. Shocklike Dynamics of Inelastic Gases. *Physical Review Letters*, 83:4069–4072, November 1999.
18. D. Benedetto, E. Caglioti, and M. Pulvirenti. A Kinetic equation for granular media. *Math. Mod. Num. Anal.*, 31(5):615–641, 1997.
19. S. S. Hsiau and M. L. Hunt. Granular thermal diffusion in flows of binary-sized mixtures. *Acta Mech.*, 114(1):121–137, March 1996.

10 Simulation du flux de chaleur dans un plasma modérément couplé

Eur. Phys. J. D (Atomic, Molecular, Optical and Plasma Physics), soumis (2007)

EPJ manuscript No.
(will be inserted by the editor)

Ab initio simulations of the heat flux in a moderately coupled plasma and steep temperature gradients

Arnaud Beck and Filippo Pantellini

Observatoire de Paris, LESIA, 5 Place Jules Janssen, 92195 Meudon, France
e-mail: Arnaud.Beck@obspm.fr

Abstract. We use ab initio numerical simulations of a moderately coupled (Coulomb logarithm $\lambda = 3.8$), classical, electron-proton plasma to investigate the electron heat flux in a steep temperature gradient. The temperature gradient is forced by confining the plasma within a cylinder with "thermal" walls at both ends. The thermal Knudsen number $K_{e,T}$, defined as the ratio of the electron mean free path to the characteristic scale of variation of the temperature, is in the range $10^{-3} \lesssim K_{e,T} \lesssim 10^{-1}$. We show that under such circumstances the electron heat flux is approximately 3/4 of the canonical Spitzer&Härm value for $K_{e,T} \lesssim 5\ 10^{-2}$. For $K_{e,T} \gtrsim 5\ 10^{-2}$ the non local contribution to the heat flux from the thermal walls is no longer negligible and the heat flux saturates at roughly 10^{-1} times the free streaming value. The simulations are based on $N-$body techniques which are widely used in the context of gravitationally interacting bodies but rarely in the context of interacting charges. Such simulations have the advantage of not relying on any particular choice of the collision operator in Boltzmann's equation.

PACS. 52.25.Fi Transport properties – 45.50.Tn Collisions – 44.10.+i Heat conduction

1 introduction

We adapted the FalcON code, originally developed by W. Dehnen [1] for system of gravitationally interacting bodies, to the case of a system of a large number of interacting positive and negative charges.

More specifically, in this paper we apply the N-body technique to the study of the heat flux in an, overall neutral, and moderately coupled electron-proton plasma characterized by a Coulomb logarithm in the range $2 \lesssim \lambda \lesssim 10$ (cf. equation (1)). The Coulomb logarithm λ for an electron-proton plasma at temperature T and electron density n_e is a dimensionless parameter usually defined as

$$\lambda \equiv \ln\left(\frac{\lambda_D}{r_s}\right). \tag{1}$$

where $\lambda_D \equiv (k_B T \epsilon_0 / n_e e^2)^{1/2}$ is the Debye length, k_B the Boltzmann constant, $r_s \equiv e^2/12\pi\epsilon_0 k_B T$ the strong interaction radius, e the absolute value of the electron charge and ϵ_0 the electrical permittivity of free space. The Debye length λ_D is the typical spatial scale required by the plasma to screen a local charge excess. Indeed, despite the electrostatic interaction being a long distance interaction, any two charged particles in the plasma do not interact if their separation exceeds the Debye length. Thus, at a given time, any particle in the plasma interacts simultaneously with all particles within a distance of order λ_D. Most of these interactions have little influence on the particle's trajectory unless the interacting distance is not much larger than the strong interaction radius r_s. The latter corresponds to the distance between two electrons such that their interaction energy $e^2/4\pi\epsilon_0 r_s$ is twice their individual characteristic kinetic energy $\frac{3}{2}k_B T$. The strong interaction radius r_s corresponds to the impact parameter for a 90° deflection of a thermal electron interacting with a stationary positive ion of charge e. In extremely hot plasmas the strong interaction radius eventually becomes shorter than the mean electron De Broglie length $\lambda\!\!\!^{-}_e = \hbar/m_e\langle v^2\rangle^{1/2}$ (where $\langle v^2\rangle = 3k_B T/m_e$, $\hbar = h/2\pi$ and h is the Planck constant) and quantum effects can no longer be neglected in the treatment of close encounters. In such an event our model, which is based on classical electrostatics, fails as most close encounters will be dominated by quantum mechanical effects, and the Coulomb logarithm definition of Equation (1) is no longer the pertinent dimensionless parameter characterizing the plasma. The requirement $r_s \gtrsim \lambda\!\!\!^{-}$ for the validity of the classical approach requires temperatures $T \lesssim 10^5 K$.

A plasma is said to be weakly coupled if $\lambda \geq 10$ and strongly coupled if $\lambda \leq 1$. In this paper we consider a moderately coupled plasma with $\lambda = 3.8$, which corresponds to a Coulomb coupling parameter $\Gamma = 0.11$. The coupling parameter Γ is the average ratio of the electrostatic to kinetic energy of neighbor electrons in the plasma, i.e.

$$\Gamma \equiv \frac{e^2}{4\pi\epsilon_0 a k_B T} \tag{2}$$

where $a \equiv (3/4\pi n_e)^{1/3}$ is the Wigner-Seitz radius. We note that the coupling parameter Γ and the Coulomb logarithm λ are equivalent parameters as they are linked by the relation

$$\lambda = \ln\left(\frac{\sqrt{3}}{\Gamma^{3/2}}\right) = \ln(9N_D) \tag{3}$$

From equation 3 it follows that the number of electrons N_D enclosed by a sphere of radius λ_D is larger than unity when $\lambda \gtrsim 2$. Consequently, a moderately coupled plasma, unlike the weakly coupled ones, does not necessarily have much more than one electron in this sphere. In this particular case, the use of statistical means (i.e. particle distribution functions) to compute the plasma's spatial and temporal behavior may be inappropriate. Another difference between weakly and moderately coupled plasmas is that, with $\lambda \gtrsim 10$, the number of particles making distant collisions is so much larger than the number of particles making close collisions, that the latter's contribution to the transport coefficients can be neglected. Under such conditions, relatively simple collision operators, including only the first moment of the distribution function, can satisfactorily be used in the Boltzmann equation in transport coefficient computations [see e.g. 2]. Whereas in moderately coupled plasmas, when λ is reduced below ~ 10, the relative importance of close encounters becomes increasingly large and the collision operators, required to increase accuracy to better than $\sim \lambda^{-1}$, become increasingly complicated and unpractical [3, 2]. On the other hand, the $\lambda \lesssim 10$ regime appears to be particularly well suited for, ab initio N-body simulations where all kind of collisions are naturally included. In such numerical models, the limitations are merely computational, as in N-body simulations the spatial resolution of the particles' trajectories must be of the order of the strong interaction radius $r_s \ll \lambda_D$ while the typical system size must extend over several times λ_D in order to account for the effects of distant encounters. In practice classical N-body simulations are limited to classical plasmas in the moderately coupled regime $2 \lesssim \lambda \lesssim 10$.

Laser plasmas and inertially confined fusion plasmas are sometimes in the moderately coupled regime (see [4] and [5] for references). The solar interior is also in the moderately coupled regime, with the upper 70,000 km of the convection zone being in the classical regime with $r_s \gtrsim \lambda\!\!\!^{-}_e$.

The problem of the heat conduction in a strong temperature gradient has been investigated theoretically a few decades ago in the case of weakly coupled plasmas [6, 7, 8]. Using the physically justified technique of forcing the anisotropic portion of the electron distribution function $f_1(v)$ to be smaller than the isotropic portion $f_0(v)$ such that the total distribution f remains positive in the Legendre development $f = f_0 + \mu f_1$ used in the standard Spitzer and Haïrm procedure. Bell et al [6] and Shvarts et al [7] suggest that the electron heat flux q_e is always substantially smaller than the free streaming limit $q_0 \equiv n_e(k_B T)^{3/2}/m_e^{1/2}$ confirming the experimental findings of [9]. Shvarts et al [7] do also indicate that q_e falls below the canonical Spitzer and Haïrm value $q_{e,S}$ for $K_{e,T} \gtrsim 2.\ 10^{-3}$. Luciani et al [8] use a non local extension of the classical Spitzer-Haïrm expression of the electron heat flux which includes the contributions from the temperature profile up to a distance of the order of the mean free path from the point of observation. The Luciani et al expression only depends on the temperature and density profile in the vicinity of the observation point and not on a manipulation of $f_1(v)$. Despite being quite different from the approach of [6, 7] Luciani et al [8] do also find that the maximum heat flux is limited to about $0.1 q_0$, a value which is consistent with our results (see Figure 3).

In this paper we show that in a moderately coupled plasma the electron heat flux is substantially smaller than the Spitzer flux $q_{e,S}$ over the entire investigated range $10^{-3} \gtrsim K_{e,T} \gtrsim 10^{-1}$, if the classical estimate of the mean free path (presumably valid in the $\lambda \gtrsim 10$ regime) is used in the definition of the Knudsen number $K_{e,T}$. The electron heat flux is shown to peak at $q_e \approx 10^{-1} q_0$ for the $K_{e,T} \approx 5\ 10^{-2}$. We note that in the collisionless limit the Knudsen number is undefined but not the heat flux which can be calculated analytically [10]

$$q_{NC} = \sqrt{\frac{8}{\pi}} \frac{n_e k_B^{3/2}}{m_e^{1/2}} \left(T_1 T_2^{1/2} - T_2 T_1^{1/2} \right) \tag{4}$$

In the numerical set-up, the non collisional (non local) contribution to the heat flux q_{NC} due to the free streaming of electrons from the thermostats only becomes relevant for $K_{e,T} \gtrsim 5.\ 10^{-2}$ when $q/q_{NC} \gtrsim 0.35$ (see Table 1). One possible interpretation is that the classical collision frequency resulting from the Spitzer and Härm treatment for weakly coupled plasmas underestimates the real collision frequency in moderately coupled plasmas.

2 The model

We simulate the stationary state of N mutually interacting charged particles ($N/2$ protons and $N/2$ electrons) confined within a cylinder of height L and radius R. Values of L and R for all runs are given in Table 1. The basic setup for the simulations is shown in figure 1. Particles reaching one of the two boundaries of the cylinder at $z = 0$ and $z = L$ are re-injected following resting Maxwellian velocity distributions at temperatures T_1 and $T_2 > T_1$, respectively. Particles hitting the curved wall of the cylinder are reflected back elastically into the cylinder's interior. Because of the upper thermostat being hotter than the lower thermostat a heat flux q is expected to flow down the temperature gradient. The heat flux intensity in the cylinder is a function of the plasma parameters. We note that this experimental set-up is similar to the set-up in the heat front simulations of Luciani et al [8] where a hot and a cold region are connected by steep temperature and density profiles. The main parameters which affect the heat flux intensity are the Coulomb logarithm λ and the thermal Knudsen number $K_{T,\alpha}$ defined as

$$K_{T,\alpha} \equiv \frac{l_\alpha}{L_T} \tag{5}$$

where l_α is the collisional mean free path for a typical particle of species α and $L_T \equiv \partial(\ln T)/\partial z$ is the characteristic scale of variation of the temperature profile along the z direction.

The definition of the collisional mean free path l_α in terms of fluid quantities, such as the density, the temperature and λ is model dependent as the definition depends on the actual choice of the collision operator [see e.g. 3]. In order to facilitate comparisons with other authors, we adopt the canonical collision times for both electrons and protons in a quasi neutral and weakly coupled plasma [3, 2],

$$\tau_e = \frac{3 m_e^{1/2} (k_B T_e)^{3/2}}{4 \sqrt{2\pi}\, n \lambda e^4} \tag{6}$$

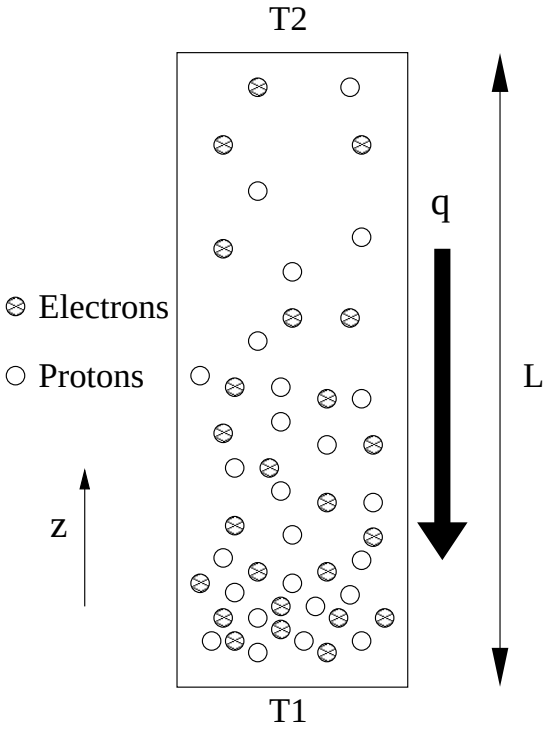

Fig. 1. Schematic illustration of the simulated system: a collection of $N/2$ electrons and $N/2$ protons confined within a cylinder of length L and radius R. The temperature gradient imposed by the thermostat at both ends of the cylinder at temperature T_1 (at $z = 0$) and $T_2 > T_1$ (at $z = L$) drive a heat flux q.

$$\tau_{\rm i} = \frac{3 m_{\rm p}^{1/2} (k_{\rm B} T_{\rm p})^{3/2}}{4\sqrt{\pi}\, n \lambda e^4} \tag{7}$$

where $n = n_{\rm e} = n_{\rm p}$ is either the proton or the electron number density. These collision times are pertinent to plasmas with $\lambda \gtrsim 10$. In a moderately coupled plasma where $10 \gtrsim \lambda$, the above collision times may merely represent a zero order estimate of the effective collision times. However, the advantage of using the collision times (6) and (7) for all values of λ permits the unambiguous definition of the Knudsen number which is the crucial parameter which determines the heat flux intensity in a plasma (see below). The mean free path l_α for a particle of species α is a function of the collision times (6) and (7) and the species characteristic velocity v_α (thermal velocity)

$$v_\alpha \equiv \left(\frac{2 k_{\rm B} T_\alpha}{m_\alpha} \right)^{1/2}. \tag{8}$$

The mean free path is then simply given by

$$l_\alpha = \tau_\alpha \, v_\alpha. \tag{9}$$

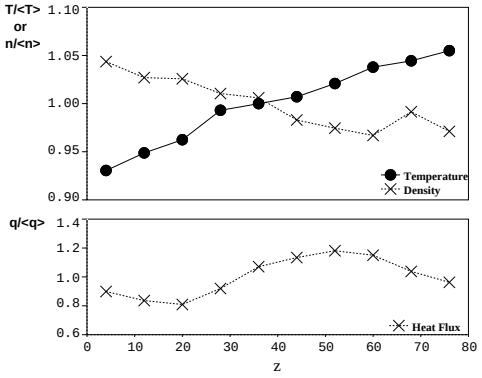

Fig. 2. Run 5: Electron density and temperature (top panel) and electron heat flux (bottom panel) from ten bins along the cylinder axis. All quantities are normalized to their average value in the cylinder.

which we use to characterize the plasma's collisionality independently of whether or not the collision times (6) and (7) represent good estimates of the effective collision times.

Concerning the temperature length scale $L_{\rm T}$ in the simulations, we note that when the temperature difference between the two thermostats is small, such that $(T_2 - T_1)/T_1 \ll 1$, $L_{\rm T}$ can be assumed to be constant:

$$L_{\rm T} \equiv \left[\frac{\partial (\ln T)}{\partial z} \right]^{-1} \simeq \frac{L}{2} \, \frac{T_2 + T_1}{T_2 - T_1}. \tag{10}$$

We restrict our simulations to the limit of small temperature variations in the system such that the $L_{\rm T}$ can effectively be assumed to be spatially constant. As an example, Figure 2 shows the density, temperature and heat flux as a function of z for Run 5. Apart from the statistical fluctuations, the temperature is seen to increase linearly with z, by about 10%, between the thermostats. The density decreases linearly by the same amount ensuring a constant pressure. The electron heat flux has a clearly defined mean value but is not completely constant over the whole simulation domain, indicating that the system is still relaxating.

3 Simulation parameters

We show results from eight runs. In all runs the plasma is characterized by the same Coulomb logarithm $\lambda = 3.8$ while the thermal Knudsen number $K_{\rm T,e}$ ranges approximately from 10^{-3} to 10^{-1}. As already stated, there are five free parameters: the cylinder length L, the cylinder radius R, the total number of particles N, and the temperatures T_1 and T_2 of the thermostats at both ends of the cylinder. We are interested in the role of the collisions in the transport properties of the plasma so it is essential that a thermal particle makes at least a few collisions on its way from one thermostat to the other. This requirement, which is also a necessary condition for a temperature gradient to exist, can be expressed as $l_{\rm e}/L < 1$.

Run	$K_{T,e}$	L/λ_D	R/λ_D	q/q_{NC}	l_e/L
1	$1.25\ 10^{-3}$	280	5.2	0.15	0.07
2	$2.50\ 10^{-3}$	198	6.2	0.19	0.10
3	$3.07\ 10^{-3}$	161	6	0.22	0.13
4	$5.33\ 10^{-3}$	140	7	0.23	0.15
5	$1.70\ 10^{-2}$	443	6	0.25	0.13
6	$2.90\ 10^{-2}$	161	10	0.32	0.23
7	$4.98\ 10^{-2}$	90	11	0.34	0.30
8	$7.40\ 10^{-2}$	70	24	0.67	2.1

Table 1. All parameters listed are computed using the temperature and densities at the center of the cylinder, at $z = L/2$. Proton to electron mass ratio is $m_p/m_e = 50$ for all runs.

The cylinder radius R is typically of the order of a few $\gtrsim \lambda_D$ and $L/\lambda_D \gg 1$. All simulations are performed with a proton to electron mass ratio $m_p/m_e = 50$. This helps reducing computational times considerably without any significant impact on the numerical values of the transport properties as the condition $m_p \gg m_e$ is still holding.

The relevant parameters for the eight runs are shown in Table 1.

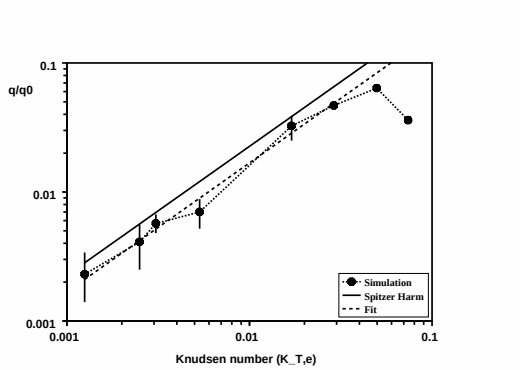

Fig. 3. Circles show the normalized electron heat flux measured in the 8 runs listed in Table 1 as a function of the Knudsen number $K_{T,e}$. The normalized Spitzer&Härm electron heat flux is shown as a reference. The linear fit, based on the 6 points to the left corresponds to a heat flux which is only 3/4 of the Spitzer&Härm flux. The Coulomb logarithm is $\lambda = 3.8$ for all runs.

4 Results

In all runs, particles are initially uniformly distributed inside the cylinder, following a Maxwellian distribution at temperature $\frac{1}{2}(T_1 + T_2)$. The system then freely evolves under the effect of the sole electrostatic forces towards a stationary state, with stable temperature and density profiles and approximately constant proton and electron heat fluxes. Asymptotically the system reaches a state of energy equipartition between species (i.e. $T_e = T_p$) and quasi neutrality $n_e = n_p$ except near the boundaries overs scales of the order of the Debye length $\lambda_D \ll L$. Figure 3 shows the electron heat flux q_e, normalized to the free streaming flux $q_0 = n_e(k_B T)^{3/2}/m_e^{1/2}$, for the eight runs of Table 1 once a stationary state with an approximately spatially and temporally constant electron heat flux has been reached. The temperature used to determine q_0 is the initial temperature $\frac{1}{2}(T_1 + T_2)$ which is also the temperature in the middle of the cylinder once the stationary state is reached. The heat flux values and the associated error bars in Figure 3 represent the average and the standard deviation obtained by measuring the heat flux in 10 equally spaced bins along the z axis as illustrated in Figure 2. We note that the Spitzer&Härm flux given by [11, 12]

$$q_{e,S} = 3.2 \frac{k_B T}{m_e} n_e \tau_e \nabla(k_B T) \tag{11}$$

only depends on the Knudsen number and the free streaming flux q_0. In normalized units we then write

$$\tilde{q}_{e,S} = \frac{q_{e,S}}{q_0} = 2.26\, K_{T,e}. \tag{12}$$

Figure 3 shows that the measured heat flux systematically lies below the Spitzer&Härm flux, even at low Knudsen numbers. The normalized heat flux appears to depend linearly on the Knudsen numbers, exactly as $\tilde{q}_{e,S}$, provided the temperature gradient is not too steep, i.e. $K_{T,e} \lesssim 5\,10^{-2}$. A linear fit (excluding the two points corresponding to the steepest temperature gradients) gives

$$\tilde{q} = \frac{q}{q_0} \simeq 1.68\, K_{T,e} \tag{13}$$

Finding an electron flux which is systematically smaller than $\tilde{q}_{e,S}$ is not necessarily surprising as the computation of $q_{e,S}$ is based on a collision operator which neglects terms in λ^{-1} and the moments of the velocity distribution function of order ≥ 2 (see [2, 3] for a discussion on this point). Corrections of order λ^{-1} may be neglected in the weakly coupled plasma regime $\lambda \gtrsim 10$ but not for $\lambda = 3.8$. In [5], Li and Petrasso use a modified collision operator including λ^{-1} terms which are shown to effectively reduce the conventional Spitzer&Härm flux. However, the modification of the heat flux predicted by Li and Petrasso [5] is only of order $1/6\lambda$ which is much smaller than observed in our simulations. The Li and Petrasso correction is clearly insufficient to explain the result of Figure 3.

When the temperature gradients are as steep as in the simulations shown in this paper, non local contributions to the heat flux may not be negligible. In order to evaluate the non local contributions to the heat flux, we have computed the collisionless electron heat flux q_{NC} (see equation (4)) for all runs, i.e. the heat flux generated by the thermostats if the electrons were allowed to stream freely (with no velocity variations) from one thermostat to the other. Table 1 shows that the collisionless flux q_{NC} is always substantially larger than the measured flux q excepted for Run 8. We conclude, that, at least in the case of Maxwellian boundaries, the non local contribution to the heat flux is not dominant as long as $K_{e,T} \lesssim 5\,10^{-2}$. In the high Knudsen number domain ($K_{T,e} \gtrsim 0.05$), the heat flux appears to saturate at a level $\lesssim 10^{-1} q_0$, as already mentioned in [9] and [7] for the $\lambda \gtrsim 10$ case.

5 Conclusion

Numerical simulations of a moderately coupled electron-proton plasma in the classical regime (Coulomb logarithm $\lambda = 3.8$) have been used to quantify the strength of the electron heat flux in a steep temperature gradient. The simulations are based on N-body techniques which are particularly well suited for moderately coupled plasmas and have the enormous advantage of producing results which do not depend on a particular choice of the collision operator in the Boltzmann equation.

As expected for the highest Knudsen numbers ($K_{\mathrm{T,e}} \gtrsim 510^{-2}$), when non local (collisionless) contributions to the heat flux become dominant, the electron heat flux q_{e} is seen to saturate at $\sim 10^{-1}$ times the free streaming flux q_0. For $K_{\mathrm{T,e}} \lesssim 5\ 10^{-2}$ the normalized flux q_{e}/q_0 linearly depends on the Knudsen number $K_{\mathrm{T,e}}$. However, the intensity of the flux is found to be only about 75% of the classical Spitzer & Härm flux.

References

1. W. Dehnen. A hierarchical O(N) Force Calculation Algorithm. *Journal of Computational Physics*, 179:27–42, June 2002.
2. V.E. Golant, A.P. Zhilinsky, and I.E. Sakharov. *Fundamantals of plasma physics*. John Wiley & Sons, New York, 1980.
3. S.I. Braginskii. Transport processes in plasmas. In M.A. Leontovich, editor, *Reviews of Plasma Physics*, volume 1, pages 205–311. Consultants Bureau, New York, 1965.
4. R. D. Petrasso. Plasmas everywhere. *Nat*, 343:21–22, January 1990.
5. C. Li and R.D. Petrasso. Fokker-planck equation for moderately coupled plasmas. *Phys. Rev. Lett.*, 70:3063–3066, May 1993.
6. A. R. Bell, R. G. Evans, and D. J. Nicholas. Electron energy transport in steep temperature gradients in laser-produced plasmas. *Physical Review Letters*, 46:243–246, January 1981.
7. D. Shvarts. Self-consistent reduction of the spitzer-härm electron thermal heat flux in steep temperature gradients in laser-produced plasmas. *Phys. Rev. Lett.*, 47:247–250, July 1981.
8. J.F. Luciani and P. Mora. Nonlocal heat transport due to steep temperature gradients. *Phys. Rev. Lett.*, 51:1664–1667, October 1983.
9. D. R. Gray and J. D. Kilkenny. The measurement of ion acoustic turbulence and reduced thermal conductivity caused by a large temperature gradient in a laser heated plasma. *Plasma Physics*, 22:81–111, February 1980.
10. S. Landi and F.G.E. Pantellini. On the temperature profile and heat flux in the solar corona: Kinetic simulations. *A&A*, 372:686–701, June 2001.
11. L. Spitzer and R. Härm. Transport phenomena in a completely ionized gas. *Phys. Rev.*, 89:977–981, March 1953.
12. J.D. Huba. Nrl plasma formulary. *Office of Naval Research*, 2006.

11 Expansion d'un plasma dans le vide

Plasma Physics and Controlled Fusion, 51, 015004, 2009

Spherical expansion of a collisionless plasma into vacuum: self-similar solution and ab initio simulations

Arnaud Beck and Filippo Pantellini

LESIA, Observatoire de Paris, CNRS, UPMC, Université Paris Diderot;
5 Place Jules Janssen, 92195 Meudon, France

E-mail: Arnaud.Beck@obspm.fr, Filippo.Pantellini@obspm.fr

PACS numbers:
52.50.Jm Plasma production and heating by laser beams (laser-foil, laser-cluster, etc.)
52.38.Kd Laser-plasma acceleration of electrons and ions
52.65.Cc Particle orbit and trajectory

To be published in *Plasma Phys. Control. Fusion*
Submitted: 1 July 2008
Accepted: 30 September 2008

Abstract. We present a self similar three dimensional and spherically symmetric fluid model of the expansion of an either globally neutral or globally charged collisionless plasma into vacuum. As in previous works by other authors the key parameter of the model is the ratio of the electron Debye length to the radius R of the expanding ion sphere. The main difference with respect to the recently published model of Murakami and Basko [1] is that the electron temperature is spatially non uniform. The major consequence of the spatial variability is that the self-similar solution is characterized by the presence of a sharp electron front at some finite distance ahead of the ion front. Explicit analytic expressions for the self-similar profiles of the ion and electron densities, the electron temperature and the heat flux are given for the region inside the ion front. The model is shown to be in good qualitative agreement with results from ab initio plasma simulations.

1. Introduction

Plasmas freely expanding into vacuum are commonly observed in the astrophysical context. Examples are the negatively charged dust particles in cometary tails expanding into the interplanetary space [2, 3] or the expansion of the solar wind plasma into the wake region of inert objects such as asteroids or the moon [4]. Besides the astrophysical studies, most of the material on freely expanding plasmas has been published in the context of laser-matter generated plasmas [5, 6, 7, 8] or discharge generated plasmas [9]. During the last decade, the particular case of the collisionless spherical expansion has focused attention after the experimental confirmation that the irradiation of small cluster of deuterium atoms with high intensity laser pulses can produce a sufficiently large number of up to MeV ions for efficient fusion reactions to occur [10]. In a typical laser-cluster fusion experiment all, or just a fraction of the electrons are instantly stripped from the cluster atoms or molecules and heated to up to keV energies by the laser field [11, 10, 6]. The heated electrons depart from the cluster leaving a clump of positively charged ions which become accelerated under the action of their mutual electrostatic repulsion. To lowest order, the spatial structure of the expanding plasma consists in two distinct regions. An inner region (the ion sphere), surrounding the expansion centre, where both ions and electrons are present, and an outer region, populated by electrons only [12, 1, 13]. The detailed structure is generally more complex, especially in the case of large clusters where the initial heating is spatially non uniform. In this case a two-component electron distribution and intricate spatial and temporal structures of the expanding plasma are expectd [14, 15]. As shown in [6, 16] the minimum cluster size for a two-component electron distribution to form is a function of the cluster's chemical composition and of the lasers' characteristics.

Numerical studies have shown that even in the most simple case with only one single Maxwellian electron population the initial evolution of the system is characterized by wave steepening of the ion fluid velocity profile with associated formation of a peaked ion front and development of plasma microinstabilities as the ion velocity becomes multi-valued [17, 18]. Thus, as first pointed out on theoretical grounds in [17] and subsequently observed in plasma discharge experiments [9], the late time (self-similar) ion density profile is sometimes expected to be smoothed out by the microinstabilities at the ion front. Recent two and three-dimensional kinetic simulations [14, 13] have also pointed out how critically the expanding plasma depends on the characteristics of the laser pulses used to heat the electrons. However, a model is only useful if it is simple and if it contains all of the fundamantal ingredients of the problem. We therefore restrict our model to the case of one single, not necessarily isothermal electron fluid, and an infinitely steep ion front. The model describes the self-similar expansion of one single, spherically symetric plasma plunged in an infinite empty volume. As already pointed out in [17] it is expected that the expansion is self-similar when the radius of the expanding plasma bubble largely exceeds the initial radius of the bubble, i.e. after a time long enough for the memory of the initial conditions to be lost. Ions are assumed to be cold with

a discontinuous ion-front while the electrons' density and temperature are related to each other by a simple polytropic law. The ion and electron fluid velocities are assumed to be shear-free, meaning that they vary linearly with the distance from the expansion centre [19]. The linear variation of the fluid velocity with respect to the radial distance is necessary condition for the solution to be self-similar unless some special conditions are assumed near the expansion centre [20].

The self-similar solution we propose differs from previously published self-similar solutions [1, 8] in that the electrons are not assumed to be spatially isothermal, in accordance with results from two dimensional PIC simulations [14] and our N-body simulation of Section 3. The implications of a spatially varying electron temperature is that the electron heat flux is finite with energy flowing towards the expansion centre. In addition, the electron density drops to zero at some distance ahead of the ion front while it extends to infinity in the Murakami and Basko model. For completeness, we note that self-similar isothermal solutions similar to the one discussed in [1, 8] but with a moving inner boundary, have been published in [21, 22, 20].

The paper is divided into two main sections. In section 2 we present the complete theory of the self-similar model. In section 3 we compare the model with results from a numerical N-body simulation.

2. Self-similar two fluid model

We describe the self-similar expansion of a plasma into vacuum within the context of a two species (ions and electrons) spherically symmetric fluid model. The main difference with respect to the self-similar model of Murakami and Basko [1] is that the electron temperature is not assumed to be spatially uniform. The spatial dependence of the electron temperature being confirmed by the case simulation presented in section 3. As in the Murakami and Basko model we do consider the limit where the thermal energy of the electron fluid is much larger that the thermal energy of the ion fluid (cold ion limit).

2.1. Basic assumptions and equations

In this section, for the sake of completeness and to avoid ambiguities, we do briefly present the definitions and assumptions whereon our model is based.

2.1.1. Definition of the plasma We consider a non magnetized two species collisionless electron-ion plasma with an electron to ion mass ratio $m_\mathrm{e}/m_\mathrm{i} \ll 1$. For simplicity we assume single ionized ions with charge $q_\mathrm{i} = e$ (e is the elementary charge) the generalization to higher ionization levels being a trivial extension of the model.

2.1.2. Fluid equations The collisionless hypothesis allows the systematic construction of fluid equations by computing the velocity moments of Vlasov's equation [23].

Assuming spherical symmetry, and postulating isotropic velocity distribution functions, the order zero and order one velocity moments of the non relativistic Vlasov equation for species $j = i, e$ (ions and electrons) lead to the continuity and momentum equations in the form

$$\frac{\partial n_j}{\partial t} + \frac{1}{r^2}\frac{\partial}{\partial r}(r^2 n_j v_j) = 0 \tag{1}$$

$$\varrho_j \left(\frac{\partial v_j}{\partial t} + v_j \frac{\partial v_j}{\partial r} \right) = -\frac{\partial p_j}{\partial r} + n_j q_j \mathcal{E} \tag{2}$$

where n_j, $\varrho_j \equiv m_j n_j$, v_j and p_j are the number density, the mass density, the fluid velocity and the pressure for species j. As usual, the electric field $\mathcal{E}$ appearing in the momentum equation is implicitly determined by the spatial distribution of ions and electrons via Poisson's equation

$$\frac{1}{r^2}\frac{\partial}{\partial r}(r^2 \mathcal{E}) = 4\pi e(n_\mathrm{i} - n_\mathrm{e}). \tag{3}$$

The system of fluid equations is closed with a barotropic equation of state for the electrons

$$p_\mathrm{e} = p_\mathrm{e}(\varrho_\mathrm{e}) = A\varrho_\mathrm{e}^\gamma. \tag{4}$$

and $p_\mathrm{i} = 0$ for the ions. As already pointed out in [1] the only choice for the polytropic index which is compatible with a self-similar solution of the equations is $\gamma = \frac{4}{3}$, unless the plasma is quasi-neutral in all points of space, as for the self-similar solutions proposed in [18]. We discuss this point in more details in section 2.2.

2.1.3. Shear-free flow In addition to the spherical symmetry of the flow we postulate it to be shear-free. As shown in [19] the shear-free hypothesis implies that the fluid velocity v_j must be a linear function of the radial coordinate r multiplied by an arbitrary function of time $H_j(t)$, i.e. $v_j = rH_j(t)$. Of course shear-free flows are a rather restrictive class of spherically symmetric flows. For example, it has been first pointed out in [17] for the quasi-neutral planar case and more recently in [24, 13] for the so-called Coulomb explosion, the case where the totality of the electrons can escape from the cluster, that for non uniform initial ion densities the ion velocity profile inevitably steepens until it becomes multiple-valued and potentially unstable to plasma microinstabilities. The shear-free assumption may still be pertinent for the late time evolution of the system when the volume occupied by the expanding plasma greatly exceeds the initial volume, and all wave activity has been damped out through wave-particle interactions.

The consequence of the shear-free flow assumption is that the continuity equation (1) reduces to

$$\frac{\partial \tilde{n}_j}{\partial t} + rH_j \frac{\partial \tilde{n}_j}{\partial r} = 0, \quad \text{with } \tilde{n}_j \equiv n_j r^3 \tag{5}$$

whose general solution is $\tilde{n}_j = \tilde{n}_j(r/R_j)$ where the spatial scale R_j is a function of time such that $H_j = \dot{R}_j/R_j$, where overdots represent the time derivative d/dt. Thus,

assuming flow velocities of the type

$$v_j = r\frac{\dot{R}_j}{R_j} \equiv \xi_j \dot{R}_j \tag{6}$$

ensures both, that the flow is shear-free, and that the continuity equation (1) is identically satisfied for any density profile $\tilde{n}_j = \tilde{n}_j(\xi_j)$ where $\xi_j = r/R_j$ is the self-similar coordinate for species j. We conclude this section by noting that velocity profiles that are not linear in r can lead to self-similar solutions in a limited region of space. For example, in [20] the fluid velocity is assumed to be zero at an inner boundary $r = r_0 > 0$.

2.1.4. Zero electron-ion drift velocity In the previous section we did not put any constraints on the temporal evolution of the scaling lengths R_j. However, because of the electrostatic coupling between species, we do not expect ions and electrons to evolve on different scales. We then postulate the same scaling length $R(t) \equiv R_\mathrm{i} = R_\mathrm{e}$ for both species, which is equivalent to assuming equal fluid velocities $v \equiv v_\mathrm{e} = v_\mathrm{i}$. The overall fluid motion for both ions and electrons is therefore a function of just one single scaling length R:

$$v = \xi \dot{R}. \tag{7}$$

For example, the zero drift assumption implies that the density ratio $n_\mathrm{i}/n_\mathrm{e}$ at the self-similar position $\xi = r/R$ does not change in time.

2.1.5. Cold ions approximation Given the zero drift hypothesis $v_\mathrm{e} = v_\mathrm{i}$ and assuming that the ion pressure term $\varrho_\mathrm{i}^{-1}\partial p_\mathrm{i}/\partial r$ is small compared to the electron pressure term $\varrho_\mathrm{e}^{-1}\partial p_\mathrm{e}/\partial r$, it follows from (2) that the electric field within the ion sphere, where both electrons and ions coexist, only depends on the spatial variation of the electron pressure:

$$\frac{e\mathcal{E}}{m_\mathrm{e}} = -\frac{m_\mathrm{i}}{m_\mathrm{e}+m_\mathrm{i}}\,\frac{1}{\varrho_\mathrm{e}}\frac{\partial p_\mathrm{e}}{\partial r} \approx \frac{1}{\varrho_\mathrm{e}}\frac{\partial p_\mathrm{e}}{\partial r} \tag{8}$$

Using the above expression for the electric field, instead of Poisson's equation (3), does considerably simplify the electron momentum equation within the ion sphere leading to simple analytic expressions for the density and temperature profiles in that particular region.

2.2. Plasma structure inside of the ion sphere

We chose the ion front to be located at $r = R(t)$, or, in terms of the self-similarity variable ξ, at $\xi = 1$. All of the ions are therefore located within the spherical volume $\xi \leq 1$ where the electric field is given by equation (8). Substituting this expression for the electric field in the momentum equation for the electrons (2) leads to the simpler form

$$\varrho_\mathrm{e}\left(\frac{\partial v_\mathrm{e}}{\partial t} + v_\mathrm{e}\frac{\partial v_\mathrm{e}}{\partial r}\right) = -\alpha\frac{\partial p_\mathrm{e}}{\partial r} \tag{9}$$

where we have defined the small, dimensionless variable $\alpha \equiv m_\mathrm{e}/(m_\mathrm{e}+m_\mathrm{i}) \approx m_\mathrm{e}/m_\mathrm{i}$. Using the barotropic closure (4) and the shear-free flow (7) one can write (9) in terms of a differential equation for the dimensionless electron density $N_\mathrm{e} \equiv n_\mathrm{e}R^3 = \tilde{n}_\mathrm{e}/\xi^3$:

$$N_\mathrm{e}\xi\ddot{R}R^2 = -\alpha\gamma A(N_\mathrm{e}m_\mathrm{e})^{\gamma-1}R^{-3\gamma+4}\frac{\partial N_\mathrm{e}}{\partial\xi}. \tag{10}$$

The general solution of this equation is not self-similar as it depends explicitly on the spatial scale R. However, one can make the left-hand side of equation (10) independent of R by setting $\ddot{R}R^2 = k_1$. The meaning of the constant k_1 becomes clear immediately by noting that in a self-similar solution the net charge of the plasma within an arbitrary sphere of radius ξ must be constant in time. Thus, if $Q(\xi)$ is the net charge within a sphere of radius ξ we can write the momentum equation (2) for the ions as

$$m_\mathrm{i}\xi\ddot{R}R^2 = e\frac{Q(\xi)}{\xi^2}. \tag{11}$$

and consequently $k_1 = eQ_1/m_\mathrm{i}$ is just a measure of the net charge $Q_1 \equiv Q(1)$ of the ion sphere $\xi \leq 1$. The explicit dependence on the spatial scale R in the right-hand side of equation (10) is then easily eliminated by setting $\gamma = \frac{4}{3}$ leading to the simple equation

$$\frac{\partial}{\partial\xi}\left(\frac{N_\mathrm{e}}{N_1}\right) = -k_2(1+\alpha)\xi\left(\frac{N_\mathrm{e}}{N_1}\right)^{2/3} \tag{12}$$

where $N_1 = N_\mathrm{e}(1)$ is a reference density which we chose to be the electron density at the edge of the ion sphere and where k_2 is a dimensionless parameter denoting the relative importance of electrostatic and kinetic energy of an electron at $\xi = 1$

$$k_2 \equiv \frac{3}{4}\,\frac{eQ_1}{R}\,\frac{1}{k_\mathrm{B}T(1)}. \tag{13}$$

In (13) k_B is the Boltzmann constant and $T(1)$ the electron temperature at $\xi = 1$. As k_2 is not allowed to vary in time we deduce that in the self-similar solution the electron temperature goes as $T(\xi) = T_0(\xi)R_0/R$ and where the index 0 refers to time $t = 0$ (also see [1]).

2.2.1. Electron density profile inside of the ion sphere The solution of equation (12) is a simple polynomial

$$\begin{aligned}\frac{N_\mathrm{e}}{N_1} &= \left[1-\frac{k_2}{6}(1+\alpha)(\xi^2-1)\right]^3 \\ &\approx \left[1-\frac{k_2}{6}(\xi^2-1)\right]^3.\end{aligned} \tag{14}$$

The smaller k_2, i.e. the hotter the plasmas, the flatter the electron density profile. A schematic representation of the electron density profile in the inner region is shown in figure 1.

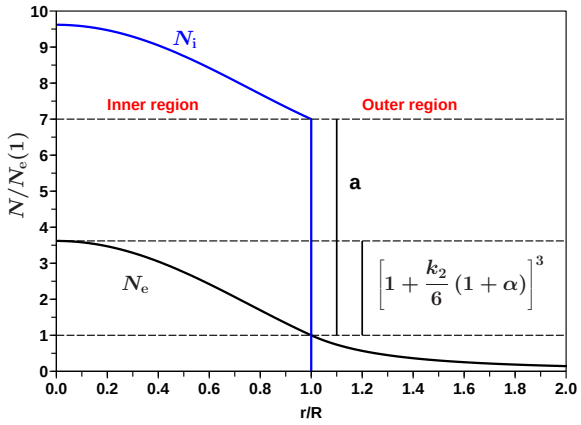

Figure 1. Dependence of the ion and electron density profiles on the parameters a and k_2. The departure from charge neutrality in the inner region is specified by the parameter $a = [N_i(1) - N_e(1)]/N_e(1)$ and the curvature of the density profiles near $r = 0$ by k_2. As shown in section 2.3, the parameters a and k_2 are not independent of each other.

2.2.2. Electric field and ion density profiles inside the ion sphere The electric field in the inner region is given by equation (8), together with the polytropic approximation $p_e \propto \varrho_e^{4/3}$ and the equation for the electron density (14). Not considering the constant factors one then easily finds that the $r^2\mathcal{E} \propto \xi^3$. With Q_1 being the net charge of the ion sphere, the electric field at $\xi = 1$ is just $\mathcal{E}(1) = eQ_1/R^2$ and the electric field in the inner region must be

$$E(\xi \leq 1, t) = \frac{Q_1}{R(t)^2}\,\xi. \tag{15}$$

We note that the electric field always peaks at the edge of the ion sphere ensuring that any given ion is always less accelerated that all ions ahead of it. Thus, as it must necessarily be, no ion overtaking occurs during the self-similar phase of the expansion. Ion overtaking is nevertheless a common event during the early, non self-similar phase of the expansion, unless very special initial conditions are chosen such that the electric field increases monotonically from $r = 0$ to $r = R$ [24, 13].

In order to compute the ion density we multiply Poisson's equation (3) by R^3 and rewrite it in terms of the self-similar variable ξ

$$\frac{\partial}{\partial\xi}\left(r^2\mathcal{E}\right) = 4\pi e\xi^2(N_i - N_e). \tag{16}$$

Since $r^2\mathcal{E} \propto \xi^3$ it follows that $N_i - N_e$ is a constant:

$$\frac{N_i(\xi)}{N_1} = \frac{N_e(\xi)}{N_1} + a, \quad \text{for} \quad \xi \leq 1 \tag{17}$$

where, as before, $N_1 = N_e(1)$ and where the constant $a = 3Q_1/(4\pi eN_1)$ is settled by the constraint that the net charge in the ion sphere is $Q_1 = \int_0^1 dx\, 4\pi x^2(N_i - N_e)$. The

dimensionless constant a can therefore be interpreted as the relative departure from charge neutrality at $\xi = 1$, i.e. $a = [N_\mathrm{i}(1) - N_\mathrm{e}(1)]/N_\mathrm{e}(1)$ (see figure 1).

2.3. Structure of the plasma outside of the ion sphere

The region $\xi > 1$ is populated by electrons only. The electric field for this region is obtained by integration of the Poisson equation (16) with $N_\mathrm{i} = 0$

$$\mathcal{E} R^2 = \frac{1}{\xi^2}\left(Q_1 - 4\pi e \int_1^\xi dx\, x^2 N_\mathrm{e}(x)\right). \tag{18}$$

Plugging this expression for the electric field into the electron momentum equation (2) for $j = \mathrm{e}$ conducts to the integro-differential equation for the electron density in the region ahead of the ion sphere

$$\frac{1}{N_1^{1/3}}\frac{N_\mathrm{e}'}{N_\mathrm{e}^{2/3}} = -k_2\left[\alpha\xi + \frac{1}{\xi^2}\left(1 - \frac{3}{a\, N_1}\int_1^\xi dx\, x^2 N_\mathrm{e}(x)\right)\right] \tag{19}$$

where the prime symbol $'$ stands for the derivative with respect to the self-similar variable $\partial/\partial\xi$. Equation (19) must be integrated numerically. We used a standard adaptive Runge-Kutta solver for all figures of the paper. However, even without performing the integration, the equation tells us that the electrons extends to a maximum radial distance ξ_f. For example, in the particular case of overall neutral plasma, for $\xi \to \infty$ the second term on the right-hand side of (19), which is essentially the electric field, must vanish. In this case, sooner or later, it must be that the electron density decreases as $N_\mathrm{e} \propto -\xi^6$ which necessarily implies $N_\mathrm{e} = 0$ for a finite value of ξ. Knowing that both the density and the electric field vanish at some finite distance $\xi = \xi_\mathrm{f}$ (the electron front) we conclude that at that particular distance $N_1^{-1/3} N_\mathrm{e}'/N_\mathrm{e}^{2/3} = -k_2\alpha\xi_\mathrm{f}$ and that therefore in the vicinity of ξ_f the density rapidly falls off as $N_\mathrm{e} \propto (\xi_\mathrm{f} - \xi)^3$. This is an important difference with respect to the infinite electron precursor of the Murakami and Basko model [1].

Equation (19) is a function of two constants a and k_2 which are apparently independent of each other. However, if one assumes that the electron density is not discontinuous in $\xi = 1$ so that $N_\mathrm{e}(1^+)/N_1 = 1$ can be used as a boundary condition, the two constants a and k_2 are constraint by the requirement that the electric field and the density both vanish at $\xi = \xi_\mathrm{f}$. The former condition implies that $3(a\, N_1)^{-1}\int_1^{\xi_\mathrm{f}} dx\, x^2 N_\mathrm{e}(x) = 1$. The $k_2(a)$ dependence for an overall neutral plasma and an electron to ion mass ratio $\alpha = 1/50$ is graphically illustrated in figure 2. The fact that a and k_2 are not independent shows that for a given choice of the charge separation parameter a there is only one possible choice of the parameter k_2 such that the electron density and the electric field both vanish at exactly the same position ξ_f. Thus, the behaviour of the system depends on the value of one single dimensionless parameter. For coherence with previous works on the subject [1, 13] we use a combination of a and k_2 to define the key parameter

$$\Lambda^2 \equiv \frac{a}{4k_2} = \left[\frac{\lambda_\mathrm{D1}}{R}\right]^2 \tag{20}$$

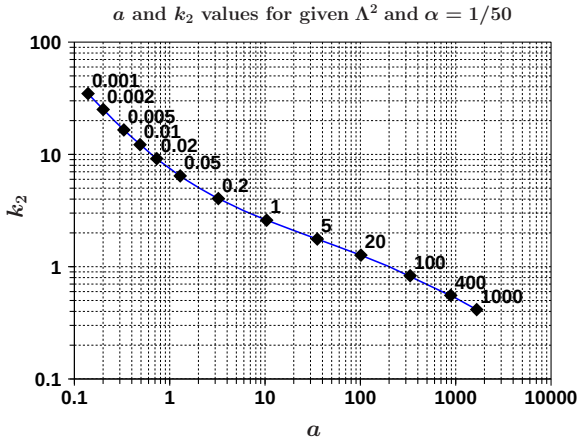

Figure 2. Relation between the parameters a, k_2 and $\Lambda^2 \equiv (\lambda_{\rm D1}/R)^2$ for an overall neutral plasma and $\alpha = 1/50$ obtained by numerically solving the differential equation for the electron density ahead of the ion front (19).

where $\lambda_{\rm D1} = [kT(1)/4\pi e^2 n_{\rm e}(1)]^{1/2}$ is the electron Debye length at the ion front $\xi = 1$. An additional parameter is required if the plasma of the self-similar solution is not globally neutral (see section 2.3.1).

Two examples illustrating a moderate and a strong charge separation, respectively, are shown in figure 3. As the charge separation grows with growing temperature we may class the two examples as mild and hot, respectively. Not surprisingly, the electrons being less coupled to the ions in the hot case (right panels) the electron precursor extends to a significantly larger distance ahead of the ion front with an overall flatter density profile. In figure 4 the profiles for 4 different values of Λ^2 are shown starting form a quasi-neutral (mild) case with $\Lambda^2 = 0.02$ where electrons hardly detach from the ion sphere up to the hot case with $\Lambda^2 = 3$ which already resembles to a Coulomb explosion [13].

2.3.1. Overall charged plasma In the previous section we considered the case of an overall neutral plasma, i.e. a plasma where the total number of ions $\mathcal{N}_{\rm i}$ equals the total number of electrons $\mathcal{N}_{\rm e}$. However, in some experiments (real or numerical), as in the numerical simulation presented in the Section 3, a non negligible fraction of electrons may be sufficiently energetic to become completely decoupled from the ion sphere. These electrons do essentially conserve their original speed and their evolution is trivial. Only the electrons which remain coupled to the ions do then participate to the self-similar evolution of the remnant which is not necessarily globally neutral.

If we assume that the plasma remnant's global charge is $Q_{\rm f} \equiv e(\mathcal{N}_{\rm i} - \mathcal{N}_{\rm e})$, one has to integrate equation (19) under the condition that the electric field at the electron front is just $E(r_{\rm f}) = Q_{\rm f}/r_{\rm f}^2$ which corresponds to let $(...) \to Q_{\rm f}/Q_1$ for

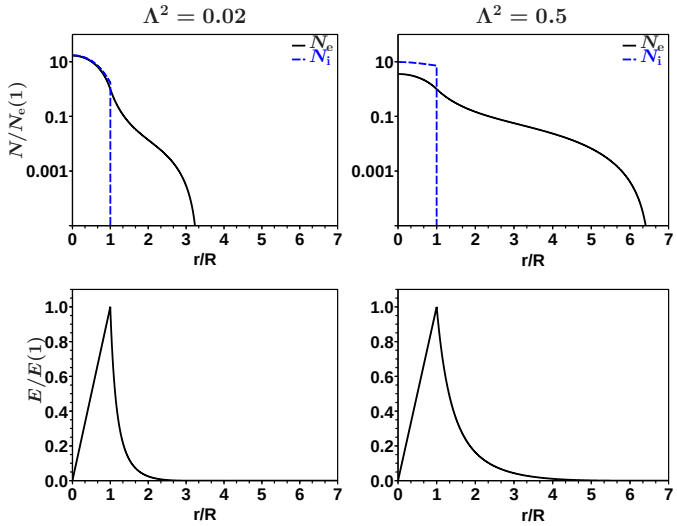

Figure 3. Electron and ion density profiles (top panels) and electric field profiles for two different values of Λ^2. The left panels correspond to a quasi-neutral (mild) case with $\Lambda^2 = 0.02$. The right panels correspond to a strongly non neutral (hot) case with $\Lambda^2 = 0.5$.

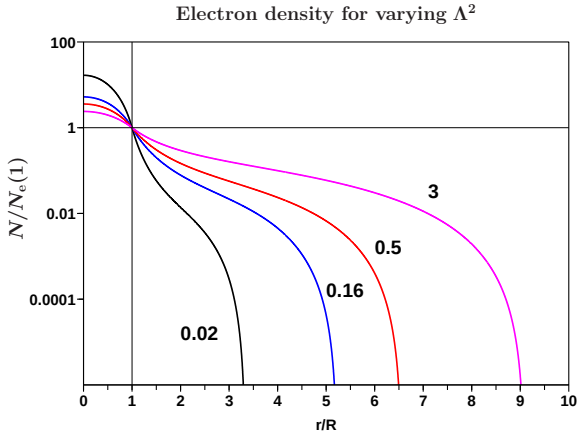

Figure 4. Electron density profiles for an overall neutral plasma and various values of Λ^2. The electron to ion mass ratio is $\alpha = 1/50$ for this figure and for all figures in the paper.

$\xi \to \xi_f$ in (19). Near the electron front, the differential equation (19) reduces to $N_1^{-1/3} N_e'/N_e^{2/3} = -k_2[\alpha\xi_f + \xi_f^{-2} Q_f/Q_1]$ while the electric field is $E(\xi_f)/E(1) = \xi_f^{-2} Q_f/Q_1$. Thus, in the charged case, as in the neutral case discussed in the previous section, the electron density decreases as $N_e \propto (\xi_f - \xi)^3$ for $\xi \to \xi_f$. In figure 5 the self-similar profiles for a neutral plasma (left panels) and a charged plasma (right panels) are shown. Both

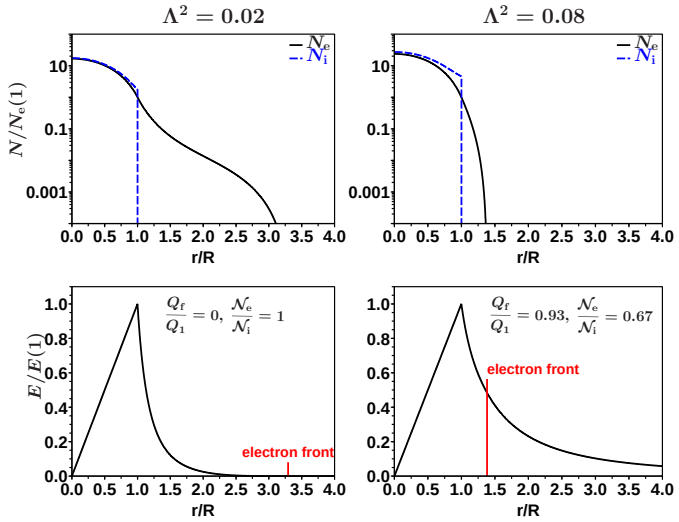

Figure 5. Electron and ion density profiles (top panels) and electric field profiles for two different values of the total charge Q_f/Q_1 and Λ^2. The total number of electrons in the charged system is only 67% of the total number of ions so that the electric field is not zero at the electron front. In the neutral case $\Lambda^2 = 0.02$ with $(a, k_2) = (0.73, 9.16)$ (left panels) while for the charged case $\Lambda^2 = 0.08$ with $(a, k_2) = (3.6, 11)$ (right panels). The electron front is much closer to the ion front in the charged case, despite being characterized by a larger value of Λ. These two particular examples are discussed further in connection with the numerical simulation of section 3.

cases are rather mild with ($\Lambda^2 = 0.02$ and $\Lambda^2 = 0.08$ respectively. In the charged case, the total number of electrons is only 2/3 of the total number of ions. Not surprisingly, the electron front is substantially closer to the ion front in the charged case compared to the neutral case because of the missing electrons. The k_2 parameter being larger in the charged case, both the ion and electron densities decrease faster in the charged case than in the neutral case, even though the latter is the coldest of the two. The plasma parameters for the two examples in figure 5 have been chosen for the ion density profiles to fit the density profile of the case simulation presented in section 3.

2.4. Ion front motion

The position of the ion front $R(t)$ can be computed explicitly from the equation of motion by integrating the condition $\ddot{R}R^2 = k_1 = eQ_1/m_i$ which expresses the conservation in time of the net charge of the ion sphere. Thus, the differential equation for $R(t)$ can be written in the form

$$\dot{R}^2 = -2\frac{k_1}{R} + V_\infty^2 \tag{21}$$

where V_∞ is to the asymptotic velocity of the ion front. If we assume that the ion front is initially at rest, then $V_\infty^2 = 2k_1/R_0$ and therefore

$$\dot{R}^2 = V_\infty^2 \left(1 - \frac{R_0}{R}\right). \tag{22}$$

Multiplying equation (22) by $(R_0\omega_{e,1})^{-1}$, where $\omega_{e,1} = [4\pi e^2 n_e(1)/m_e]^{1/2}$ is the electron plasma frequency at $\xi = 1$, leads to the differential equation in the normalized time variable $\tilde{t} \equiv t\omega_{e,1}$ and the normalized ion front position $\tilde{R} \equiv R/R_0$

$$\frac{d\tilde{R}}{d\tilde{t}} = \left(\frac{2a\alpha}{3}\right)^{1/2} \left(1 - \frac{1}{\tilde{R}}\right)^{1/2} \tag{23}$$

whose solution is

$$\tilde{t}\left(\frac{2a\alpha}{3}\right)^{1/2} = \left[\tilde{R}(\tilde{R}-1)\right]^{1/2} + \ln\left(\sqrt{\tilde{R}} + \sqrt{\tilde{R}-1}\right). \tag{24}$$

We note that for $a \gg 1$ one has $\omega_{e,1}\sqrt{a\alpha} \approx \omega_{i,1}$ (see (17)) and (24) reduces to the expression given in [13] for the case of a pure Coulomb explosion. The solution (24) shows that the characteristic time scale for approaching the asymptotic velocity is of order of $(\omega_{e,1}\sqrt{a\alpha})^{-1}$ indicating that acceleration time and wave period of Langmuir oscillations near the ion front are of the same order for $\sqrt{a\alpha}$ of order unity.

2.5. Ion energy distribution

Using (15) the total (kinetic + electrostatic) energy of an ion at any position $\xi \leq 1$ can be written as

$$E = \frac{1}{2} m_i \xi^2 \dot{R}^2 - \frac{1}{2}\frac{eQ_1}{R}\xi^2. \tag{25}$$

From the ion front equation of motion (21) and the equation for the electric field (15) one finds that the energy of an ion at position ξ grows in time as

$$E(\xi, t) = \left[\frac{1}{2} m_i V_\infty^2 - \frac{3}{2}\frac{eQ_1}{R(t)}\right]\xi^2. \tag{26}$$

approaching the asymptotic value $E(\xi) \approx \frac{1}{2} m_i \xi^2 V_\infty^2$ for $t \to \infty$. Given that the ion density profile $N_i(\xi)$ is known through equations (17) and (14) the number of ions in the interval $[\xi, \xi + d\xi]$ (normalized to the total number $\mathcal{N}_i$) is explicitly given by

$$dN_i([\xi, \xi + d\xi]) = 4\pi\xi^2 N_i(\xi^2) d\xi. \tag{27}$$

Using the energy-position relation (25) and the density distribution (27), one obtains the number of ions in the energy interval $[\tilde{E}, \tilde{E} + d\tilde{E}]$:

$$dN_i([\tilde{E}, \tilde{E} + d\tilde{E}]) = 2\pi\tilde{E}^{1/2} N_i(\tilde{E}) d\tilde{E}. \tag{28}$$

where $\tilde{E} = E/E(1) = \xi^2$ is the energy of an ion at position ξ normalized to the energy of an ion at $\xi = 1$. The distribution $dN_i/d\tilde{E}$ of the ions kinetic energy in the system is shown in figure 6 for various values of Λ^2.

We note that for $\Lambda^2 \gtrsim 0.2$ the distribution peaks at the maximum energy, corresponding to the contribution of the ions at $\xi = 1$. For $\Lambda^2 \lesssim 0.2$ the contribution

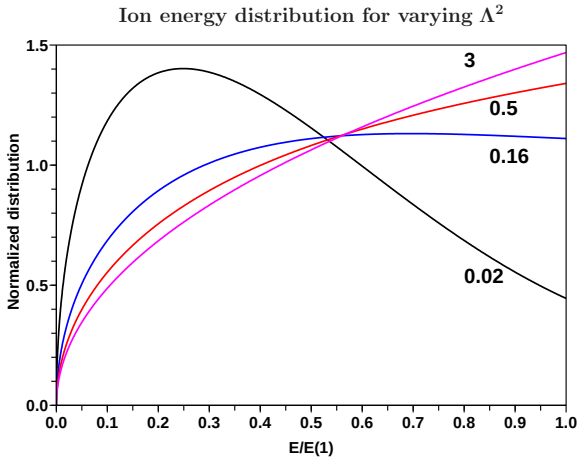

Figure 6. Ion energy distribution for $\alpha = 1/50$ and various values of Λ^2. The figure is qualitatively similar to results from numerical simulations shown in figure 9 of [13].

from the ions near the front $\xi = 1$ is no longer dominant since their relative number decreases with decreasing Λ^2 as shown by equations (14) and (17) or even figure 4. The structure of the ion energy spectrum and its dependence on Λ^2 is qualitatively similar to the spectra in [25, 13].

2.6. Electron heat flux

In order to compute the heat flux q carried by the electrons we write the energy equation in Lagrangian form, derived from the collisionless Boltzmann equation, for a spherically symmetric flow and isotropic electron temperature [26]:

$$\frac{3}{2}\left(\frac{\partial T}{\partial t} + v\frac{\partial T}{\partial r}\right) = -\frac{T}{r^2}\frac{\partial}{\partial r}\left(vr^2\right) - \frac{1}{n_e k_B\, r^2}\frac{\partial}{\partial r}\left(qr^2\right) \tag{29}$$

The first term on the right corresponds to the cooling of the fluid element du to the expansion, the second term to the cooling (or heating) of the fluid element collisionless heat conduction. For a polytropic fluid with $T \propto n_e^{\gamma-1}$ equation (29) can be written in the form:

$$\frac{3}{2}\left(\frac{\gamma - \frac{5}{3}}{\gamma - 1}\right) n_e k_B \frac{DT}{Dt} = -\frac{1}{r^2}\frac{\partial}{\partial r}\left(qr^2\right) \tag{30}$$

where $D/Dt \equiv \partial/\partial t + v\partial/\partial r$ is the convective derivative. As expected, equation (30) shows that the electron heat flux vanishes when the polytropic index equals the adiabatic value $\gamma_{ad} = \frac{5}{3}$ and infinity for the isothermal index $\gamma = 1$. Since the spatial profiles of both density and temperature are flat near the expansion centre we find that the heat flux near the expansion centre is given by $q(r) \simeq \frac{1}{2} n_e k_B\, r\, \partial T/\partial t < 0$, indicating that energy is transported in the direction of decreasing r, i.e. in the direction of increasing temperature. The reason for this non intuitive behaviour is that the energy flux goes

from high to low entropy regions but not necessarily from regions of high to regions of low temperature. In general, in a collisional gaz or in a fluid, temperature and entropy vary together and energy effectively flows down the temperature gradient. In the polytropic approximation entropy variations ds and temperature variations dT are related via [27]

$$\frac{ds}{\mathcal{R}} = \frac{3}{2}\left(\frac{\gamma - \frac{5}{3}}{\gamma - 1}\right)\frac{dT}{T} = -\frac{3}{2}\frac{dT}{T} \tag{31}$$

where $\mathcal{R}$ is the gaz constant and where $\gamma = \frac{4}{3}$ has been set. The entropy-temperature relation indicates that spatial and temporal variations of the electron temperature are opposite with respect to the spatial and temporal variations of the entropy. Thus, in the self-similar solution of the expansion problem, entropy increases spatially away from the expansion centre with a logarithmic divergence $s \propto -\ln(\xi_\mathrm{f} - \xi)$ for $\xi \to \xi_\mathrm{f}$. Similarly, in the central region, near $r = 0$, one has $\partial s/\partial t = -\frac{3}{2}\mathcal{R}\partial \ln T/\partial t > 0$. Entropy grows in time because the reduction of entropy due to cooling is more than compensated by the entropy increase due to the fluid expansion.

Specialising to shear-free flows $v = \xi\dot{R}$ with the self-similar polytropic index $\gamma = \frac{4}{3}$, the energy equation (30) simplifies to

$$\frac{3}{2}k_\mathrm{B}TN_\mathrm{e}\frac{\dot{R}}{R^3} = -\frac{1}{\xi^2}\frac{\partial}{\partial\xi}(\xi^2 q) \tag{32}$$

The left-hand side of this expression is strictly positive indicating that the heat flux is directed towards the expansion centre, against the temperature gradient, in all parts of the fluid. Equation (32) can be solved for the heat flux which after some rearrangements becomes

$$q(\xi, t) = -6\pi e^2 N_1^2 \Lambda^2 \frac{\dot{R}}{R^4}\frac{1}{\xi^2}\int_0^\xi \left[\frac{N_\mathrm{e}(x)}{N_1}\right]^{4/3} x^2 dx. \tag{33}$$

This equation shows that at any given time t the energy $|4\pi\xi^2 R^2 q(\xi, t)|$ which flows towards the centre through the sphere of radius ξ increases monotonically with the distance ξ, reaching a maximum at the electron front $\xi = \xi_\mathrm{f}$. The heat flux at any position ξ varies in time as $-\dot{R}/R^4$. Thus, according to (33), the heat flux, which is initially zero if the initial expansion velocity is assumed to be zero, first grows in time until it reaches a maximum intensity at the time when $R = \frac{9}{8}R_0$. At later times the heat flux intensity decreases everywhere monotonically and, in particular for $R \gg 1$, the expansion velocity can be assumed to be constant and $q \propto R^{-4} \propto t^{-4}$.

3. Ab initio simulation

In this section we present a numerical case simulation of a two species collisionless plasma expanding into vacuum. We use a slightly modified version of Walter Dehnen's non relativistic N-body code [28], initially conceived for gravitational problems. N-body simulations have the advantage of not resting on simplyfing assumptions being merely based on Newton's second law of motion and Coulomb's law to compute the self-consistent evolution of a system of point charges. The major disadvantage of

N-body simulations, compared to either fluid [29, 30], semi-kinetic [13] or even fully kinetic simulations [31, 14, 4] resides in the computational difficulty to follow the plasma evolution over a sufficiently long physical time for the system to enter into a clean self-similar phase. The choice of an artificially small mass ratio $m_\mathrm{i}/m_\mathrm{e}$, necessary to keep the computational time within reasonable limits, is another drawback of the N-body simulations. On the other hand, N-body simulations are more realistic representations of collisionless systems with a small number of particles than ideal, noise-free, simulations based on the Vlasov-Poisson system. Strictly speaking the Vlasov-Poisson equations are only applicable to plasmas where the number of electrons within the Debye sphere tends to infinity. However, in real plasma-cluster experiments the number of atoms in a cluster is rather small, ranging between 10^3 [32] and 10^7 [6]. Accordingly, in the simulation of this section a total number of $1.5\,10^5$ ions and an equal number of electrons have been chosen. The parameter Λ having been selected in the the most interesting regime for numerical simulations $\Lambda = \mathcal{O}(0.1)$ (see Section 3.1), the expected number of electrons in Debye sphere is of order 10^2. As explained in [33], the applicability of a Vlasov-Poisson model for a system with such a small number of particles is questionable since a non negligible fraction of orbits are expected to become chaotic, i.e. non reversible, during the time of the simulation. Thus, contrary to the prediction of the Vlasov-Poisson model, in the N-body and in the corresponding real system, the total Gibbs entropy is not constant but a growing function of time.

3.1. Plasma parameters and initial conditions

We simulate a total of $1.5\,10^5$ single ionized ions and an equal number of electrons. The ion to electron mass ratio is $m_\mathrm{i}/m_\mathrm{e} = 50$. Such a mass ratio is sufficiently large for the two fluid model of Section 2 to be applicable.

At $t = 0$ ions and electrons are distributed uniformly within a sphere of radius R_0. Initially, all ions are motionless whereas the electrons's velocities are drawn following a Maxwell-Boltzmann distribution at temperature T_0 and zero bulk velocity.

The initial temperature T_0 and density $n_{\mathrm{i},0} = n_{\mathrm{e},0} = n_0$ are selected for the expansion to be in the mild regime with $\Lambda = \mathcal{O}(0.1)$, the hot case $\Lambda \gg 1$ corresponding to the Coulomb explosion and the cold case $\Lambda \ll 1$ to the quasi-neutral case.

The strong interaction radius $r_\mathrm{s} \equiv e^2/3k_\mathrm{B}T$, representing the characteristic distance for binary collisions, is taken to be much smaller than the ion sphere R and even much smaller that the average distance between electrons $n_\mathrm{e}^{-1/3}$. The mean free path for a binary collisions of a test electron with another electron in the system can be estimated to be $\lambda_{\mathrm{ee,bin}} = 1/n_\mathrm{e}4\pi r_\mathrm{s}^2 = 9(k_\mathrm{B}T)^2/4\pi e^4 n_\mathrm{e}$. Using the definition of the key parameter $\Lambda^2 = k_\mathrm{B}TR^{-2}/4\pi n_\mathrm{e}e^2$, and the polytropic relation $T \propto N_\mathrm{e}^{1/3}$, the normalized mean free path for binary collisions becomes

$$\frac{\lambda_{\mathrm{ee,bin}}(\xi)}{R} = 36\pi\Lambda^4 N_\mathrm{e}(1)\,\left[\frac{N_\mathrm{e}(\xi)}{N_\mathrm{e}(1)}\right]^{-4/3} \tag{34}$$

which shows explicitly that in the self-similar model the collisionality does not evolve

in time as the right-hand side of (34) is constant. In weakly coupled plasmas where the Coulomb logarithm $\ln(\lambda_D/r_s) \gtrsim 5$, binary collisions are unimportant compared to the cumulative effect of long distant interactions with impact parameters of the order $\lambda_D \gg r_s$. The mean free path can then be obtained in the Fokker-Planck approximation which is given, within a constant factor of order unity, by $\lambda_{ee,FP} \sim \lambda_{ee,bin} \ln^{-1}(\lambda_D/r_s)$ [34].

In the simulation the Coulomb logarithm is larger than unity, the density at the ion front $N_1 \approx 2 \times 10^3$ and the key parameter $\Lambda^2 \gtrsim 0.02$ (see figure 7). We can then make an estimate of the mean free path at the ion front $\lambda_{ee,FP}(1) \sim \lambda_{ee,FP}(1) \gtrsim 90R \gg R$. which confirms that the plasma is collisionless and that it can be treated in the frame of the collisionless fluid model of section 2.

3.2. Density and temperature profiles inside of the ion sphere

Figure 7 shows that the simulated ion density profile can be fairly well approximated using the self-similar density from (17) with $\Lambda^2 = 0.02$ and an overall neutral plasma. On the other hand, the electron density predicted by the model are substantially higher than the density observed in the simulation everywhere within the ion sphere. A much better agreement for both ion and electron densities can be obtained by assuming that the plasma is not globally neutral as shown in the right panel of figure 7 where the total number of electrons is only 2/3 of the total number of ions and $\Lambda^2 = 0.08$. The fact that the non neutral model provides a better approximation is the consequence of a non negligible fraction of electrons having a sufficiently high initial energy to escape from the system keeping the memory of the initial condition which is not compatible with the self-similar solution. The flattening of the electron density profile from the simulation for $\xi \gtrsim 1.6$ is a trace of these escaping electrons which are even better visible in figure 9. Figure 9 also shows that some of the electrons located ahead of the ion front are falling back towards the ion sphere on time scales which are of the order of the simulation time. These slowly falling electrons do still carry the memory of the initial conditions and may not yet be entirely compatible with the asymptotic solution.

The small ion excess observed in the simulation when approaching the ion front is due to ion overtaking which has been shown to occur whenever the electric field maximum occurs in a region of decreasing ion density [24, 13].

In figure 8 the electron temperature profile at the end of the simulation is compared to the model predictions based on the same two sets of parameter used for figure 7. As already announced, the electron temperature measured in the simulation is strongly dependent on the spatial variable ξ despite having been uniform at $t = 0$. The agreement between simulation and model prediction is rather satisfactory for $\xi \lesssim 0.8$ for both the overall neutral and the overall charged case. In particular the convex shape of the temperature profile predicted by the theory is apparent in the simulated profile. The spike in the temperature near $\xi = 0.9$ is a transient feature due to the presence of counterstreaming electron beams. Indeed, as shown in figure 9, electron beams are

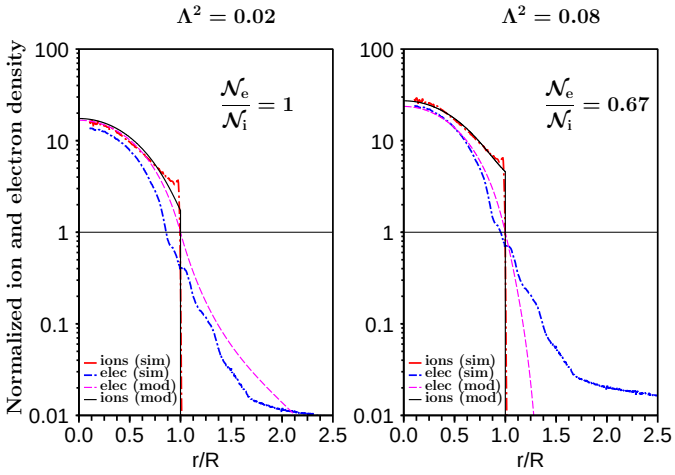

Figure 7. Rescaled density profiles for both ions and electrons from the simulation compared to model profiles. The model profiles in the left panel correspond to those of an overall neutral plasma and $\Lambda^2 = 0.02$. The model profiles in the right panel correspond to those of a globally charged plasma with $\Lambda^2 = 0.08$. and a total number of electrons $\mathcal{N}_e$ which is only 67% of the total number of ions $\mathcal{N}_i$. The experimental profiles have been obtained by averaging the densities from the simulation during the time interval $7 \leq t\omega_{e0} \leq 41$ (see figure 9). The model densities have been normalized as to make the total number of ions in the simulation to be equal to the total number of ions in the model. All densities have been normalized to the model electron density $N_e(1)$ (see equation (14)).

sporadically expelled from the ion sphere. Most of these beams, except the very first one, are not energetic enough to escape and fall back into the ion sphere where they first appear as inward propagating beams and later, passed the pericentre, again as outward propagating beams.

3.3. Ion front expansion and electron density fluctuations

Figure 9 shows the electron density in arbitrary units and the position of the ion front as a function of time. Given the difficulty of predicting the value of Λ^2 based on the initial choice of the electron temperature we fit the ion front position using equation (24). The fit produces an estimate of the parameter a and, from which, using figure 2, one deduces the value of the key parameter $\Lambda^2 = 0.08$ and the scaling of the time axis in terms of the electron plasma frequency.

The figure shows that regardless of the strong electron density fluctuations around the ion front, the latter closely follows the temporal evolution of equation (24). The time period of the electron density fluctuations near the ion are compatible with a period of the order $2\pi/\omega_e(1)$. The slowing down of the oscillation frequency with time is a consequence of the decreasing plasma frequency $\omega_e(t) \propto n_e^{1/2} \propto R^{-3/2}$. Individual

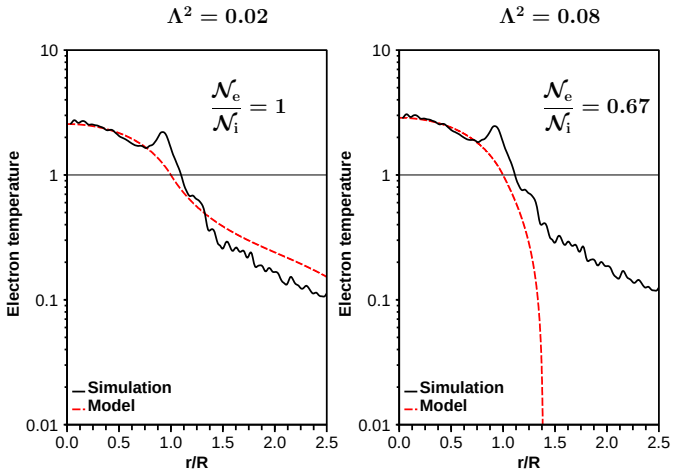

Figure 8. Electron temperature profiles at the end of the simulation compared to model profiles for an overall neutral model with $\Lambda^2 = 0.02$ (left pannel) and for a globally charged plasma with $\Lambda^2 = 0.08$. and a total number of electrons which is only 0.67% of the total number of ions (right panels).

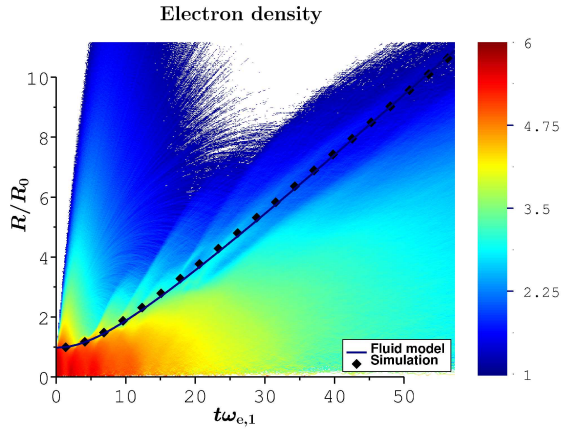

Figure 9. Logarithm of the electron density and ion front position measured in the simulation (diamonds). The $\tilde{R}(t)$ curve has been obtained by forcing the self-similar solution (24) to pass through the latest position of the ion front observed in the simulation with $\Lambda^2 = 0.08$ and $\alpha = 1/50$.

electron trajectories are visible in the upper part of the figure. Some electrons are clearly "falling" back onto the expanding ion sphere. However, a non negligible fraction of electrons, of the order of $\frac{1}{3}$ the total number, have a sufficiently high initial kinetic energy to freely escape from the system. In the long run, once the not bounded electrons

have escaped, the system does more likely evolve according to the self-similar solution of a charged plasma with $Q_\mathrm{f}/Q_1 = 0.33$ as suggested by the good agreement between the profile from the simulation and the manual fit in the right panel of figure 7.

3.4. Ion energy distribution

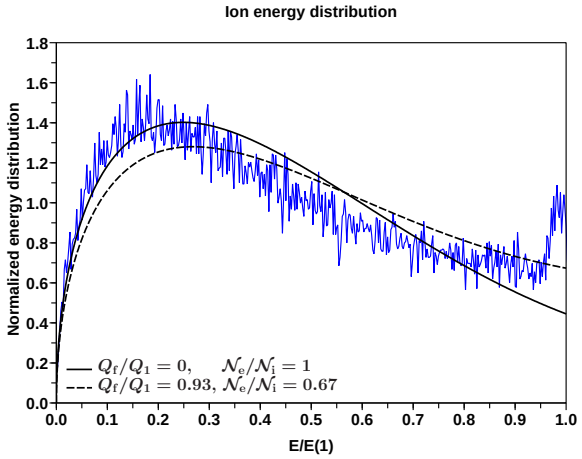

Figure 10. Ion energy distribution at the end of the simulation compared to the energy distributions from the self-similar model for the neutral case with $\Lambda^2 = 0.02$ and the charged case with $\Lambda^2 = 0.08$ and $Q_\mathrm{f}/Q_1 = 0.93$ corresponding to a plasma where the total number of electrons is 67% of the total number of ions.

The energy spectrum of the ions in the simulation is shown in figure 10 at the end of the simulation when the ion front velocity can be assumed to be constant and the electrostatic energy stored in the ions negligible. Also shown are the model energy distributions for the two sets of plasma parameters used for the two panels in figure 7. Both the charged and the neutral case do qualitatively agree with the distribution from the simulation. The main difference between simulation and model is the existence of a secondary peak in the ion energy distribution from the simulation. This secondary peak at the ion front is a remnant of the initial condition, due, at least in part, to ion overtaking as described in [17, 18] for the quasi-neutral case and in [24, 13] for the Coulomb explosion case. Ion overtaking does also manifest itself with the formation of a peak in the ion density profile which is visible on the ion density profiles near $\xi = 1$ in figure 7. However, as shown in [20], a spike near the maximum energy can also be part of a self-similar solution by relaxing the zero velocity condition at $\xi = 0$.

4. Conclusions

We have presented a new spherically symmetric self-similar solution for the problem of the expansion of a collisionless, either globally neutral or globally charged plasma,

into vacuum. The model is based on a two fluid system of equations derived from the collisionless Boltzmann equation with a polytropic closure for the electrons and a zero temperature closure for the ions. The model is similar to the one recently published in [1] with the notable difference that electrons are non isothermal. The consequence is the appearance of a sharp electron front at some distance ahead of the ion front and an inwards directed heat flux. Analytic expressions for the ion and electron densities as well as for the electron heat flux and the ion energy distribution are given for the region inside the ion sphere. The self-similar solution has been found to be in good qualitative agreement with results from an ab initio numerical simulation. Longer simulations than the one presented are needed to establish if the self-similar solution is effectively an "attractor" for the late evolution of the system, when the memory of the initial conditions are lost. We note that the fluid model is based on the restrictive assumption that the radial and tangential temperatures of the electron fluid are equal. This condition is not necessarily satisfied in the collisionless limit where the pressure tensor can be anisotropic. Thus, an even better agreement between model and numerical simulations may be obtained by assuming a non isotropic pressure tensor for the electron fluid which is a current assumption in the context of solar wind modelling [26] possibly with a different equation of state for the radial and tangential directions. However, allowing for the pressure to be anisotropic does only make sense if some physical mechanism (e.g. plasma instability) triggering the degree of anisotropy has been previously identified.

We conclude by observing that the presented self-similar solution is expected to apply to the late expansion of a plasma resulting from the irradiation of small clusters of atoms where the totality of the electrons are heated to high energies independently of their original location within the cluster. The case of an expanding plasma with two distinct electron populations is certainly a more realistic representation of the case of large clusters [16, 15, 1] worth being addressed in a future publication. In this repect, we note that the two populations case with a mild, cluster bounded population, and a hot, escaping population, has already been discussed implicitly in Section 2.3.1 where we have treated the case of an overall charged plasma. The generalization of the solution to the case of two or more populations of electrons with different temperatures and densities should be straightforward and much easier to carry out than the more ambitious generalization to an anisotropic electron pressure tensor.

References

[1] M. Murakami and M. M. Basko. Self-similar expansion of finite-size non-quasi-neutral plasmas into vacuum: Relation to the problem of ion acceleration. *Physics of Plasmas*, 13:2105–+, January 2006.

[2] S. R. Pillay, S. V. Singh, R. Bharuthram, and M. Y. Yu. Self-similar expansion of dusty plasmas. *Journal of Plasma Physics*, 58:467–474, October 1997.

[3] K. E. Lonngren. Expansion of a dusty plasma into a vacuum. *Planetary and Space Science*, 38:1457–1459, November 1990.

[4] P. C. Birch and S. C. Chapman. Two dimensional particle-in-cell simulations of the lunar wake. *Physics of Plasmas*, 9:1785–1789, May 2002.

[5] S. Ter-Avetisyan, M. Schnürer, H. Stiel, U. Vogt, W. Radloff, W. Karpov, W. Sandner, and P. V. Nickles. Absolute extreme ultraviolet yield from femtosecond-laser-excited Xe clusters. *Phys. Rev. E*, 64(3):036404–+, September 2001.

[6] I. Last and J. Jortner. Tabletop Nucleosynthesis Driven by Cluster Coulomb Explosion. *Physical Review Letters*, 97(17):173401–+, October 2006.

[7] P. Mora. Thin-foil expansion into a vacuum. *Physical Review E*, 72(5):056401–+, November 2005.

[8] N. Qi and M. Krishnan. Experimental verification of a simple, one-dimensional model for the hydrodynamic expansion of a laser-produced plasma into vacuum. *Physics of Fluids B*, 1:1277–1281, June 1989.

[9] G. Hairapetian and R. L. Stenzel. Particle dynamics and current-free double layers in an expanding, collisionless, two-electron-population plasma. *Physics of Fluids B*, 3:899–914, April 1991.

[10] T. Ditmire, J. Zweiback, V. P. Yanovsky, T. E. Cowan, G. Hays, and K. B. Wharton. Nuclear fusion from explosions of femtosecond laser-heated deuterium clusters. *Nature*, 398:489–492, April 1999.

[11] D. M. Villeneuve, G. D. Enright, R. Fedosejevs, M. D. J. Burgess, and M. C. Richardson. Energy partition in CO2-laser-irradiated microballoons. *Physical Review Letters*, 47:515–518, August 1981.

[12] P. Mora. Plasma Expansion into a Vacuum. *Physical Review Letters*, 90(18):185002–+, May 2003.

[13] F. Peano, J. L. Martins, R. A. Fonseca, L. O. Silva, G. Coppa, F. Peinetti, and R. Mulas. Dynamics and control of the expansion of finite-size plasmas produced in ultraintense laser-matter interactions. *Physics of Plasmas*, 14:6704–+, May 2007.

[14] Y. Kishimoto, T. Masaki, and T. Tajima. High energy ions and nuclear fusion in laser-cluster interaction. *Physics of Plasmas*, 9:589–601, February 2002.

[15] B. N. Breizman and A. V. Arefiev. Ion acceleration by hot electrons in microclusters. *Physics of Plasmas*, 14(7):073105–+, July 2007.

[16] B. N. Breizman, A. V. Arefiev, and M. V. Fomyts'kyi. Nonlinear physics of laser-irradiated microclusters. *Physics of Plasmas*, 12(5):056706–+, May 2005.

[17] C. Sack and H. Schamel. Nonlinear dynamics in expanding plasmas. *Physics Letters A*, 110:206–212, July 1985.

[18] C. Sack and H. Schamel. Plasma expansion into vacuum - A hydrodynamic approach. *Physics Reports*, 156:311–395, December 1987.

[19] E. N. Glass. Newtonian spherical gravitational collapse. *Journal of Physics A Mathematical General*, 13:3097–3104, September 1980.

[20] N. Kumar and A. Pukhov. Self-similar quasineutral expansion of a collisionless plasma with tailored electron temperature profile. *Physics of Plasmas*, 15(5):053103–+, May 2008.

[21] R. F. Schmalz. New self-similar solutions for the unsteady one-dimensional expansion of a gas into a vacuum. *Physics of Fluids*, 28:2923–2925, September 1985.

[22] R. F. Schmalz. Free unsteady expansion of a polytropic gas: Self-similar solutions. *Physics of Fluids*, 29:1389–1397, May 1986.

[23] T. H. Stix. *Waves in plasmas*. American Institute of Physics Press, 1992.

[24] A. E. Kaplan, B. Y. Dubetsky, and P. L. Shkolnikov. Shock Shells in Coulomb Explosions of Nanoclusters. *Physical Review Letters*, 91(14):143401–+, October 2003.

[25] F. Peano, F. Peinetti, R. Mulas, G. Coppa, and L. O. Silva. Kinetics of the Collisionless Expansion of Spherical Nanoplasmas. *Physical Review Letters*, 96(17):175002–+, May 2006.

[26] E. Endeve and E. Leer. Coronal heating and solar wind acceleration; gyrotropic electron-proton solar wind. *Solar Physics*, 200:235–250, May 2001.

[27] L.D. Landau and E.M. Lifshits. *Fluid mechanics. 2nd ed. Volume 6 of Course of Theoretical Physics. Transl. from the Russian by J. B. Sykes and W. H. Reid.* Pergamon Press, 1987.

[28] W. Dehnen. A hierarchical $\mathcal{O}$(N) Force Calculation Algorithm. *Journal of Computational Physics*, 179:27–42, June 2002.

[29] C. Sack and H. Schamel. SUNION-An Algorithm for One-Dimensional Laser-Plasma Interaction. *Journal of Computational Physics*, 53:395–+, March 1984.

[30] H. Schamel. Lagrangian fluid description with simple applications in compressible plasma and gas dynamics. *Physics Reports*, 392:279–319, March 2004.

[31] T. Grismayer, P. Mora, J. C. Adam, and A. Héron. Electron kinetic effects in plasma expansion and ion acceleration. *Physical Review E*, 77(6):066407–+, June 2008.

[32] T. Ditmire, J. W. G. Tisch, E. Springate, M. B. Mason, N. Hay, J. P. Marangos, and M. H. R. Hutchinson. High Energy Ion Explosion of Atomic Clusters: Transition from Molecular to Plasma Behavior. *Physical Review Letters*, 78:2732–2735, April 1997.

[33] H. E. Kandrup, I. V. Sideris, and C. L. Bohn. Chaos and the continuum limit in charged particle beams. *Physical Review Special Topics Accelerators and Beams*, 7(1):014202–+, January 2004.

[34] J.D. Huba. *NRL Plasma Formulary*. Naval Research Laboratory, Washington, DC, 2006.

12 Modification de l'algorithme FalcON pour la simulation d'un plasma

Note de travail

Modifying the falcON code for plasma simulations

A. Beck and F. Pantellini

February, 2006

1 Introduction

FalcON is a hierarchical $\mathcal{O}(N)$ force calculation code for the approximate computation between N mutually interacting bodies. The underlying algorithm, mainly intended for gravitationally interacting bodies, has been extensively described in the reference article by the author of the code W. Dehnen (1) (hereafter D2002). This note is about a possible extensions of the basic algorithm to make it applicable to plasma simulations, i.e. with the possibility of having both attractive and repulsive forces in the system, while keeping the $\mathcal{O}(N)$ computational complexity of the algorithm. Even though, both electrostatic and gravitational force fields are governed by the Poisson equation, non exact methods (like the falcON algorithm) to solve Poisson's equation in the gravitational case may not be uncritically transposed to the electrostatic case. For example, the electrostatic field due to a system of positive and negative charged particles can vanish exactly, whereas any system of gravitationally interacting bodies induces a non vanishing gravitational field. Concerning falcON, the most important difference arises because in a globally neutral plasma of N particles the monopole contribution to the electrostatic field is zero, whereas in the gravitational case the monopole term is proportional to the sum of all masses in the system which is always positive. In addition, given that in the original version of falcON the multipole expansion of the field is barycentric, the dipole term is zero by construction. In a plasma, the dipole term is often dominant, the monopole term being generally small or zero.

Details on the falcON algorithm can be found in Dehnen's article ((1)). In section 2 we propose a better suited definition of the expansion center for the approximate and in section 3 the associated expansion coefficients.

2 Modifying the definition of the expansion center

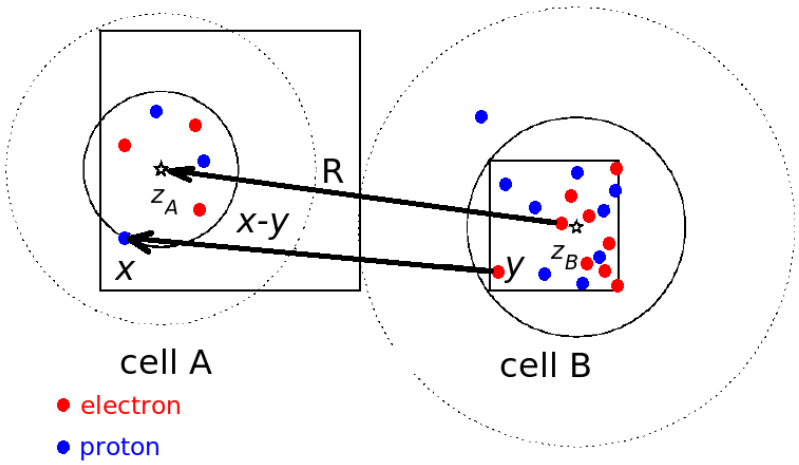

Figure 1: Two interacting cells (boxes). The stars indicate the position of the "center of mass" based on the sum of the absolute value of the charges μ_i in the corresponding cell according to equation (1). The figure has been adapted from Fig 1 in reference (1).

The algorithm is based on a multipole expansion of the electrostatic force acting on the bodies in cell A due to all bodies in cell B for well separated cells (see figure 1). The key point is a convenient definition of the expansion center z_{B}based on the position and on the *electric charge* μ_i of all charges i in cell B. It is reasonable to set

$$z_{\mathrm{B}} \equiv \frac{\sum_i |\mu_i| y_i}{\sum_i |\mu_i|}. \tag{1}$$

This new definition of the expansion center has the advantage of being identical to the original definition in Dehnen's paper when all μ_i in the system are positive. In the case of two charges of equal strength and opposite sign (e.g. an electron and a proton) $z_{\mathrm{B}}$is locate at half the distance between the two charges, which is a convenient location for a multipole expansion. With the old definition in D2002 one has μ_i instead of $|\mu_i|$ in (1). In this case the expansion center would be located at $z_{\mathrm{B}} \rightarrow \infty$ because of the vanishing denominator !

3 The new version of the field tensors

The potential at every position x in cell A generated by all charges in cell B is given by the expansion

$$\Phi_{\mathrm{B}\to\mathrm{A}}(x) = -\sum_{m=0}^{p} \frac{1}{m!}(x - z_{\mathrm{A}})^{(m)} \odot \mathbf{C}^{m,p}_{\mathrm{B}\to\mathrm{A}} + \mathcal{R}_p(\Phi_{\mathrm{B}\to\mathrm{A}}) \tag{2}$$

where $x^{(n)}$ indicates the n-fold outer product of the vector x with itself, $\odot$ the tensor inner product and $\mathcal{R}_p$ the Taylor reminder due to multipole terms of order higher than p. Given the definition (1) of the expansion center z_{B}, the field tensors $\mathbf{C}^{m,p}_{\mathrm{B}\to\mathrm{A}}$in equation (2) do now depend on the dipole moment M^1, which vanishes by construction in the gravitational case. The general expression for the field tensors in (2) is

$$\mathbf{C}^{m,p}_{\mathrm{B}\to\mathrm{A}} = \sum_{n=0}^{p-m} \frac{(-1)^n}{n!} \nabla^{(n+m)} g(\mathbf{R}) \odot \mathbf{M}^n_{\mathrm{B}} \tag{3}$$

$$\mathbf{M}^n_{\mathrm{B}} = \sum_{y_i \in B} \mu_i (y_i - z_{\mathrm{B}})^{(n)} \tag{4}$$

where $\mathbf{R} \equiv z_A - z_B$ and $g(\mathbf{R}) = 1/|\mathbf{R}|$ is the spherical Green function. As in the D2002 we limit the expansion to the order $p = 3$. Using the following definition for the operator D^m

$$D^m \equiv \left(\frac{1}{r}\frac{\partial}{\partial r}\right)^m g(r) \Big| r = |\mathbf{R}| \tag{5}$$

so that, for example, D^2 writes

$$D^2 = \frac{1}{r}\frac{\partial}{\partial r}\left(\frac{1}{r}\frac{\partial g(r)}{\partial r}\right) \Big| r = |\mathbf{R}| \tag{6}$$

The explicit form of the relevant coefficients (using Einstein's sum convention), including contributions proportional to the non vanishing dipole M^1,

can the be written as (assuming Einstein's summation convention)

$$\begin{aligned}
\mathbf{C}^{0,3}_{\mathrm{B}\to\mathrm{A}} &= M^0 D^0 + \frac{1}{2} M^2_{ii} D^1 + \frac{1}{2} R_i R_j M^2_{ij} D^2 \\
&\quad \boxed{-R_i M^1_i D^1} + \mathcal{O}(M^3) \qquad (7) \\
\mathbf{C}^{1,3}_{\mathrm{B}\to\mathrm{A},i} &= R_i \left(M^0 D^1 + \frac{1}{2} M^2_{jj} D^2 + \frac{1}{2} R_j R_k M^2_{jk} D^3 \right) + R_j M^2_{ij} D^2 \\
&\quad \boxed{-M^1_i D^1 - R_i R_j M^1_j D^2} \qquad (8) \\
\mathbf{C}^{2,3}_{\mathrm{B}\to\mathrm{A},ij} &= M^0 (\delta_{ij} D^1 + R_i R_j D^2) \\
&\quad \boxed{-M^1_k \left[(\delta_{ij} R_k + \delta_{ki} R_j + \delta_{jk} R_i) D^2 + R_i R_j R_k D^3 \right]} \qquad (9) \\
\mathbf{C}^{3,3}_{\mathrm{B}\to\mathrm{A},ijk} &= M^0 \left[(\delta_{ij} R_k + \delta_{ki} R_j + \delta_{jk} R_i) D^2 + R_i R_j R_k D^3 \right]. \qquad (10)
\end{aligned}$$

Box surrounded terms are new with respect to D2002. Note that the octopole term M^3 only appears in the $\mathbf{C}^{0,3}_{\mathrm{B}\to\mathrm{A}}$. Following D2002 we ignore this contribution since it does not affect the force field $\nabla\Phi$.

References

[1] W. Dehnen. A Hierarchical $\mathcal{O}(N)$ Force Calculation Algorithm. *Journal of Computational Physics*, 179:27–42, June 2002.

Index